



**UNIVERSIDAD DE CANTABRIA**

---

**TESIS DOCTORAL**

**MODELADO Y ANÁLISIS DE LA  
OPERACIÓN Y MANTENIMIENTO EN  
PARQUES EÓLICOS FLOTANTES**

---

Presentada por:

**MICHELE MARTINI**

Dirigida por:

**DR. ÍÑIGO J. LOSADA RODRÍGUEZ**

**DR. RAÚL GUANCHE GARCÍA**

Febrero 2017



**UNIVERSITY OF CANTABRIA**

---

**DOCTORAL THESIS**

**MODELIZATION AND ANALYSIS OF  
OPERATION AND MAINTENANCE OF  
FLOATING OFFSHORE WIND FARMS**

---

Prepared by:

**MICHELE MARTINI**

Advised by:

**DR. ÍÑIGO J. LOSADA RODRÍGUEZ**

**DR. RAÚL GUANCHE GARCÍA**

February 2017

*To Chiara*

This page is intentionally left blank.

# **Declaration**

I declare that this thesis was composed by myself, that the work contained herein is my own except where explicitly stated otherwise in the text, and that this work has not been submitted for any other degree or professional qualification except as specified.

Michele Martini

---

---

# Abstract

---

---

Nowadays, wind energy is one of the most competitive and reliable renewable sources for power generation. The installation of bottom-fixed wind turbines at sea is rapidly taking off due to high energy resource, proximity to demand centers and reduced availability of onshore sites. The use of floating platforms, proved by few pilot systems, could open up vast potential markets and help offshore wind reaching a relevant role in the renewable energy mix worldwide.

Operation, inspection and maintenance represent critical activities for a cost-effective implementation of offshore wind energy. They can account for up to a quarter of the final energy cost. This is mainly due to the difficulty of working at sea, far from the coast and in harsh weather conditions. This dissertation aims at reducing the risks and uncertainties associated to the long-term operation and maintenance (O&M) of floating wind farms.

Four specific problems were studied: the relationship between operational stops and energy yield, the temporal and spatial variability of accessibility, the risk of walk-to-work transfer and the impact of failures on electricity generation. Several innovative methodologies were developed in order to quantify long-term energy production, accessibility and safety of personnel transfer at sea.

It was possible to quantify the impact that downtime may have on the long-term energy yield and financial risk of floating farms. Platform motions and failures can affect significantly energy production and thus incomes. A vast accessibility analysis was carried out for the North Sea, and several indicators were quantified based on high-resolution hindcast data. A significant seasonal and year-by-year variability was observed. The feasibility of walk-to-work transfer was

found to be dependent not only on wave height, but also on wave period, direction and spreading. Results were determined by the specific vessel-platform combined response.

This work highlights the importance of using long-term metocean data when designing O&M strategies for offshore wind. In addition, it offers suggestions for improving current access procedures and “walk-to-work” personnel transfer. Finally, it provides recommendations to optimize existing strategies and adjust them for future floating farms.

---

---

## Acknowledgements

---

---

This thesis is the result of two years of intense activity at IH Cantabria. Such work was possible thanks to the “OceaNET” project, which received funding from the European Union’s 7<sup>th</sup> Framework Programme (G.A. Nr. 607656) under Marie Curie Actions for Initial Training Networks.

During this period, many people contributed to both my professional and human growth. I am grateful to every single person I met. To those who challenged me, for giving me the chance to beat them. To those who helped me, for making this thesis possible. Among the latter, some deserve special thanks:

Raúl Guanche, for his every-day wisdom, supervision, vision, strength and honesty.

Iñigo Losada, for his precious advice and activity behind the scenes.

The “Offshore Engineering and Ocean Energy group” at IH Cantabria, for its willingness.

The “International Network on Offshore Renewable Energy”, for its warmth.

The “OceaNET” fellows, for their professionalism during the time we shared.

Camilo, for its pure gentleness and friendship.

Matteo and Francesco, for lighting up many lonely nights regardless of the distance.

My family, for believing in me and respecting my choices.

Chiara, for her unconditioned love and trust.

---

---

# Table of contents

---

---

<b>ABSTRACT .....</b>	<b>6</b>
<b>ACKNOWLEDGEMENTS.....</b>	<b>8</b>
<b>TABLE OF CONTENTS.....</b>	<b>9</b>
<b>CHAPTER 1 INTRODUCTION.....</b>	<b>12</b>
1.1 RENEWABLE ENERGY FOR POWER GENERATION.....	12
1.2 THE ROLE OF OFFSHORE WIND ENERGY.....	14
1.3 FLOATING WIND TURBINES .....	17
<b>CHAPTER 2 PROBLEM STATEMENT .....</b>	<b>24</b>
2.1 THE <i>AVAILABILITY</i> CHALLENGE .....	24
2.2 OPERATION, INSPECTION AND MAINTENANCE.....	27
2.3 POSSIBLE SCENARIO FOR FLOATING SYSTEMS.....	32
<b>CHAPTER 3 OBJECTIVES AND STRUCTURE OF THE THESIS.....</b>	<b>33</b>
<b>CHAPTER 4 DESCRIPTION OF BASELINE DATA .....</b>	<b>35</b>
4.1 METOCEAN DATA .....	35
4.2 FLOATING WIND TURBINE CONCEPT DESCRIPTION .....	36
<b>CHAPTER 5 OPERATIONAL STOPS AND LONG-TERM ENERGY YIELD .....</b>	<b>43</b>
5.1 MOTIVATION AND STATE-OF-THE-ART REVIEW .....	43
5.2 METHODOLOGY .....	44
5.3 RESULTS: FLOATING WIND TURBINE IN SANTANDER, SPAIN .....	55
5.4 RESULTS: ACCURACY AND IMPACT OF SUBSET SIZE .....	70
5.5 CONCLUSIONS.....	76

<b>CHAPTER 6 TEMPORAL AND SPATIAL VARIATION OF ACCESSIBILITY .....</b>	<b>78</b>
6.1 MOTIVATION AND STATE-OF-THE-ART REVIEW .....	78
6.2 METHODOLOGY .....	79
6.3 RESULTS: NORTH SEA ACCESSIBILITY .....	86
6.4 RESULTS: ACCESSIBILITY OF EXISTING OR PLANNED WIND FARMS.....	98
6.5 CONCLUSIONS.....	104
<b>CHAPTER 7 MODELLING OF WALK-TO-WORK ACCESS .....</b>	<b>106</b>
7.1 MOTIVATION AND STATE-OF-THE-ART REVIEW .....	106
7.2 METHODOLOGY .....	107
7.3 RESULTS: TRANSFER TO THE OC4 FLOATING PLATFORM .....	117
7.4 RESULTS: COMPARISON WITH FIXED WIND TURBINE .....	137
7.5 RESULTS: LONG-TERM APPROACHABILITY IN AGUÇADOURA, PORTUGAL.....	140
7.6 CONCLUSIONS.....	149
<b>CHAPTER 8 DOWNTIME AND FLOATING WIND FARM ENERGY YIELD.....</b>	<b>152</b>
8.1 MOTIVATION AND STATE-OF-THE-ART REVIEW .....	152
8.2 METHODOLOGY .....	153
8.3 RESULTS: FLOATING WIND FARM IN SANTANDER, SPAIN .....	163
8.4 CONCLUSIONS.....	176
<b>CHAPTER 9 CONCLUSIONS .....</b>	<b>178</b>
<b>ANNEX I RESUMEN EN CASTELLANO .....</b>	<b>182</b>
1. INTRODUCCIÓN .....	182
2. PLANTEAMIENTO DEL PROBLEMA .....	186
3. OBJETIVOS .....	191
4. DATOS REFERENTES A LA CLIMATOLOGÍA Y A LA PLATAFORMA UTILIZADA.....	192
5. PARADAS OPERACIONALES Y PRODUCCIÓN DE UNA TURBINA FLOTANTE.....	193
6. VARIABILIDAD DE LOS PARÁMETROS DE ACCESIBILIDAD.....	199

7.	MODELADO DEL ACCESO <i>WALK-TO-WORK</i> A TURBINAS FLOTANTES.....	206
8.	IMPACTO DE LOS FALLOS SOBRE LA PRODUCCIÓN DE UN PARQUE FLOTANTE.....	212
9.	CONCLUSIONES.....	217
<b>ANNEX II SCIENTIFIC CONTRIBUTION OF THIS THESIS.....</b>		<b>220</b>
	PAPERS PUBLISHED OR UNDER REVIEW IN PEER REVIEWED SCI JOURNALS .....	220
	PAPERS IN OTHER JOURNALS .....	221
	CONFERENCE PAPERS .....	221
	CONFERENCE POSTERS .....	222
<b>REFERENCES .....</b>		<b>223</b>

---

---

# Chapter 1

## Introduction

---

---

### 1.1 Renewable energy for power generation

Signs of change in global energy trends have become evident in the last decades. The share of electricity produced with non-hydroelectric renewable sources passed from 0.6% in 1973 to 5.7% in 2013 [1], exceeding 4700 billion kWh in 2012 [2]. Figure 1 shows the year-by-year trend of renewable generated electricity worldwide.

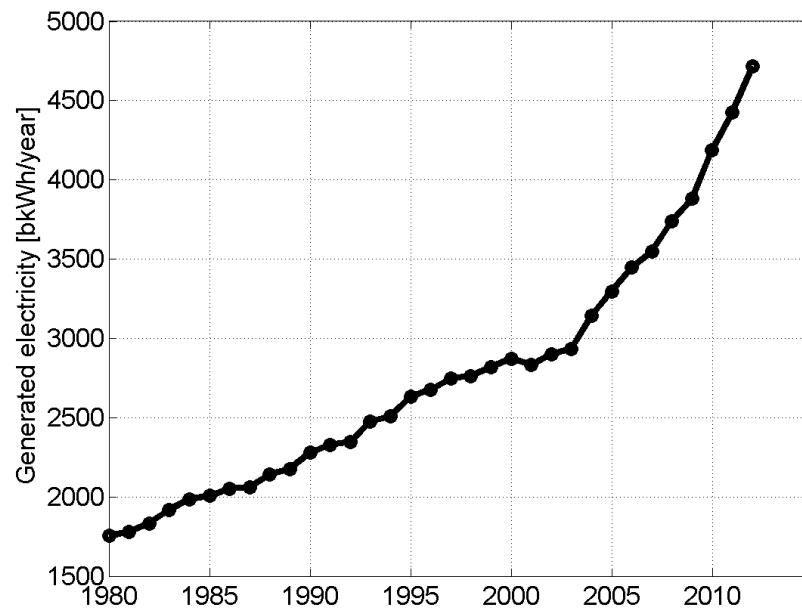


Figure 1: Worldwide renewable electricity generation, 1980-2012 [2].

Growth has been confirmed in 2014, despite a backdrop in global energy consumption and the decline of oil and gas prices: non-hydroelectric renewable power generation grew at its fastest

yearly rate to date (97 GW) and accounted for more than 34 % of net additions to the worldwide installed capacity [3], [4]. During the same year, data showed for the first time a marked decoupling in the relationship between economic growth and CO<sub>2</sub> emissions [5]. China, India and Brazil have been leaders in such development and are foreseen to account for two-thirds of the renewable expansion in the medium term [3]. Climate change, local pollution, energy security and geo-political instability of oil producing countries accelerated the development of renewable energy technologies for power generation. Figure 2 shows the annual investment in renewable energy in the decade 2004-2013. The average value has been 146 billion euros and the decrease in 2012 and 2013 was attributed to the fall of photovoltaic prices. For the fifth consecutive year, in 2014, renewables outpaced fossil fuels in terms of net investment in power capacity additions. An average annual investment of 203 billion euros is forecasted until 2020 [4].

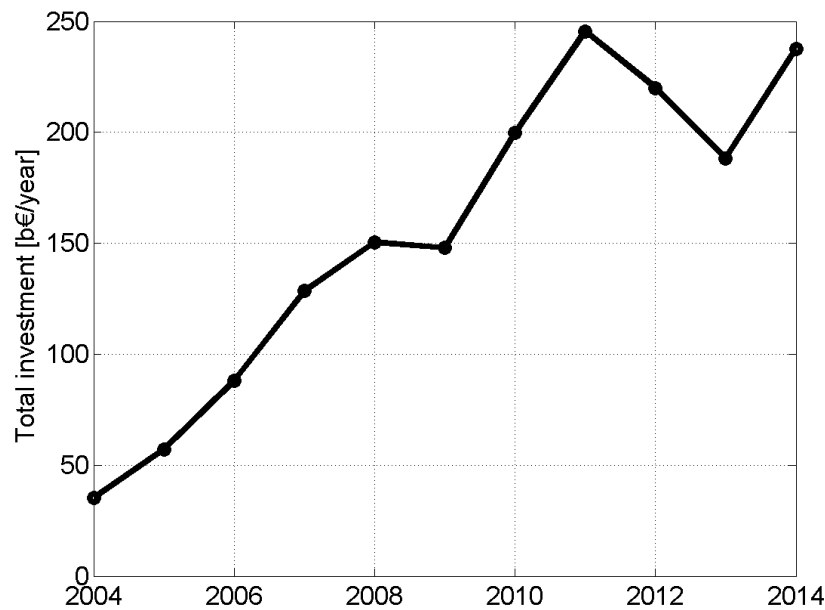


Figure 2: Worldwide investments in renewable energy, 2004-2014 [6].

The development of renewable energy has been shaped mostly by government policies. Mechanisms such as feed-in tariffs or subsidized tendering helped in increasing the investors'

confidence. In 2014, 164 countries had renewable policy targets while 108 jurisdictions had enacted feed in-policies at a national or state level [4]. Nevertheless, the increasing cost-competitiveness of renewable energy played a vital role in its successful development.

Among renewables, onshore wind leads the global growth having represented a third of the renewable capacity increase in 2014 [3]. Its cost of generation is progressively becoming comparable to that of fossil fuels: wind energy can be contracted today at a price of 53-70 €/MWh and in the best cases at 44 €/MWh (Brazil, Egypt, South Africa, part of US) [7]. That is, in several regions wind energy today is the most competitive renewable energy source.

## **1.2 The role of offshore wind energy**

According to the United Nations, 44% of the worldwide population lives in coastal areas [8]. Consequently, such regions most often present a very high energy demand. In addition, they frequently have limited space to develop land-based renewable resources.

Harnessing energy at sea, such as offshore wind, may thus become important from a strategic point of view. Offshore wind presents several advantages, compared to onshore: winds are less turbulent and more sustained, giving higher energy yield and higher power quality, while visual pollution and noise are largely reduced (which allows to increase machine size and efficiency).

The offshore wind industry is young, since it officially began in 1991 with the installation of the first offshore farm in Denmark. The 4.95 MW Vindeby farm, placed 2 km off the shore of Lolland in a water depth of approximately 5 m, was recently decommissioned [9]. Offshore wind technology took off quite rapidly since then. By the end of 2015 the capacity installed worldwide

reached 12 GW [10]. Europe, which leads the way with a share of 11 GW [11], has been showing an important growing trend in terms of annual installed capacity (see Figure 3).

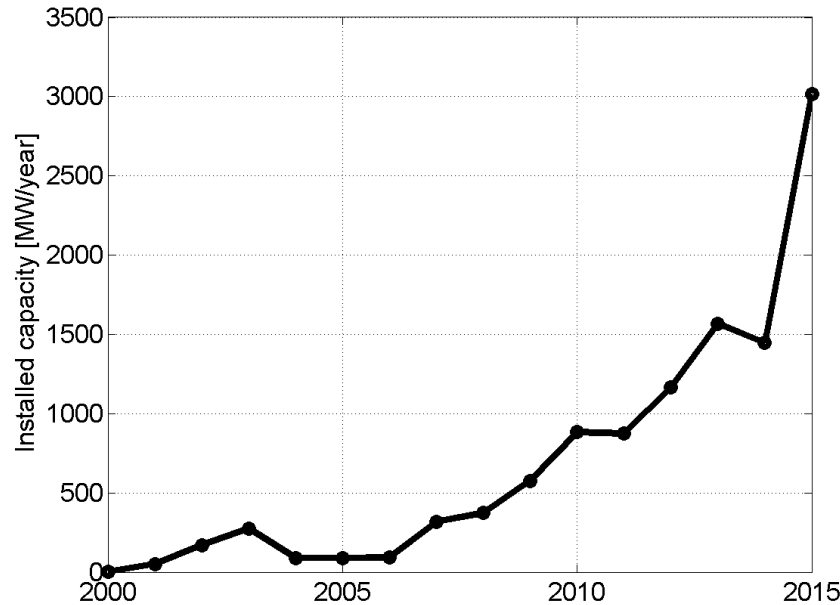


Figure 3: Annual offshore wind installed capacity in Europe [11].

The UK has the largest amount of installed offshore wind capacity, representing 45.9% of all installations. Germany follows with a share of 29.9%. Most of the farms are located in the North Sea (69%), where a high wind resource and a vast continental shelf boosted the market. The turbines are installed on monopiles (80%), gravity foundations (9.1%) jackets (5.4%) and tripods/tripiles (5.3%). Wind turbine size has grown by 41.1% from 2010 to 2015, passing from 3.0 MW to 4.2 MW, which reflects a continuous technological development to increase energy yields at sea. During the same time span, the average farm size has more than doubled from 155.3 MW to 337.9 MW. The consents recently granted in the North Sea provide indications for larger farms in the longer term [11]. In 2015 the total investment has been 13.3 billion euros, the highest ever recorded [12]. Remarkably, the wind industry is dedicating large resources to research and development: in 2010, the R&D expenditure accounted for 5.1% of industry's turnover, compared

to an average 2.1% of other sectors [13]. It is worth pointing out that data indicated in this paragraph refer to Europe only.

Figure 4 shows the average Levelized Cost Of Energy (LCOE) for offshore wind in the period 2000-2020, for both commissioned and proposed projects [14]. As it can be seen, the trend has been gradually increasing until 2012. The main reason for this is the increasing distance from the shore, which reflects national maritime spatial planning and developers' desire to harness larger energy resource but also increases costs in many aspects of the supply chain. In 2012 the average distance from the coast was 29 km and the average water depth 22 m. Looking at future consented projects, it is clear that this tendency will continue also in the future. The cost trend after 2012 is more encouraging, as the LCOE stabilized in the range between 106 and 176 €/MWh [14]. The expectation is that by 2020 the cost should drop to 100 €/MWh. It is remarkable that in a number of cases reality has gone far beyond expectations: in 2016, Dong has won a bid for the Borssele 1 and 2 wind farms (350 MW, Netherlands) at 72.70 €/MWh [15], while Vattenfall reached 49.90 €/MWh for the Kriegers Flak wind farm (600 MW, Denmark) [16]. These represent historical milestones that witness the fast evolution of the offshore wind market and the increasing affordability of new installations.

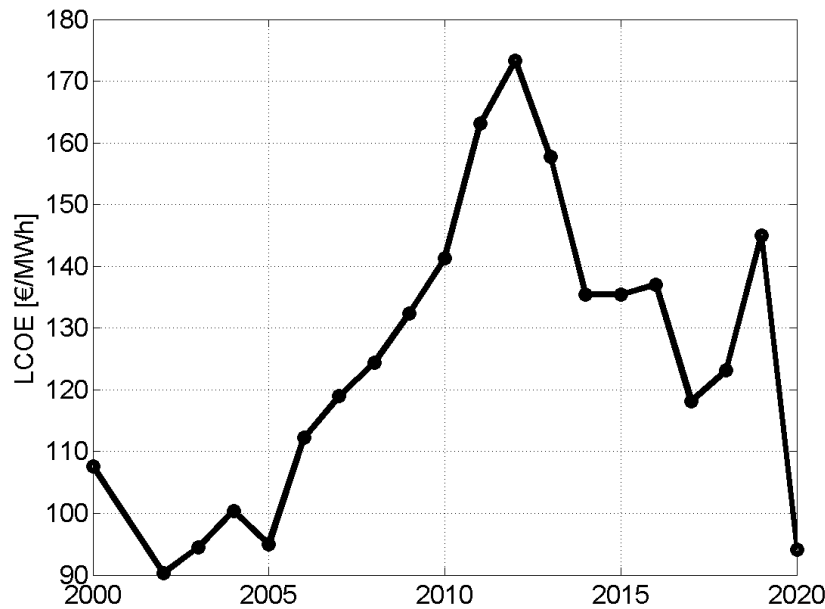


Figure 4: LCOE for offshore wind commissioned and proposed projects, 2000-2020 [14].

The price of offshore wind is likely to remain higher than onshore wind in the near future. This is due the increased investments in constructing and installing foundations at sea, transporting the structures, laying offshore cables and maintaining the turbines offshore. Nevertheless, offshore wind was proven an efficient and reliable renewable energy source. Considering also the progressive lack of land with good onshore resource and the reduced social acceptance close to demand centers, it is foreseen to play a major role in the future energy mix, particularly in Europe [7].

### 1.3 Floating wind turbines

Offshore wind energy development based on fixed foundations suffer a major constraint: it is not economically feasible for water depths exceeding 50 m [17]. The limited amount of shallow water locations restrains importantly the future market of such technology. Figure 5, Figure 6 and Figure 7 show the water depth for Europe, North America and a portion of Asia [18].

Regions colored in white are those for which water depth is below 50 m. Many regions do not present favorable bathymetry for the development of offshore wind with the current technology: among them Spain, Portugal, most of the Mediterranean countries, US west coast, China east coast and Japan.

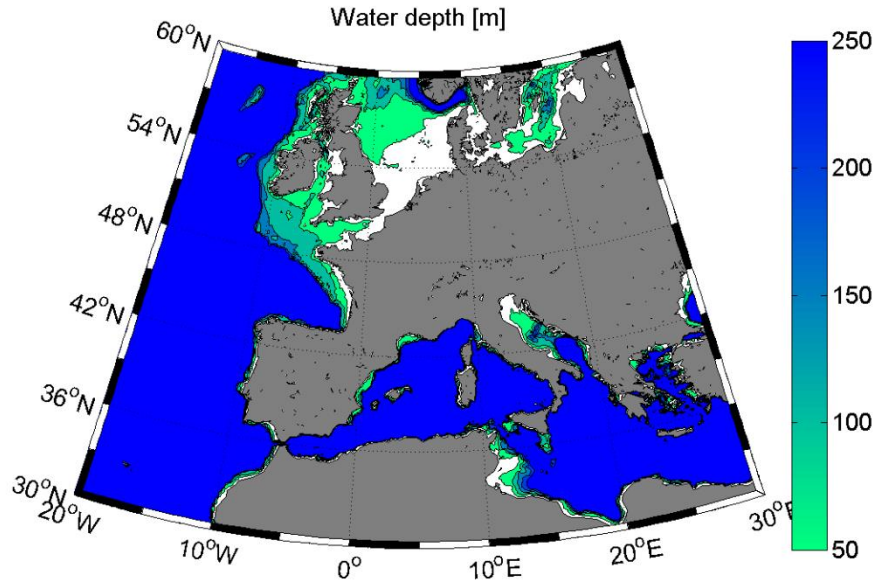


Figure 5: Water depth in Europe [18].

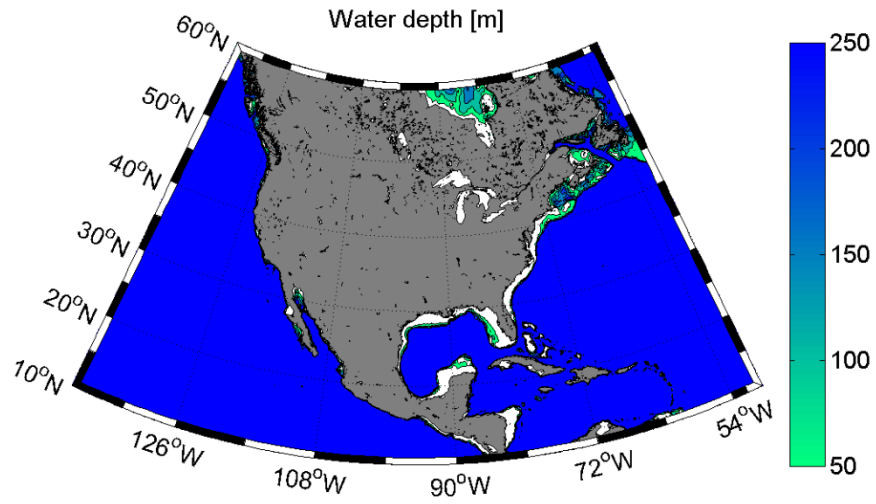


Figure 6: Water depth in North America [18].

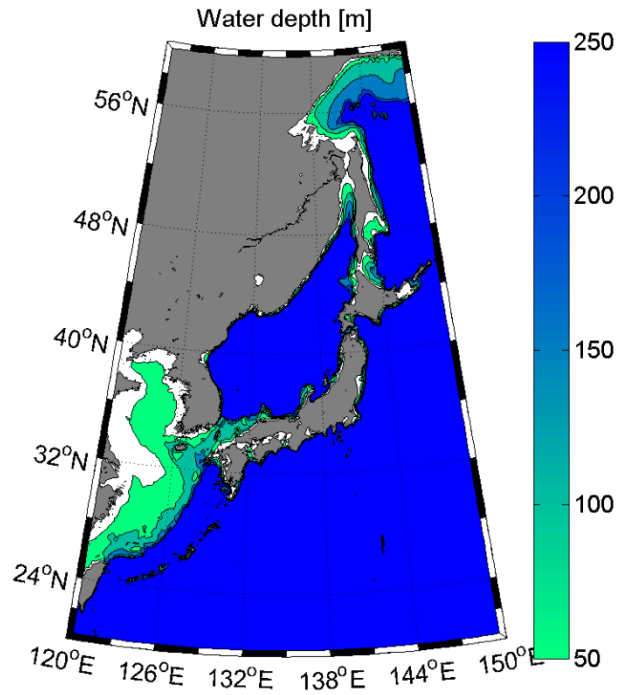


Figure 7: Water depth in Japan [18].

The natural alternative to fixed structures is to install wind turbines on floating platforms. This would help both in unlocking offshore markets close to coastal demand centers and in exploiting far offshore wind resource. The use of floating systems in deep water is not new: the oil and gas industry has been installing floating drilling units for decades worldwide. The experience gained with such structures represents an important benefit for the consolidation of the floating wind technology.

Different floating wind turbine concepts are being developed nowadays. The most used are the spar buoy, the semi-submersible and the tension leg platform, shown in Figure 8 from left to right, respectively. Each of them has different advantages and disadvantages, related to static stability, dynamic stability, production and installation costs [19].



*Figure 8: Different concepts of floating platform for offshore wind applications (courtesy of DNV)*

At the moment, only few full-scale prototypes have been deployed and tested at sea. In June 2009, Statoil installed the Hywind pilot in Norway in 220 m water depth (see Figure 9) [20]. It is a spar-type platform, with 5300 m<sup>3</sup> displacement moored to the seabed through three catenary mooring lines attached to anchor piles. Hywind mounts a 2.3 MW Siemens variable speed, variable

pitch wind turbine and has been successfully operating for 7 years now. The encouraging results obtained convinced Statoil to further develop the technology through the installation of the world's first floating wind farm. This will be located off the coast of Aberdeen, Scotland and consist of 5 turbines with rated power of 6 MW; fabrication of floaters has already begun and final commissioning is expected in 2017 [21], [22].



*Figure 9: The Hywind demo by Statoil (courtesy of Statoil).*

In October 2011, Principle Power and EDP deployed the WindFloat demo 6 km offshore of Agucadoura, Portugal in 50 m water depth (see Figure 10) [23]. The system consists of a three-legged semi-submersible platform with a water entrapment plat at each column base, with active ballast control. A 2 MW Vestas variable speed, variable pitch wind turbine is mounted on one of the three columns. The system operated well and Principle Power is planning the construction of floating farms both in Portugal and US [24].



*Figure 10: The WindFloat demo by Principle Power and EDP (courtesy of EDP).*

Remarkable milestones have been reached by Japan, in an extremely short time (since 2011). The Fukushima FORWARD project, funded by the Ministry of Economy, Trade and Industry, led to the installation of a 2 MW semi-submersible wind turbine, the first world floating substation, a 7 MW semi-submersible wind turbine and a 5 MW spar-type wind turbine [25] [26] [27]. Figure 11 shows a view of the assembly of the 7 MW system.



*Figure 11: The 7MW floating wind turbine by Fukushima FORWARD consortium (courtesy of consortium).*

The cost of floating wind systems is surely higher than that of fixed turbines. A study performed by Garrad Hassan calculated that, for a 500 MW floating wind farm at 50 m water depth, the cost of energy could be as low as 128 €/MWh [28]. However, there is room for important cost reductions. As they can accommodate larger turbines and be installed farther offshore, energy yield can be substantially increased. Furthermore, they can usually be assembled onshore and then towed out at sea, which reduces the duration of work at sea and the use of large vessels.

EWEA forecasts that by 2020 the offshore wind capacity in Europe may be 40 GW, and increase to 150 GW in 2030 [17]. Such growth is only achievable through the deployment of floating systems in deep waters.

---

---

## Chapter 2

### Problem statement

---

---

#### 2.1 The *availability* challenge

The *availability* of a wind turbine is defined as the percentage of time it is capable of producing electricity. As opposite, *downtime* is defined as the percentage of time it is incapable of generating energy. Downtime usually occur in correspondence of equipment stoppage, preventive maintenance or operational stops.

Equipment stoppage is caused by failures in any of the mechanical, electrical or structural components of the wind turbine. Its duration mainly depends on the size of the component to replace, on the complexity of the reparation and on the accessibility of the offshore farm location. Preventive maintenance is typically performed to preserve or restore equipment reliability by replacing worn components before failure. Such activities include overhauls at specific periods, lubrication, oil changes etc. and are usually executed during summer periods to reduce energy loss. Operational stops consist in shutting down the wind turbine in severe meteorological conditions, to avoid damage of the machine.

Current offshore wind farms typically achieve an availability between 80% and 95% while onshore values up to 97% are typically reached [29]. In early periods of operation, during running-in, availability might be even lower as reported for the UK Round 1 offshore wind farms [30]. Figure 12 shows availability data gathered by Fraunhofer-IWES for different offshore wind farms [31]. They are ordered chronologically by date of start-up: as it can be noticed, some had very low

availability in specific years of operation. It is nevertheless encouraging looking at the positive trend of the Egmond (Netherlands) and Alpha Ventus (Germany) farms.

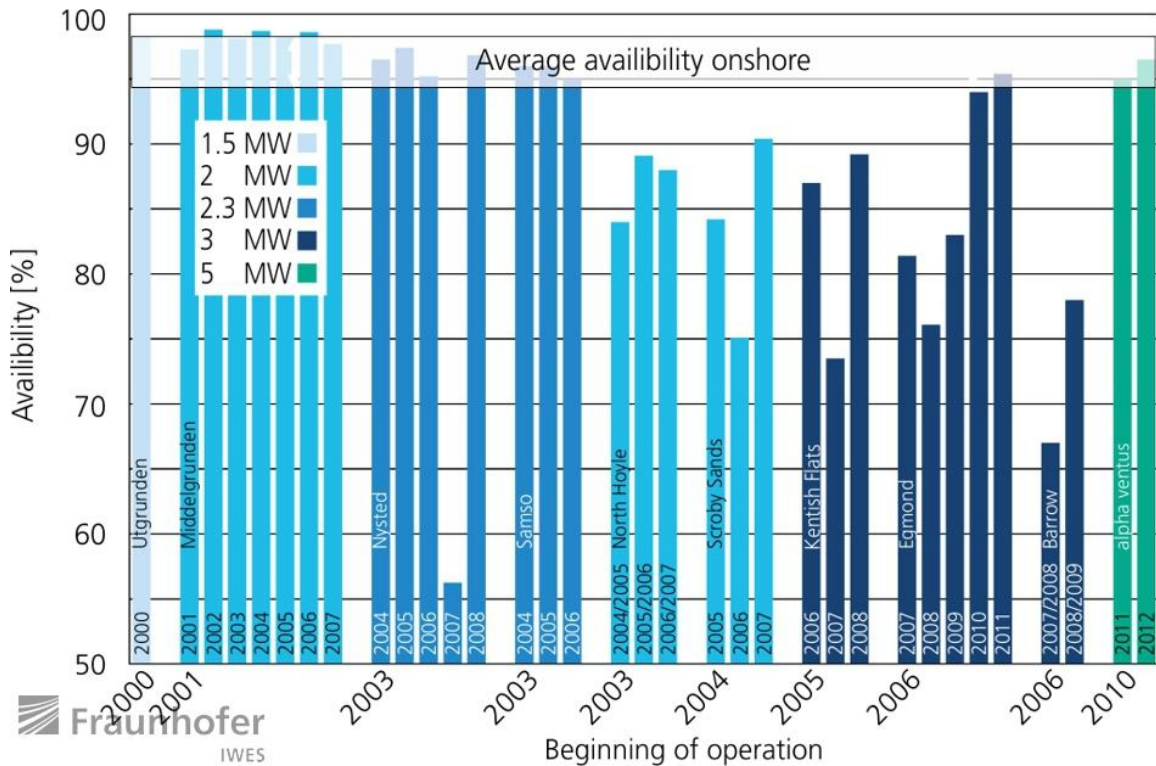


Figure 12: Availability of offshore wind farms in the period 2000-2010 (courtesy of Franuhofer-IWES).

To understand the complexity of reaching high values of availability, it was interesting to gather information about the operation of some of the currently installed largest wind farms: Anholt, London Array and Bard Offshore 1.

DONG Energy has declared that the Anholt 400 MW wind farm, located in the Danish portion of the Baltic Sea, achieved an availability of 97% in 2014 [32]. However, this target was not reached in 2015: a fault occurred on February, 21<sup>st</sup> on the farm export cable has prevented the transmission of electricity to land for weeks, being eventually fixed on March, 30<sup>th</sup> [33], [34]. Weather conditions were told to delay the identification of the fault and its reparation.

The London Array wind farm (630 MW) in England achieved a 95% availability during its first two years of operation [35]. In the same period, three major repairs took place: a main bearing,

a gearbox and a turbine transformer had to be replaced. Remarkably, the transformer fault put the respective turbine out of action for three months, due to difficulty in finding suitable vessels to carry it onshore [36].

The German wind farm Bard Offshore 1 (400 MW) faced serious technical problems which prevented energy generation for months [37], [38]. Stormy weather has been responsible for delays in construction and operation of the farm, which is installed at 100 km from the coast in 40 m waters.

The availability of an offshore wind farm is strongly correlated to its LCOE, which is most important indicator from an operator perspective. Figure 13 shows the relationship between availability and LCOE found by Douglas-Westwood in 2011 [39] for two case studies. It is evident that making offshore wind competitive does not depend only on reducing capital expenditure, but also on operating the wind farms effectively in the long-term.

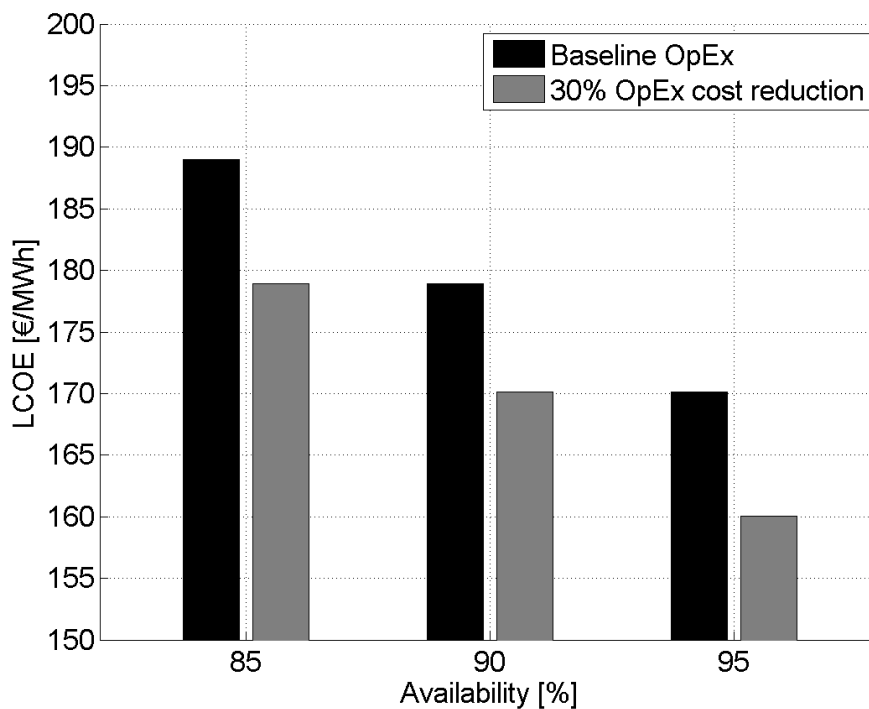


Figure 13: Impact of availability on LCOE, study realized by Douglas-Westwood in 2011 [39]

## 2.2 Operation, inspection and maintenance

The operation of a wind farm includes all the activities needed to ensure a safe and continuous production of electricity. In order to achieve high levels of availability and survive the offshore environment, adequate inspection and maintenance activities must be carried out.

Typically, an offshore wind farm is designed for a lifespan of 20-25 years. During this period, inspections must take place in order to detect or prevent failures. In its published offshore standards, the classification society Det Norske Veritas (DNV) suggests that activities should concern [40]:

- wind turbines;
- structural systems above water;
- structural systems below water;
- submerged power cables;
- offshore substations.

If floating systems are considered, mooring lines and anchors shall be added to this list [41]. For wind turbines, structural systems above water, offshore substations and other components regarded as critical, inspections should be performed at least once a year. For submerged power cables and structural systems below water, the time interval between inspections should be not longer than five years [40], [42]. In addition to this, the wind farm must be accessed in case of failure of any of its components, to reduce downtime and thus energy loss. The data collected during the “Scientific Measurement and Evaluation Programme” (WMEP) [43] showed that for onshore wind turbines there are, on average, 2.4 failures a year which result in 6 days of downtime. To the author’s knowledge, such a complete analysis is not available for offshore locations yet. Nevertheless those findings can be expected to be worse, taking into account that turbines tend to

be larger (thus likely to have higher failure rates [44]) and that weather can complicate inspection and maintenance operations, resulting in long down-times. These difficulties may result in a significant number of visits that have to be paid to the farm (four to six visits per wind turbine per year have been averagely estimated [45]). Condition monitoring systems represent a valid alternative to try optimizing the access frequency to offshore wind farms [46], [47].

Offshore wind turbines can be accessed either by helicopter or by boat. Boats can ensure personnel transfer in two ways: either landing through a fender on bumpers mounted on the wind turbine transition piece (see Figure 14) and allowing technicians to jump on a structure-mounted ladder, or using gangways through which people can walk to the tower, without any contact between the vessel and the turbine structure (see Figure 15). The green light for starting any operation is usually given by the metocean conditions and the associated vessel motions.



*Figure 14: Service vessel with fender, courtesy of Northern Offshore Services.*



Figure 15: Service vessel with gangway, courtesy of Ampelmann.

With no doubt, all the operations related to access, inspection and maintenance of offshore systems must be performed within rigorous safety limits to prevent any accident that would endanger the health of the personnel involved. The experience of the oil and gas industry, where several fatalities have occurred during personnel transfer [48], [49], and a series of near misses in the offshore wind industry [50], impose to use caution with the topic. Table 1 summarizes data about reported incidents for the offshore wind sector in 2014 [51].

<b>Key facts</b>	
959	Reported incidents
0	Fatalities
44	Total lost work days
651	Incidents occurred on operational sites

<b>Work process</b>	
228	Incidents during marine operations
140	Lifting operation incidents
134	Incidents occurred when operating plant and machinery

<b>Incident area</b>	
369	Incidents occurred in the turbine region
315	Incidents occurred onshore
243	Incidents occurred on vessels

Table 1: Reported incidents in offshore wind industry, 2014.

Several guidelines exist to regulate marine operations [52], [53] and offshore personnel transfer [54]–[56]. Many of them highlight the importance of using reliable weather data and forecasts, both at the design and the operational stage of wind farm life. Concerning data, seasonal variability should be taken into account [52] based on long periods of collection (up to twenty years [57]).

Operation and maintenance (O&M) typically have both fixed and variable costs. Fixed costs include service contracts for scheduled maintenance, insurance, administration and grid access fees. Variable costs include lost production due to downtime, unscheduled maintenance, parts replacement, materials and other labor costs [58]. Total costs of Operational Expenditure (OpEx) are expected to vary considerably according to different wind farm locations. Among other factors, the largest drivers of O&M costs have been recognized to be the distance between the farm and the maintenance facilities, and the metocean conditions at the project site [59]–[62].

Greater distances from the shore mean larger travel time between the port and the farm, which reduces the effective length of the working days. Precise and robust information about weather windows and their spatial/temporal variation becomes thus vital for planning effective long-term O&M strategies.

Greater distances from the shore also mean that turbines are exposed for longer periods to severe metocean conditions and thus likely to have higher failure rates [44]. The impact of failures and downtime on energy production of offshore wind in the long haul is still plenty of uncertainty.

Due to the youngness of offshore wind industry and site-specific particularities, it is difficult to have precise estimates of the O&M costs. Garrad Hassan estimates that O&M may represent about 25% of the LCOE [63]. The International Renewable Energy Agency (IRENA) stated that overall O&M costs are expected to be in the range 24 to 47 €/MWh [7]. Deloitte

quantified OpEx cost between 20.4 and 44 €/MWh [64]. It is interesting to mention that the first Scottish offshore wind farm (Robin Rigg, 174 MW) has been operated between 2010 and 2011 with an operational expenditure (OpEx) of 20 €/MWh [65]. Figure 16 shows the breakdown of the operational expenditure as estimated by Deloitte in which maintenance, port activities and operations have the largest impact.

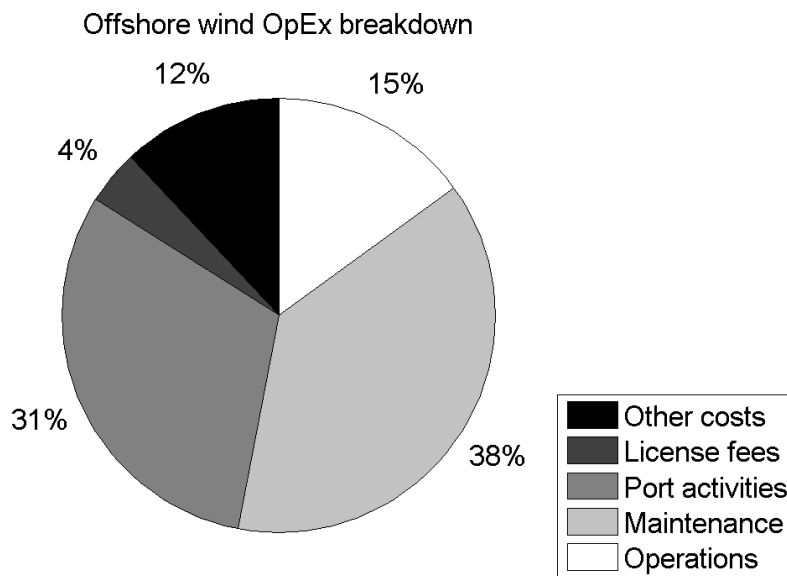


*Figure 16: Breakdown of OpEx for offshore wind in 2015, study realized by Deloitte in 2015 [64].*

Gathered data indicate that O&M represent a major challenge for both present and future farms. The growing offshore wind industry needs to combine both cost-effective and safe strategies to ensure successful long-term operations and make the technology more and more competitive.

## **2.3 Possible scenario for floating systems**

The complexity of O&M activities and their impact on the energy cost might be even more relevant for floating systems. All the problems for fixed structures related to greater distances from the shore equally apply to floating wind. In addition, platform motions are likely to increase difficulty in different aspects of O&M [19].

The inertial loading that originates from system accelerations may decrease the reliability of several subsystems and components. Operational stops, which usually prevent turbine from being damaged by severe wind conditions, may be needed for wind speeds below cut-out if wave-current conditions induce large platform motions. Access of the wind turbine for inspection and maintenance, by means of boats or helicopters, might be more complicated due to the relative motions between the access mean and the platform.

The short experience with real scale prototypes is reflected into a relevant level of uncertainty with the long-term performance of floating wind turbines. Reducing costs, uncertainty of O&M and thus financial risk is crucial.

---

---

## Chapter 3

# Objectives and structure of the thesis

---

---

The main objective of this dissertation is to provide tools for the reduction of uncertainty and risks in the long-term operation and maintenance of floating wind turbines. Based on the information gathered in the previous chapters, this topic is identified as major challenge for the future cost-competitiveness of floating wind energy. The following points specifically give motivation for such effort:

- the growing trend of offshore wind in the global renewable energy mix;
- the potential for market and cost reduction of floating technologies;
- the impact that O&M have on the LCOE of offshore wind;
- the risks that are associated with access of marine structures.

The short experience with full-scale floating turbines at sea enhances the need for research and development on the matter. This work is far from providing a definitive solution to operation and maintenance of offshore wind, which falls beyond the possibilities of a Ph.D. thesis given the broadness of the topic. Nevertheless, four specific problems have been detected as of primary importance and found to be weakly (or not at all) treated in the literature. This led to the development of methodologies that can hopefully fill the identified gaps and help the progress of the sector. The studied topics are:

- the relationship between operational stops and long-term energy yield;
- the temporal and spatial variability of offshore accessibility parameters;

- the evaluation of walk-to-work transfer for floating platforms;
- the impact of failures and downtime on electricity generation of a floating wind farm.

A separate section is dedicated to each topic (Chapter 5, Chapter 6, Chapter 7 and Chapter 8, respectively), comprising detailed motivation state-of-the-art review, methodology, results and discussion. Chapter 9 finally contains conclusions and recommendations for future work.

As long-term behavior is detected as a major source of uncertainty for floating wind energy, a large use of hindcast metocean data is made throughout this dissertation. Therefore, Chapter 4 is dedicated to describe and qualify the databases used to obtain wind and wave data. In addition, the same Chapter contains information about an open-source floating wind platform that is widely used in this work to apply the proposed methodologies.

---

---

## Chapter 4

# Description of baseline data

---

---

### 4.1 Metocean data

In recent years, climate reanalysis databases have become a valuable source of information for a wide range of ocean and coastal engineering applications. Generated by third generation models, they are nowadays able to hindcast useful data about metocean climate to complement instrumental measurements [66]–[68].

This investigation makes an extensive use of the reanalysis databases developed at the Environmental Hydraulics Institute of Cantabria (IH Cantabria). Long-term time series of wind and wave conditions are available with high spatial and temporal resolution. These were calibrated with satellite data and validated against field data. Regarding sea state parameters, IH Cantabria has generated a global wave dataset named GOW (Global Ocean Waves) [69], simulated with the model WaveWatch III [70] and driven by the NCEP-CFS reanalysis winds and ice fields [67]. The model includes modelling of non-linear wave-wave interactions, whitecapping and effects of depth-induced refraction. The spatial resolution is  $0.125^\circ$  both in latitude and in longitude, the time resolution is 1h and data is available from 1979 to 2014. Data is provided in form of wave significant wave height, peak period, mean direction and mean directional spreading.

The use of these data is not directly recommended in very shallow water coastal areas ( $\sim 10$  m), river estuaries or where island blocking plays a role, since dynamics associated to diffraction

and reflection phenomena are not well solved. For such locations, a dynamic downscaling of ocean data should be carried out [71]–[73].

Wind data comes from the database named SeaWind II [74], simulated with the model WRF (Weather Research & Forecasting) and the module ARW (Advanced Research dynamical solver) developed by NCAR (National Center for Atmospheric Research) [75], and driven by ERA-Interim wind fields [76]. The spatial resolution is  $0.125^\circ$  both in latitude and in longitude, the time resolution is 1h and data is available from 1990 to 2013. Data is provided in form of undisturbed wind mean speed (extracted at a height of 90 m, which is a reference for 5 MW wind turbines [77], [78] used in this work) and mean direction.

As a convention, wind and wave are defined to have a 0 degrees direction when heading from North to South, a 90 degrees direction when heading from East to West.

## **4.2 Floating wind turbine concept description**

### **4.2.1 General information**

The floating wind turbine considered in this dissertation is the composed by the OC4-DeepCwind semi-submersible platform (“OC4” from now on) [79] and the NREL 5 MW machine [78]. This system consists in a main central column and three offset columns (equipped with heave plates) and is moored to the seabed by means of three catenary lines.

Table 2 includes a summary of its properties (mass and geometry). Furthermore, Figure 17 defines the default orientation of the inertial coordinate system  $(x_g, y_g, z_g)$  with respect to the cardinal points, and the orientation of the platform with respect to it at rest. The  $x_g$ - $y_g$  plane lies on the still water plane in conditions static equilibrium (i.e. buoyancy and gravity balance out).

**Mass and geometry**

Displacement	13473	t
Total draft	20	m
Diameter of main column	6.5	m
Diameter of offset columns	12	m
Diameter of heave plates	24	m
Depth to centre of mass	13.46	m
Roll/pitch inertia	6.827E+9	kg m <sup>2</sup>
Yaw inertia	1.226E+10	kg m <sup>2</sup>

Table 2: Main properties of the OC4 semi-submersible platform [79].

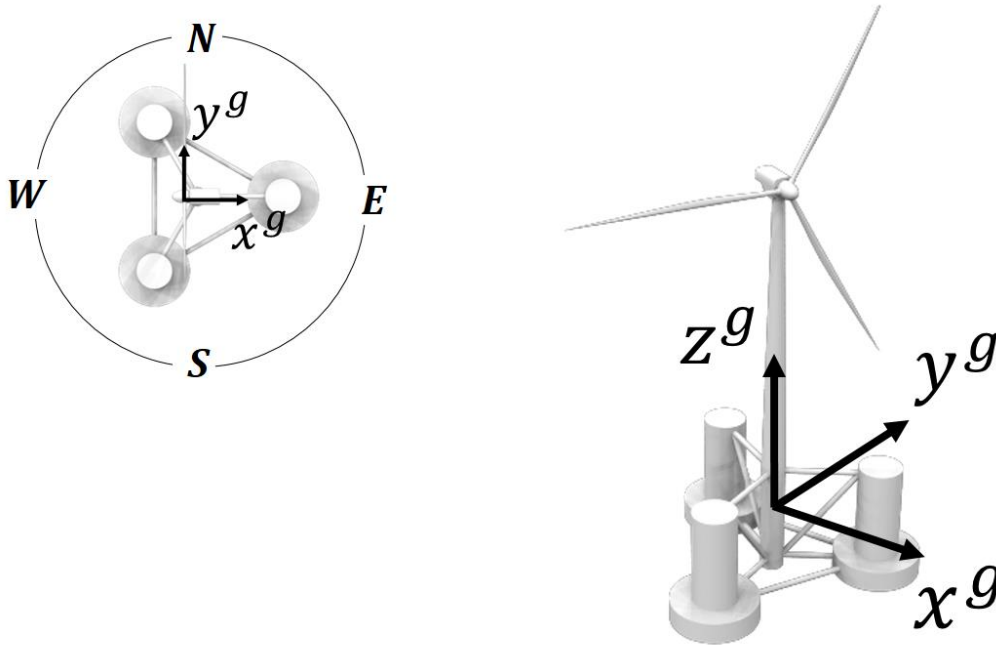


Figure 17: Sketch of the OC4 platform with the NREL 5 MW offshore wind turbine.

### 4.2.2 Hydrodynamic properties

A hydrodynamic analysis has been performed on the OC4 platform using HydroD, the boundary-element potential-flow solver of the software SESAM by DNV-GL. Table 3 shows the hydrostatic stiffness matrix of the platform while Figure 18, Figure 19 and Figure 20 show the Response Amplitude Operators (RAOs) of the unmoored system (for three different wave headings).

Description of baseline data

	Surge	Sway	Heave	Roll	Pitch	Yaw
Surge	0 N/m	0 N/m	0 N/m	0 N/rad	0 N/rad	0 N/rad
Sway	0 N/m	0 N/m	0 N/m	0 N/rad	0 N/rad	0 N/rad
Heave	0 N/m	0 N/m	3.79E+06 N/m	0 N/rad	0 N/rad	0 N/rad
Roll	0 Nm/m	0 Nm/m	0 Nm/m	8.81E+08 Nm/rad	0 Nm/rad	0 Nm/rad
Pitch	0 Nm/m	0 Nm/m	0 Nm/m	0 Nm/rad	8.81E+08 Nm/rad	0 Nm/rad
Yaw	0 Nm/m	0 Nm/m	0 Nm/m	0 Nm/rad	0 Nm/rad	0 Nm/rad

Table 3: Hydrostatic stiffness matrix of the OC4 platform.

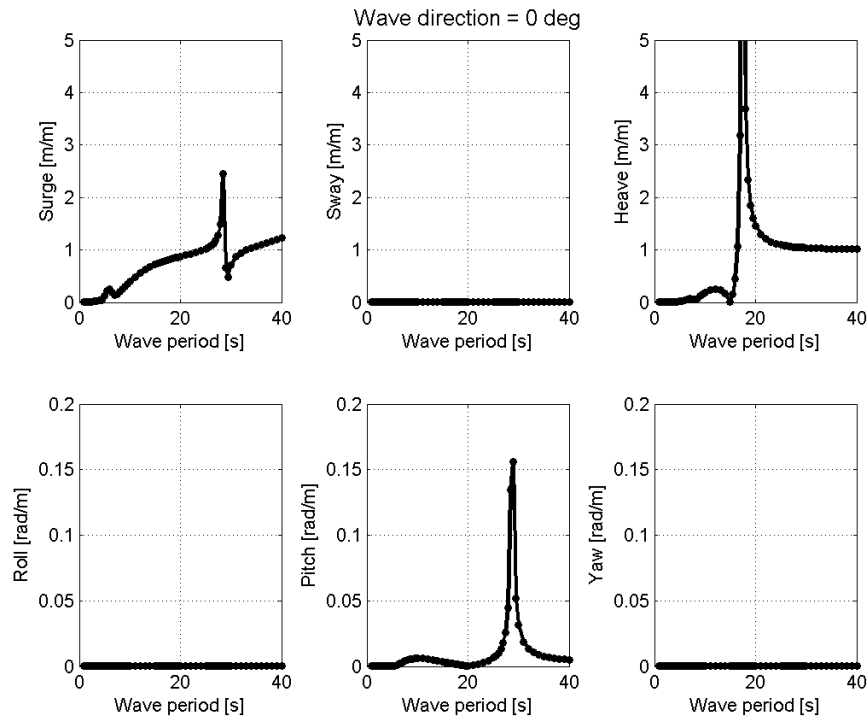


Figure 18: RAOs of the unmoored OC4 platform, wave direction is 0 degrees.

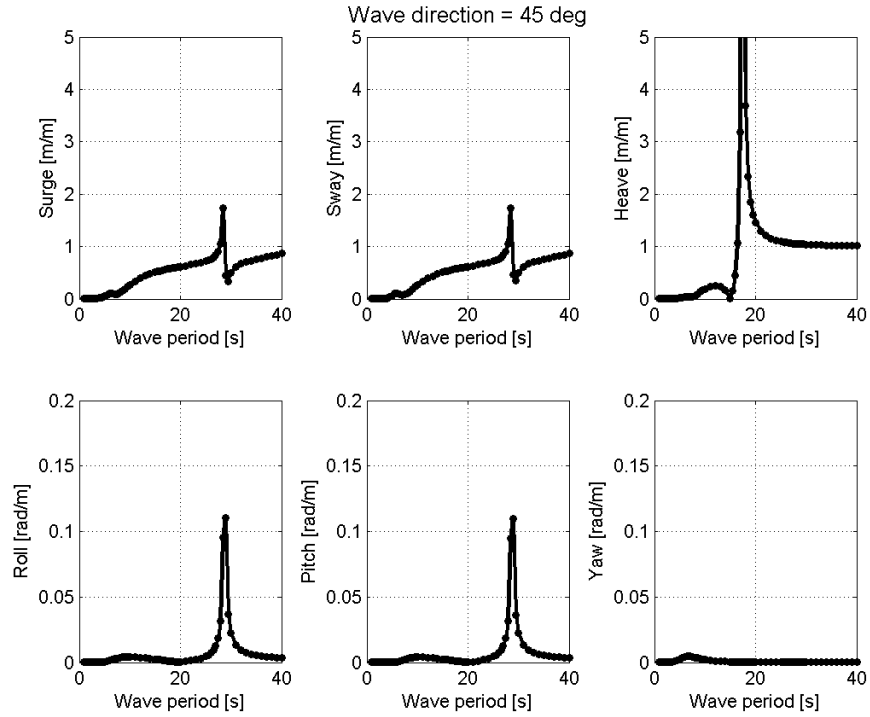


Figure 19: RAOs of the unmoored OC4 platform, wave direction is 45 degrees.

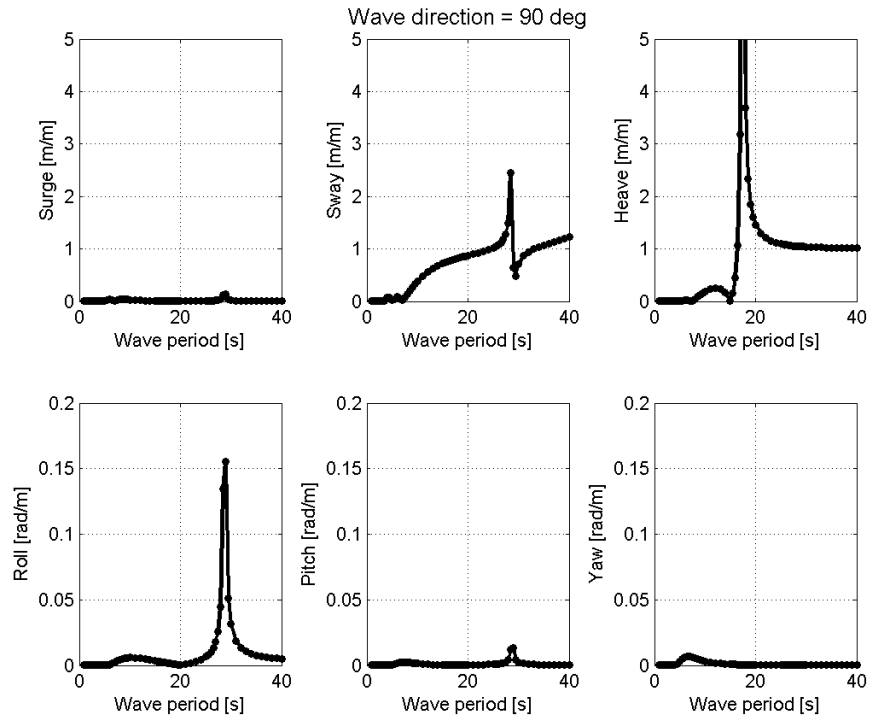


Figure 20: RAOs of the unmoored OC4 platform, wave direction is 90 degrees.

Table 4 contains the infinite-frequency added mass matrix as calculated by HydroD. Furthermore, viscous effects are modelled using a quadratic damping matrix, reported in Table 5. These coefficients were calibrated by NREL through numerical simulations in which the platform columns were modelled as Morison elements [79].

	Surge	Sway	Heave	Roll	Pitch	Yaw
Surge	6.33E+06 kg	0 Kg	0 kg	0 N/(rad/s <sup>2</sup> )	8.55E+07 N/(rad/s <sup>2</sup> )	0 N/(rad/s <sup>2</sup> )
Sway	0 kg	6.33E+06 Kg	0 kg	8.54E+07 N/(rad/s <sup>2</sup> )	0 N/(rad/s <sup>2</sup> )	0 N/(rad/s <sup>2</sup> )
Heave	0 kg	0 Kg	1.50E+07 kg	0 N/(rad/s <sup>2</sup> )	0 N/(rad/s <sup>2</sup> )	0 N/(rad/s <sup>2</sup> )
Roll	0 Nm/(m/s <sup>2</sup> )	8.55E+07 Nm/(m/s <sup>2</sup> )	0 Nm/(m/s <sup>2</sup> )	7.35E+09 kg m <sup>2</sup>	0 kg m <sup>2</sup>	0 kg m <sup>2</sup>
Pitch	8.54E+07 Nm/(m/s <sup>2</sup> )	0 Nm/(m/s <sup>2</sup> )	0 Nm/(m/s <sup>2</sup> )	0 kg m <sup>2</sup>	7.35E+09 kg m <sup>2</sup>	0 kg m <sup>2</sup>
Yaw	0 Nm/(m/s <sup>2</sup> )	0 Nm/(m/s <sup>2</sup> )	0 Nm/(m/s <sup>2</sup> )	0 kg m <sup>2</sup>	0 kg m <sup>2</sup>	4.90E+09 kg m <sup>2</sup>

Table 4: Infinite-frequency added mass matrix of the OC4 platform.

	Surge	Sway	Heave	Roll	Pitch	Yaw
Surge	3.95E+05 N/(m/s) <sup>2</sup>	0 N/(m/s) <sup>2</sup>	0 N/(m/s) <sup>2</sup>	0 N/(rad/s) <sup>2</sup>	0 N/(rad/s) <sup>2</sup>	0 N/(rad/s) <sup>2</sup>
Sway	0 N/(m/s) <sup>2</sup>	3.95E+05 N/(m/s) <sup>2</sup>	0 N/(m/s) <sup>2</sup>	0 N/(rad/s) <sup>2</sup>	0 N/(rad/s) <sup>2</sup>	0 N/(rad/s) <sup>2</sup>
Heave	0 N/(m/s) <sup>2</sup>	0 N/(m/s) <sup>2</sup>	3.88E+06 N/(m/s) <sup>2</sup>	0 N/(rad/s) <sup>2</sup>	0 N/(rad/s) <sup>2</sup>	0 N/(rad/s) <sup>2</sup>
Roll	0 Nm/(m/s) <sup>2</sup>	0 Nm/(m/s) <sup>2</sup>	0 Nm/(m/s) <sup>2</sup>	3.70E+10 Nm/(rad/s) <sup>2</sup>	0 Nm/(rad/s) <sup>2</sup>	0 Nm/(rad/s) <sup>2</sup>
Pitch	0 Nm/(m/s) <sup>2</sup>	0 Nm/(m/s) <sup>2</sup>	0 Nm/(m/s) <sup>2</sup>	0 Nm/(rad/s) <sup>2</sup>	3.70E+10 Nm/(rad/s) <sup>2</sup>	0 Nm/(rad/s) <sup>2</sup>
Yaw	0 Nm/(m/s) <sup>2</sup>	0 Nm/(m/s) <sup>2</sup>	0 Nm/(m/s) <sup>2</sup>	0 Nm/(rad/s) <sup>2</sup>	0 Nm/(rad/s) <sup>2</sup>	4.08E+09 Nm/(rad/s) <sup>2</sup>

Table 5: Additional quadratic damping matrix of the OC4 platform.

### 4.2.3 Mooring system properties

The OC4 platform is secured with three catenary lines that are spread symmetrically about the platform  $z_g$ -axis. Each fairlead is connected to the top edge of a heave plate. When the platform is at rest, the first line is directed along the  $x_g$ -axis while the remaining two lines are located 120 degrees apart, when looking from the top (see Figure 21). The main properties of the mooring lines are reported in Table 6.

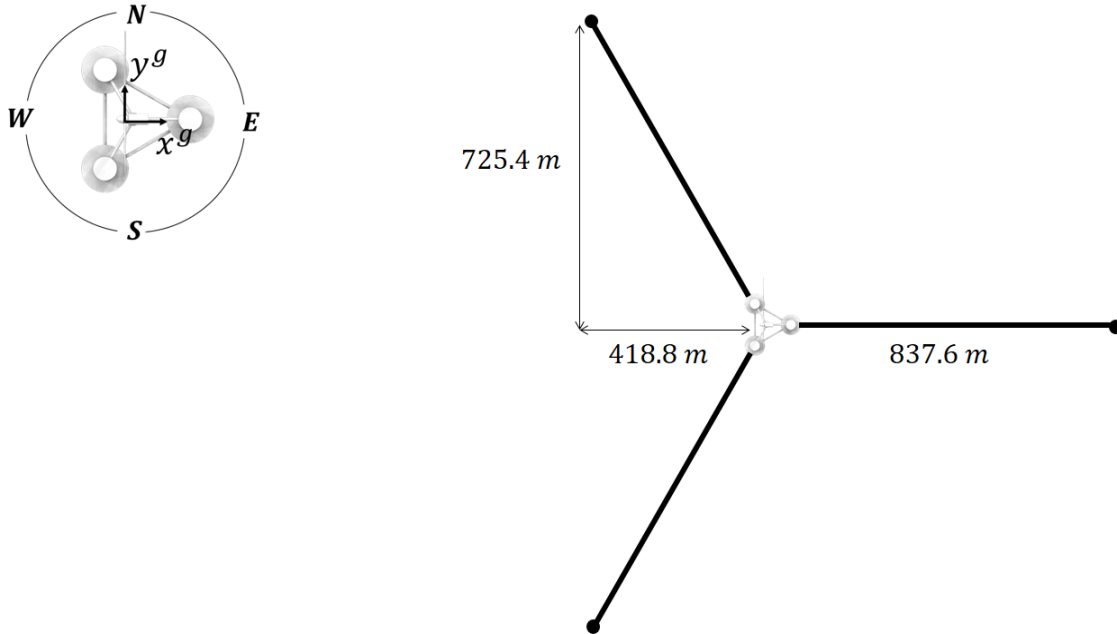


Figure 21: Mooring layout of the OC4 platform. Drawing is out of scale.

Mooring system		
Number of lines	3	-
Depth to anchors	200	m
Depth to fairleads	14	m
Unstretched line length	835.5	m
Radius to anchors from platform centreline	837.6	m
Line diameter	0.0766	m
Line mass in water	108.63	kg/m
Equivalent extensional stiffness	753.6	MN

Table 6: Mooring line properties of the OC4 platform [79].

#### 4.2.4 Wind turbine properties

The NREL 5 MW reference wind turbine is a conventional three-bladed upwind variable-speed variable blade-pitch-to-feather-controlled turbine. A summary of its properties is contained in Table 14. Furthermore, Figure 22 shows the variation of the thrust coefficient,  $C_T$  and the power coefficient,  $C_P$  with the wind speed.

Wind turbine		
Power rating	5	MW
Rotor, hub diameter	126, 3	M
Hub height	90	m
Cut-in, rated, cut-out wind speed	3, 11.4, 25	m/s
Cut-in, rated rotor speed	6.9, 12.1	rpm
Overhang, shaft tilt precone	5, 5, 2.5	m, deg, deg
Rotor, nacelle, tower mass	110, 240, 347.46	tons

Table 7: Main properties of the NREL 5 MW reference wind turbine [78].

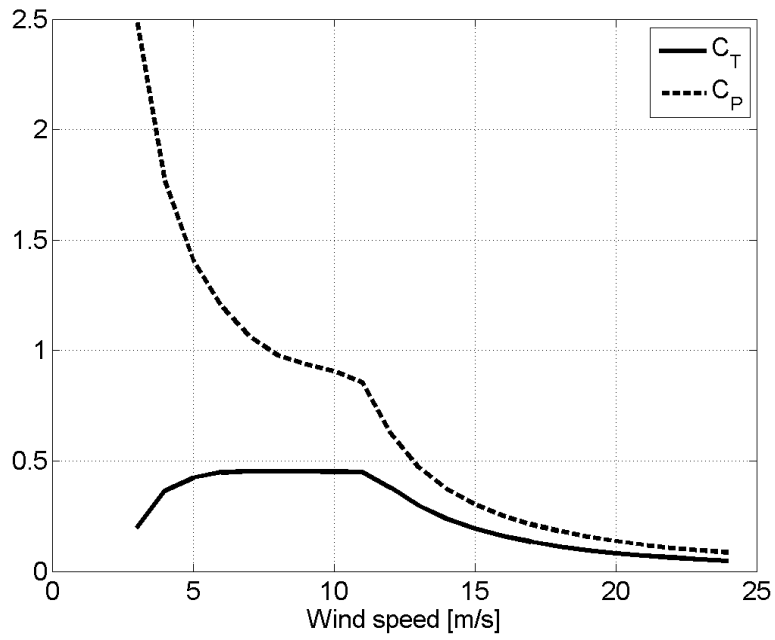


Figure 22: Thrust and power coefficient of NREL 5 MW reference wind turbine [78].

# Operational stops and long-term energy yield

---

---

## 5.1 Motivation and state-of-the-art review

Floating wind turbines are complex systems subject to the combined action of wind, waves and currents. The platform motions resulting from fluid-structure interaction generate forces that do not exist for fixed turbines. High or abnormal loading conditions may thus occur for wind speeds below conventional cut-out values for fixed structures ( $25 \text{ ms}^{-1}$ , typically) and impose an “operational stop” i.e. switching off the machine to avoid undesired damage of any component. The resulting downtime is associated to a decrease of availability and a loss of energy production. Operational stops may be triggered by platform motions exceeding certain safety thresholds.

It is difficult to determine a-priori when the turbine can be operated and when not, as its response depends on a large number of metocean parameters (among them: wave significant height, peak period, spectrum shape, mean direction, directional spreading; wind mean speed, mean direction, turbulence; current mean speed, mean direction). Wind turbines are conceived for a lifetime of 20-25 years and usually their design relies on long-term hindcast data. Since metocean information are often provided with a time resolution of 1-3 hours, it might be computationally expensive to calculate the platform motions for each available data sample. For example, if the simulation of a single sea state takes 1 minute, and 20 years of data are available with 1-hour resolution, the total simulation time would be about 2920 hours.

This Chapter illustrates a methodology that aims at evaluating the impact of operational stops on the long-term energy production of a floating wind turbine, with a reduced computational effort.

It was difficult to find studies with similar purposes in the literature, though operational shutdowns are contemplated in existing normative [41], [80]. Ren et al. [81] evaluated the energy production of a combined wind/wave platform for a large number of metocean data samples. However, this was only a secondary result of a study dedicated to mooring fatigue damage and performed using a scatter diagram (thus with a lower detail level compared to hindcast data), without investigating the impact of operational thresholds or providing a solution to decrease computational cost. Amundsen [82] assessed the influence of introducing a cut-out wave height on the energy yield of a floating wind turbine, though without bridging metocean conditions and system response. The work presented in this Chapter is based on previous research developed by Guanche Y. [83] and Guanche R. [84], which focused on the life-cycle loads of floating and fixed wind turbines for survivability purposes. That methodology is here extended and applied for energy production calculations.

## **5.2 Methodology**

The proposed methodology is based on the following five steps:

- 1) selection of a subset of metocean data through advanced selection techniques;
- 2) direct simulation of turbine response for the selected subset of metocean data;
- 3) identification of relevant wind turbine operating parameters;
- 4) reconstruction of operating parameters over the original metocean database through non-linear interpolation techniques;

5) evaluation of the impact of operational stops on the long-term energy yield.

Each of the five steps is discussed in the following pages, from Section 5.2.1 to Section 5.2.5. The illustrated methodology is then applied to a floating wind turbine located off the coast of Santander, Spain in Section 5.3. Finally, Section 5.4 contains an assessment of the results' accuracy and Section 5.5 conclusions about this Chapter.

### **5.2.1 Selection of a subset of metocean data**

Several selection techniques were proposed to handle engineering problems dealing with large amounts of data. Among them, it is worth mentioning K-means algorithms [85], self-organizing maps [86] and Maximum Dissimilarity Algorithms (MDA) [87]. Based on previous successful experience both in coastal and offshore engineering applications [72], [88], [89], the MDA is chosen for this work.

The purpose of the MDA is to select, from a database consisting of  $N$  samples, a representative data subset consisting of  $M$  samples with  $M < N$ . If the database is  $X = \{\mathbf{x}_1, \mathbf{x}_2, \dots, \mathbf{x}_N\}$ , this algorithm picks out a data subset  $S_M = \{s_1, s_2, \dots, s_M\}$  trying to maintain the variability of the original information. The higher the value of  $M$ , the more the subset is able to represent the database variability but also the more computationally expensive is the algorithm. The elements  $\mathbf{x}_i$  and  $s_j$  are in general vectors of dimension  $n$ . The selection starts choosing an initial subset vector  $s_1$  from the database. The remaining  $M-1$  elements are selected recursively, calculating the dissimilarity between each sample remaining in the database and the elements already in the subset, and transferring the most dissimilar one to the subset. The process ends when  $M$  iterations are reached.

Several algorithm variants were developed [90], depending upon the selection of the initial subset vector and the numerical definition of “dissimilarity”. In this work, the “MaxMin” version of the algorithm is applied and here illustrated.

As an example let the subset  $S_R$  be composed by  $R$  vectors with  $R < M$ , during the algorithm execution. The dissimilarity  $d_{i,S_R}$  between the vector  $\mathbf{x}_i$  and the subset  $S_R$  is evaluated as:

$$d_{i,S_R} = \min\{\|\mathbf{x}_i - \mathbf{s}_j\|\}; j = 1, \dots, R \quad \text{Equation 1}$$

where the symbol “ $\| \ / \ \|$ ” represents the Euclidean-Circular norm i.e. for directional data the distance between 0 deg and 360 deg is zero. The next data sample joining the subset is selected as the one with the highest dissimilarity among the  $N-R$  analysed i.e. the one for which  $d_{i,S_R}$  is largest:

$$\mathbf{s}_{R+1} = \{\mathbf{x}_i \in X - S_R | d_{i,S_R} \text{ is largest}\} \quad \text{Equation 2}$$

In order to reduce the computational effort of the MDA, which is  $O(M^2N)$ , the algorithm developed by Polinsky [91] is applied. This allows reducing the number of computations to  $O(MN)$ . The calculation of  $d_{i,S_R}$  is modified so that it does not imply to evaluate all the norms  $\|\mathbf{x}_i - \mathbf{s}_j\|$ . Its value is defined instead as the minimum between two quantities: the dissimilarity between  $\mathbf{x}_i$  and the last vector transferred to the subset, and the dissimilarity between  $\mathbf{x}_i$  and the  $R-2$  vectors of the subset determined in the second-last cycle. Therefore:

$$d_{i,S_R} = \min(\|\mathbf{x}_i - \mathbf{s}_{R-1}\|, d_{i,S_{R-2}}) \quad \text{Equation 3}$$

being:

$$d_{i,S_{R-2}} = \min\|\mathbf{x}_i - \mathbf{s}_j\|, j = 1, \dots, R - 2 \quad \text{Equation 4}$$


---

As an example, the MDA has been applied to a cloud of bi-dimensional ( $n=2$ ) data with  $N=1000$  samples, generated with a random Gaussian distribution. A subset of  $M=10$  samples has been picked up. Figure 23 shows the results of the selection: black points are database samples, red points are subset samples. Number aside of red points represents the progressive numbering of subset elements. It can be noticed how the algorithm picks up subset elements that try to keep the original data variability.

Once the amount of metocean data is reduced, platform motions are calculated for each of the subset samples using a floating turbine numerical model.

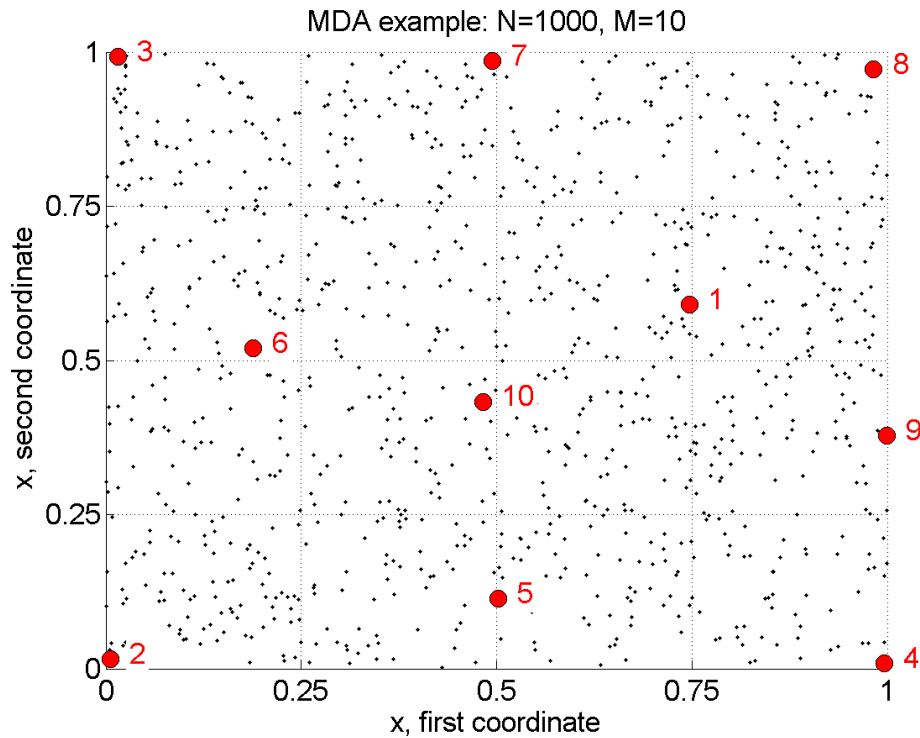


Figure 23: Application of MDA to a sample cloud of data.

## 5.2.2 Simulation of floating wind turbine response

The response of the floating wind turbine is simulated through a numerical model that solves rigid-body dynamics under the action of aerodynamic, hydrodynamic and mooring forces.

Currents are not considered at this stage. The motion of the system is described in body-fixed coordinates through Cummins' time domain equation [92]:

$$(\mathbf{M} + \mathbf{A}_\infty)\ddot{\boldsymbol{\zeta}}(t) + \int_0^t \mathbf{h}_r(t - \tau)\dot{\boldsymbol{\zeta}}(\tau)d\tau + \mathbf{C}\boldsymbol{\zeta}(t) = \mathbf{F}_h(t) + \mathbf{F}_a(t) + \mathbf{F}_m(t) \quad \text{Equation 5}$$

In the expression above  $t$  represents the time,  $\boldsymbol{\zeta}$  the platform six degrees of freedom displacement vector (surge, sway, heave, roll, pitch and yaw),  $\mathbf{M}$  the inertia matrix,  $\mathbf{A}_\infty$  the added mass matrix for infinite oscillation frequency,  $\mathbf{C}$  the hydrostatic restoring matrix due to buoyancy and gravity,  $\mathbf{h}_r$  the impulse response function matrix of the radiation forces. On the right hand side  $\mathbf{F}_h$  is the wave force vector,  $\mathbf{F}_a$  the aerodynamic force vector and  $\mathbf{F}_m$  the mooring force vector. It is worth recalling that using Equation 5 implies that inertias and moments must be calculated with respect to the centre of gravity of the system.

### 5.2.2.1 Hydrodynamics

The hydrodynamic properties of the floater are identified once the values of  $\mathbf{A}_\infty$ ,  $\mathbf{h}_r$  and  $\mathbf{F}_h$  are known. Neglecting for the moment aerodynamic and mooring forces, Cummins' equation can be converted to frequency domain as [93]:

$$\{-\omega^2[\mathbf{M} + \mathbf{A}(\omega)] + j\omega\mathbf{B}(\omega) + \mathbf{C}\}\boldsymbol{\zeta}(j\omega, \theta) = \frac{H}{2}\mathbf{f}_h(j\omega, \theta) \quad \text{Equation 6}$$

where  $j$  is the imaginary unit,  $\omega$  the wave frequency,  $\theta$  the wave heading,  $\mathbf{A}$  and  $\mathbf{B}$  the frequency-dependent real-valued added mass and potential damping matrices,  $\mathbf{f}_h$  the complex-valued wave excitation force coefficients vector and  $H$  the wave height. The relationship between time domain and frequency domain parameters was shown by Ogilvie [94] as:

$$\mathbf{A}(\omega) = \mathbf{A}_\infty - \frac{1}{\omega} \int_0^\infty \mathbf{h}_r(t) \sin(\omega t) dt \quad \text{Equation 7}$$

$$\mathbf{B}(\omega) = \int_0^{\infty} \mathbf{h}_r(t) \cos(\omega t) dt \quad \text{Equation 8}$$

It therefore also follows that:

$$\mathbf{h}_r(t) = \frac{2}{\pi} \int_0^{\infty} \mathbf{B}(\omega) \cos(\omega t) d\omega \quad \text{Equation 9}$$

$$\mathbf{A}_{\infty} = \mathbf{A}(\omega) + \frac{1}{\omega} \int_0^{\infty} \mathbf{h}_r(t) \sin(\omega t) dt \quad \text{Equation 10}$$

In this Chapter, the coefficients  $\mathbf{A}$ ,  $\mathbf{B}$ ,  $\mathbf{C}$  and  $\mathbf{f}_h$  are calculated using software HydroD developed by DNV [95], which is based on a boundary element method potential-flow solver. Once such coefficients are known, it is possible to calculate  $\mathbf{h}_r$  and  $\mathbf{A}_{\infty}$  using Equation 9 and Equation 10 [96]. It is worth mentioning that commercial softwares often provide directly the  $\mathbf{A}_{\infty}$  matrix. Excitation forces  $\mathbf{F}_h$  are defined by means of a random-phase first order wave load model as:

$$\mathbf{F}_h(t) = \sum_{k=1}^K \sqrt{2S_{\eta\eta}(\omega_k)\Delta\omega_{\eta\eta}} |\mathbf{f}_h(\omega_k, \theta)| [\cos \omega_k t + \psi_k + \angle \mathbf{f}_h(\omega_k, \theta)] \quad \text{Equation 11}$$

where  $S_{\eta\eta}$  is the one-sided wave spectrum,  $\Delta\omega_{\eta\eta}$  the angular frequency resolution of the wave spectrum,  $\psi_k$  a random phase and  $K$  the number of discrete frequencies considered. Wave spreading and second order hydrodynamic loads are not considered at this stage.

### 5.2.2.2 Aerodynamics

Aerodynamic forces acting on a wind turbine are typically calculated by means of unsteady blade element momentum theory [97]. Often, such models are coupled with multi-body solvers to take into account elastic deformation of blades and tower [98]. However, to predict platform motions of a floating turbine, a simpler formulation may be used.

First, the motions of a floating wind turbine are dominated by rigid-body motion rather than elastic deformations. This makes it possible to neglect structural elasticity and explains the use of the Cummins' equation. In second place, the floating platform natural periods associated to its rigid-body motion are usually in the order of tens of seconds. This means that forces varying at a much smaller time scale, such as unsteady aerodynamic loads given by high frequency turbulence and wind shear, have a minor impact on its response. This suggests to approximate the flow-turbine interaction using a thrust force acting on the rotor hub, proportional to the wind turbine static thrust coefficient and the relative wind speed seen at the hub itself. This approach was proposed by Karimirad and Moan [99] and gave acceptable results for the nacelle motions, when compared against HAWC2 by DTU [100].

The relative wind speed seen by the wind turbine hub,  $v_h^*$ , is calculated as:

$$v_h^*(t) = v(t)\mathbf{n}_v - [\mathbf{v}_G(t) + \mathbf{\Omega}(t) \times \mathbf{r}_{G,h}] \quad \text{Equation 12}$$

where  $v$  is the undisturbed axial wind speed at hub height,  $\mathbf{n}_v$  the unit vector in the direction of the axial wind speed,  $\mathbf{v}_G$  the translational velocity of the floating platform centre of gravity,  $\mathbf{\Omega}$  the angular velocity of the floating platform and  $\mathbf{r}_{G,h}$  the position of the hub relative to the platform centre of gravity. The wind speed  $v$  is calculated as:

$$v(t) = \sum_{q=1}^Q \sqrt{2S_{vv}(\omega_q)\Delta\omega_{vv}} \cos(\omega_q t + \psi_q) \quad \text{Equation 13}$$

where  $S_{vv}$  is the wind speed spectrum,  $\Delta\omega_{vv}$  the angular frequency resolution of the wind spectrum,  $\psi_q$  a random phase and  $Q$  the number of discrete frequencies considered. Neither longitudinal nor lateral wind speed components are considered at this stage.

It is assumed that only the component of the relative wind speed normal to the rotor contributes to the thrust, and that the nacelle is always aligned with the main wind direction. If  $\mathbf{n}_r$  is the unit vector normal to the rotor plane, the “effective” wind speed seen by the hub,  $\mathbf{v}_h$ , is therefore:

$$\mathbf{v}_h = (\mathbf{v}_h^* \cdot \mathbf{n}_r) \mathbf{n}_r \quad \text{Equation 14}$$

Then, the thrust force  $\mathbf{T}$  is calculated as:

$$\mathbf{T}(t) = \left[ \frac{1}{2} A \rho \|\mathbf{v}_h(t)\|^2 C_T(\|\mathbf{v}_h(t)\|) \right] \mathbf{n}_r \quad \text{Equation 15}$$

where  $A$  is the rotor area,  $\rho$  the air density and  $C_T$  the static thrust coefficient. The aerodynamic force vector  $\mathbf{F}_a$  is finally calculated as:

$$\mathbf{F}_a(t) = \left\{ \begin{array}{l} \mathbf{T}(t) \\ \mathbf{r}_{G,h} \times \mathbf{T}(t) \end{array} \right\} \quad \text{Equation 16}$$

Gyroscopic effects, arising from the interaction between the rotor angular momentum and the floating platform angular speed, are neglected.

The use of the steady thrust coefficient calculated considering a conventional blade pitch controller, which has a negative slope for wind speed above rated, may introduce negative damping at the platform pitch natural frequencies [101]. The operation with a well-designed blade pitch controller which avoids this phenomenon, such as that implemented on the Hywind demo by Statoil [102], is simulated applying a band-reject filter centred at the pitch natural frequency to the calculated relative wind speed, before using it for the calculation of the rotor thrust [99]. The implementation of the filter is done in time domain using a recursive formula [103].

### 5.2.2.3 *Mooring forces*

The mooring system action is simulated using a quasi-static formulation. With this approach, mooring forces only depend on the elastic properties of the line and the instantaneous position of the platform. Inertia and damping effects on the lines are not considered. This approach is well-known in the field of offshore engineering and not discussed here; a more detailed formulation, in the context of floating wind energy, was given by Jonkman [98] and Masciola [104]. It is important to state that the quasi-static formulation works sufficiently well when the displacements of the floating platform are small, which often occurs during operating conditions. On the other side, such model is not able to model the forces resulting from large displacements which are typical of extreme sea and wind states.

### 5.2.3 **Identification of relevant operating parameters**

A wind turbine is designed to operate within certain load limits, in order to avoid damage or failure of any mechanical and electrical component. For floating systems, these limits may be related to platform motions. From the structural point of view, platform motions give additional loading on critical components of the system. For example, the tower-base bending moment gets two additional contributions if compared to bottom-fixed turbines: the static combined effect of tower inclination and tower-top mass overhang, and the inertial contribution due to the nacelle accelerating mass [105]. The heeling angle of the tower can also alter, negatively, lubrication distribution in gearboxes or bearing loading [19]. Nacelle acceleration and tower inclination are also considered critical parameters in relevant DNV guidelines [41].

Based on these considerations platform roll, platform pitch and wind turbine hub acceleration (norm of the vector) are chosen as relevant operating parameters for a floating wind

turbine. This means that their value should be below given safety thresholds to ensure a safe operation of the system.

#### 5.2.4 Reconstruction of operating parameters

Once operating parameters are identified and simulated for the selected subset of metocean data, it is possible to extrapolate results for the original set of metocean conditions through non-linear interpolation techniques. The method used here is based on Radial Basis Functions (RBF), which is considered convenient for scattered and multivariate data. The RBF approximation has been applied successfully in many fields, including to coastal engineering applications [72], often obtaining a higher accuracy when compared to other interpolation methods [106].

Let us assume that  $y=f(\mathbf{x})$  is the real-valued objective function that needs to be approximated. The available data consists of  $M$  values of the objective function,  $\{y_1, y_2, \dots, y_M\}$ , evaluated in correspondence of the subset data samples  $\{s_1, s_2, \dots, s_M\}$ , such that:

$$y_j = f(\mathbf{s}_j), j = 1, \dots, M \quad \text{Equation 17}$$

The RBF interpolation method is based on a weighted sum of radially symmetric basic functions located at the subset data points. The approximation function  $\tilde{f}$  takes the form:

$$\tilde{f}(\mathbf{x}) = p(\mathbf{x}) + \sum_{j=1}^M a_j \Phi(\|\mathbf{x} - \mathbf{s}_j\|) \cong f(\mathbf{x}) \quad \text{Equation 18}$$

where  $\Phi$  is the radial basis function,  $p(\mathbf{x})$  is a monomial basis formed of  $n$  monomials of degree 1 and a monomial of degree 0, being  $\mathbf{b} = \{b_0, b_1, \dots, b_n\}$  the coefficients of these monomials.

The RBF coefficients and the monomial coefficients  $\mathbf{b}$  can be calculated by enforcing the interpolation constraints:

$$\tilde{f}(\mathbf{s}_j) \equiv f(\mathbf{s}_j) = y_j, j = 1, \dots, M \quad \text{Equation 19}$$

The radial basis function  $\Phi$  may take several forms and a Gaussian shape is used here as:

$$\Phi(\|\mathbf{x} - \mathbf{s}_j\|) = e^{-\left(\frac{\|\mathbf{x} - \mathbf{s}_j\|}{r_0}\right)^2} \quad \text{Equation 20}$$

The parameter  $r_0$  affects the shape of the radial basis function and thus have an important impact on the accuracy of the interpolation. An algorithm for choosing its value was proposed by Rippa [107] and applied here. This consists in minimizing a cost function that imitates the error between the radial interpolant and the unknown function from which the data vector was sampled. Using the RBF approximation, through Equation 18 to Equation 20, the chosen operating parameters can therefore be interpolated over the original, entire set of metocean conditions.

### **5.2.5 Impact of operational stops on long-term energy yield**

When any of the operating parameters exceeds a specific threshold, the wind turbine is supposed to be shut down and thus not to generate electricity. In order to quantify these effects, the floating wind turbine availability and capacity factor are calculated. It is here recalled that availability is the percentage of time the turbine is producing electricity, while the capacity factor is the ratio between the produced energy and the energy that would be produced if the machine were working always at its rated power.

## 5.3 Results: floating wind turbine in Santander, Spain

### 5.3.1 Offshore climate

The illustrated methodology is applied to a hypothetical floating wind turbine located off the coast of Santander, Spain (latitude: 43.5000°, longitude: -3.8125°), where the water depth is 55 m. Wave and wind data with 1 hour resolution were extracted from the reanalysis database of IH Cantabria (see Chapter 4), for a twenty year period (1994-2013). Figure 24 and Figure 25 show roses for significant wave height and mean wind speed, respectively. It is possible to notice that there is only one predominant wave direction, which is NW. This direction is also associated with the highest values of the significant wave height. On the other hand, wind has three preferred directions that are W, E and S-SW. The extreme wind events are associated mainly with the W direction.

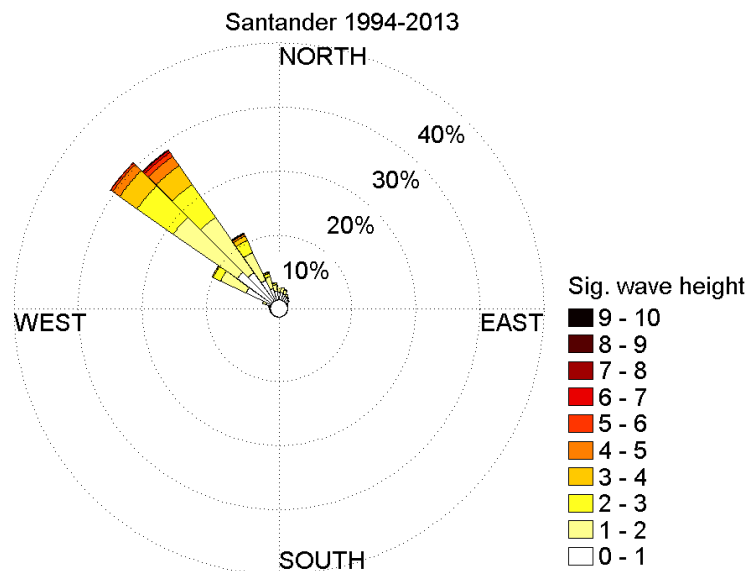


Figure 24: Wave rose for Santander, Spain in the period 1994-2013.

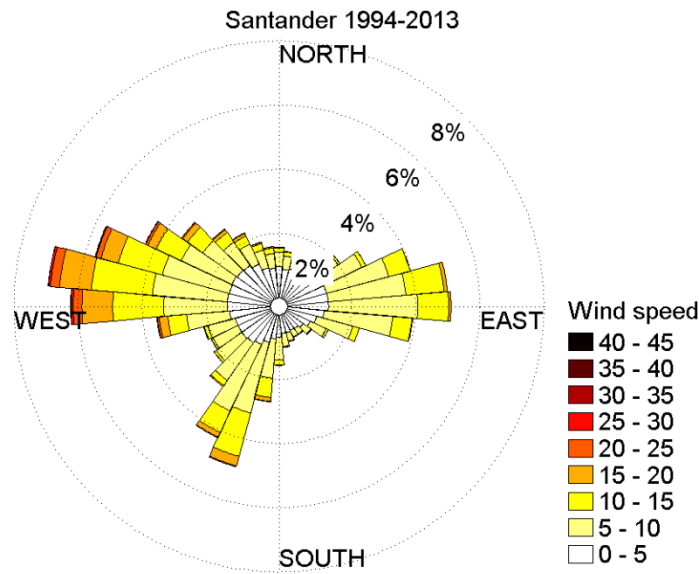


Figure 25: Wind rose for Santander, Spain in the period 1994-2013.

### 5.3.2 Metocean data selection

The MDA algorithm was applied to the available metocean data characterizing the chosen offshore location. In this case, each vector of the data sample has five components: significant wave height, wave peak period, wave mean direction, mean wind speed, wind mean direction. The number of data samples is  $N=175220$ . The number of subset elements was selected to be  $M=1000$ , while the subset initial vector chosen is the one with the highest wave power. Figure 26 depicts the original data set (black points) and the selected subset (red points). The execution of the algorithm took about 24 hours<sup>1</sup>. It is possible to notice how the samples that the MDA has selected for the subset span a very high variability, including extreme events characterized by high values

<sup>1</sup> On a desktop PC Intel(R) Core(TM) i7 CPU @2.67 GHz. Other computational times mentioned in this chapter refer to the same computer.

of wave height and wind speed. The selected 1000 ocean climate conditions were used to generate wind and wave time-series using Equation 11 and Equation 13. Wave spectrum was set to JONSWAP with a shape factor equal to 3.3. Wind spectrum was set to Kaimal, for which the wind speed standard deviation  $\sigma_v$  is calculated based on the mean wind speed  $V$  as suggested by the International Electrotechnical Commission [108]:

$$\sigma_v = I_{Ref}(0.75V + 5.6); V \text{ in } \text{ms}^{-1} \quad \text{Equation 21}$$

where value  $I_{ref} = 0.12$  is chosen, which is typical for offshore wind turbines.

Santander 1994-2013; M = 1000

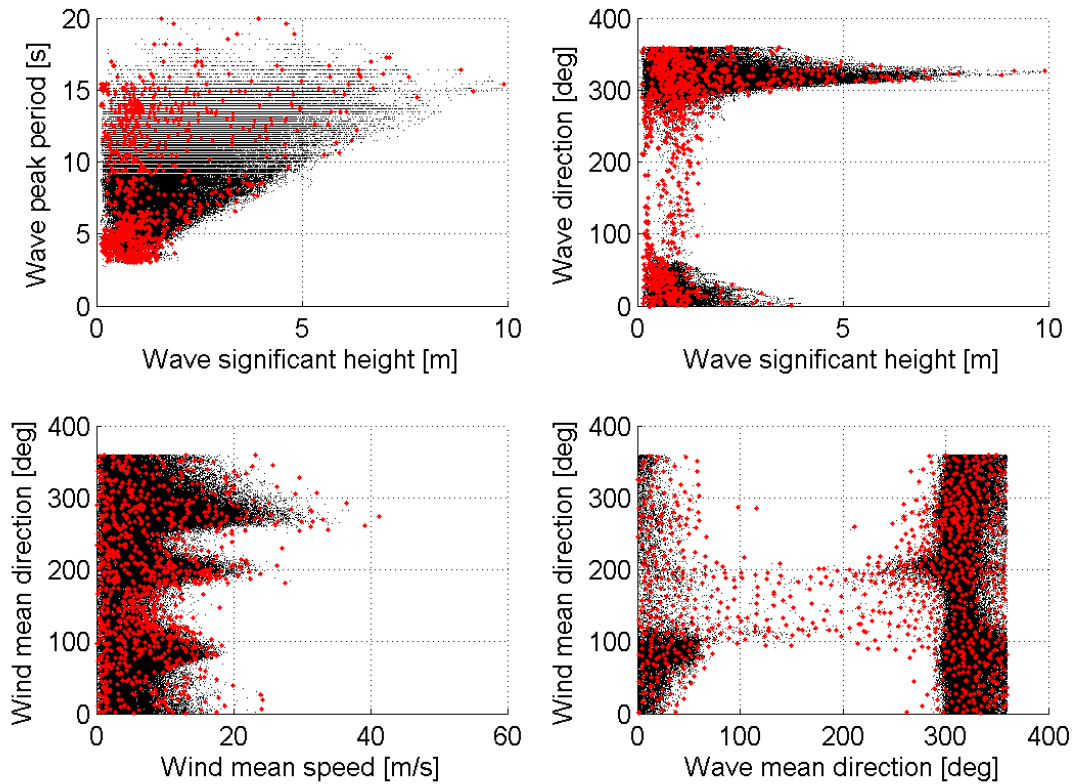


Figure 26: MDA results for Santander, Spain (1994-2013). Original dataset (black) and selected subset (red)

### 5.3.3 Verification of floating wind turbine model

In order to assess its accuracy, the implemented floating turbine model has been compared against FAST (version v8.08.00c) the open-source software developed by NREL[109]. The floating wind turbine under investigation is the OC4 platform mounting the NREL 5 MW wind turbine (see Chapter 4). The OC4 mooring system is originally designed for a water depth of 200 m. It is here supposed that the platform is equipped with an equivalent mooring system that, for a water depth of 55 m, preserves the global stiffness characteristics of the original one. Such design could be achieved using, for example, truncation methods [110].

The first numerical test consisted in evaluating the steady platform displacement corresponding to a constant, uniform wind in still water. Results for surge and pitch are illustrated in Figure 27, which shows a minimal difference between the codes.

The second numerical test included simulation with irregular waves (significant wave height 6 m, wave peak period 10 s, JONSWAP spectrum) and turbulent wind (Kaimal spectrum). Results are shown in Figure 28 and again show a good agreement with FAST. Though not fully comprehensive, these numerical experiments gave confidence in using the developed numerical model for the calculation of the floating platform response. It is worth reminding that the purpose of this methodology goes beyond the numerical simulation of a floating body, for which a relevant amount of literature already exists.

Wind turbine motions were then simulated for the selected 1000 metocean conditions. This took approximately 17 hours.

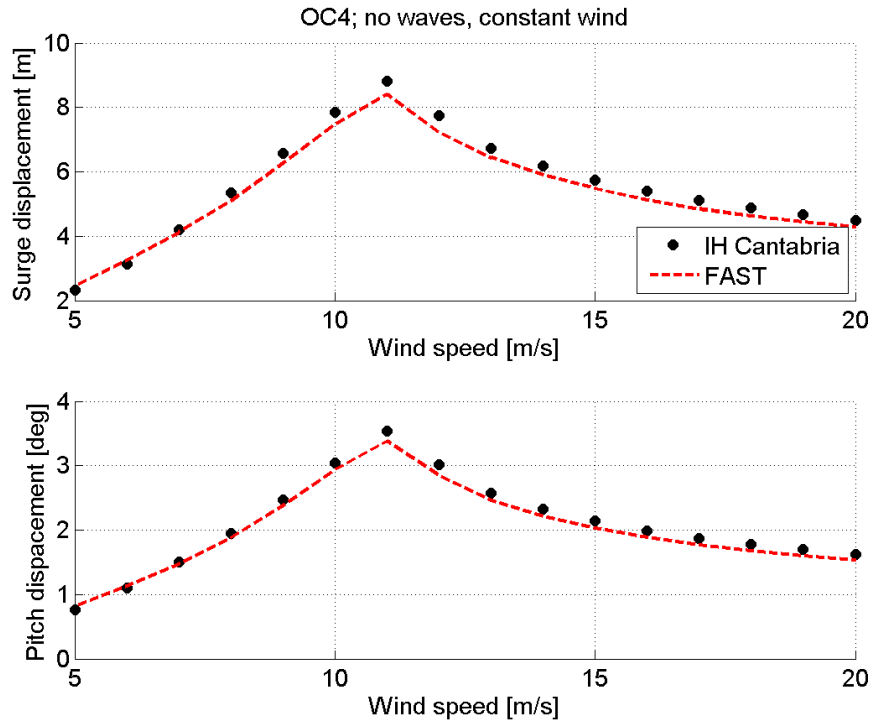


Figure 27: Comparison between IH Cantabria model and FAST. Tests in still water with constant, uniform wind.

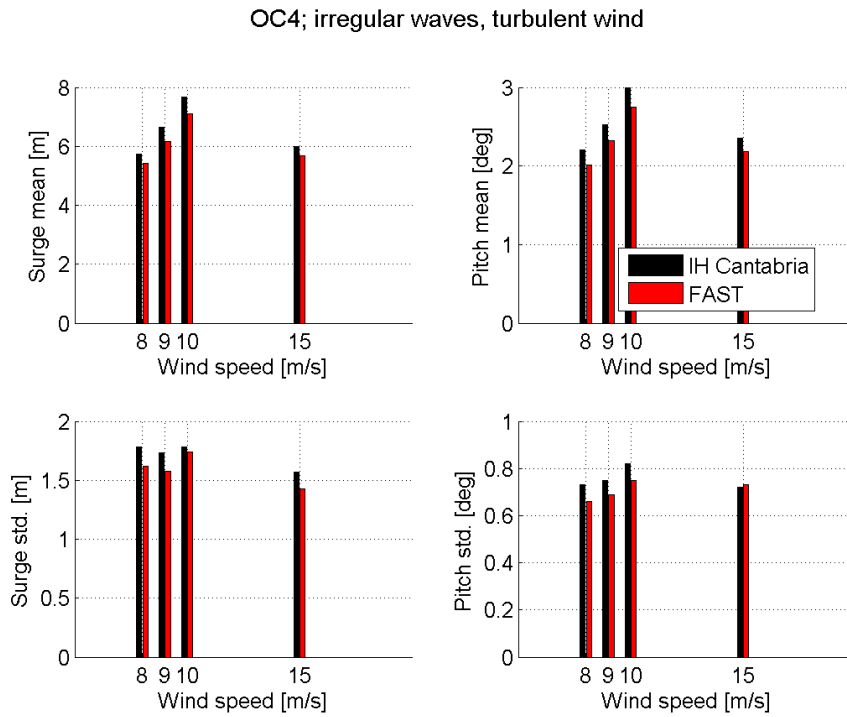


Figure 28: Comparison between IH Cantabria model and FAST. Tests in irregular waves, turbulent wind.

### 5.3.4 Reconstruction of operating parameters

For each of simulated sea state, the floating wind turbine numerical model provided time-series of the selected operating parameters (platform roll, pitch and norm of turbine hub acceleration). Each time-series was used to calculate a probability distribution curve and relative quantiles of occurrence (0.03%, 5%, 10%, 25%, 50%, 75%, 90%, 95% and 99.7%). Figure 29 shows a sample probability distribution curve and the relationship between probability of occurrence and quantile values.

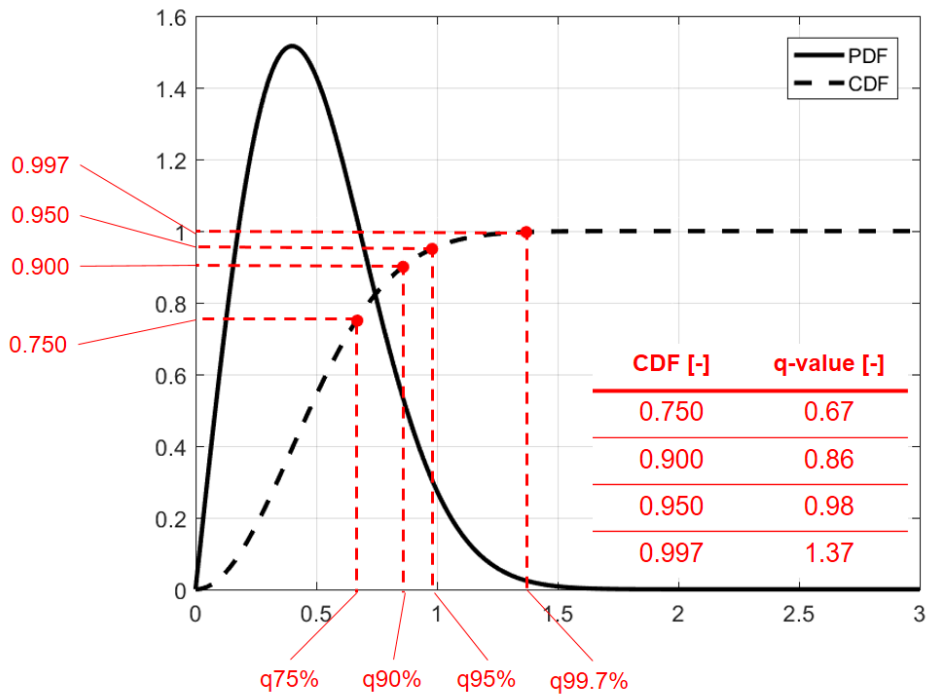
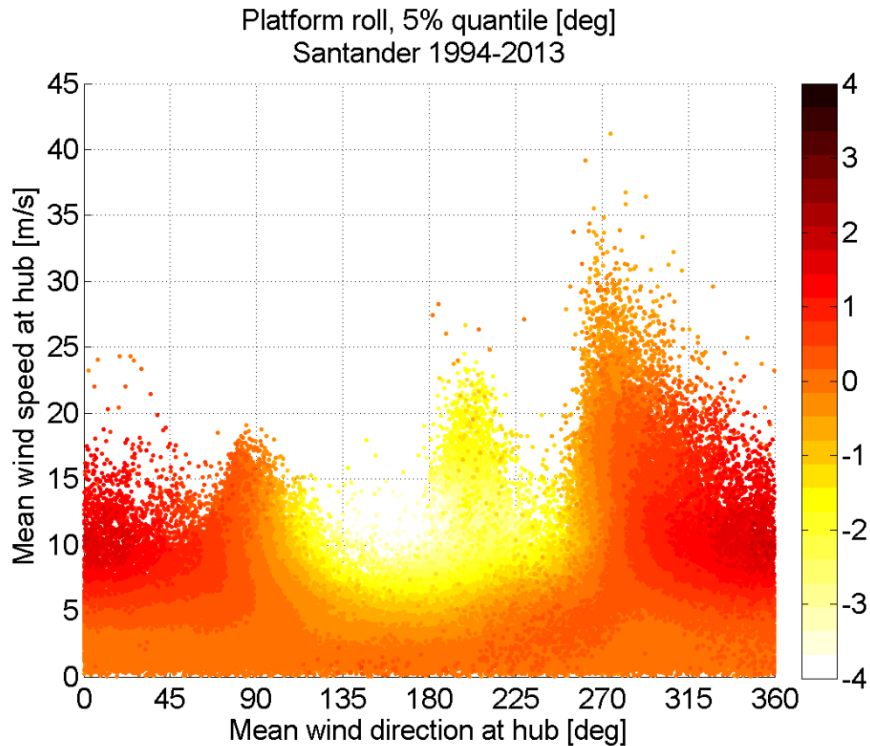


Figure 29: Sample probability distribution and quantiles of occurrence.

Long-term values of these 9 quantiles were then reconstructed, for the 3 chosen operating parameters, for the rest of the metocean data samples using the RBF method (27 reconstructions totally). This took approximately 30 hours. The total simulation time of the proposed methodology

was then about 71 hours, which is far less than the 2920 hours estimated at the beginning of this chapter.

The following illustrations represent some of the results obtained. Figure 30 and Figure 31 show a clear correlation between platform roll displacement and mean wind speed. When the wind heads from North (i.e. direction is  $0^\circ$ ) it causes positive roll displacements, while when it comes from South (i.e. direction is  $180^\circ$ ) it causes negative roll displacements. Pitch displacements are in line with this, as shown in Figure 32 and Figure 33. This is consistent with the coordinate system defined in Chapter 4. Largest roll and pitch motions occur at a wind speed of  $11 \text{ ms}^{-1}$ , which is the nominal wind speed (i.e. maximum thrust force) for the selected wind turbine. Data variability on top of this correlation is given by wave climate. The 95% quantile of occurrence is used to highlight large positive displacements, while the 5% quantile to highlight large negative displacements.



*Figure 30: Platform roll (5% quantile) as a function of mean wind speed and direction.*

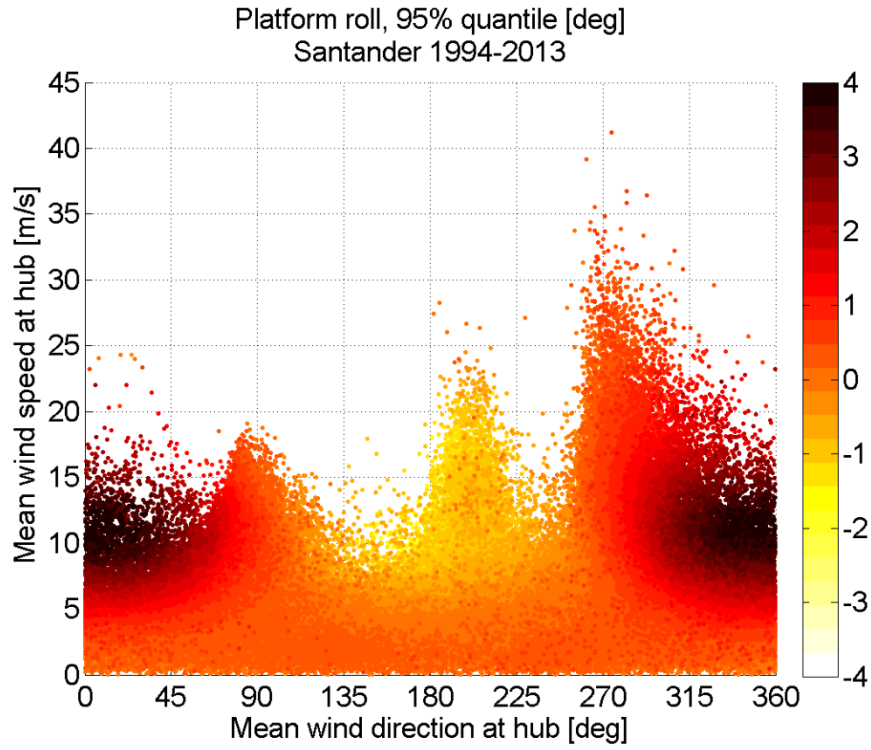


Figure 31: Platform roll (95% quantile) as a function of mean wind speed and direction.

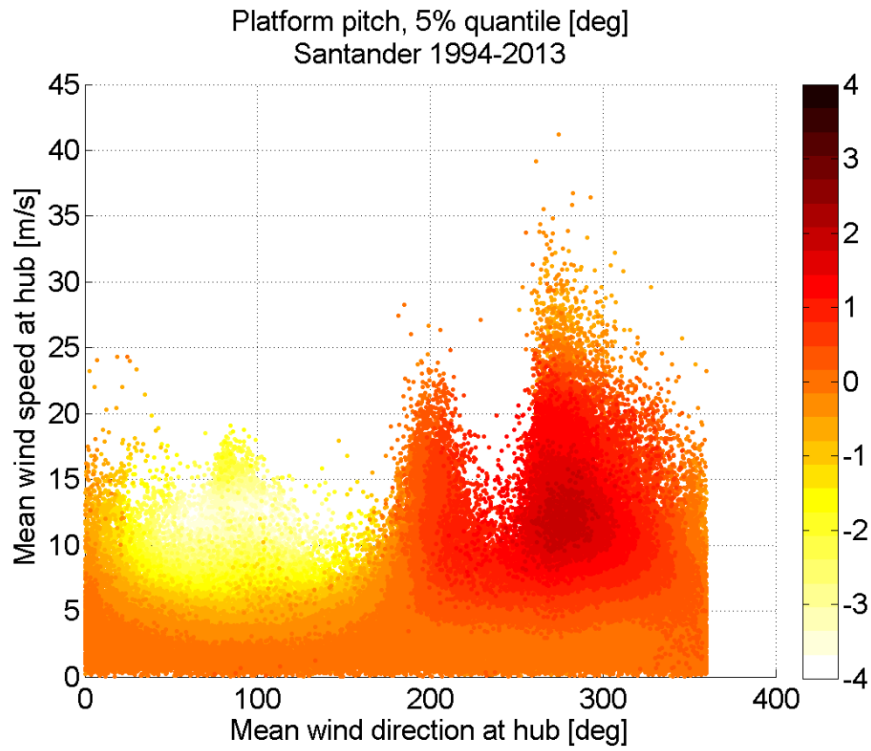


Figure 32: Platform pitch (5% quantile) as a function of mean wind speed and direction.

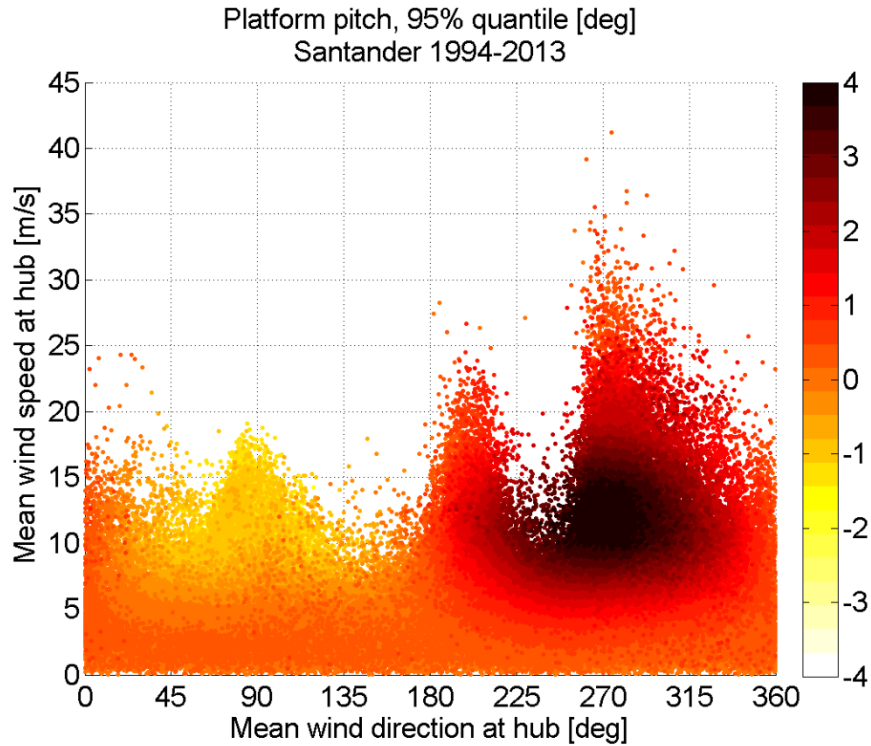


Figure 33: Platform pitch (95% quantile) as a function of mean wind speed and direction.

On turn, wave conditions importantly affect the norm of the hub acceleration. Figure 34 shows an increasing trend of its value (95% quantile) not only with wind speed, but also with significant wave height. It is remarkable that large accelerations shall be expected also for relatively low wind speeds, below cut-out (which is  $25 \text{ ms}^{-1}$  for the considered wind turbine). Furthermore, it is interesting to notice that the highest values occur when wind and waves have a small misalignment, as illustrated in Figure 35. In such conditions, the wind and wave energy fluxes sum up and result in an increased excitation of the floating platform.

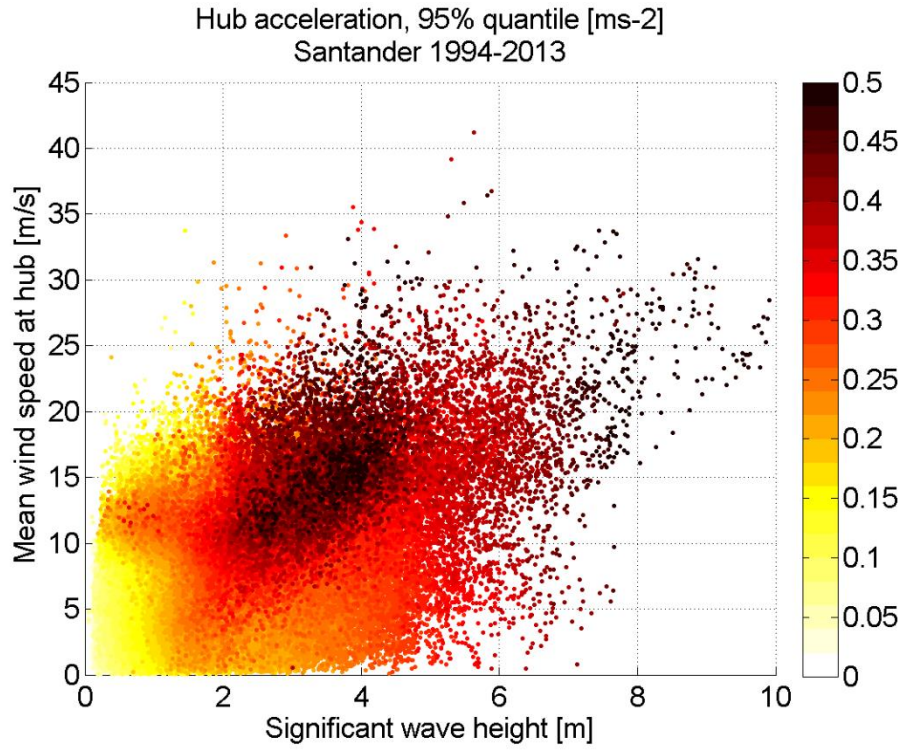


Figure 34: Hub acceleration (95% quantile) as a function of mean wind speed and significant wave height.

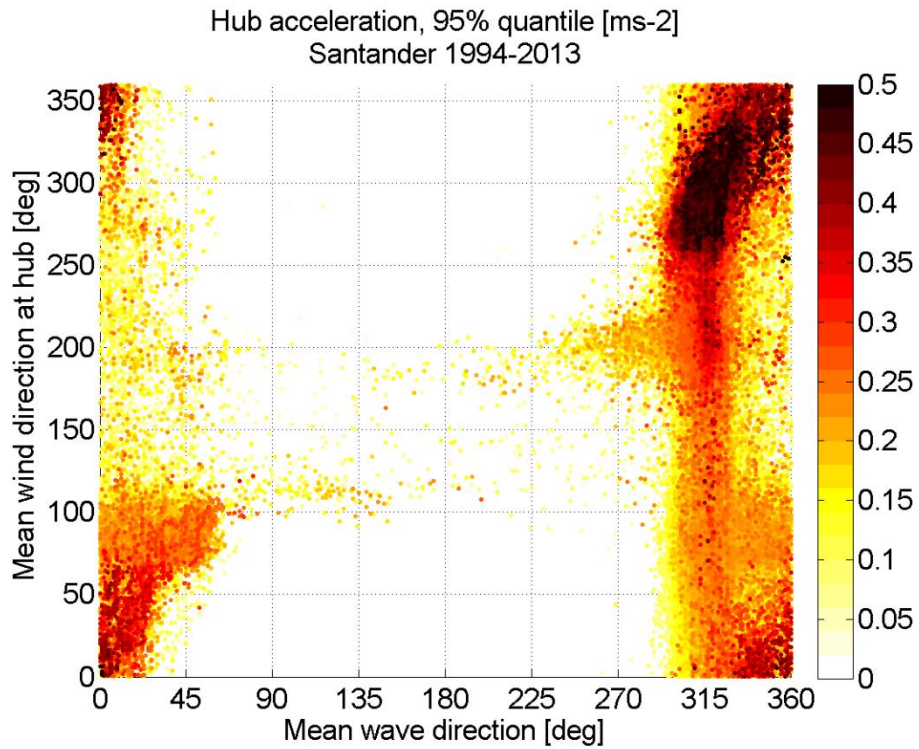


Figure 35: Hub acceleration (95% quantile) as a function of mean wind direction and mean wave direction.

Differently from the operating parameters, mean generated electrical power  $P$  is reconstructed simply following the steady curve of the wind turbine as:

$$P(V) = \frac{1}{2} A \rho V^3 C_P(V) \quad \text{Equation 22}$$

where  $A$  is the area of the wind turbine rotor,  $C_P$  the static power coefficient and  $\rho$  the air density ( $1.2 \text{ kg m}^{-3}$ ). This approximation is considered valid based on the results obtained with the operation of the WindFloat demo, for which Principle Power declared that platform motions had no influence on the wind turbine power curve [24]. This reduces the computational time and avoids unnecessary calculations.

### 5.3.5 Impact of operational stops on long-term energy yield

When any of the operating parameters is above threshold, the wind turbine is supposed to be switched-off and thus availability and energy production decrease. Operating parameters can be evaluated according to different quantiles of occurrence. For example, the 95% quantile of occurrence represents the response value that is higher than 95% of the recorded values. It results then that the 95% quantile has a larger value than the 90%, 75% quantiles and so on. The higher the quantile used, the larger the number of sea states for which the considered operating parameter exceeds a given operational threshold and thus the lower the availability and energy production.

Assuming continuous operation with no stops (i.e. 100% availability), the capacity factor for this case study was 32.9%. Figure 36 and Figure 37 show the long-term availability of the floating wind turbine, as a function of hub acceleration and tower tilt operational thresholds. Similarly, Figure 38 and Figure 39 illustrate results for the long-term capacity factor. Results are given evaluating the operating parameters with four different quantiles of occurrence (75%, 90%, 95% and 99.7%). For platform roll and pitch, which can have negative values, the 25%, 10%, 5%

and 0.03% quantiles are used if their absolute value is higher than the 75%, 90%, 95% and 99.7% quantiles). In the figures, “tower tilt” refers to either platform roll or tilt i.e. when any of the two is above threshold the turbine is switched-off. Findings indicate that both availability and capacity factor of the turbine decrease non-linearly and monotonically, as the operation thresholds are lowered. Remarkably, the steepness of the curves highly depends on the quantile chosen for representing the operating parameters. A hub acceleration operational limit of  $0.40 \text{ m s}^{-2}$  gives an availability of 98.8% and 97.1% respectively for quantiles of occurrence of 90% and 95%. This corresponds to capacity factors of 31.8% and 30.2%. A tower tilt operational limit of 4 degrees gives an availability of 98.3% and 93.0%, respectively for quantiles of occurrence of 90% and 95%, which corresponds to capacity factors of 31.4% and 27%. These results suggest using caution in choosing the statistical parameter to evaluate the selected operating parameter.

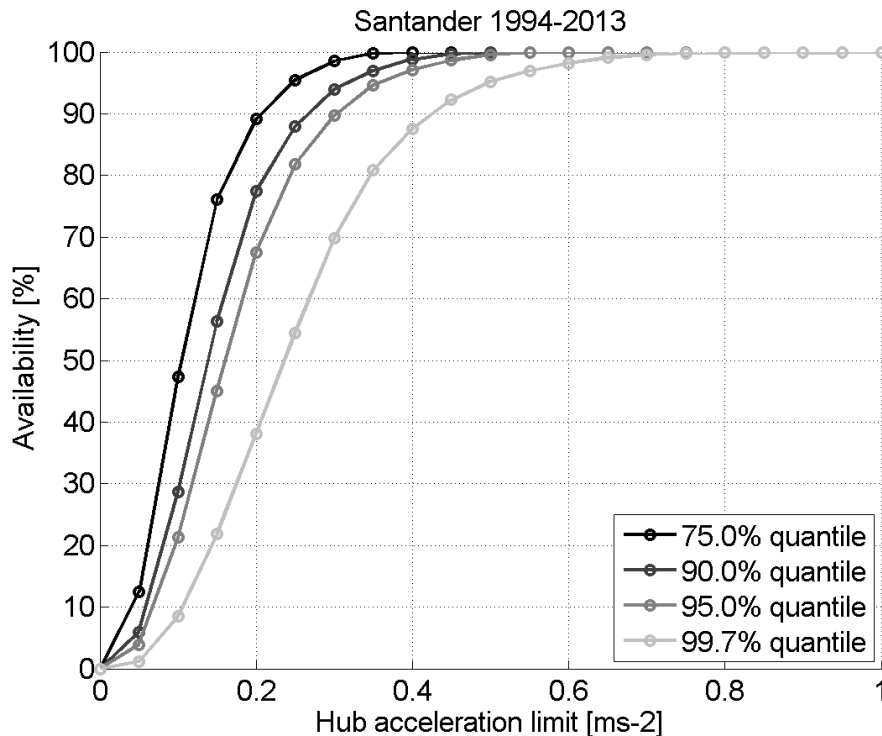


Figure 36: Long-term availability as a function of hub acceleration threshold.

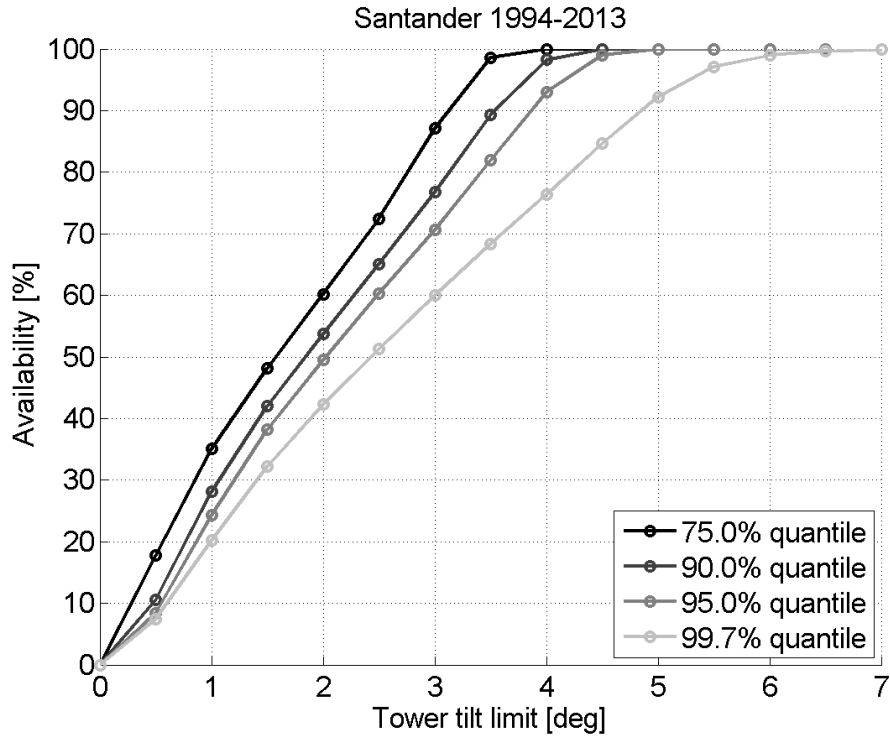


Figure 37: Long-term availability as a function of tower tilt threshold.

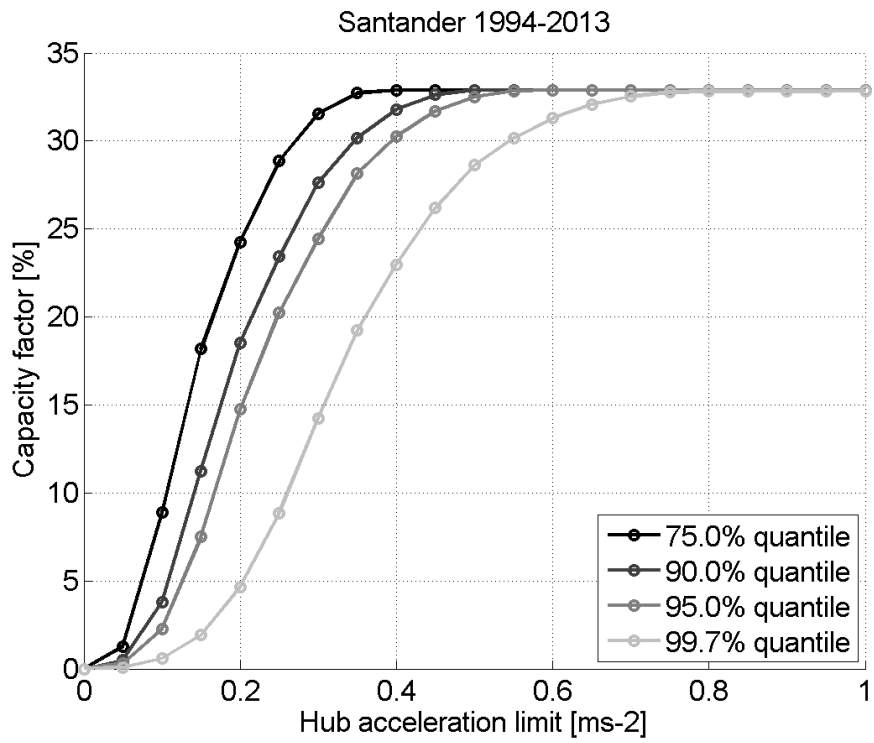


Figure 38: Long-term capacity factor as a function of hub acceleration threshold.

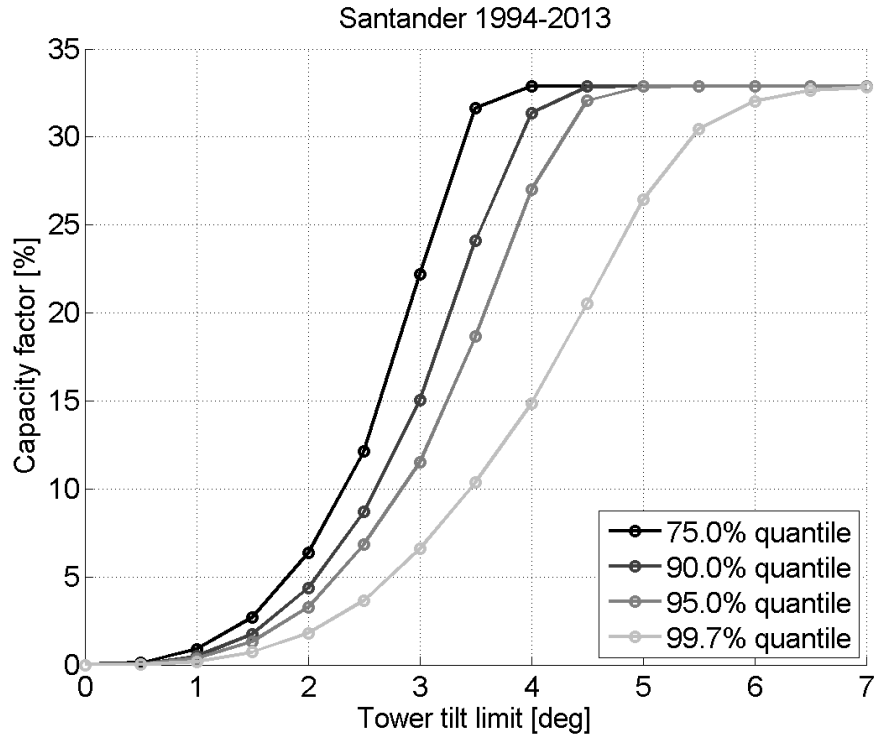


Figure 39: Long-term capacity factor as a function of tower tilt threshold.

Table 8 and Table 9 highlight the results obtained for specific thresholds, where darkest cells refer to lowest values of both availability and capacity factor.

	Quantile [%]			Quantile [%]			
	75	90	95	75	90	95	
Threshold [m s <sup>-2</sup> ]	0.2	89.4	77.2	68.4	24.1	17.7	14.9
	0.4	99.8	98.8	97.1	32.8	31.8	30.2
	0.6	100	100	99.9	32.9	32.9	32.9
	Availability			Capacity factor			

Table 8: Brief summary of the results. Operating parameter: hub acceleration.

	Quantile [%]			Quantile [%]			
	75	90	95	75	90	95	
Threshold [deg]	3.0	87.4	76.5	70.6	22.3	15.0	12.2
	3.5	98.8	89.7	81.8	31.8	24.5	17.6
	4.0	99.3	98.3	93.0	32.1	31.4	27.0
	Availability			Capacity factor			

Table 9: Brief summary of the results. Operating parameter: tower tilt.

It is interesting to see the effect of imposing, simultaneously, operating thresholds to both hub acceleration and tower tilt. Figure 40 and Figure 41 define the variation of availability and capacity factor change according to the selected safety limits, evaluated through their 95% quantile of occurrence. An area of combined influence clearly arises: considering a threshold of  $0.4 \text{ m s}^{-2}$  for the hub acceleration, and of 4 degrees for the tower inclination results in an availability of 90.4% and a capacity factor of 24.7%. It is worth noticing both values are lower when the two operating parameters are considered simultaneously (compare with those previously shown), since this further restricts the range of operation of the machine.

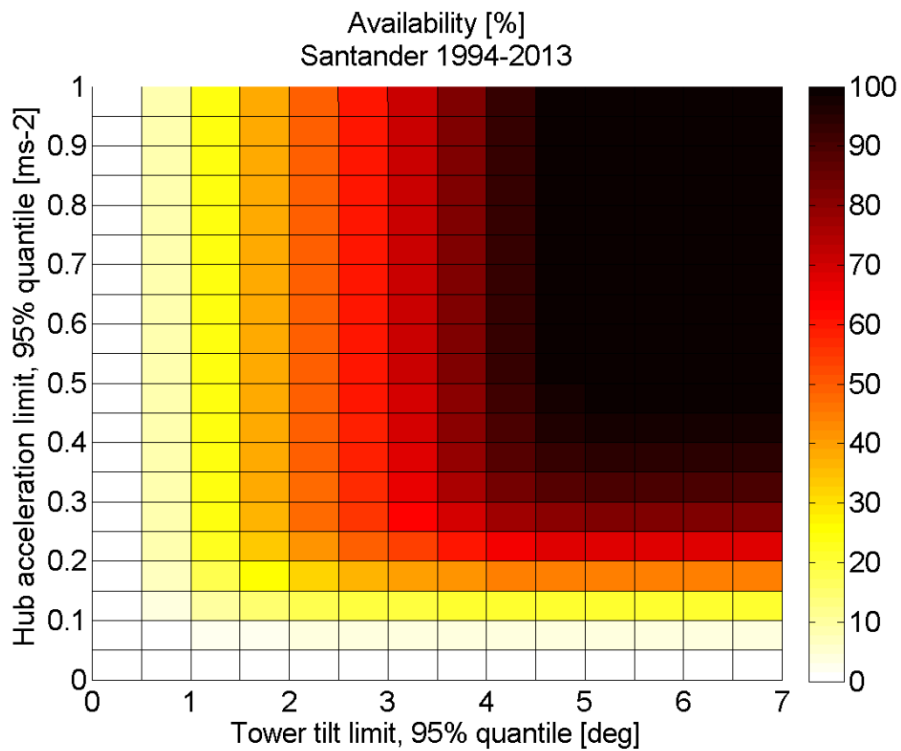


Figure 40: Long-term availability as function of combined hub acceleration and tower tilt thresholds.

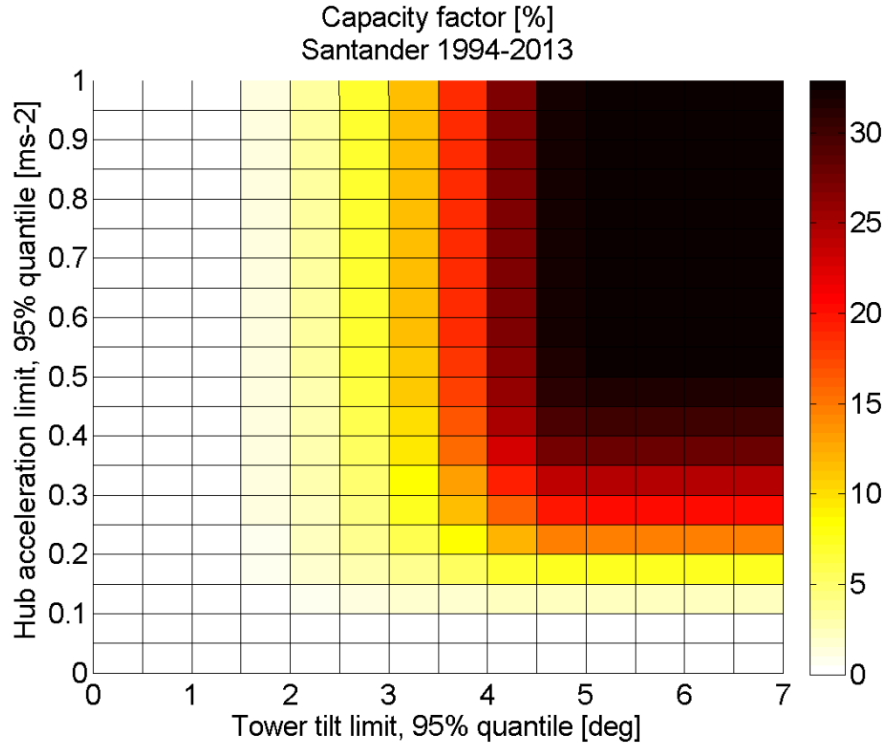


Figure 41: Long-term capacity factor as function of combined hub acceleration and tower tilt thresholds.

## 5.4 Results: accuracy and impact of subset size

The illustrated methodology has, among others, one free parameter that has a great impact on the quality of the results: the size  $M$  of the metocean data subset. This value should be high enough such data subset is able to represent the metocean climate variability, and small enough to reduce the total computational effort for simulating the platform response. Clearly, a trade-off between both requirements should be pursued. In the case study presented in this chapter, it was chosen to use  $M = 1000$ . This section offers a justification for such choice, providing a comparison of the results against direct numerical simulation (i.e. the floating turbine model is used for all samples in the metocean data set without using RBF).

Calculations were performed for  $M = 250$ ,  $M = 500$ ,  $M = 750$  and  $M = 1000$ . First, a comparison of the accuracy of the results for  $M = 500$  and  $M = 1000$  is presented. Figure 42, Figure

43 and Figure 44 show the correspondence between the interpolated operating parameters (normalized with the results of the direct numerical simulation) and the results of the direct numerical simulation itself, for different quantiles of occurrence and considering a subset size of  $M = 1000$ . Black points represent the calculated data, the green line the bisector and the red line a linear fit to the data. Points lying on the bisector represent perfect match between RBF and direct simulation. The title of each subplot contains the root-mean-square error of the RBF interpolation.

As it can be noticed, the interpolation accuracy gets worse as it tries to reconstruct values at the tail of the distribution (i.e. high quantiles of occurrence). Indeed, both the root-mean-square error and the deviation of the linear approximation from the bisector increase as the evaluated quantile of occurrence increases. This is related to the fact that random seeds are used to generate wind speed and wave elevation time series, which generates a relevant variability at the tails of the respective distributions. This variability is reflected onto the forces acting on the system and thus onto the floating platform response. In addition, there is a marked trend of the interpolation to overestimate results: indeed, the linear approximation is always below the bisector for large interpolated values (i.e. when direct numerical model gives results close to 1).

Figure 45, Figure 46 and Figure 47 show the results obtained considering a subset size of  $M = 500$  which highlight a lower accuracy, as expected.

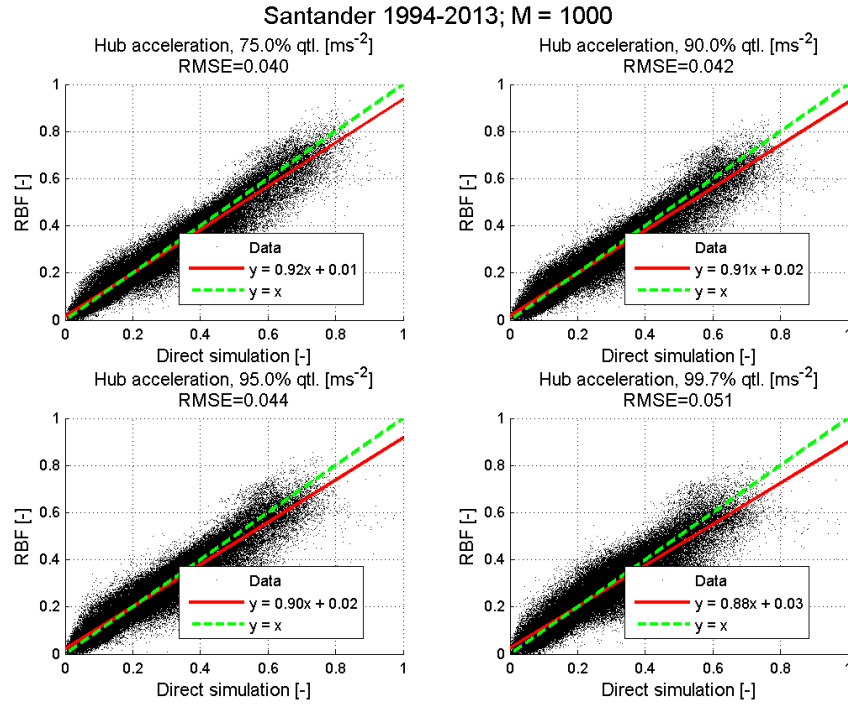


Figure 42: Accuracy in interpolation of hub acceleration,  $M = 1000$ .

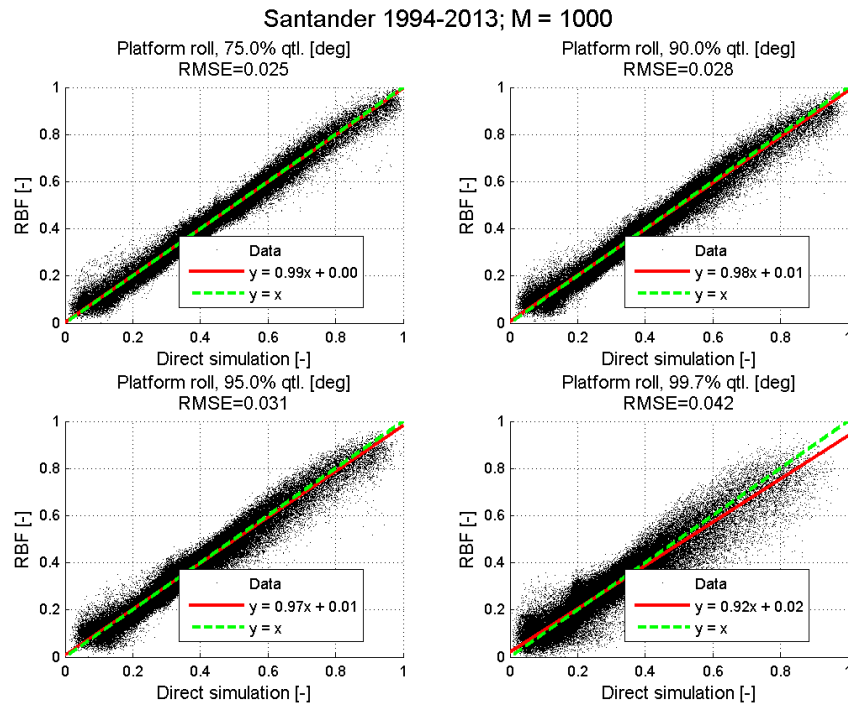


Figure 43: Accuracy in interpolation of platform roll,  $M = 1000$ .

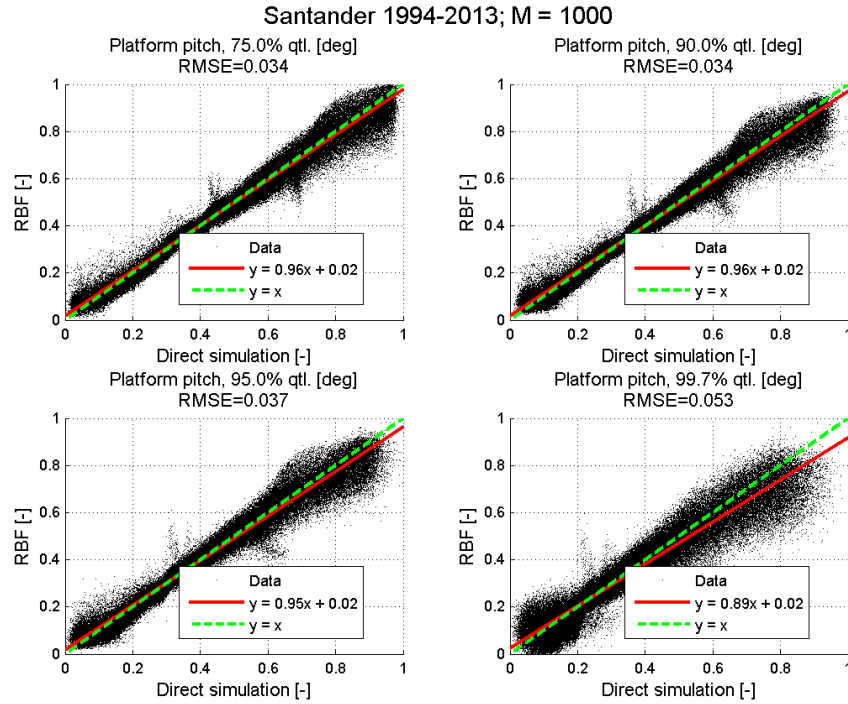


Figure 44: Accuracy in interpolation of platform pitch,  $M = 1000$ .

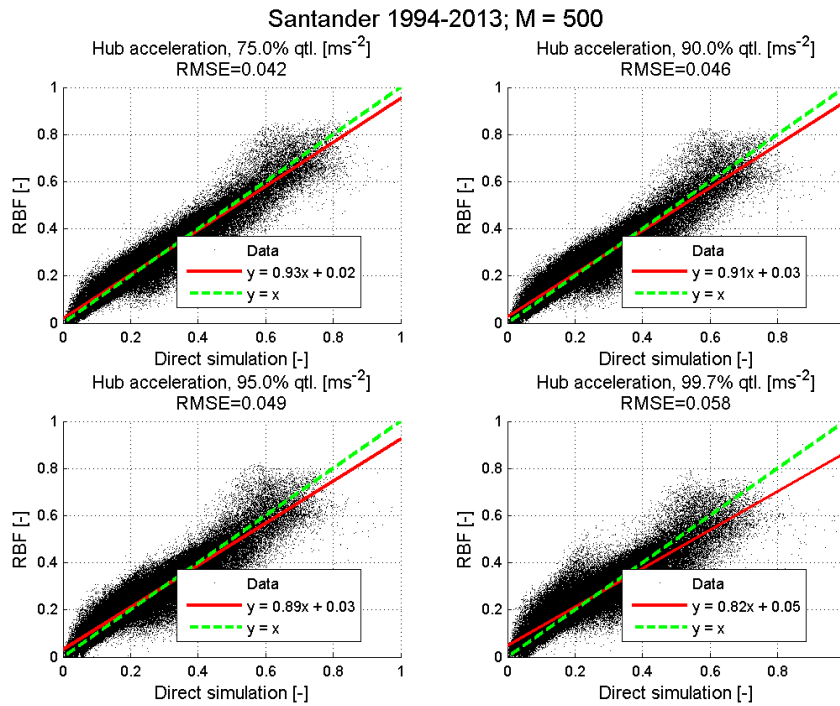


Figure 45: Accuracy in interpolation of hub acceleration,  $M = 500$ .

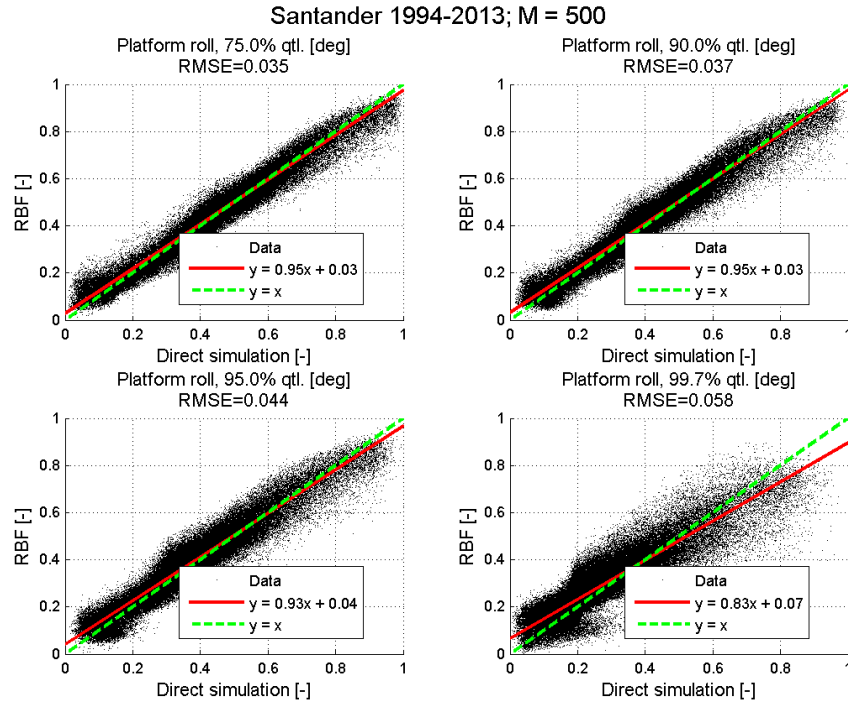


Figure 46: Accuracy in interpolation of platform roll,  $M = 500$ .

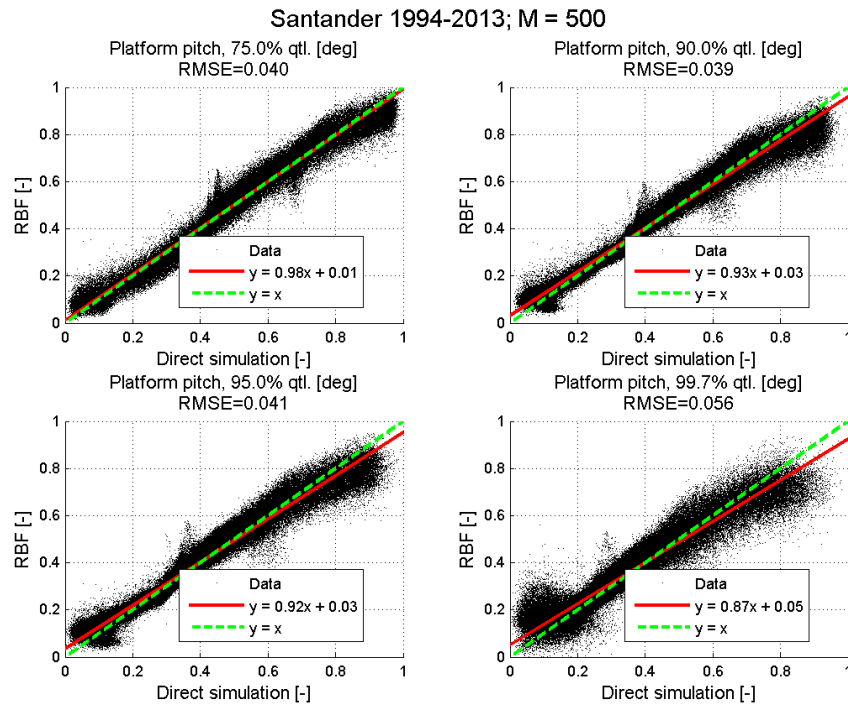


Figure 47: Accuracy in interpolation of platform pitch,  $M = 500$ .

Table 10 and Table 11 summarize the results obtained in terms of root-mean-square error of the RBF interpolation. Darkest cells are related to largest errors.

		Quantile [%]			
		75.0	90.0	95.0	99.7
Operating parameter	Roll	0.025	0.028	0.031	0.042
	Pitch	0.034	0.034	0.037	0.053
	Hub acc.	0.040	0.042	0.044	0.051

Table 10: Root-mean-square error (on normalized results) for RBF interpolation.  $M = 1000$ .

		Quantile [%]			
		75.0	90.0	95.0	99.7
Operating parameter	Roll	0.035	0.037	0.044	0.058
	Pitch	0.040	0.039	0.041	0.056
	Hub acc.	0.042	0.046	0.049	0.058

Table 11: Root-mean-square error (on normalized results) for RBF interpolation.  $M = 500$ .

Then, it is necessary to evaluate how the accuracy in calculating the platform displacements is reflected into the calculation of availability and capacity factor. Table 12 shows values of long-term availability and capacity factors, as a function of the data subset size  $M$  and the acceleration threshold, where a 95% quantile is considered. In the last row,  $M=175220$  just represents results obtained for the direct numerical simulation (i.e. without interpolating). The following Table 13 shows the error of the RBF on the calculation of the long-term availability and capacity factor, where darkest cells are related to largest errors. As it can be seen, using  $M=1000$  allowed keeping the error below 2.5% which is considered acceptable for the purposes of this work. Lower sizes for the data subset give larger inaccuracy. It is interesting that RBF for  $M=500$  and  $M=1000$  underestimates the availability and capacity factor, which is consistent with the fact that it overestimates large platform motions as shown in Figure 42 and Figure 45. Results for other

operating parameters and quantiles of occurrence are not included not to overwhelm the reader; nevertheless, they were in line with those presented here.

		Acceleration threshold [m s <sup>-2</sup> ]			Acceleration threshold [m s <sup>-2</sup> ]		
		0.20	0.30	0.40	0.20	0.30	0.40
Subset size, M	250	59.4%	74.1%	81.5%	10.1%	23.1%	33.1%
	500	61.1%	82.1%	94.8%	12.3%	21.4%	28.2%
	750	74.3%	84.5%	95.3%	14.2%	22.5%	27.0%
	1000	68.4%	87.2%	97.1%	14.9%	24.7%	30.2%
	175220	70.7%	88.6%	97.8%	16.2%	25.8%	30.6%
<i>Availability</i>				<i>Capacity factor</i>			

Table 12: Long-term availability and capacity factor for different sizes of data subset M and acceleration thresholds (95% quantile).

		Acceleration threshold [m s <sup>-2</sup> ]			Acceleration threshold [m s <sup>-2</sup> ]		
		0.20	0.30	0.40	0.20	0.30	0.40
Subset size, M	250	-11.3%	-14.5%	-16.3%	-6.1%	-2.7%	2.5%
	500	-9.6%	-6.5%	-3.0%	-3.9%	-4.4%	-2.4%
	750	3.6%	-4.1%	-2.5%	-2.0%	-3.3%	-3.6%
	1000	-2.3%	-1.4%	-0.7%	-1.3%	-1.1%	-0.4%
<i>Availability</i>				<i>Capacity factor</i>			

Table 13: Error on long-term availability and capacity factor for different sizes of data subset M and acceleration thresholds (95% quantile).

## 5.5 Conclusions

This chapter illustrated a methodology to evaluate the effect of metocean conditions over the long-term energy production of an offshore floating wind turbine. This approach is based on the use of a multivariate data selection method (Maximum Dissimilarity Algorithm, MDA), a wind turbine dynamic time-domain model and a scattered data interpolation method (Radial Basis Functions, RBF). Platform roll, platform pitch and hub acceleration have been identified as most relevant operating parameters, being related to both static and dynamic loading of the system. Platform roll and pitch are strongly dependent on the mean wind speed and direction and their

largest values occur in the rated wind speed region. Hub acceleration, on the other hand, is influenced also by wave conditions being highest when wind and waves are aligned. Remarkably, large accelerations may occur far below the turbine cut-out wind speed. When the safety threshold of any of these parameters is exceeded, the wind turbine is supposed to be shut down in order to avoid damage or failure of any component of the system. Wind turbine availability and capacity factor decrease non-linearly, as operating thresholds are decreased. Results depend also on the quantile of occurrence of the chosen operating parameters.

This methodology was applied to a sample floating wind turbine located off the coast of Santander, Spain using twenty years of hindcast data. The capacity factor corresponding to an availability of 100% was found to be 32.9%. Considering a threshold of  $0.4 \text{ m s}^{-2}$  for the hub acceleration and of 4 degrees for the tower inclination (both evaluated with their 95% quantile) would have decreased availability to 90.4% and capacity factor to 24.7%.

The number of subset samples has a great impact on the accuracy of the results. The interpolation of platform motions, availability and capacity factor was very good, when the data subset consisted of 1000 samples. Using less samples was not considered sufficient, since it would have given errors above 2.5% in the estimation of the availability and capacity factor.

The illustrated methodology may results helpful at several engineering stages of the wind farm lifespan. Indeed, at both the design and the operational stages it may give important guidelines in evaluating the best trade-off between system reliability and energy production.

# Temporal and spatial variation of accessibility

---

---

## 6.1 Motivation and state-of-the-art review

To achieve high levels of availability and survive the offshore environment, wind turbines shall undergo dedicated inspection and maintenance activities. As these have to be carried on mostly onsite, their efficient planning and execution passes by a precise definition and assessment of accessibility. To be effective in the long-term, O&M strategies must consider the temporal variation of accessibility and evaluate the influence that access thresholds have on it. In addition, understanding its spatial variation may be helpful when evaluating multiple possible locations for the installation of an offshore wind farm.

This chapter aims at providing a mathematical definition of accessibility and determining its spatial and temporal variation, through the extensive use of long-term, high-resolution time series of hindcast data. The goal is to provide a solid basis for the design of long-term maintenance strategies (i.e. the definition of fleet and personnel requirements, at the design stage, for an offshore wind farm). The analysis is focused on the North Sea due to its importance in the current and future development of offshore wind: at the beginning of 2015 it had the highest share for wind farms constructed, under construction and consented in Europe (63.3%, 84.8% and 75%, respectively [111]).

This work fills three gaps identified in the literature: (1) the absence of a mathematical definition of accessibility parameters; (2) the lack of studies investigating accessibility variation

over large domains and (3) the small amount of works dedicated to the use of hindcast data for long-term maintenance design (compared to the larger number of studies for decision support based on short-term weather forecast).

Silva and Estanqueiro [112] developed an accessibility analysis for three locations along the coast of Portugal using 10 years hindcast data. van Bussel and Bierbooms [113], [114] evaluated the use of different means of transportation for a reference wind farm in the Netherlands, using 30 years of hindcast data. Dowell et al. [115] developed a similar work using 6 years of real data from the FINO1 weather station in the North Sea. O'Connor et al. [116] used buoy data for investigating accessibility results in two spots of the Irish west coast. The methodology proposed in this Chapter aims at extending these works (and other similar ones found in the literature), adding valuable information for wind farm operators.

## **6.2 Methodology**

The methodology applied to pursue the objectives of this chapter is based on two steps. First, a review of current access strategies for maintenance and inspection of offshore wind farms is performed. This is needed in order to identify the metocean parameters that affect offshore access and their typical safety thresholds. In second place, relevant accessibility indicators are defined mathematically through the help of set theory. This helps in clarifying basic concepts and developing an algorithm for numerical implementation. Sections 6.2.1 and 6.2.2 provide details about these two topics.

Accessibility parameters are then evaluated for the North Sea, based on hindcast data and illustrated in Section 6.3. Results are extrapolated for specific locations corresponding to either

existing or planned offshore wind farms and presented in Section 6.4. Finally, Section 6.5 contains conclusions about findings of this Chapter.

## **6.2.1 Review of access strategies**

Two types of maintenance activities, which require different access means, usually take place in offshore wind farms: inspection or light repair and heavy repair.

### ***6.2.1.1 Case I: inspection or light repair operations***

In this case, small crews are needed and usually mobilized with workboats or helicopters. Workboats are most often catamaran vessels for transportation of personnel and small equipment (up to 2000 kg) from the shore (or the offshore base) to the wind farm. Some of them also provide support for repair and inspection under water (foundations, scour protection). Typically, they can operate up to 1.5-2.0 m of significant wave height [29], [60] and transport up to 12 passengers with a maximum speed between 10 and 13 m s<sup>-1</sup>. Their cost is estimated to be between 2.5 and 3.7 M€/year for a 500 MW wind farm [29].

Helicopters allow access of personnel to the wind farm in otherwise inaccessible sea conditions. Use is limited by poor visibility or high wind speeds, which may limit the safe winching down and subsequent work in the nacelle of technicians. Limit mean wind speed is in the range of 12 – 20 m s<sup>-1</sup> [60], [116], [117]. They can transport 4-6 passengers and cost between 1.9 and 3.7 M€/year/aircraft [29].

### ***6.2.1.2 Case II: heavy repair operations***

In this case, offshore crane barges are needed for replacing large components. They are typically either jack-up vessels or anchor spread supported vessels and are required for major turbine repair operations and repairs to other components such as transformers. Their cost may be

between 5 and 15 M€/year [29]. Different restrictions on both wind and wave climate apply at different stages such as jacking-up, crane usage or crew access, and depend on the vessels used.

Remarkably, a certain degree of uncertainty is associated to sea state and wind speed limits, which are subject to interpretations and not always given clearly by suppliers. One should also bear in mind that for floating systems these limits might be more restrictive, since platform movements may reduce the safeness of planned activities.

## 6.2.2 Mathematical definition of accessibility parameters

The accessibility of a wind farm can be evaluated according to several parameters, which depend on the selected access strategy and the statistical properties of relevant metocean variables. In the following, a formulation of such parameters is presented by means of the set theory.

This section is divided into three different subsections: the first one provides definitions of accessibility parameters for a simple access strategy; the second one illustrates an example to better understand the definitions introduced; the third one contains a generalization of the concepts when multiple access strategies are analysed.

### 6.2.2.1 Definition of accessibility parameters for a simple access strategy

Let  $\mathcal{T}$  be a discrete time set, composed by  $N$  elements equally spaced with sampling time  $dt$ , such that:

$$\mathcal{T} = \{t_n: t_{n+1} - t_n = dt, n = 1, 2, \dots, N - 1\} \quad \text{Equation 23}$$

where the symbol “:” stands for “such that”. Also, let  $x$  be a metocean variable (e.g. wave significant height) defined in  $\mathcal{T}$  and conditioning the studied access strategy. It is then possible to define:

**Approachability.** The *approachability*  $A$  of an offshore location is defined as the normalized amount of time that  $x$  is below a given safety threshold  $x^{lim}$ . In order to calculate this parameter it is necessary to introduce  $\mathcal{J}^{app}$ , the set of “approachability times”:

$$\mathcal{J}^{app} = \{t_n \in \mathcal{T}: x(t_n) \leq x^{lim}, n = 1, 2, \dots, N\} = \{t_k^{app}, k = 1, 2, \dots, K\} \quad \text{Equation 24}$$

where  $K$  is the number of elements of  $\mathcal{J}^{app}$ . Approachability  $A$  is then calculated as:

$$A = \frac{\#\mathcal{J}^{app}}{\#\mathcal{T}} = \frac{K}{N} \quad \text{Equation 25}$$

where the symbol “#” stands for “cardinality” (i.e. the number of distinct elements in the set).

**Weather window.** A *weather window*  $\tau$  is a set of  $l$  consecutive discrete time instants for which access is possible. By definition, we assume that a time instant cannot belong to more than one weather window i.e. overlapping weather windows are not considered<sup>2</sup>. Based on that, weather windows can be calculated according to the following iterative procedure:

**while**  $t_i^{srt} \neq \{\emptyset\}$

$$t_i^{srt} = \min\{t_k^{app} \in \mathcal{J}^{app}: t_{k+l-1}^{app} - t_k^{app} = (l-1)dt\} \quad \text{Equation 26}$$

$$t_i^{end} = t_i^{srt} + (l-1)dt \quad \text{Equation 27}$$

---

<sup>2</sup> Please notice that this corresponds to an approximation that is helpful in simplifying the notation of this paper. In principle, overlapping weather windows shall be considered to take into account that in real-sea operations, access may be required at any time instant, when the need arises. This would also help in mitigating the built-in granularity of a discrete time series.

$$\tau_i = \{t_k^{app} \in \mathcal{J}^{app} : t_i^{srt} \leq t_k^{app} \leq t_i^{end}\} \quad \text{Equation 28}$$

$$\mathcal{J}^{app} = \mathcal{J}^{app} - \tau_i \quad \text{Equation 29}$$

$$i = i + 1$$

**end**

The starting time of the  $i$ -th weather window,  $t_i^{srt}$ , is calculated as the smallest element of  $\mathcal{J}^{app}$  which belongs to a group of  $l$  consecutive elements, through Equation 26. The ending time  $t_i^{end}$  is calculated as the starting time plus the length of the searched weather windows, through Equation 27. The  $i$ -th weather window  $\tau_i$  is thus defined as the set of approachability times between  $t_i^{srt}$  and  $t_i^{end}$ , using Equation 28. The set of approachability times is then updated removing the elements of  $\tau_i$ , through Equation 29. The weather windows counter is updated as well, and the iterative procedure continues until no more weather windows are found (i.e. until  $t_i^{srt}$  is an empty set  $\{\emptyset\}$ ). Obviously,  $t_i^{srt}$  and  $i$  need to be opportunely initialized.

**Accessibility.** *Accessibility*  $A^*$  is defined as the approachability of a given offshore location, by means of weather windows of length  $l$ . It can be calculated as:

$$A^* = \frac{\sum_{i=1}^l \#\tau_i}{\#\mathcal{J}} \quad \text{Equation 30}$$

This definition implies that:  $A^* \leq A$ .

**Waiting period.** A *waiting period* is here defined as a time interval between two waiting windows of length  $l$ , i.e. a set of unsuitable conditions. The waiting period  $\omega_i$  can be expressed as:

$$\omega_i = \{t_n \in \mathcal{J} : t_i^{end} < t_n < t_{i+1}^{srt}, i = 1, 2, \dots, l - 1\} \quad \text{Equation 31}$$

where  $I$  is the total number of weather windows. Please notice that the definitions above implies that a waiting period can be an empty set. The mean waiting period  $T$  is calculated as:

$$T = \frac{\sum_{i=1}^{I-1} \#\omega_i}{I-1} \tag{Equation 32}$$

### 6.2.2.2 Sample calculation for a single strategy

This section provides a simple example to clarify the definition provided in the previous paragraph. Let  $\mathcal{T}$  be a set of  $N=20$  discrete time instants  $\{1, 2, \dots, 20\}$ ,  $x$  a metocean variable defined on it and  $x^{lim}$  its related safety threshold. Let also be the length of the searched weather windows to be  $l=3$ . Figure 48 illustrates this example.

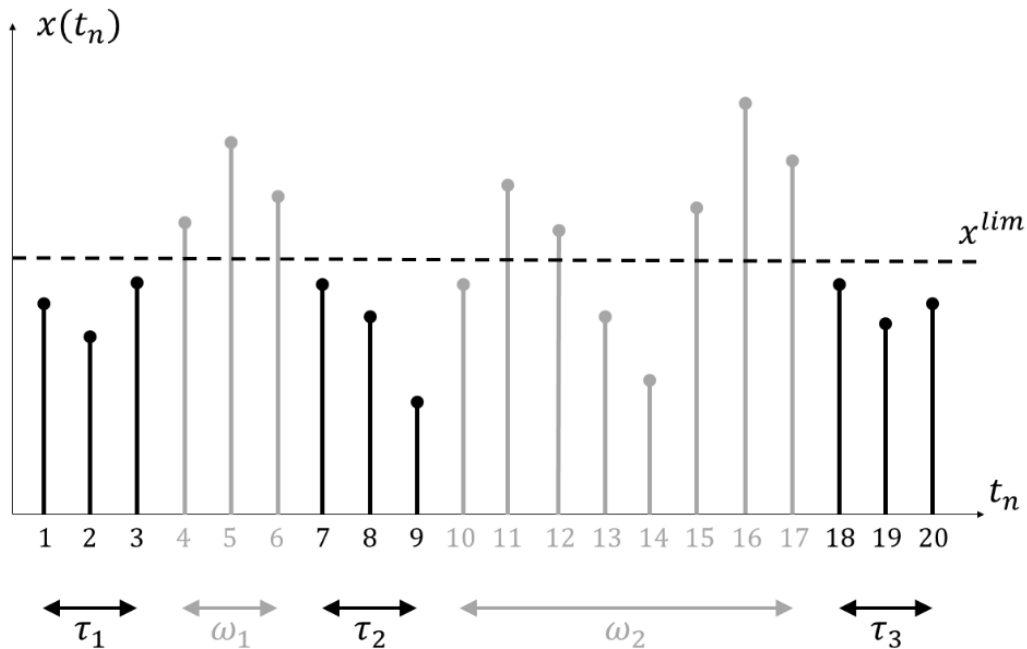


Figure 48: Sample discrete metocean variable time history, weather windows and waiting periods.

Considering the definitions introduced previously, it results that:

Set	Description	Elements	Properties
$\mathcal{T}$	Discrete time domain	{1,2,...,20}	N=20
$\mathcal{T}^{app}$	Approachability times	{1,2,3,7,8,9,10,13,14,18,19,20}	K=12
$\tau_1$	First weather window	{1,2,3}	i=1
$\tau_2$	Second weather window	{7,8,9}	i=2
$\tau_3$	Third weather window	{18,19,20}	i=3
$\omega_1$	First waiting period	{4,5,6}	i=1
$\omega_2$	Second waiting period	{10,11, ..., 17}	i=2

Table 14: Relevant sets for the sample access strategy.

It is worth noticing that the element  $t_{10}=t_7^{app}=10$  does not belong to any window, since the time elements 7, 8 and 9 had already been assigned to weather window  $\tau_2$ . Also, elements  $t_{13}=t_8^{app}=13$  and  $t_{14}=t_9^{app}=14$  compose a weather window of length  $2<l=3$  that therefore is not considered. This directly leads to the calculation of the following accessibility parameters, according to Equation 25, Equation 30 and Equation 32 :

Parameter	Description	Value
$A$	Approachability	0.60
$A^*$	Accessibility	0.45
$T$	Mean waiting time	5.50

Table 15: Accessibility parameters for the sample access strategy.

### 6.2.2.3 Generalization to multiple access strategies

When multiple access strategies are available, each of them conditioned by one or more metocean variables, the definitions above need to be generalized. Given  $M$  access strategies  $s_1, s_2, \dots, s_M$ , conditioned by  $V$  metocean variables  $x_1, x_2, \dots, x_V$  defined in the discrete time domain  $\mathcal{T}$ , then Equation 24 for the  $m$ -th access strategy resembles as:

$$\mathcal{J}_m^{app} = \bigcap_{v=1}^V \{t_n \in \mathcal{T} : x_v(t_n) \leq x_{v,m}^{lim}, n = 1, 2, \dots, N\} \quad \text{Equation 33}$$

where  $x_{v,m}^{lim}$  is the threshold for the metocean variable  $v$  and maintenance strategy  $m$ . This definition is appropriate when a certain access strategy is conditioned by more metocean variables (e.g. wave height and wave period, or wave height and wind speed). The set of discrete times for which access is possible, for multiple maintenance strategies, is then defined as:

$$\mathcal{J}^{app} = \bigcup_{m=1}^M \mathcal{J}_m^{app} \quad \text{Equation 34}$$

This models the case in which more access strategies are available to reach the offshore location. Equation 25 to Equation 32 then apply as illustrated in the previous sections.

## 6.3 Results: North Sea accessibility

### 6.3.1 General considerations

The North Sea is an enclosed basin located between the British Isles and the mainland of North-Western Europe. It is connected to the Atlantic by the Strait of Dover and opens directly onto the ocean between the Orkney and the Shetland islands. Figure 49 shows its bathymetry, in steps of 25 m. It can be seen that the Southern part of this region is characterized by lower water depths (below 50 m), even at considerable distances from the coast. On the other hand, Scotland and Norway possess waters with larger depths, exceeding 50 m also at short distances from the coast.

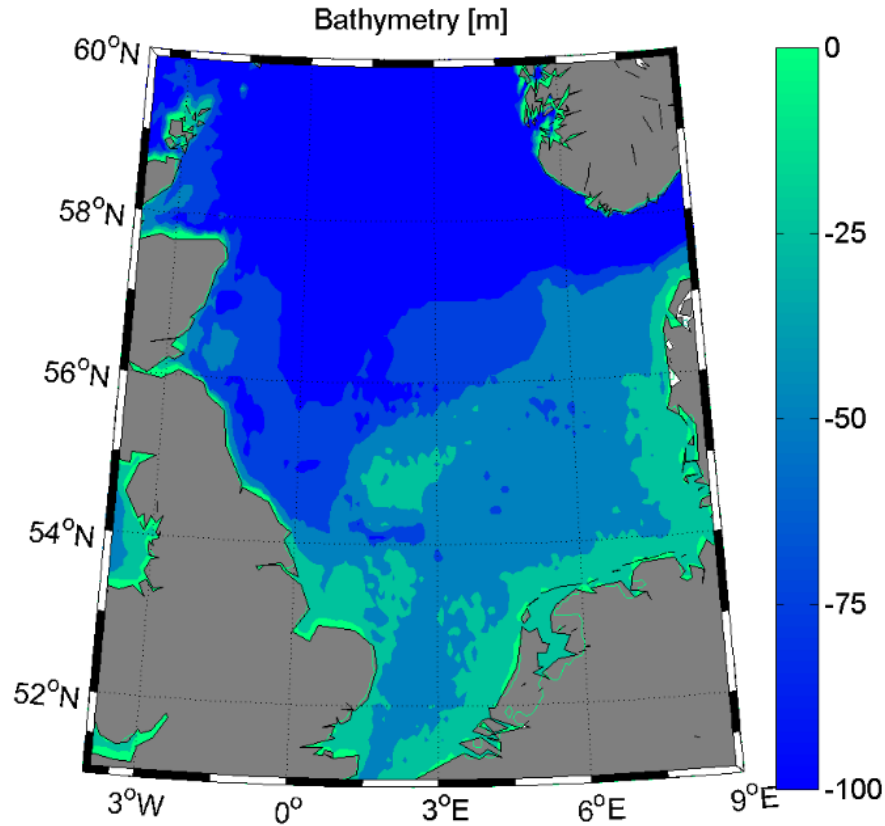


Figure 49: Bathymetry of the North Sea.

Time histories of wind and wave parameters were extracted with hourly resolution from the IH Cantabria databases (see Chapter 4) for all the available nodes in the quadrant  $[4^{\circ}\text{W}, 9^{\circ}\text{E}; 51^{\circ}\text{N}, 60^{\circ}\text{N}]$ . A total number of 2477 grid points was evaluated. The reference period (i.e. the time domain  $\mathcal{T}$ , see Equation 23) spans from 1990 to 2012, which results in more than 200000 time samples for each node, for each variable. For the purposes of this paper, two variables ( $V=2$ ) are considered of interest: significant wave height ( $H_s$ ) and mean wind speed at 90 m of height ( $W_s$ ). Two cases are investigated:

### 6.3.1.1 Case I: inspection or light repair operations

This case represents a useful exercise for light repair operations, which require small crews. Two access strategies are considered ( $M=2$ ):

- $s_1$ : access by workboat. This strategy is conditioned by significant wave height solely, for which the chosen limit is 1.5 m.
- $s_2$ : access by helicopter. This strategy is conditioned by mean wind speed solely, for which the chosen limit is  $12 \text{ m s}^{-1}$ .

The analysis of two complementary strategies as those above may be useful at the design stage, when inspection and maintenance logistics need to be defined according to the climate at the farm location. Table 16 summarizes input data for this case.

		Variable types, $x_{v,m}$		Variable limits, $x^{lim}_{v,m}$		
		m		m		
		1	2	1	2	
Case I	v	1	$H_s$	$H_s$	1.5 m	inf
	2	$W_s$	$W_s$	inf	$12 \text{ m s}^{-1}$	

*Table 16: Summary of input data for this investigation. Case I.*

### 6.3.1.2 Case II: heavy repair operations

Differently from before, this case is a meaningful exercise for heavy repair operations, such as gearbox replacement. A single access strategy is considered ( $M=1$ ):

- $s_1$ : access by crane vessel. This strategy is conditioned by significant wave height, for which the chosen limit is 1.5 m, and wind speed, for which the chosen limit is  $12 \text{ m s}^{-1}$ .

Though the real pattern of required conditions is more complex, this application can represent the need of weather windows conditioned by wave height for crew transfer, and by wind speed for crane operations. Table 17 summarizes the input data for Case II.

		Variable types, $x_{v,m}$		Variable limits, $x_{v,m}^*$	
		m		m	
		1	1	1	1
Case II	v	1	$H_s$	$H_s$	1.5 m
	2	$W_s$	$W_s$	$W_s$	$12 \text{ m s}^{-1}$

*Table 17: Summary of input data for this investigation. Case II.*

The limits considered for the calculation of the accessibility parameters are chosen based on what is found in the literature. In the tables above, “inf” stands for “infinite” i.e. that access

strategy does not depend on that metocean variable. As highlighted by DNV, when dealing with marine operations of limited duration, it is fundamental to take into account the seasonality of the metocean conditions [52]; therefore, results will be presented separately for each season.

It was not possible to keep consistent colour scales through all the figures. Indeed, colour scales were first chosen to be equal for winter/autumn and summer/spring, and then adjusted to make the spatial variation of each parameter as clear as possible. All the results are strictly dependent on the chosen limits for the selected metocean variables.

### **6.3.2 Wind speed and wave height spatial distributions**

In Figure 50 the mean value of the significant wave height is depicted for winter, spring, summer and autumn. Roughly speaking, harshest conditions occur in the northern sector of the basin, which is more exposed to the North Atlantic storms. In the southern sector, a milder wave climate is observed: this is also likely to be due to a smaller fetch length, given by the coastline, as well as to shallow water conditions (see Figure 49) which are responsible for energy dissipation phenomena. In addition, the eastern sector undergoes slightly more severe conditions than the western one, for similar distances from the coast. In the entire basin, a strong seasonality is ascertained.

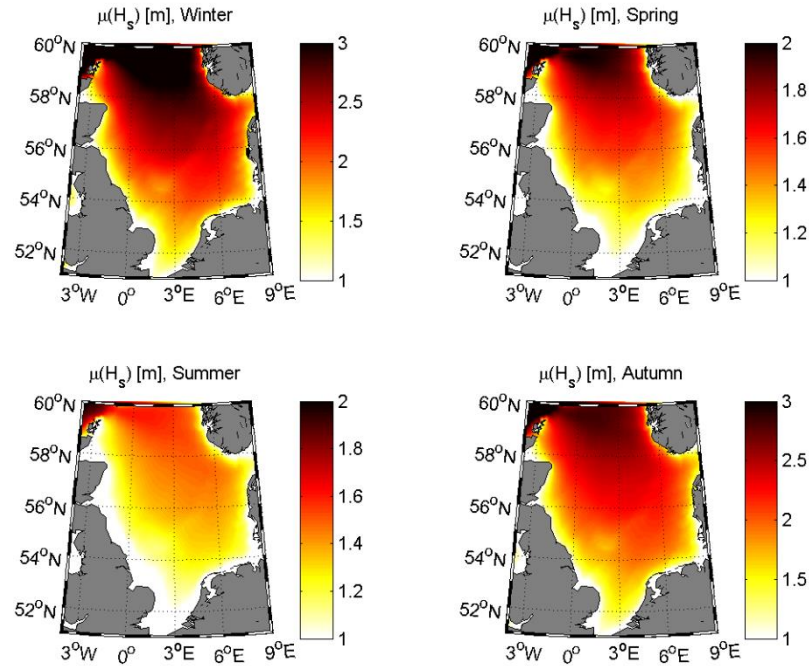


Figure 50: Mean wave significant height in the North Sea, 1990-2012.

The mean wind speed distribution is shown in Figure 51. Again, a strong seasonality appears to characterize the climate variability, being winter the season with higher mean wind speeds. In general, the trend of harsher climate (and thus, in this case, larger resource) in the northern and eastern sector is kept. In the southern area of the basin, the lower wind speed is most likely due to the sheltering effects of the UK Island and the Northern Europe mainland. In addition, it is worth noticing that the area south of Norway experiences slightly higher mean wind speeds compared to other regions, especially during spring and summer and at relatively small distances from the coast.

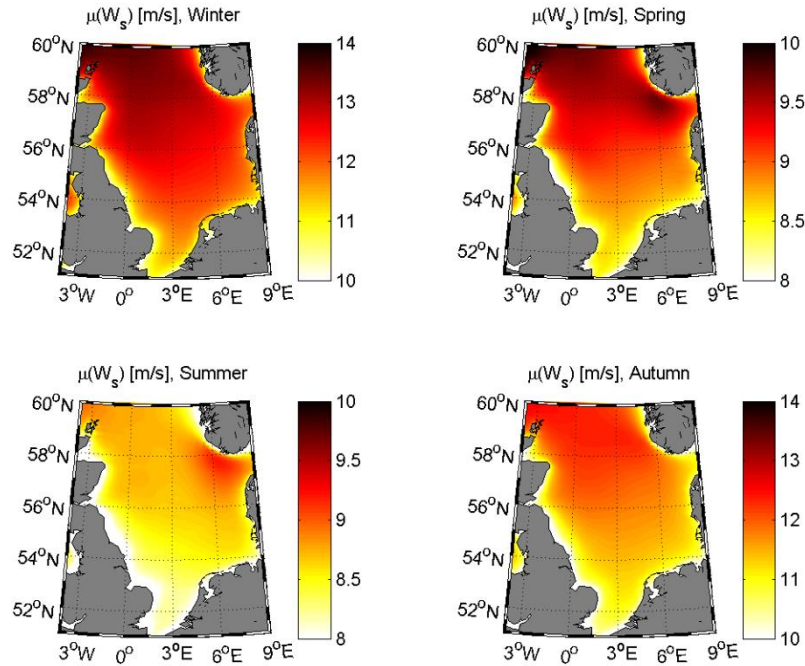


Figure 51: Mean wind speed in the North Sea, 1990-2012.

### 6.3.3 Results for Case I: light repair operation

#### 6.3.3.1 Approachability

Approachability is directly related to the probability distribution of the selected metocean parameters, see Section 6.2.2. Nevertheless, a clear correlation with their mean value is found, as shown in Figure 52 and Figure 53, which depict the average seasonal approachability by workboat and helicopter, respectively. The seasonal and spatial variations of mean significant wave height and mean wind speed are directly reflected in the approachability maps. Generally speaking, approachability by workboat is harder than by helicopter; furthermore, it can be observed that the spatial variability of accessibility is more significant when conditioned by wave height, more than by wind speed. It is worth remembering that results are strongly dependent on the chosen limits for wave height and wind speed.

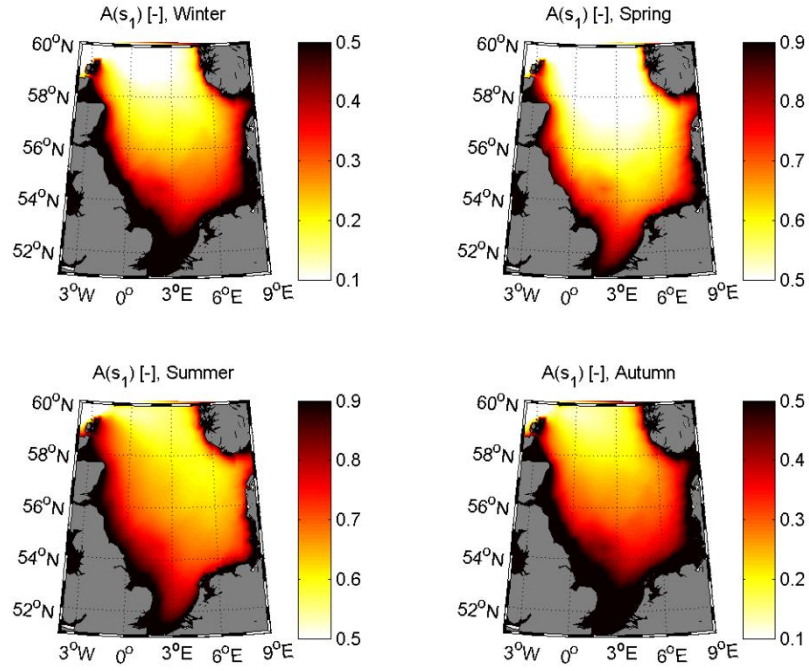


Figure 52: Case I. Approachability with workboat,  $A(s_1)$ .

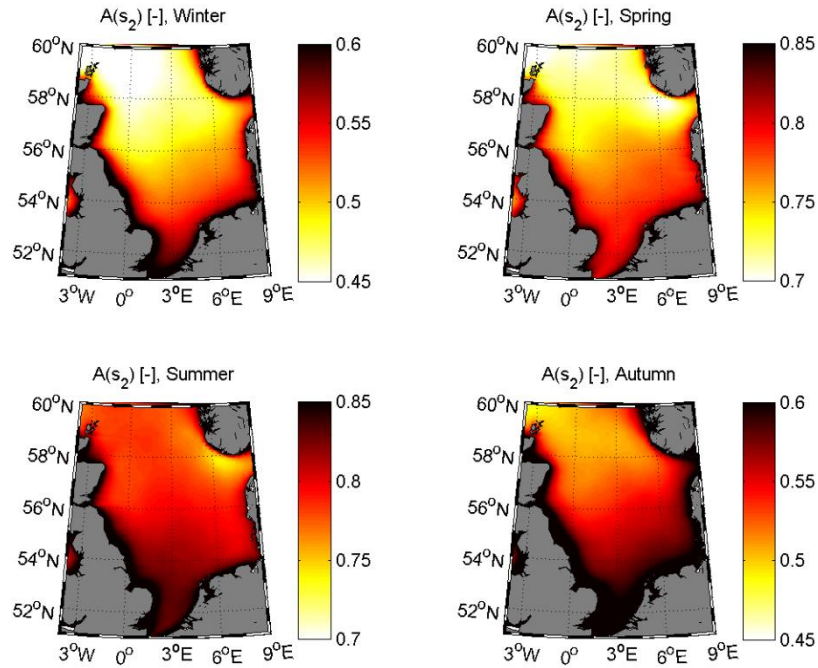


Figure 53: Case I. Approachability with helicopter,  $A(s_2)$ .

Figure 54 shows the mean approachability for multiple access strategies, representing the probability that a location is approachable either by boat or by helicopter. It is possible to see that approachability in this case is everywhere higher than when calculated only for one single access strategy. Moreover, it is found that both wave height and wind speed influence approachability, without any of the two being clearly dominant (for the chosen limits). The coast of UK results to be one of the most approachable areas in the basin, with values of approachability higher than 65% in winter and higher than 90% in summer, differently from the coast of Norway, which highlights poor accessibility rates for similar distances from the coast.

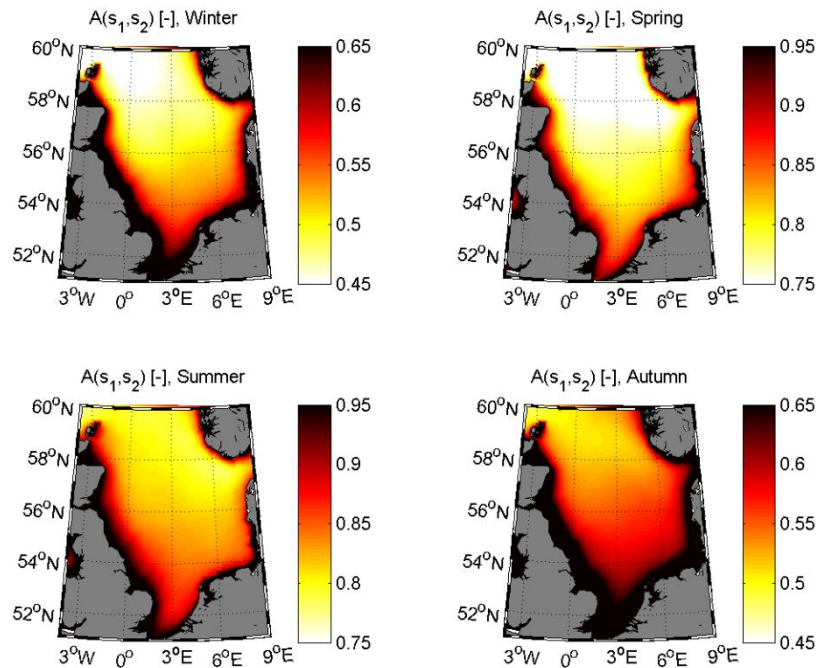


Figure 54: Case I. Approachability with either workboat or helicopter,  $A(s_1, s_2)$ .

### 6.3.3.2 Accessibility

Weather windows are essential in evaluating the persistence of metocean conditions for offshore maintenance purposes. Figure 55 depicts the average accessibility  $A^*$ , evaluated for weather windows of 8 hours length; results are presented for multiple access strategies. Color scale

is equal to that of Figure 54, to facilitate comparison between approachability and accessibility. The amount of time for which access is possible reduces considerably, especially in the northern region of the basin, which means that there is a relevant number of weather windows shorter than 8 hours. This enhances accessibility easiness in the southern part of the basin.

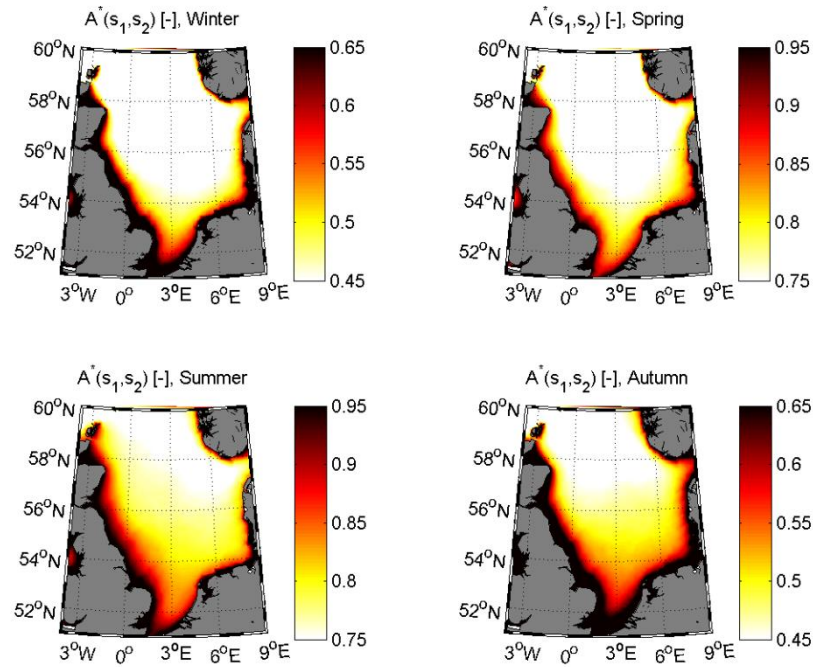


Figure 55: Case I. Accessibility with either workboat or helicopter,  $A^*(s_1, s_2)$ .

### 6.3.3.3 Mean waiting period

The mean waiting period for two consecutive weather windows of 8 hours is shown in Figure 56, for multiple access strategies. The waiting time is very small during summer and spring, with values often smaller than 4 hours. On the other hand, the mean waiting time in winter and autumn is mostly below 16 hours. Again, the whole UK coast presents better results, since the waiting time is the smallest in the whole region, for similar distances from the coast.

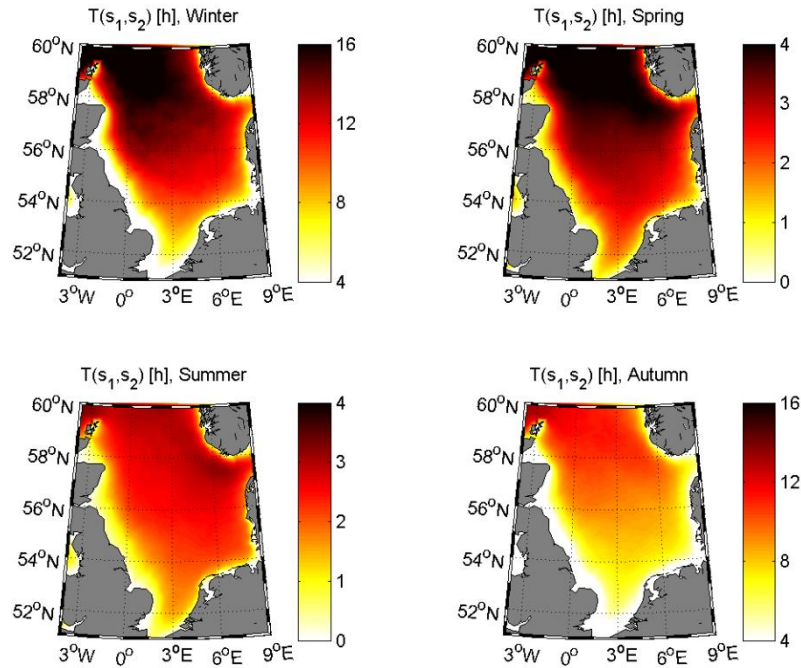


Figure 56: Case I. Mean waiting period with either workboat or helicopter,  $T(s_1, s_2)$ .

#### 6.3.3.4 Access during daytime

Often, inspection or maintenance for light repair operations can be performed only during daylight periods [60], [118]. It is therefore very interesting to evaluate weather windows occurring during daytime. Daylight hours essentially change according to geographical location and date. For each grid node, the number of daylight hours was calculated as the difference between the sunset hour and the sunrise hour, obtained by means of reduced accuracy expressions suggested by the U.S. Naval Observatory [119]. In Figure 57 and Figure 58, it is possible to examine results of accessibility and mean waiting time for daytime. It can be noticed how accessibility drops to values lower than 15% during winter and autumn, and how waiting times are increased if activities have to be worked out during daylight. Indeed, during winter and autumn one could have to wait up to 4 or 5 days, before a new 8 hours weather window is available, especially close to the coasts of Denmark and Norway, and in the North sector of the basin.

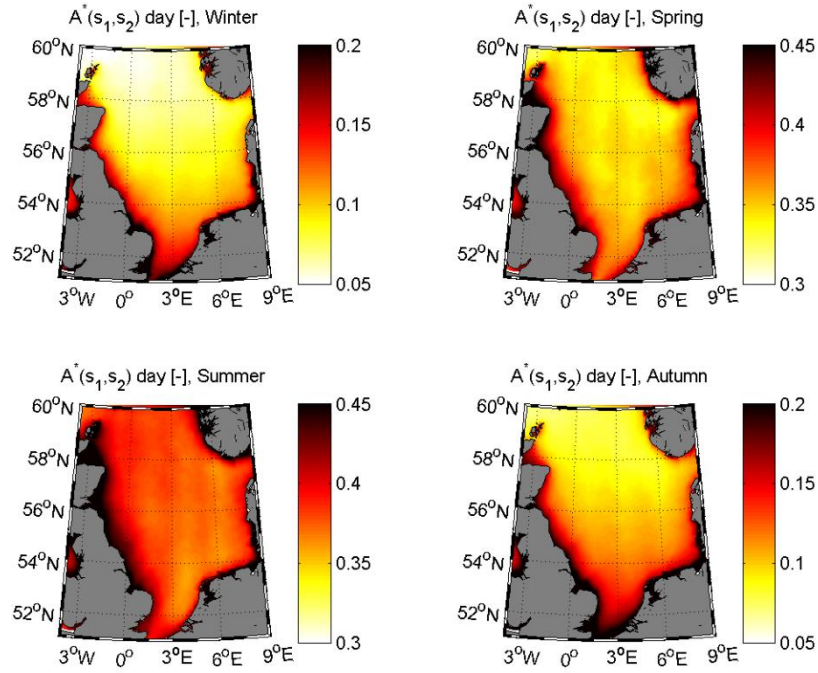


Figure 57: Case I. Accessibility with either workboat or helicopter during daytime,  $A^*(s_1, s_2)$  day.

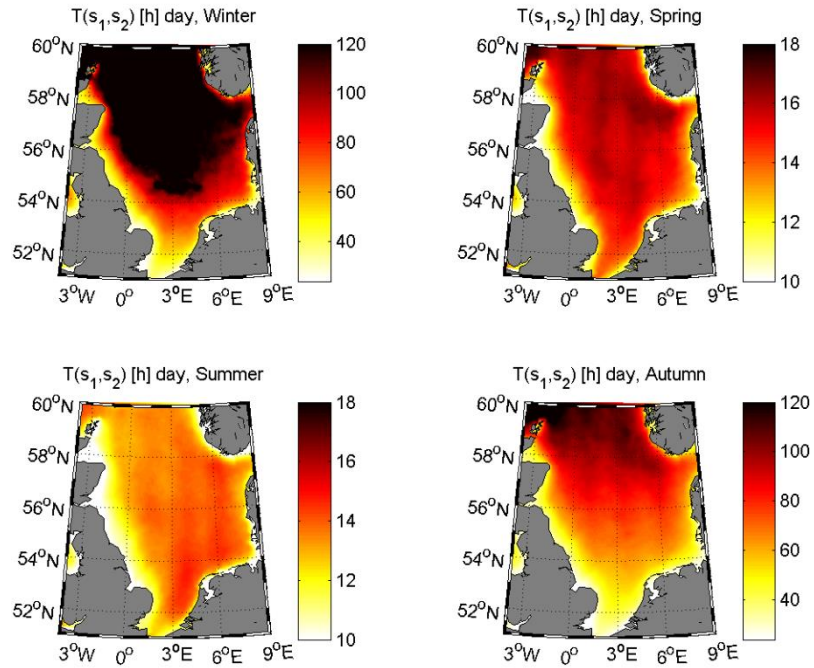


Figure 58: Case I. Mean waiting time with either workboat or helicopter during daytime,  $T(s_1, s_2)$  day.

It is interesting to see the difference between the mean waiting time with and without daylight regime. Figure 59 shows that the increase in the waiting time during winter and autumn is more relevant in the northern sector of the basin: this is because, here, there is a lower number of daylight hours and a harsher climate, compared to the southern sector, which reduces the chance to find useful weather windows. On the other hand, during spring and summer, the southern sector of the basin that gets a larger increase in the mean waiting time. This is probably because of the reduced number of daylight hours, compared to the northern sector, and generally mild climate in the whole basin at that reduces the North-South accessibility difference (see also Figure 57).

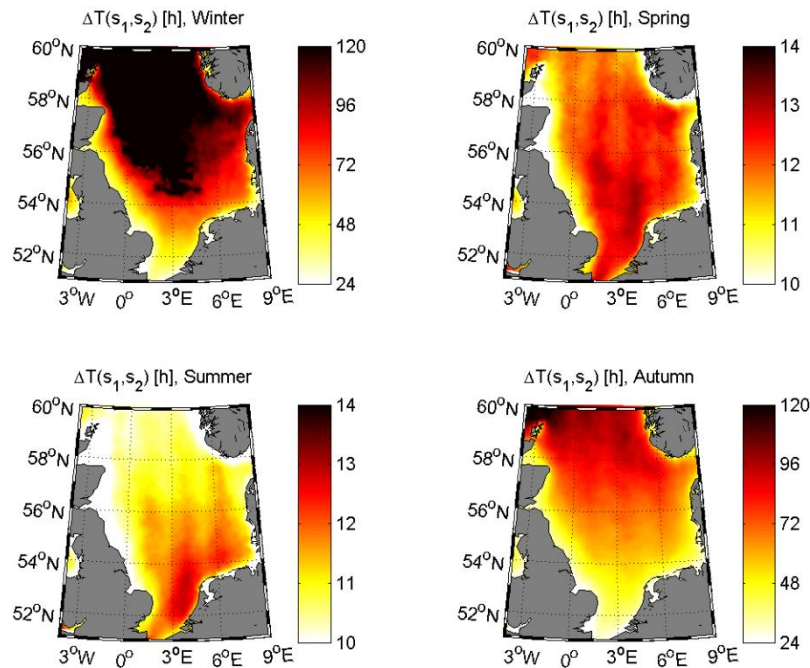


Figure 59: Case I. Change in mean waiting time with/without daylight with either workboat or helicopter,  $\Delta T(s_1, s_2)$ .

### 6.3.4 Results for Case II: heavy repair operation

The analysis carried out for Case II is related to the use of offshore crane vessels, where there is need for an access strategy that is conditioned both by wave height and wind speed, see Table 17. In Figure 60 it possible to appreciate the mean waiting period, considering windows of

8 hours length. As expected, mean waiting periods are much larger than those for Case I (light repair operation, see Figure 56). Nevertheless, it is remarkable that during summer the mean waiting period is below 8 hours in almost the whole basin.

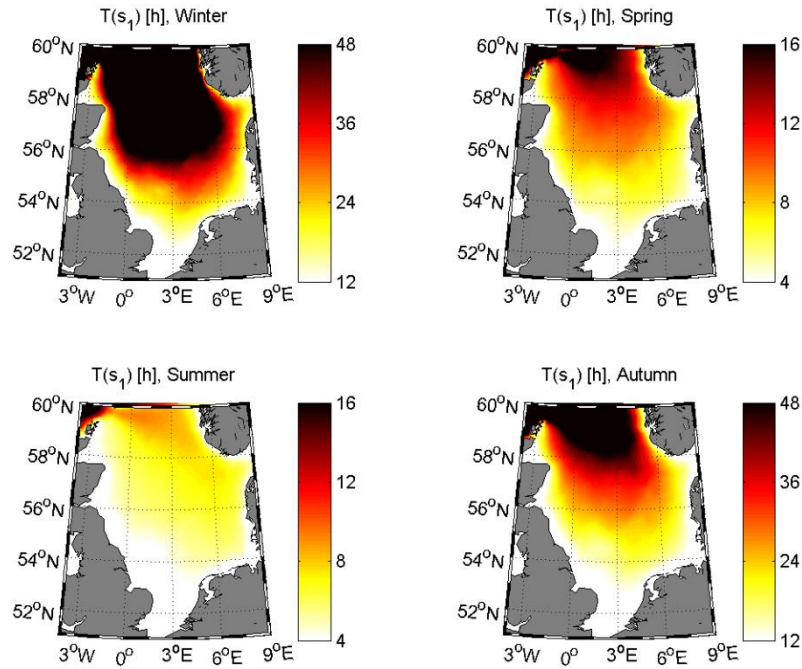


Figure 60: Case II. Mean waiting period with offshore crane vessel,  $T(s_1)$ .

## 6.4 Results: accessibility of existing or planned wind farms

A detailed accessibility analysis for existing or planned wind farms was also carried out. Figure 61 and Table 18 show the geographical distribution and some relevant characteristics of the selected wind farms.

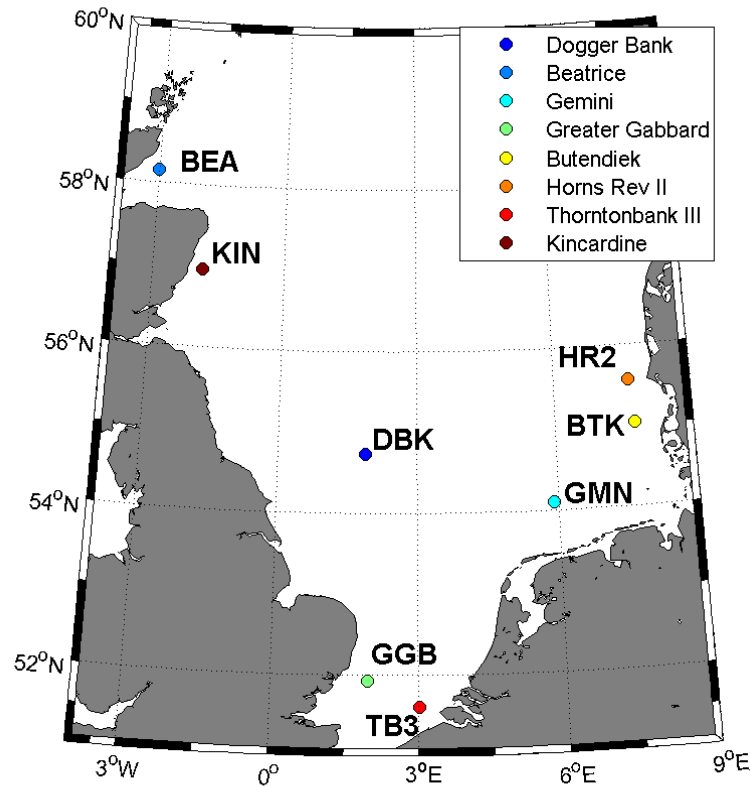


Figure 61: Location of the wind farms selected for this study.

Wind farm name	Country	Status	lat [deg]	lon [deg]	P [MW]	depth [m]	to shore [km]
Dogger Bank (DBK)	ENG	Auth.	54.75	1.92	1000.0	18-63	131.0
Beatrice (BEA)	SCO	Auth.	58.11	-3.09	664.0	35-50	13.4
Gemini (GMN)	NED	Auth.	54.04	5.97	600.0	28-36	85.0
Greater Gabbard (GGB)	ENG	Comm.	51.93	1.88	504.0	20-32	36.0
Butendiek (BTK)	GER	Constr.	55.02	7.77	288.0	17-20	35.0
Horns Rev II (HR2)	DEN	Comm.	55.60	7.59	209.3	9-17	31.7
Thorntonbank III (TB3)	BEL	Comm.	51.64	2.93	110.7	12-28	26.0
Kincardine (KIN)	SCO	Eval.	57.00	-1.88	50.0	60-80	13.0

Table 18: Main characteristics of the chosen wind farms [120].

In Table 19 the mean value of the accessibility parameters is presented, averaged over the period 1990-2012. Darkest cells are associated to worst values, in terms of accessibility easiness. Among the wind farms studied, Dogger Bank is the one with the most favorable mean wind conditions ( $10.33 \text{ m s}^{-1}$ ) while Thorntonbank III that with the worst ones ( $9.58 \text{ m s}^{-1}$ ). Gemini is

the farm with the most adverse mean wave conditions (1.59 m) while Greater Gabbard that with the best ones (1.06 m).

Regarding results for Case I (light repair operations), Thorntonbank III and Greater Gabbard show good approachability rates, being located at the East Coast of England which is not exposed to northern storms. Beatrice and Kincardine show also considerable approachability rates, being sheltered by the coast and out of the reach of Atlantic storms. Beatrice is the farm with highest values of approachability, accessibility with weather windows of 8 hours and lowest values of mean waiting period. However, when coming to mean waiting period under daylight regime, Thorntonbank III presents better values than Beatrice: this is likely because of the lower number of daylight hours during the winter and autumn seasons at Beatrice which, combined with a harsher climate, reduces the total number of weather windows in this location.

For what concerns Case II results (heavy repair operations), Greater Gabbard and Thorntonbank III are the best farm according to all the calculated accessibility parameters. This is surely due to their sheltered position, which however also means lower wind energy available. It is remarkable that Beatrice shows good accessibility parameters also in this case, except for mean waiting period during daylight regime.

		Mean accessibility results 1990-2012								
		DBK	BEA	GMN	GGB	BTK	HR2	TB3	KIN	
Case I	$\mu(Hs)$	m	1.54	1.12	1.59	1.06	1.40	1.38	1.07	1.24
	$\mu(Ws)$	m s <sup>-1</sup>	10.33	10.01	10.13	9.66	10.17	10.21	9.58	9.87
	$A(s_1, s_2)$	-	0.69	0.84	0.71	0.82	0.73	0.73	0.82	0.82
	$A^*(s_1, s_2)$	-	0.63	0.80	0.65	0.78	0.68	0.68	0.79	0.78
	$T(s_1, s_2)$	h	5.95	2.38	5.22	2.51	4.71	4.79	2.47	2.66
	$T(s_1, s_2)$ day	h	57.23	35.21	44.91	27.91	44.12	45.05	27.19	35.13
Case II	$A(s_1, s_2)$	-	0.47	0.60	0.48	0.67	0.52	0.51	0.66	0.57
	$A^*(s_1, s_2)$	-	0.43	0.53	0.44	0.61	0.47	0.47	0.60	0.51
	$T(s_1, s_2)$	h	16.16	9.19	14.66	6.04	11.99	12.55	6.23	10.64
	$T(s_1, s_2)$ day	h	111.76	82.66	109.99	41.80	84.85	110.29	41.25	80.83

Table 19: Mean value of relevant accessibility parameters for selected wind farms.

The yearly variation of mean waiting period during daylight regime is reported in Table 20, for the Dogger Bank and Thorntonbank III farms (Case I and Case II). At the end of the table, it is also possible to find the global mean and standard deviation of the mean waiting period, together with its scatter index (standard deviation divided by mean value). For both wind farms, 1990 has been a particularly severe year, which surely affects the mean results highlighted in the previous table. It is worth remarking that the mean waiting period for Dogger Bank is not only high, but also very variable for both Case I and Case II: its scatter index for the period 1990-2012 results to be 0.92 and 0.98, respectively. On the other hand, mean waiting period for Thorntonbank III has a lower scatter index (0.13 for Case I and 0.20 for Case II), which makes its accessibility much more predictable.

Mean waiting time under daylight regime [h]				
	Case I: $T(s_1, s_2)$ day		Case II: $T(s_1)$ day	
	DBK	TB3	DBK	TB3
1990	292.6	36.8	600.3	60.0
1991	42.0	24.6	76.3	32.5
1992	44.4	27.8	80.4	41.1
1993	34.6	25.4	55.4	33.6
1994	48.8	25.7	95.5	39.0
1995	67.9	31.0	134.4	56.9
1996	48.4	26.7	116.1	38.0
1997	35.3	22.6	57.5	32.4
1998	54.7	27.9	119.9	41.9
1999	43.8	28.0	94.3	44.3
2000	61.7	31.5	134.4	58.7
2001	44.7	23.9	77.2	36.9
2002	66.7	32.7	143.7	48.1
2003	36.1	24.2	69.3	32.8
2004	42.2	27.9	98.6	45.3
2005	56.9	27.9	125.0	43.8
2006	39.5	26.7	66.6	39.8
2007	43.9	27.6	76.7	41.7
2008	66.8	30.4	101.6	46.0
2009	33.1	24.4	55.9	35.1
2010	38.9	23.3	65.4	32.7
2011	37.1	23.2	64.7	31.5
2012	36.1	25.1	61.2	36.7
$\mu$	57.2	27.2	111.8	41.3
$\sigma$	52.5	3.5	110.1	8.4
$\sigma/\mu$	0.92	0.13	0.98	0.20

Table 20: Case I and II. Mean waiting time during daylight regime for DBK and TB3 farms.

Finally, it is very interesting to evaluate the influence of the wind speed and wave height limits on the accessibility parameters. Figure 62 (Case I) and Figure 63 (Case II) depict the mean waiting period, as a function of wind speed and wave height limits, for Dogger Bank. When the limits to wind speed and wave height are, respectively,  $12 \text{ m s}^{-1}$  and 1.5 m, the mean waiting time during daylight is 57.23 hours for Case I and 111.8 hours for Case II (see. Table 19). Changing

these limits results in a non-linear change of the mean waiting time. Better access means can dramatically improve the accessibility of offshore locations.

For example, the use of vessels with motion-compensated platforms (i.e. Ampelmann, which declares accessibility up to 2.5 m of significant wave height [121], [122]) can bring the mean waiting time down to 26.83 hours (53% decrease) for Case I. Similarly, the same wave height limit could decrease the mean waiting time to 73.63 hours (34 % decrease) for Case II. One should however consider that travelling with increased wave heights might induce seasickness to workers and complicate access.

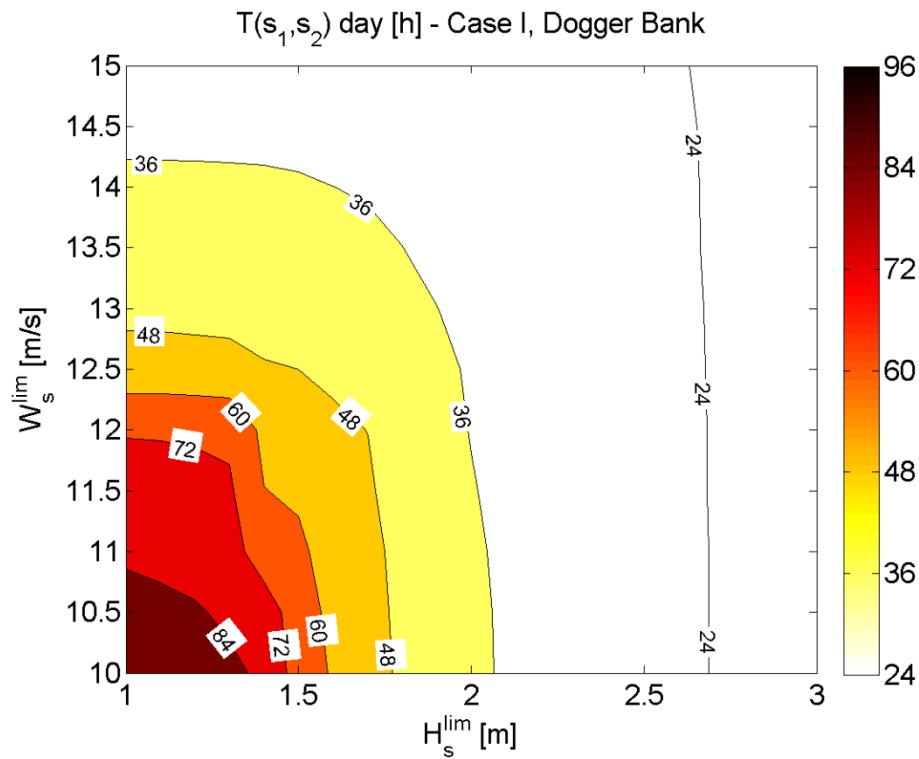


Figure 62: Case I. Sensitivity of mean waiting time to access thresholds for daylight regime, DBK wind farm.

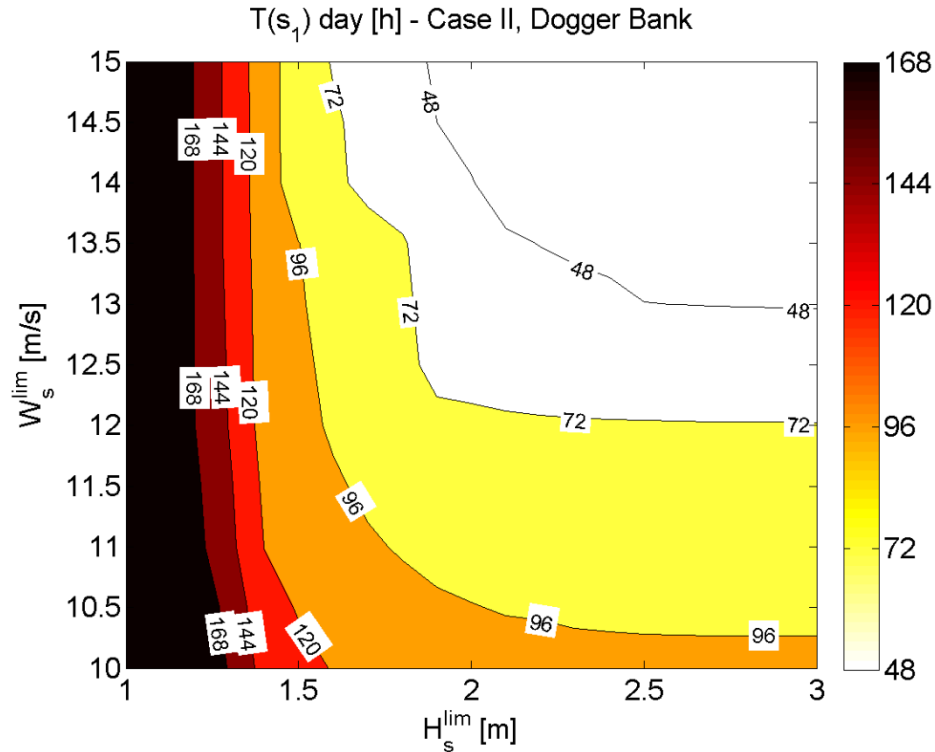


Figure 63: Case II. Sensitivity of mean waiting time to access thresholds for daylight regime, DBK wind farm.

## 6.5 Conclusions

In this Chapter a vast accessibility analysis of the North Sea was carried out, focusing on offshore wind applications. The concepts of accessibility, weather window, approachability and waiting time were mathematically defined. These parameters were evaluated for the whole basin, taking into account seasonality and daylight regime for two cases: light and heavy repair operations. The availability of reanalysis data with high spatial and temporal resolution allowed obtaining precise results, for the period 1990-2012. The Northern and Eastern sectors of the North Sea are characterized by harsher wave climate but also by higher wind resource. UK near-shore areas result then to be more accessible than those of Norway or Denmark, at the price of lower primary resource, for similar distances from the coast. This means that, in order to harvest the same wind resource, UK wind farms should be planned farther from the coast, where water depth often

exceeds 50 m (except for the Eastern coast of England). All the results highlight a strong seasonality of the climate in the basin. Results were detailed for existing or planned offshore wind farms. Among them, Dogger Bank (UK) resulted to be the one with the highest resource but lowest accessibility rates, being exposed to the ocean storms of the basin. Due to their reduced exposure, Greater Gabbard (UK) and Thornton Bank III (Belgium) are the two farms for which the mean waiting time during daytime is lower and less variable (scatter index is 0.13 for light repair operations, 0.20 for heavy repair operations). Finally, it is very relevant to notice that accessibility parameters may change non-linearly, as the wave height and wind speed limits are changed. The use of last-generation motion-compensated vessels has the potential for reducing waiting times by more than 50% for light repair operations.

This analysis put in evidence two things: the importance of using long-term metocean data, to evaluate the possible variability of accessibility parameters, and the need for breakthrough access means able to help increasing the availability of offshore wind farms.

---

---

## Chapter 7

# Modelling of walk-to-work access

---

---

### 7.1 Motivation and state-of-the-art review

As illustrated in the previous chapter, the evaluation of accessibility indicators is based on the definition of safety thresholds associated to specific metocean parameters. For example, it was mentioned that access for inspection or light maintenance, which is often granted by small crew transfer vessels (CTVs), could be performed when the wave significant height is below 1.5-2.0 m. Vessel providers usually relate access only to this metocean parameter, without taking into account wave period or wave direction. For floating turbines, vessel-platform interaction also plays a relevant role. In addition, it seems that the captain of the vessel influences often decision making during real sea operations, based on his experience. When access is realized using boats, technicians usually step over directly from the vessel to the wind turbine in the so-called *walk-to-work* approach. The risk associated to personnel transfer and the number of incidents occurred during marine operations in offshore wind (see Chapter 2) impose to search for possible design methods to complement the field experience of the involved parties.

Appropriate tools are necessary in order to predict the response of a service vessel during the transfer of technicians to and from a floating wind turbine. This Chapter aims at developing a methodology for the calculation of the combined motions of a floating wind turbine and a service vessel in a personnel transfer configuration, to define safe accessibility levels for inspection and maintenance.

Wu [123] published a very inspiring paper in which he evaluated, in the frequency domain, the docking operation onto a fixed wind turbine (neglecting however the vessel-structure hydrodynamic interaction). This work was further extended by Sperstad [124] that compared the use of single-parameter and multi-parameter wave criteria for accessibility assessment. González et al. [125] also investigated the landing of a vessel on a fixed wind turbine, comparing the results of a time-domain numerical model with experimental tests. To the Author's knowledge, for floating turbines there are no published studies yet.

## 7.2 Methodology

The system composed by a floating platform and a service vessel is modelled as a rigid, possibly constrained, multi-body system in frequency domain. This approach implies the assumption of linear force-displacements relationships; therefore, non-linear phenomena have to be linearized accordingly. Once the system transfer functions are known, it is possible to calculate short-term response extremes, for given wave conditions, based on specific statistical assumptions. The methodology proposed is thus based on the following points, detailed in Section 7.2.1 to Section 7.2.5:

- 1) definition of relevant coordinate systems;
- 2) definition of equation of motion for the vessel-platform system;
- 3) linearization of the mooring forces;
- 4) linearization of the viscous damping forces;
- 5) calculation of extreme responses.

This methodology was applied to the OC4 floating platform and two types of access vessels: results are presented in Section 7.3. In addition, long-term accessibility was calculated for

a location off the coast of Aguçadoura, Portugal and discussed in Section 7.5. Final conclusions about this chapter are contained in Section 7.6.

### 7.2.1 Definition of coordinate systems

As a first step, it is essential to define the coordinate systems used in this Chapter (see Figure 64); all of them are inertial:

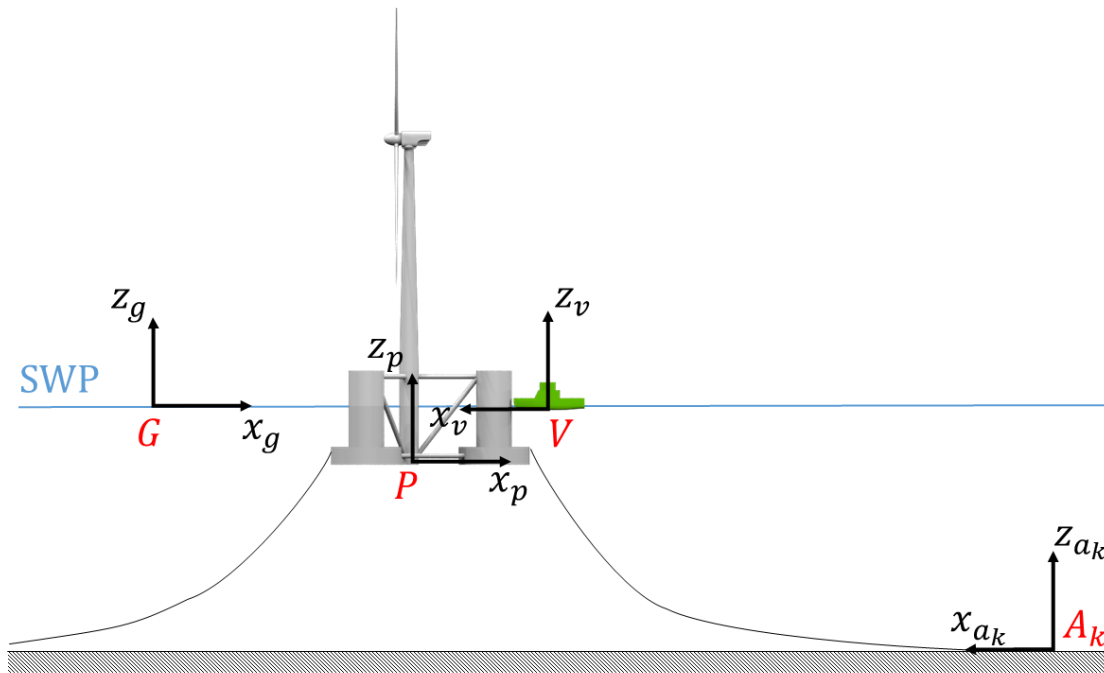


Figure 64: Coordinate systems used for walk-to-work modelling.

- *Global coordinate system (CSYS-g).* The  $x_g$ - $y_g$  plane lies on the still water plane (SWP), while the  $z_g$ -axis points upwards opposite to gravity. Its origin is the point  $G$ .
- *Vessel coordinate system (CSYS-v).* Its position and orientation with respect to CSYS-g are defined, respectively, by the position of its origin (point  $V$ ) and the rotation matrix  $\mathbf{R}_{gv}$ .
- *Platform coordinate system (CSYS-p).* Its position and orientation with respect to CSYS-g are defined, respectively, by the position of its origin (point  $P$ ) and the rotation matrix  $\mathbf{R}_{gp}$ .

- *Anchor coordinate systems (CSYS- $a_k$ )*. The  $k$ -th system is fixed to the respective anchor. Its position and orientation with respect to *CSYS- $g$*  are defined, respectively, by the position of its origin (point  $A_k$ ) and the rotation matrix  $Rga_k$ .

In this Chapter a superscript ( $^g$ ,  $^a$ ,  $^p$  or  $^v$ ) indicates in which coordinate system a given quantity is expressed, according to the definitions introduced above.

## 7.2.2 Equation of motions for the system

The system under investigation is composed of a floating wind turbine and a transfer vessel, which exchange forces at a (possible) contact point. Each body has six degrees of freedom and the frequency-dependent complex motions are expressed in body-coordinate systems (i.e. *CSYS- $v$*  and *CSYS- $p$* ), joined in a single column vector  $\zeta$  (12 x 1, in which the first six elements refer to the vessel motions  $\zeta_v$ , and the following six to the platform motions  $\zeta_p$ ). The equation of motion of the multi-body system can be written resembling the well-known Ogilvie frequency-domain formulation [94] of the Cummins' equation [92]:

$$K(j\omega, \zeta)\zeta(j\omega, \theta) = f(j\omega, \theta) \quad \text{Equation 35}$$

where:

$$K(j\omega, \zeta) = -\omega^2[\mathbf{M} + \mathbf{A}(\omega)] + j\omega[\mathbf{B}_t(\omega, \zeta)] + \mathbf{C}_t \quad \text{Equation 36}$$

In the formulas above  $j$  is the imaginary unit,  $\omega$  is the wave angular frequency,  $\theta$  the wave direction,  $f$  (12 x 1) is the wave excitation force vector,  $\mathbf{M}$  (12 x 12) the inertia matrix,  $\mathbf{A}$  (12 x 12) the added mass matrix,  $\mathbf{B}_t$  (12 x 12) the total damping matrix and  $\mathbf{C}_t$  (12 x 12) the total stiffness matrix. Please note that bold letters stand for vectors or matrices whereas non-bold stand for scalars.

No aerodynamic forces are taken into account i.e. the wind turbine is supposed to be in idle conditions. The total damping of the system can be split as:

$$\mathbf{B}_t = \mathbf{B}(\omega) + \mathbf{B}_l(\omega, \zeta) = \mathbf{B}(\omega) + \begin{bmatrix} \mathbf{B}_{lv}(\omega, \zeta) & \mathbf{0} \\ \mathbf{0} & \mathbf{B}_{lp}(\omega, \zeta) \end{bmatrix} \quad \text{Equation 37}$$

where  $\mathbf{B}$  is the potential damping matrix and  $\mathbf{B}_l$  the linearized hydrodynamic viscous damping matrix (with  $\mathbf{B}_{lv}$ ,  $\mathbf{B}_{lp}$  the corresponding 6 x 6 vessel and platform matrices). As it will be detailed in the following sections, it is worth noticing that the total damping can be a function of the displacement vector  $\zeta$  itself. The total stiffness of the system can be split as:

$$\mathbf{C}_t = \mathbf{C} + \mathbf{C}_l = \mathbf{C} + \begin{bmatrix} \mathbf{C}_{lv} & \mathbf{0} \\ \mathbf{0} & \mathbf{C}_{lp} \end{bmatrix} \quad \text{Equation 38}$$

where  $\mathbf{C}$  is the hydrostatic stiffness matrix and  $\mathbf{C}_l$  the linearized mooring stiffness matrix (with  $\mathbf{C}_{lv}$ ,  $\mathbf{C}_{lp}$  the corresponding 6 x 6 vessel and platform matrices). The constraint equation is written as:

$$\mathbf{D}\zeta = \mathbf{0} \quad \text{Equation 39}$$

where  $\mathbf{D}$  ( $D \times 12$ , being  $D$  the number of boundary conditions) is the constraint matrix. Finally, it is possible to sum up all the pieces and write the equation of motion for the constrained system as [126]:

$$\begin{bmatrix} \mathbf{K} & \mathbf{D}^T \\ \mathbf{D} & \mathbf{0} \end{bmatrix} \begin{Bmatrix} \zeta \\ \lambda \end{Bmatrix} = \begin{Bmatrix} \mathbf{f} \\ \mathbf{0} \end{Bmatrix} \quad \text{Equation 40}$$

where  $\lambda$  ( $D \times 1$ ) is the joint reaction forces vector. Solving the linear system above gives the motions and the reaction forces of the multi-body system in the frequency domain. It is

important to notice that, since  $\mathbf{K}$  depends on the displacement vector  $\zeta$ , an iterative solution of Equation 40 is necessary.

The hydrodynamic coefficients  $\mathbf{A}$ ,  $\mathbf{B}$ ,  $\mathbf{C}$  and  $\mathbf{f}$  are calculated again by means of the potential flow solver HydroD [95]. The inertia matrix  $\mathbf{M}$  is known from the platform and vessel mass distributions. The remaining matrices  $\mathbf{C}_l$  and  $\mathbf{B}_l$  need to be estimated linearizing the mooring and hydrodynamic viscous forces, respectively.

### 7.2.3 Linearization of the mooring forces

The boat is usually not moored to the seabed, and thus  $\mathbf{C}_b$  will be most often a null matrix. On turn, the floating platform is equipped with mooring lines, which are typically characterized by a non-linear force-displacement relationship. The goal here is to linearize this behaviour about a given equilibrium position. The equivalent linear stiffness matrix can be calculated as:

$$C_{lp,ij} = \left. \frac{\partial \tau_{m,i}^p}{\partial \zeta_{p,j}} \right|_{\zeta_{p,j}=0} ; i, j = 1, 2, \dots, 6 \quad \text{Equation 41}$$

where  $\tau_m^p$  represents the vector of the mooring forces, expressed in the platform coordinate system. In conditions of static equilibrium, the system setting is schematized in Figure 65: positions are indicated with the subscript “0”.

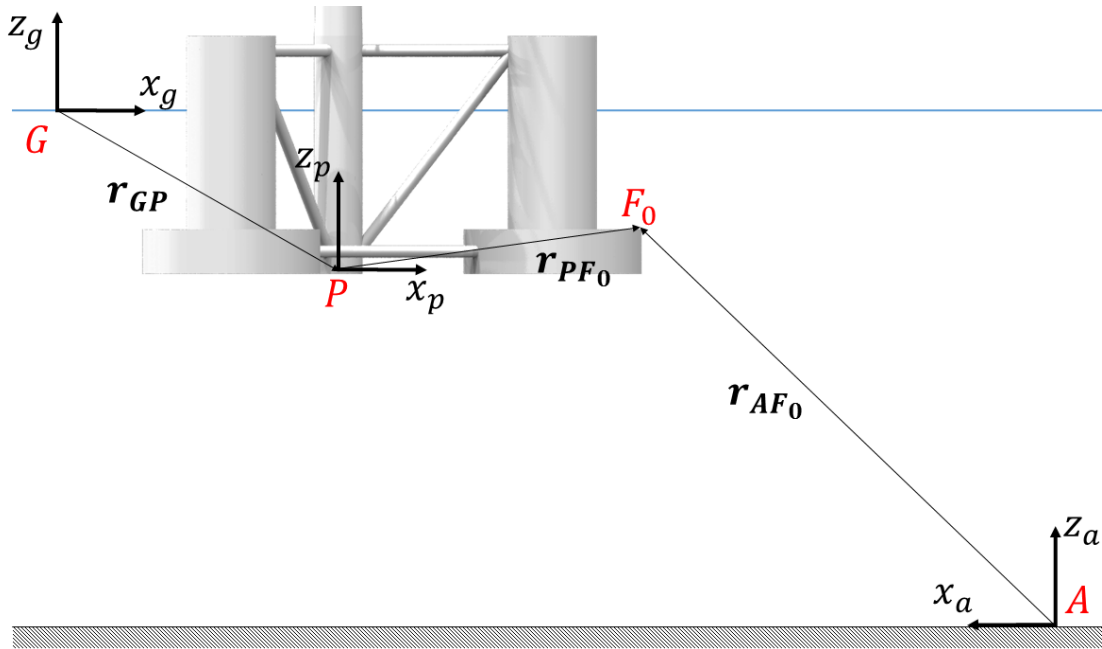


Figure 65: Platform setting configuration at in conditions of static equilibrium.

Under these conditions, it is possible to express the position of the fairlead  $F$  in the global coordinate system as:

$$\mathbf{r}_{GF_0}^g = \mathbf{r}_{GP}^g + \mathbf{R}_{gp}^T \mathbf{r}_{PF_0}^p \quad \text{Equation 42}$$

where  $\mathbf{r}_{GP}^g$  is the position vector of the platform reference point in the global coordinate system and  $\mathbf{r}_{PF_0}^p$  the position of the fairlead at rest, in the platform coordinate system. If the platform equilibrium is perturbed by a displacement vector  $\boldsymbol{\zeta}_p$  then the position of the fairlead, under the assumption of small displacements, is changed as (see Figure 66):

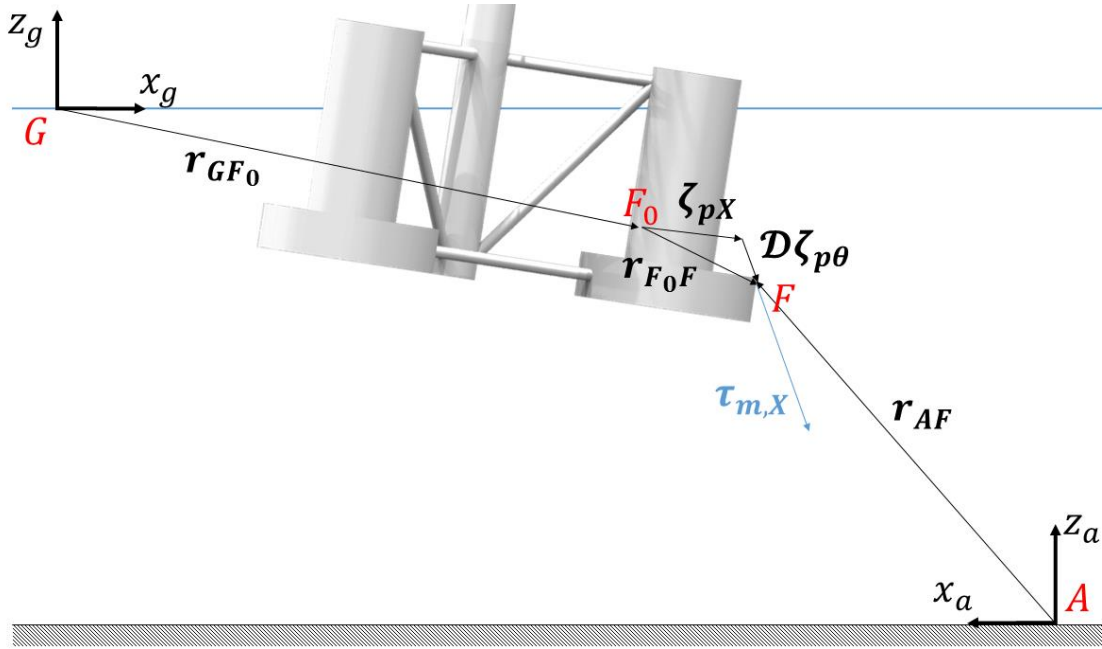


Figure 66: Platform setting configuration after a perturbation of its static equilibrium position.

$$\mathbf{r}_{GF}^g = \mathbf{r}_{GF_0}^g + \mathbf{R}_{gp}^T \mathbf{r}_{F_0F}^p = \mathbf{r}_{GF_0}^g + \mathbf{R}_{gp}^T (\zeta_{pX} + \mathcal{D} \zeta_{p\theta}) \quad \text{Equation 43}$$

In the formula above,  $\zeta_{pX}$  is the vector of translations of the floating platform i.e.  $\zeta_{pX} = [\zeta_7 \zeta_8 \zeta_9]^T$ ,  $\zeta_{p\theta}$  is the vector of rotational motions of the floating platform i.e.  $\zeta_{p\theta} = [\zeta_{10} \zeta_{11} \zeta_{12}]^T$  and  $\mathcal{D}$  can be written, knowing the fairlead positions on the platform ( $x_{PF_0}$ ,  $y_{PF_0}$ ,  $z_{PF_0}$ ), as:

$$\mathcal{D} = \begin{bmatrix} 0 & z_{PF_0}^p & -y_{PF_0}^p \\ -z_{PF_0}^p & 0 & x_{PF_0}^p \\ y_{PF_0}^p & -x_{PF_0}^p & 0 \end{bmatrix} \quad \text{Equation 44}$$

In order to calculate the mooring force, it is necessary to know the coordinates of the fairlead in the anchor coordinate system. These are calculated as:

$$\mathbf{r}_{AF}^a = \mathbf{R}_{ga}^T (\mathbf{r}_{GF}^g - \mathbf{r}_{GA}^g) \quad \text{Equation 45}$$

where  $\mathbf{r}_{GA}^g$  stands for the position of the anchor in the global coordinate system. The tension on the mooring line, and thus the horizontal and vertical components of the force exerted on the platform ( $H^*$  and  $V^*$ , respectively), can then be calculated according to quasi-static catenary equations [104]. The mooring linear force vector  $\boldsymbol{\tau}_{m,X}$  (3 x 1) can thus be expressed, in the anchor coordinate system, as:

$$\boldsymbol{\tau}_{m,X}^a = [-H^* \cos \alpha \quad -H^* \sin \alpha \quad -V^*]^T \quad \text{Equation 46}$$

where the angle  $\alpha$  is calculated as:

$$\alpha = \text{asin} \left( \frac{y_{AF}^a}{x_{AF}^a} \right) \quad \text{Equation 47}$$

Then, the mooring linear force vector  $\boldsymbol{\tau}_{m,X}^p$  can be expressed in the platform coordinate system, as:

$$\boldsymbol{\tau}_{m,X}^p = \mathbf{R}_{gp} \mathbf{R}_{ga}^T \boldsymbol{\tau}_{m,X}^a \quad \text{Equation 48}$$

The global mooring force vector  $\boldsymbol{\tau}_m^p$  (6 x 1) is therefore calculated as:

$$\boldsymbol{\tau}_m^p = \left[ \sum_{k=1}^K \boldsymbol{\tau}_{m,X_k}^p \quad \sum_{k=1}^K \mathbf{r}_{PF_k}^p \times \boldsymbol{\tau}_{m,X_k}^p \right]^T \quad \text{Equation 49}$$

where  $K$  is the number of mooring lines. Finally, the equivalent mooring stiffness matrix is calculated using Equation 41, which can be solved numerically using the central difference technique.

## 7.2.4 Linearization of viscous damping forces

Potential flow theory is not able to reproduce hydrodynamic viscous effects that may influence the overall hydrodynamic damping of a floating structure. For this reason, often, a

quadratic damping 6 x 6 matrix  $\mathbf{B}_v$  is added a-posteriori to potential flow theory results for time-domain modelling. This matrix is usually calculated by means of experimental tests or CFD calculations.

In this work, these forces are linearized by means of the so-called harmonic linearization technique [127], which consists in calculating an equivalent damping coefficient so that the work done over a wave cycle by the non-linear and equivalent linear forces is the same.

Assuming steady response in regular waves, the time-dependent displacement of the  $j$ -th degree of freedom of a given floating body can be written as:

$$z_j(t) = |\zeta_j| \cos[\omega t + \angle \zeta_j] \quad \text{Equation 50}$$

where  $\angle$  is the phase angle operator. The total non-linear viscous force acting on the  $i$ -th degree of freedom due to the motion of the  $j$ -th degree of freedom is given by:

$$F_{v,ij}(t) = B_{v,ij} \text{sign}[\dot{z}_j(t)] \dot{z}_j^2(t) \quad \text{Equation 51}$$

The work done by this force in a wave cycle can be calculated as:

$$W_{v,ij} = \oint F_{v,ij}(t) \dot{z}_i(t) dt = \oint B_{v,ij} \text{sign}[\dot{z}_j(t)] \dot{z}_j^2(t) dt \quad \text{Equation 52}$$

This integral can be solved numerically. In a completely analogous way, the work done in a wave cycle by a linear damping force would be:

$$W_{l,i} = B_{l,ij} \omega |\zeta_j| |\zeta_i| \pi \cos(\angle \zeta_j - \angle \zeta_i) \quad \text{Equation 53}$$

where  $\mathbf{B}_l$  is the sought equivalent linear damping matrix. Equating Equation 52 and Equation 53 gives  $B_{l,ij}$  as:

$$B_{l,ij}(\omega) = \frac{W_{v,ij}}{\omega |\zeta_j| |\zeta_i| \pi \cos(\angle \zeta_j - \angle \zeta_i)} \quad \text{Equation 54}$$

As previously introduced,  $B_{l,ij}$  depends displacement vector itself, which is in general not known when formulating the problem and thus imposes to use an iterative procedure to solve Equation 40.

### 7.2.5 Calculation of extreme response

Due to the linear force-displacement approximation the variance of any variable  $\psi$ ,  $\sigma_\psi$ , for a certain short-term stationary sea state, can be calculated as:

$$\sigma_\psi^2 = \int_0^{2\pi} \int_0^\infty |H_{\eta\psi}(j\omega, \theta)|^2 S_{\eta\eta}(\omega, \theta) d\omega d\theta \quad \text{Equation 55}$$

where  $H_{\eta\psi}$  is the transfer function of the response variable  $\psi$  and  $S_{\eta\eta}$  is the directional wave spectrum. The latter is calculated distributing the energy of a mono-directional spectrum about the mean wave direction with a spreading function  $g$ :

$$g(\theta) = \gamma(s) \cos^{2s} \left[ \frac{1}{2} (\theta_m - \theta) \right] \quad \text{Equation 56}$$

In the formula above,  $\theta_m$  is the mean wave direction and the coefficients  $s$  and  $\gamma$  depend on the mean wave directional spreading [128].

Assuming that the crest heights  $\psi_c$  of the response variable  $\psi$  follow a cumulative Rayleigh distribution  $F_\psi$ , then the probability  $p$  that all of them are below a certain threshold is [57], [128]:

$$p(\psi_c) = F_\psi(\psi_c)^N = \left[ 1 - e^{-\left(\frac{\psi_c}{\sqrt{2}\sigma_\psi}\right)^2} \right]^N \quad \text{Equation 57}$$

where  $N$  is the number of response crests in the considered sea state, which can be calculated as the ratio between the sea state duration and the mean zero up-crossing period of the response  $T_{\psi,02}$ . Inverting the formula above gives:

$$\psi_c = \sqrt{2\sigma_\psi^2} \left[ -\ln \left( 1 - p^{\frac{1}{N}} \right) \right]^{\frac{1}{2}} \quad \text{Equation 58}$$

The value chosen for  $p$  determines the probability that no response crests are above  $\psi_c$  and is referred to as *confidence factor* in this Chapter. This value shall be compared to some threshold for the variable  $\psi$ , to determine whether access is possible or not.

### 7.3 Results: transfer to the OC4 floating platform

The OC4 system is chosen to apply the developed methodology. The platform is assumed to be approached, for inspection or maintenance, by two types of vessels as those described in Chapter 2: a small catamaran crew transfer vessel equipped with a fender on its bow (see Figure 67), and a large offshore supply vessel mounting a motion compensated gangway (see Figure 68).

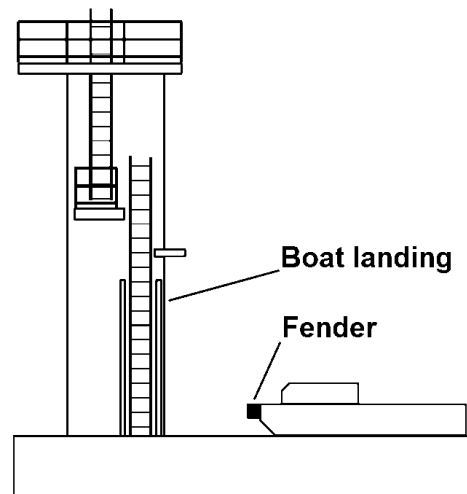


Figure 67: Simplified scheme of service vessel with fender [54].

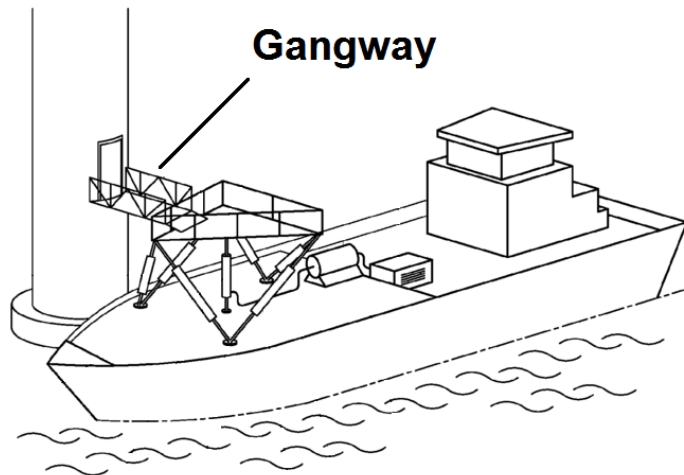


Figure 68: Simplified scheme of service vessel with gangway [122].

### 7.3.1 Service vessel with fender

The first vessel studied in this Chapter is a 24m-long catamaran crew transfer vessel (CTV24). Its main properties are summarized in Table 21 and its position with respect to the floating platform is defined by means of the coordinate systems shown in Figure 69. The distance between the vessel bow and the floating platform has been set to 0.65 m, which is suggested as maximum stepping distance for the technicians [54].

<b>Mass and geometry</b>		
Displacement	102	t
Length	24.00	m
Beam	10.00	m
Draft	1.37	m
Water plane area	94.45	m <sup>2</sup>
<b>Natural periods</b>		
Heave	3.0	s
Roll	3.5	s
Pitch	4.5	s

Table 21: Main properties of the CTV24 vessel.

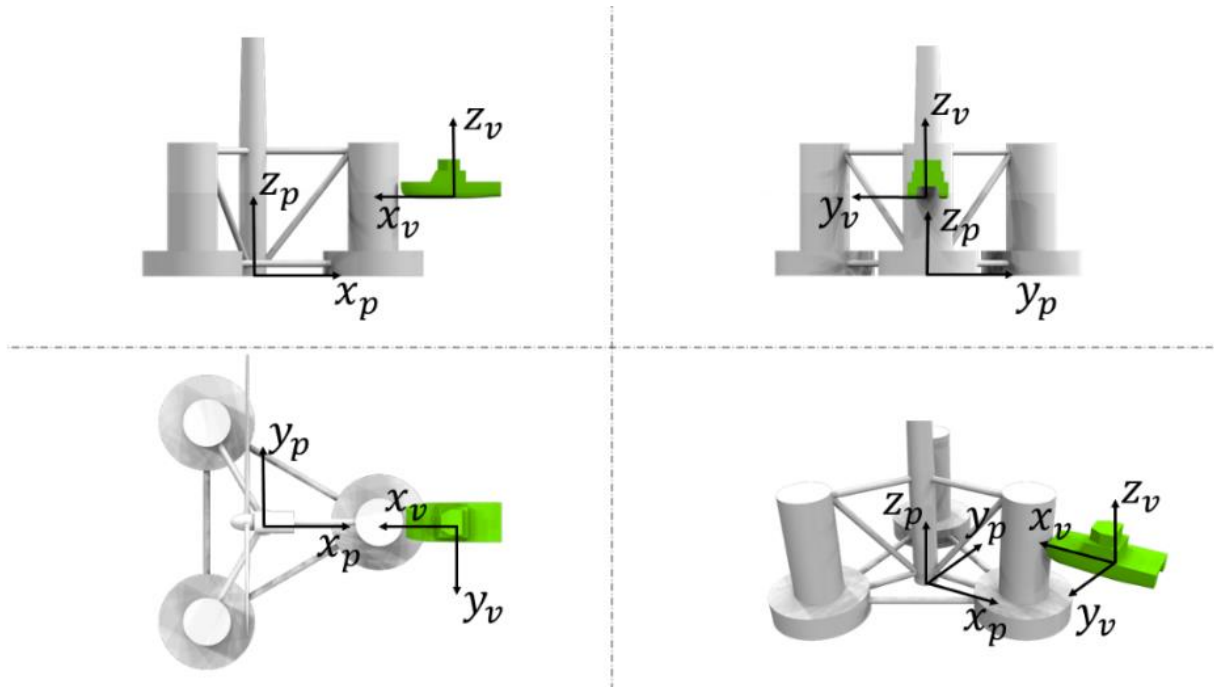


Figure 69: Coordinate systems definition for the OC4-CTV24 analysis.

### 7.3.1.1 System response

The importance of considering a multibody analysis, from the pure hydrodynamic point of view, is evident looking at Figure 70 that shows the pitch motion of the catamaran, for single-body and multibody analysis under head sea conditions. The response of the vessel is indeed importantly affected by the presence of the platform, due to radiation and diffraction effects, especially near its pitch resonant period.

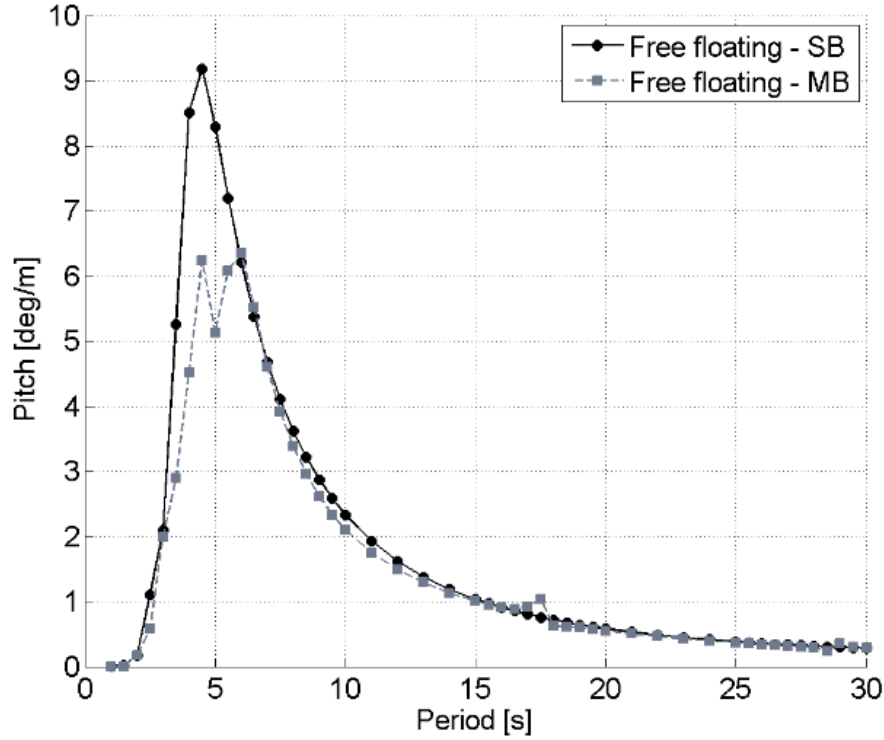


Figure 70: Pitch RAO of CTV24 (head sea) for single body (SB) and multibody (MB) analysis. No constraints.

During the transfer operation, the catamaran pushes with the fender on the boat landing structure to take advantage of static friction and avoid slip. Consequently, the platform is displaced to a certain static equilibrium position (along the  $x_g$ -axis in this case, see Figure 64), where the bollard push force  $\tau_b$  and the static mooring force are equal and opposite in sign. Assuming that  $\tau_b$  is equal to 135 kN [123], the corresponding platform  $x$ -displacement, in global coordinates, is calculated to be -1.85 m. The mooring forces are then linearized about this point and the matrix  $C_{lm}$  is calculated as:

$$C_{lp} = \begin{bmatrix} 7.55e4 \frac{N}{m} & 0 & 0 & 0 & -13.5e4 \frac{N}{rad} & 0 \\ 0 & 6.68e4 \frac{N}{m} & 0 & 8.80e4 \frac{N}{rad} & 0 & 0 \\ 0 & 0 & 1.91e4 \frac{N}{m} & 0 & 1.10e4 \frac{N}{rad} & 0 \\ 0 & 8.82e4 \frac{Nm}{m} & 0 & 8.48e7 \frac{Nm}{rad} & 0 & 0.20e7 \frac{Nm}{rad} \\ -13.7e4 \frac{Nm}{m} & 0 & 1.04e4 \frac{Nm}{m} & 0 & 9.04e7 \frac{Nm}{rad} & 0 \\ 0 & 0 & 0 & 0.18e7 \frac{Nm}{rad} & 0 & 11.8e7 \frac{Nm}{rad} \end{bmatrix} \quad \text{Equation 59}$$

The two bodies exchange forces through the fender, which is here supposed to behave as a hinge thus allowing relative rotations between the two bodies, but not relative translations. This assumption is valid as long as the fender sticks to the ladder, without slipping away from it. If  $x_H$ ,  $y_H$ ,  $z_H$  are the coordinates of the contact point between the two bodies, then the constraint matrix  $D$  is defined as:

$$D = \begin{bmatrix} 1 & 0 & 0 & 0 & z_H^v & -y_H^v & 1 & 0 & 0 & 0 & z_H^p & -y_H^p \\ 0 & 1 & 0 & -z_H^v & 0 & +x_H^v & 0 & 1 & 0 & -z_H^p & 0 & x_H^p \\ 0 & 0 & 1 & +y_H^v & -x_H^v & 0 & 0 & 0 & -1 & -y_H^p & +x_H^p & 0 \end{bmatrix} \quad \text{Equation 60}$$

It follows that the  $\lambda$  vector is composed of three reaction forces, which prevent relative translations at the contact point.

No viscous damping is given for the CTV24 and thus  $B_b$  is a null matrix; furthermore, the roll potential damping is augmented with an additional damping, corresponding to 10% of the critical one. Finally, it is possible to solve Equation 40 to get the transfer functions for the displacements and the joint reaction forces.

Figure 71, Figure 72 and Figure 73 show the response amplitude operators (RAOs) for the joint reaction forces, vessel motions and platform motions, respectively. Wave headings refer to the vessel: in head sea (*HS*) the wave is travelling from the vessel bow to the vessel stern, in head quartering sea (*HQS*) the wave forms a 45 degrees angle with respect to the head sea direction while in beam sea (*BS*) the wave forms a 90 degrees angle with the head sea direction.

Large reaction forces are expected close to the eigenperiods of the two bodies. This is the case for the reaction force  $\lambda_2$  in correspondence of the vessel roll resonant period, in beam sea. However, it is important to notice that the peaks of the vertical reaction force  $\lambda_3$  (~16.5 s and ~25.5 s) do not occur exactly in correspondence of the platform heave and pitch largest motions (18.5 s and 27.5 s, see Figure 73) but they are shifted. This is because the reaction forces are higher when

the relative motion (and not the absolute one) at the hinge would be larger, if the two bodies were free to move.

The forces exchanged with the platform importantly affect the vessel response. It is interesting to observe how its surge and pitch motions are influenced by the heave and pitch resonant modes of the platform. Noteworthy, large pitch motions occur also in beam seas at the vessel and platform heave eigenperiods, due to heave-pitch hydrodynamic couplings.

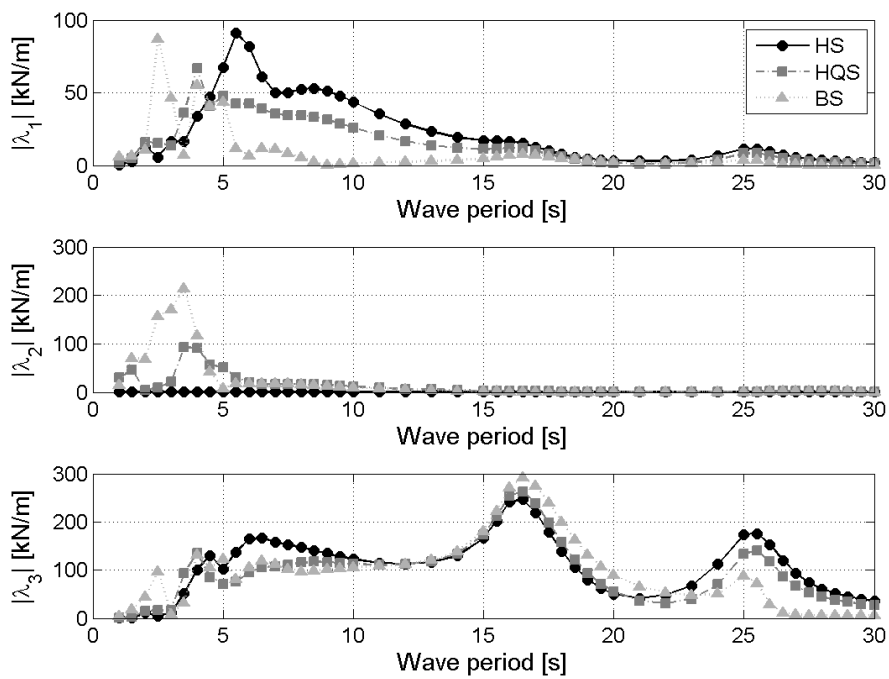


Figure 71: RAOs of joint forces for OC4-CTV24 system for different wave directions.

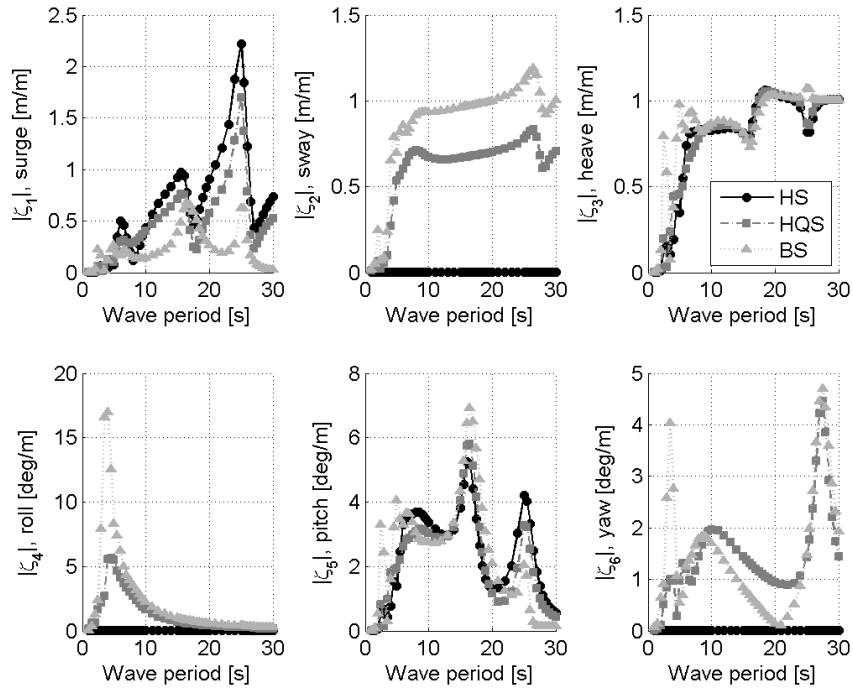


Figure 72: RAOs of CTV24 for OC4-CTV24 system for different wave directions.

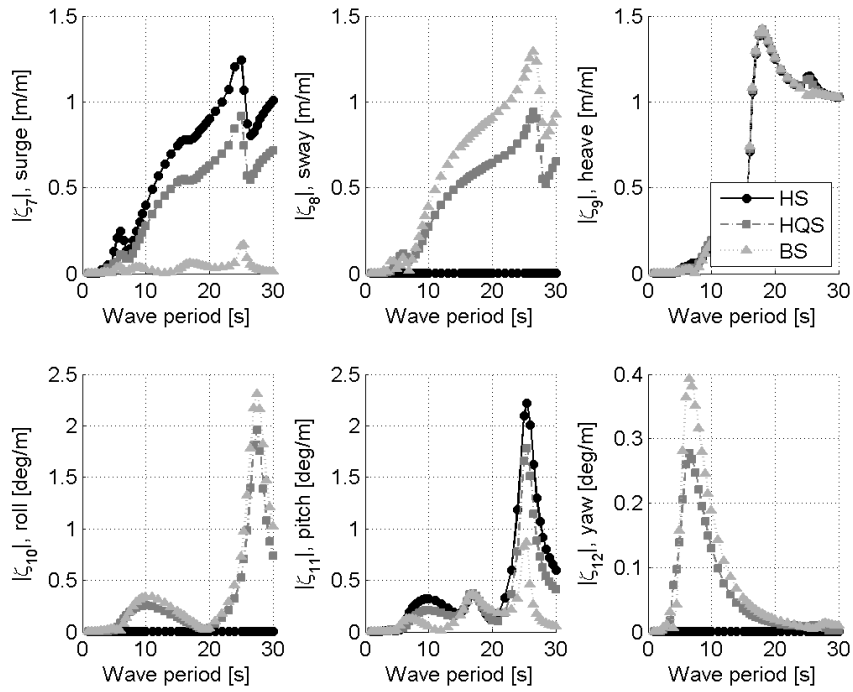


Figure 73: RAOs of OC4 for OC4-CTV24 system for different wave directions.

### 7.3.1.2 Accessibility conditions

Accessibility by catamaran is safe when no slip occurs between the fender and the ladder mounted on the floating platform. Only vertical slip, which is most likely to occur, is modelled here. The condition of no-slip, in time domain, is ensured when:

$$|\lambda_3(t)| < \mu_s[\tau_b + \lambda_1(t)] \quad \text{Equation 61}$$

where  $\lambda_3$  and  $\lambda_1$  are the vertical (along  $z_v$ -axis) and horizontal (along  $x_v$ -axis) reaction forces, respectively and  $\mu_s$  is the static friction coefficient (assumed to be 1.2 in this Section). The last equation can be split in two parts, one for upward slip and one for downward slip, and reassembled as:

$$\alpha(t) = +\lambda_3(t) - \mu_s\lambda_1(t) < \mu_s\tau_b \quad \text{Equation 62}$$

$$\beta(t) = -\lambda_3(t) - \mu_s\lambda_1(t) < \mu_s\tau_b \quad \text{Equation 63}$$

Also, it is here assumed that personnel transfer is not possible when large relative yaw and roll rotations (as seen from the vessel) occur at the joint. This is formulated as:

$$|\Delta v_H(t)| < \Delta v_{H,lim} \quad \text{Equation 64}$$

$$|\Delta \chi_H(t)| < \Delta \chi_{H,lim} \quad \text{Equation 65}$$

where  $\Delta v_H$  is the relative roll motion and  $\Delta \chi_H$  the relative yaw motion. Rotation limits are imposed to be 5 degrees in this work. For these four parameters, transfer functions are written as:

$$\alpha(j\omega) = +\lambda_3(j\omega) - \mu_s \lambda_1(j\omega) \quad \text{Equation 66}$$

$$\beta(j\omega) = -\lambda_3(j\omega) - \mu_s \lambda_1(j\omega) \quad \text{Equation 67}$$

$$\Delta v_H(j\omega) = \zeta_4(j\omega) + \zeta_{10}(j\omega) \quad \text{Equation 68}$$

$$\Delta \chi_H(j\omega) = \zeta_6(j\omega) - \zeta_{12}(j\omega) \quad \text{Equation 69}$$

The response amplitude operators for  $\alpha$  and  $\beta$  are shown in Figure 74. The position of the peaks, consistent with that of the joint forces, already give an indication of the wave periods for which slip conditions will most probably occur. Also, for most of the wave frequencies  $\alpha$  is higher in magnitude than  $\beta$  (except at roll resonant frequency in beam sea), which means that upward slip is more probable than downward slip (see Equation 62 and Equation 63).

Figure 75 depicts the RAOs for the relative roll and yaw rotations seen by the vessel. Large relative roll rotations are expected at low wave periods, while large relative yaw motions both at low and high wave periods.

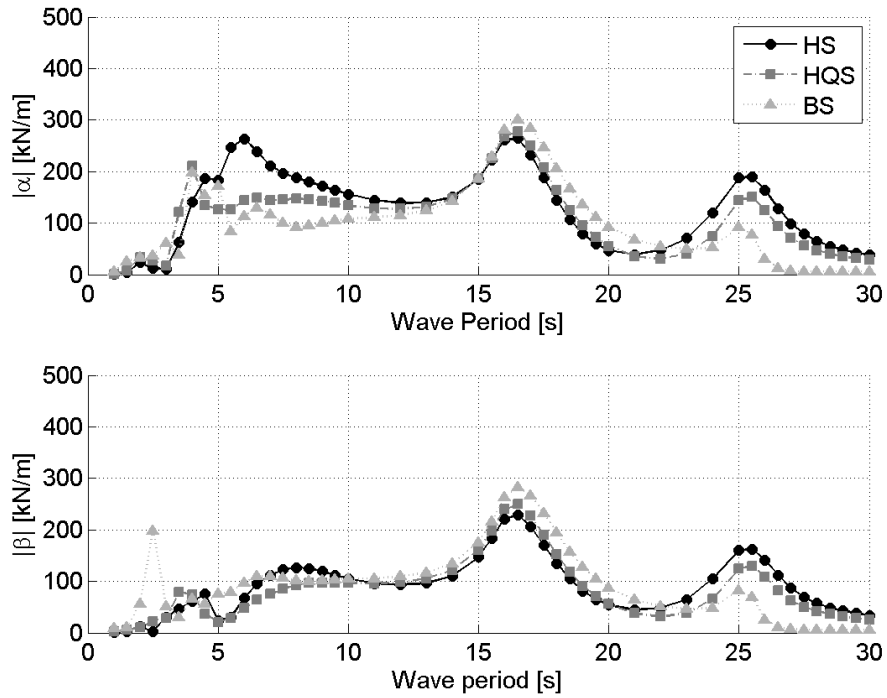


Figure 74: RAOs for  $\alpha$  and  $\beta$  for OC4-CTV24 system.

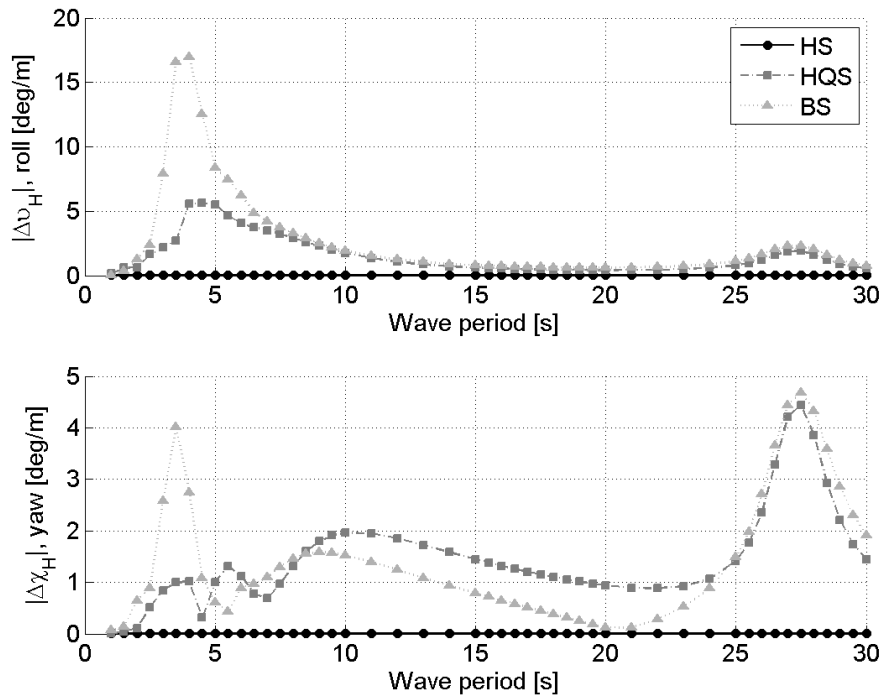
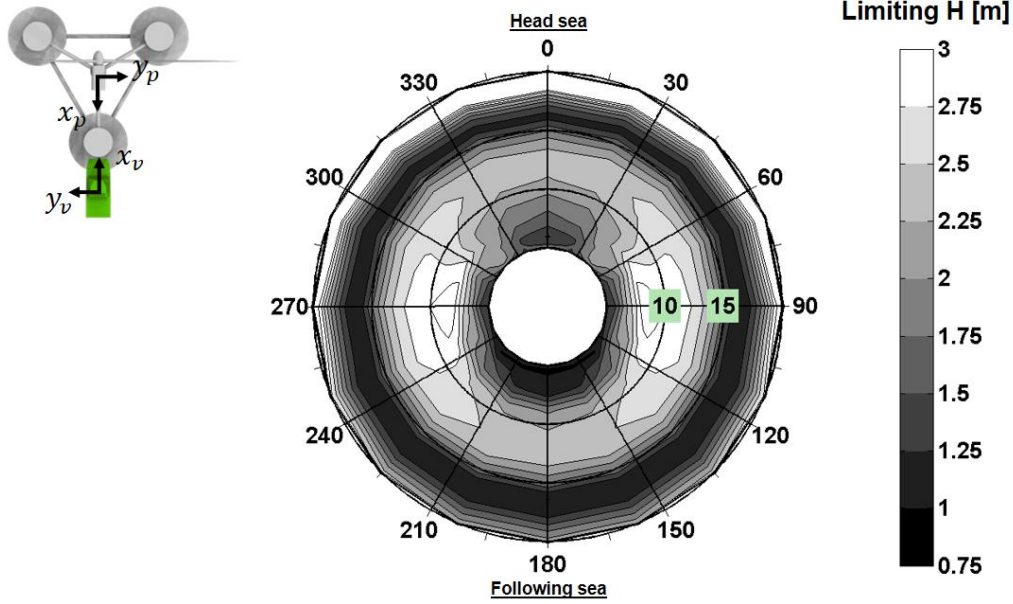


Figure 75: RAOs for  $\Delta v_H$  and  $\Delta \chi_H$  for OC4-CTV24 system.

### 7.3.1.3 Access with regular waves

The transfer functions expressed by Equation 66 to Equation 69, based on the conditions imposed in Equation 62 to Equation 65, allow calculating the maximum regular wave height for which access is possible. Results are presented in Figure 76 and Table 22. In the polar diagram, the angular coordinate represents the wave heading with respect to the vessel while the radial coordinate the wave period.

The regular wave height for which the CTV24 vessel can ensure safe personnel transfer is approximately between 1 m and 3 m. The first thing that stands out is the better performance of the vessel in head sea compared to following sea, due to the shielding effect of the floating platform which absorbs part of the energy of the incoming waves. It is therefore advisable to provide each column of the floating platform with an access ladder, and choose time by time the one which is more protected by the platform, according to the dominant wave direction. In second place, limiting wave height is lower when the relative motions of the two bodies would be larger which, as previously shown, may occur not exactly at the eigenperiods of the two independent bodies. Finally, the vessel surprisingly shows a good response also in beam seas. This was already found by Wu for fixed wind turbines [123]. It would be interesting to check this result with a time-domain non-linear model. It is important to keep in mind that all the findings obtained for the OC4-CTV24 system are strictly dependent on the shape and the mass distribution of the studied vessel and platform. Such polar diagrams can be helpful in understanding the qualitative behavior of the system under different wave periods and headings and give useful information when designing access vessels. Further results, for irregular sea states, are provided in Section 7.5.



**Floating wind turbine**

Figure 76: Limiting regular wave height for OC4-CTV24 system.

		Wave direction [deg]								
		0	45	90	135	180	225	270	315	360
Wave period [s]	5	1.78	1.81	1.20	1.37	1.28	1.37	1.20	1.81	1.78
	7.5	1.65	2.23	2.69	1.71	1.16	1.71	2.69	2.23	1.65
	10	2.08	2.41	3.01	2.56	2.19	2.56	3.01	2.41	2.08
	12	2.34	2.55	2.81	2.61	2.39	2.61	2.81	2.55	2.34
	15	1.75	1.74	1.74	1.74	1.75	1.74	1.74	1.74	1.75
	17.5	1.72	1.56	1.31	1.15	1.10	1.15	1.31	1.56	1.72
	20	6.01	5.80	3.50	2.38	2.09	2.38	3.50	5.81	6.01

Table 22: Limiting regular wave height for OC4-CTV24 system.

**7.3.2 Service vessel with gangway**

The second vessel analyzed in this work is an 80 m long platform supply vessel (PSV80), which properties are summarized in Table 23. The vessel is equipped with a motion compensated platform, which allows access to the floating platform by means of a gangway (see Figure 68).

Mass and geometry		
Displacement	5568	t
Length	80.00	m
Beam	16.45	m
Draft	5.64	m
Water plane area	1286	m <sup>2</sup>
Natural periods		
Heave	6.0	s
Roll	6.0	s
Pitch	8.5	s

Table 23: Main properties of the PSV80 vessel.

The vessel is supposed to approach the platform in two different ways: in the first one such as the gangway reaches out longitudinally (see Figure 77); in the second one, such as the gangway reaches out laterally (see Figure 78).

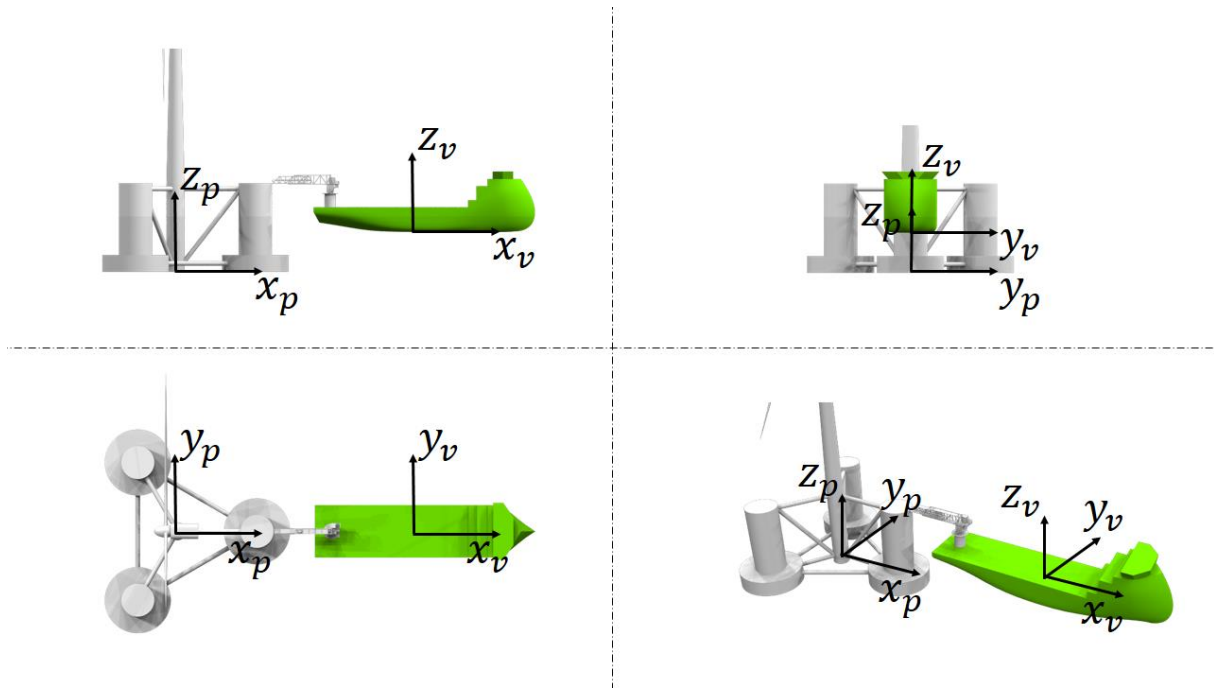


Figure 77: Coordinate systems definition for the OC4-PSV80 system, longitudinal configuration.

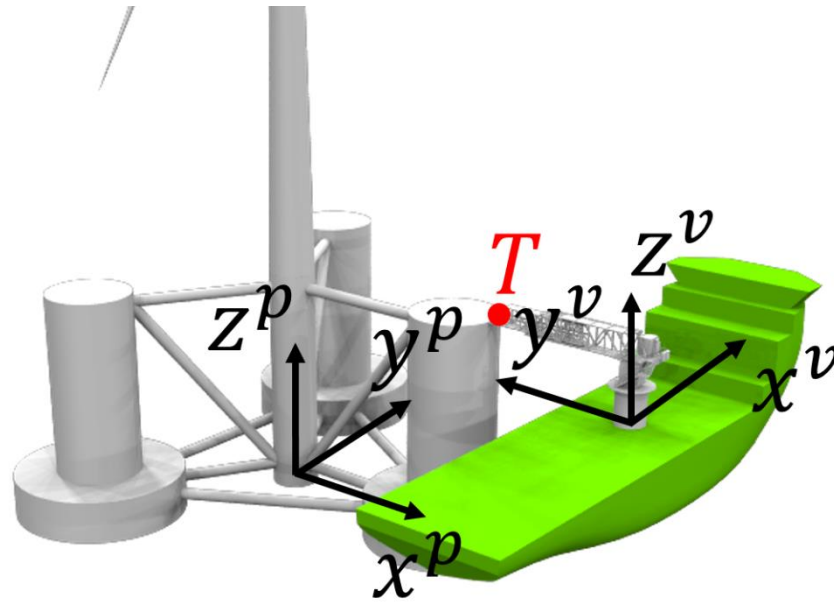


Figure 78: Coordinate systems definition for the OC4-PSV80 system, lateral configuration.

### 7.3.2.1 System response

The motion of the system was again solved using Equation 40. It is supposed that the gangway is infinitely close to the platform, without touching it. Therefore, the constraint matrix  $D$  is an empty matrix. Furthermore,  $B_{lv}$  is a null matrix (no viscous damping is modelled for the vessel) and  $C_{lp}$  is calculated about the hydrostatic equilibrium position, which values match those already calculated by NREL [79]. Furthermore, an additional roll linear damping coefficient (10% of the critical damping) was added to the vessel. The response amplitude operators of the vessel are presented in Figure 79 and Figure 80, for the two configurations.

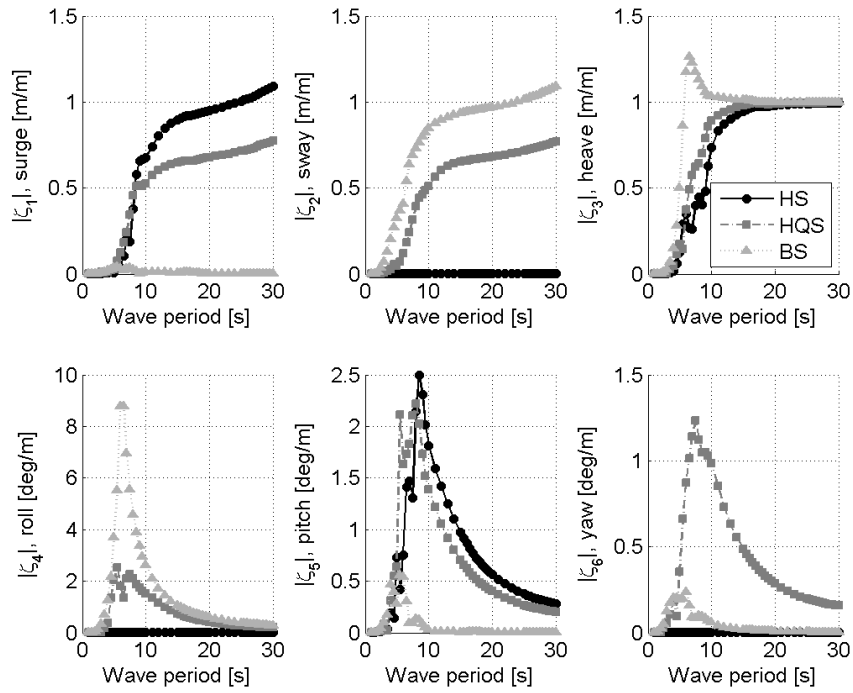


Figure 79: RAOs of PSV80 for OC4-PSV80 system for different wave direction, longitudinal configuration.

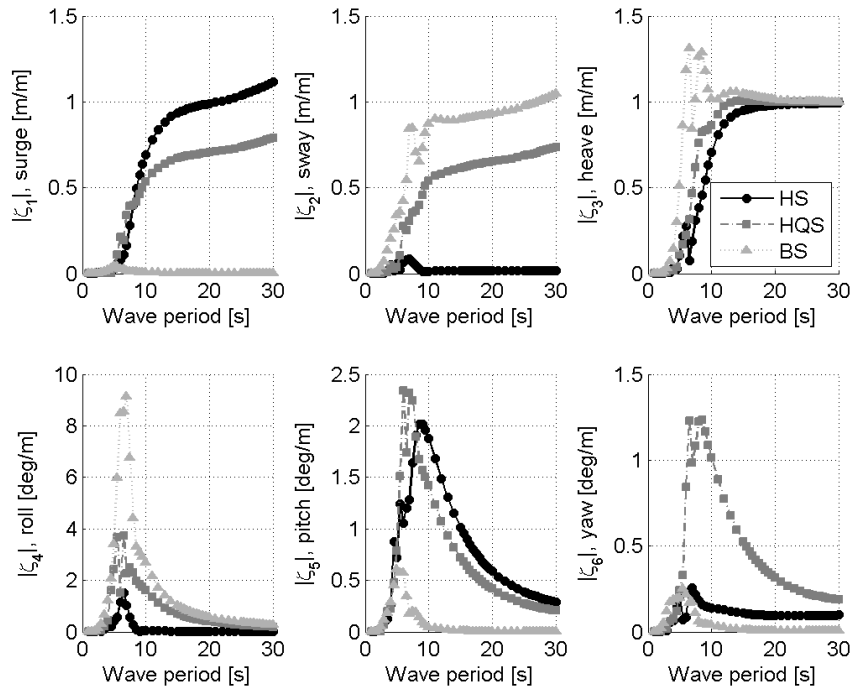


Figure 80: RAOs of PSV80 for OC4-PSV80 system for different wave direction, transversal configuration.

### 7.3.2.2 Accessibility conditions

Access is possible when the relative motions between the two bodies at the gangway tip are below the hydraulic system compensation limits. If the coordinates of the gangway tip  $T$  are  $x_T$ ,  $y_T$  and  $z_T$  then the transfer functions for the relative translations seen by the vessel in the longitudinal configuration are given by Equation 70 to Equation 75 and illustrated in Figure 81.

#### Longitudinal configuration

$$\Delta X_H = (\zeta_1 + z_T^v \zeta_5 - y_T^v \zeta_6) - (\zeta_7 + z_T^p \zeta_{11} - y_T^p \zeta_{12}) \quad \text{Equation 70}$$

$$\Delta Y_H = (\zeta_2 - z_T^v \zeta_4 + x_T^v \zeta_6) - (\zeta_8 - z_T^p \zeta_{10} + x_T^p \zeta_{12}) \quad \text{Equation 71}$$

$$\Delta Z_T = (\zeta_3 + y_T^v \zeta_4 - x_T^v \zeta_5) - (\zeta_9 + y_T^p \zeta_{10} - x_T^p \zeta_{11}) \quad \text{Equation 72}$$

$$\Delta v_T = \zeta_4 - \zeta_{10} \quad \text{Equation 73}$$

$$\Delta \phi_T = \zeta_5 - \zeta_{11} \quad \text{Equation 74}$$

$$\Delta \chi_T = \zeta_6 - \zeta_{12} \quad \text{Equation 75}$$

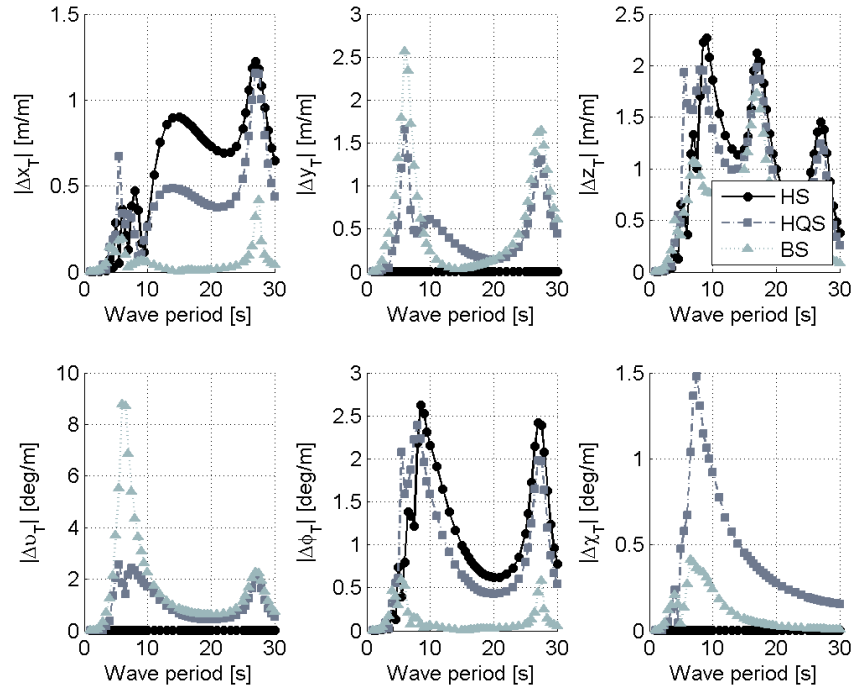


Figure 81: RAOs for relative motion at gangway tip, OC4-PSV80 system, longitudinal configuration.

On the other hand, when the vessel is in the transversal configuration, the transfer functions for the relative motions at the gangway tip are defined by Equation 76 to Equation 81 and represented in Figure 82.

### Transversal configuration

$$\Delta X_T = (\zeta_1 + z_T^v \zeta_5 - y_T^v \zeta_6) - (\zeta_8 - z_T^p \zeta_{10} + x_T^p \zeta_{12}) \quad \text{Equation 76}$$

$$\Delta Y_T = (\zeta_2 - z_T^v \zeta_4 + x_2^v \zeta_6) + (\zeta_7 + z_T^p \zeta_{11} - y_T^p \zeta_{12}) \quad \text{Equation 77}$$

$$\Delta Z_T = (\zeta_3 + y_T^v \zeta_4 - x_T^v \zeta_5) - (\zeta_9 + y_T^p \zeta_{10} - x_T^p \zeta_{11}) \quad \text{Equation 78}$$

$$\Delta v_T = \zeta_4 - \zeta_{11}$$

Equation 79

$$\Delta \phi_T = \zeta_5 + \zeta_{10}$$

Equation 80

$$\Delta \chi_T = \zeta_6 - \zeta_{12}$$

Equation 81

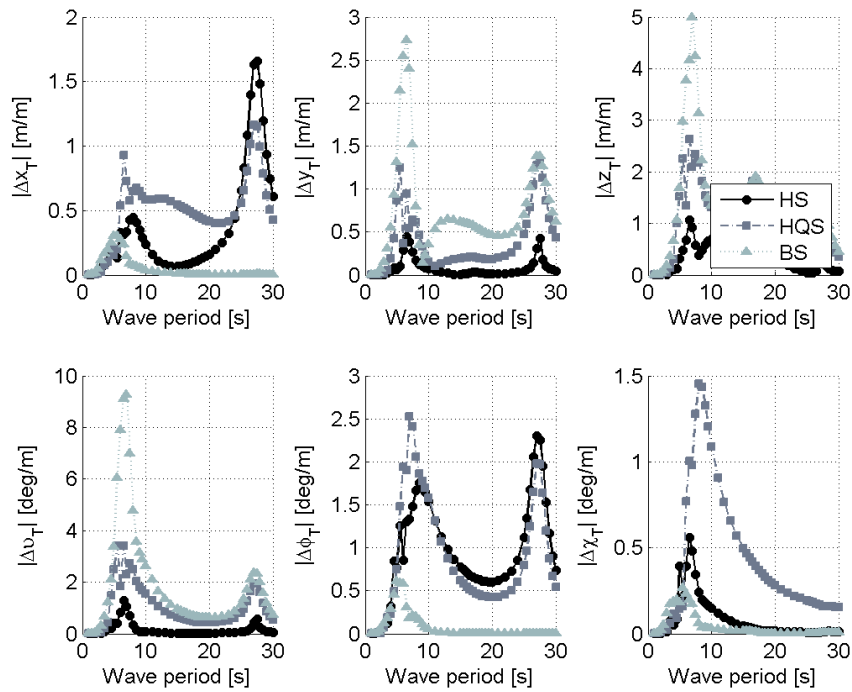


Figure 82: RAOs for relative motion at gangway tip, OC4-PSV80 system, transversal configuration.

For both configurations, relative motions are higher in correspondence of the natural periods of the two bodies. In this work, the control system and hydraulics are supposed to compensate for maximum motions as shown in Table 24.

<b>Parameter</b>	<b>Longitudinal configuration</b>	<b>Transversal configuration</b>	
x-displacement	±3.2	±3.2	m
y-displacement	±3.2	±3.2	m
z-displacement	±4.0	±4.0	m
x-velocity	±1.2	±2.0	ms <sup>-1</sup>
y-velocity	±2.0	±1.2	ms <sup>-1</sup>
z-velocity	±3.2	±3.2	ms <sup>-1</sup>
Roll angle	-	±10	deg
Pitch angle	±10	-	deg

Table 24: Compensation limits for the PSV80 hydraulic system [123].

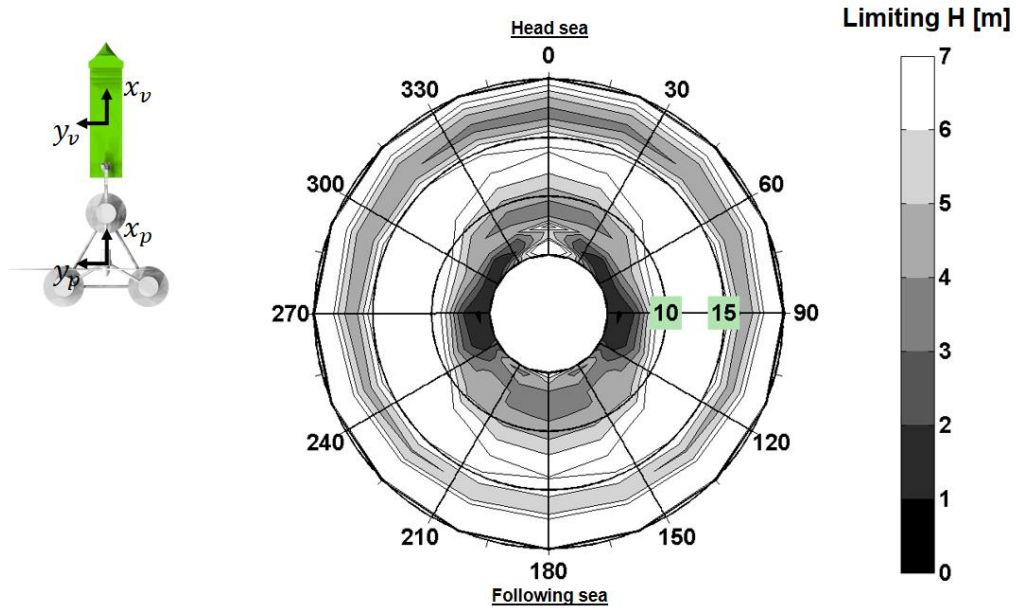
### 7.3.2.3 Access with regular waves

The RAOs of the relative displacement at the gangway tip are compared to the compensation system limits to obtain the maximum wave height for which access is possible in regular waves. Figure 83 and Table 25 show the results for the longitudinal configuration, while Figure 84 and Table 26 for transversal configuration.

The size of the PSV80 vessel is such that it allows accessing the floating platform in quite harsh sea conditions, if compared to the results for the CTV24 catamaran.

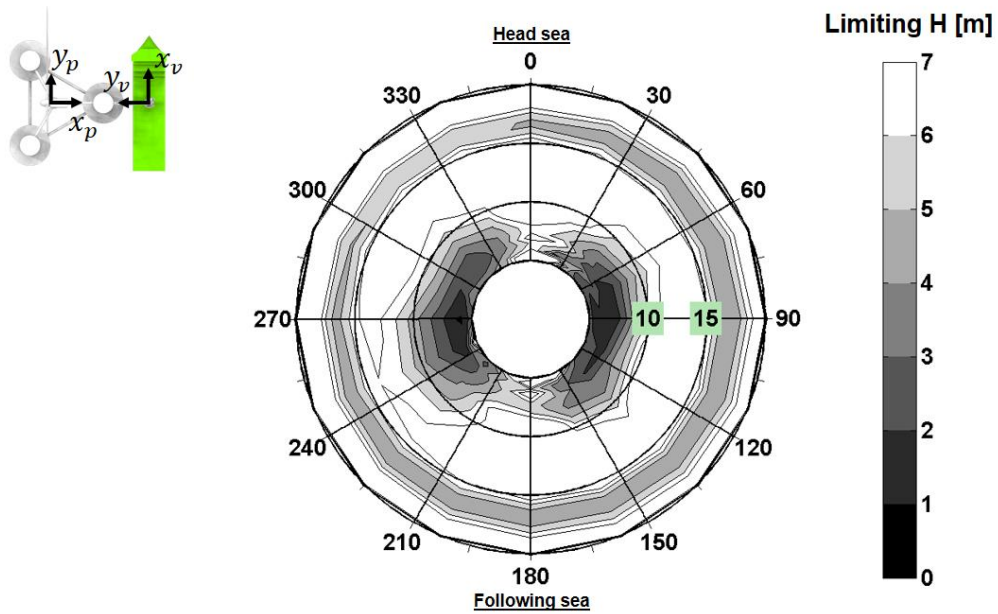
For the longitudinal configuration, results are symmetric with respect to the  $x_v$ - $z_v$  plane. Head and following sea represent good conditions when the wave period is not close to the vessel heave and pitch natural periods, and the floating platform heave natural periods. The worst conditions occur at low wave periods in beam sea, due to vessel roll resonant motions. Similar considerations apply to the transversal configuration.

The transversal configuration is generally speaking better for head and following sea conditions, while worse for beam sea conditions. It is important to remember that the results depend strongly on the geometry and mass distribution of the two bodies, and shall not be applied for other offshore service vessels or floating platforms.



**Floating wind turbine**

Figure 83: Limiting regular wave height for OC4-PSV80 system, longitudinal configuration.



**Floating wind turbine**

Figure 84: Limiting regular wave height for OC4-PSV80 system, transversal configuration.

		Wave direction [deg]								
		0	45	90	135	180	225	270	315	360
Wave period [s]	5	7.81	3.55	1.45	3.43	7.45	3.43	1.45	3.55	7.81
	7.5	7.57	4.35	2.31	4.40	3.74	4.40	2.31	4.35	7.57
	10	4.30	5.75	8.79	5.14	4.48	5.14	8.79	5.75	4.30
	12	6.03	7.56	10.83	7.43	5.96	7.43	10.83	7.56	6.03
	15	6.69	7.20	8.06	7.23	6.74	7.23	8.06	7.20	6.69
	17.5	3.92	4.28	5.09	6.08	6.94	6.08	5.09	4.28	3.92
	20	8.02	9.50	14.30	15.76	8.27	15.76	14.29	9.50	8.02

Table 25: Limiting regular wave height for OC4-PSV80 system, longitudinal configuration.

		Wave direction [deg]								
		0	45	90	135	180	225	270	315	360
Wave period [s]	5	9.92	3.34	2.42	3.34	5.15	3.15	2.49	3.73	9.92
	7.5	6.76	3.26	1.80	3.26	5.45	3.56	2.07	2.70	6.76
	10	11.61	6.10	5.94	5.45	11.69	5.17	4.47	5.69	11.61
	12	11.15	7.49	7.84	7.17	11.28	6.72	6.47	7.13	11.15
	15	8.18	7.00	7.39	9.04	8.14	6.62	6.78	8.29	8.18
	17.5	5.58	4.75	4.44	4.56	4.67	5.10	5.79	6.02	5.58
	20	17.91	12.38	9.81	9.69	11.58	14.63	13.43	14.17	17.91

Table 26: Limiting regular wave height for OC4-PSV80 system, transversal configuration.

## 7.4 Results: comparison with fixed wind turbine

It is interesting to calculate the limiting regular wave height for a fixed wind turbine, and compare results with those obtained for the floating wind turbine. Calculations for a fixed turbine can be easily done updating the constraint matrix  $D$  as:

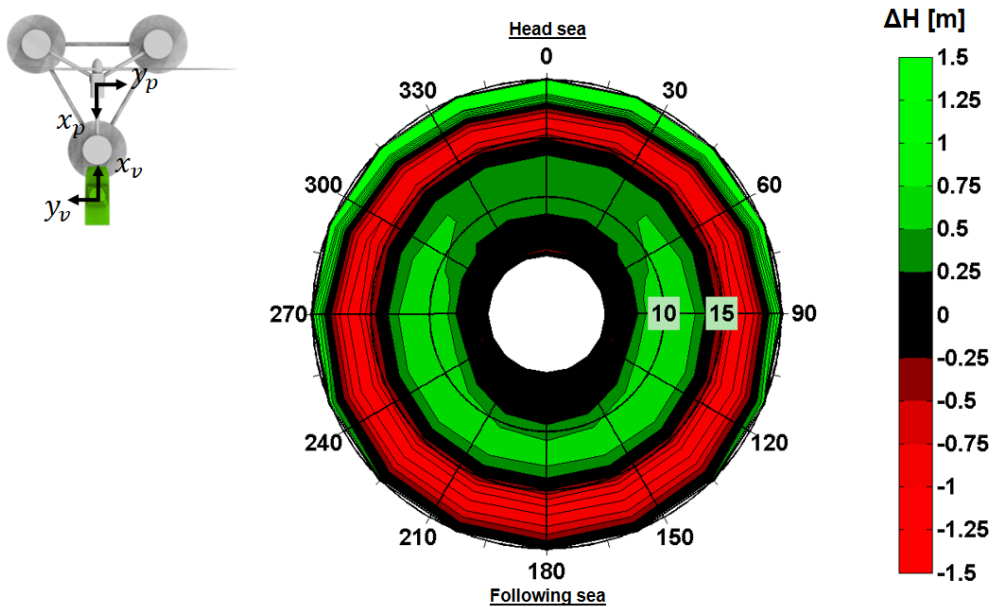
$$D = \begin{Bmatrix} D \\ \mathbf{0} & I \end{Bmatrix} \quad \text{Equation 82}$$

where  $\mathbf{0}$  is a 6 x 6 zeros matrix and  $I$  the 6 x 6 identity matrix. This just corresponds to imposing that the displacement of the second body (i.e. the floating wind turbine) are zero.

Figure 85 and Table 27 illustrate the difference between the limiting wave height for floating and the limiting wave height for fixed, considering access with the CTV24 vessel. When the difference is positive (green color), access with floating wind turbine is easier than with fixed.

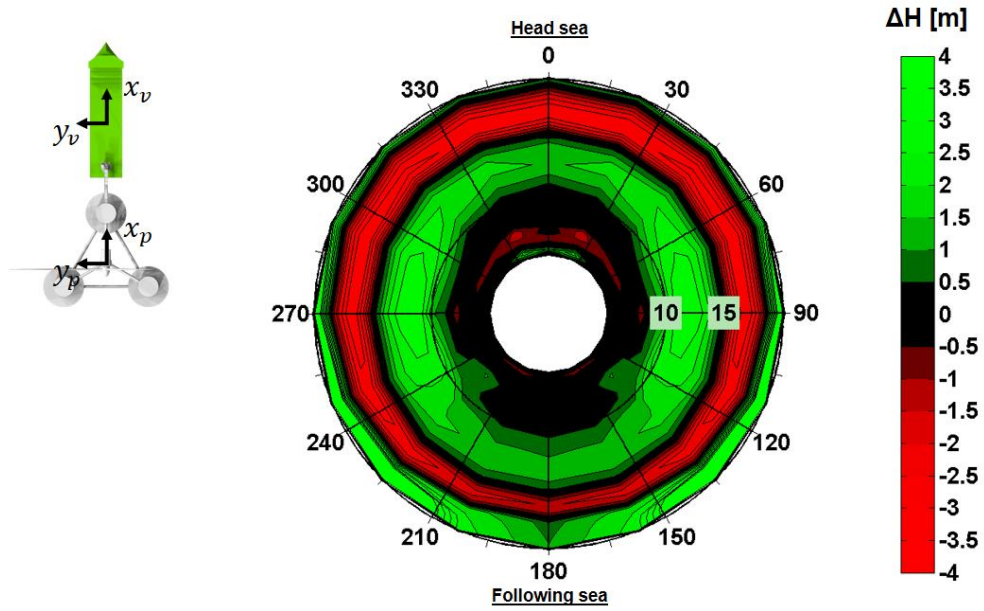
For short waves, the difference between the two cases is minimal: this is because the floating platform has a high inertia and poorly responds to low period waves, thus behaving as a fixed structure. For wave periods between 7.5 and 13 s, the performance of the floating wind turbine is higher for all wave headings. It looks that the platform motion is somehow beneficial in terms of exchanged forces at the joint. Further investigation is strongly advised. As opposite, when the waves excite the heave resonant motion of the platform its performance is worse compared to that of the fixed system.

Figure 86 and Figure 87, and Table 28 and Table 29, show results for the PSV80 vessel, for both the longitudinal and lateral configuration. Considerations similar to those for the CTV24 apply. It is remarkable that for all the studied vessels none of the two systems (floating and fixed) is better than the other in an absolute sense. Such results deserve more investigation and comparison against both experimental data.



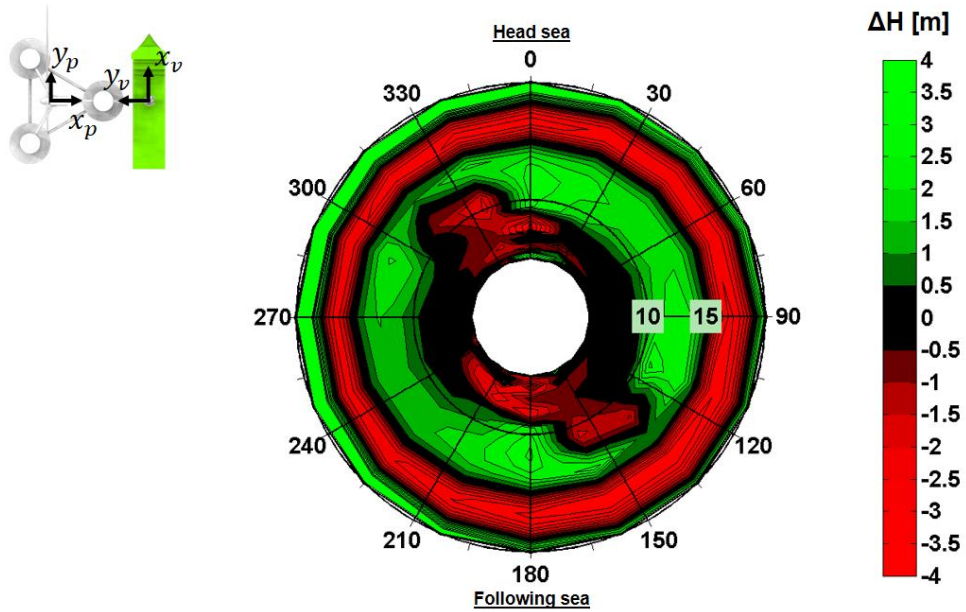
**Floating VS fixed wind turbine**

*Figure 85: Limiting regular wave height for OC4-CTV24 system: floating versus fixed turbine.*



**Floating VS fixed wind turbine**

Figure 86: Limiting regular wave height for OC4-PSV80 system, longitudinal configuration: floating versus fixed turbine.



**Floating VS fixed wind turbine**

Figure 87: Limiting regular wave height for OC4-PSV80 system, lateral configuration: floating versus fixed turbine.

		Wave direction [deg]								
		0	45	90	135	180	225	270	315	360
Wave period [s]	5	-0.11	0.08	-0.06	-0.07	-0.26	-0.07	-0.06	0.08	-0.11
	7.5	0.17	0.19	0.21	0.10	0.06	0.10	0.21	0.19	0.17
	10	0.36	0.42	0.70	0.59	0.38	0.59	0.70	0.42	0.36
	12	0.44	0.50	0.62	0.64	0.57	0.64	0.62	0.50	0.44
	15	-0.28	-0.36	-0.42	-0.31	-0.22	-0.31	-0.42	-0.36	-0.28
	17.5	-0.36	-0.56	-0.84	-0.95	-0.95	-0.95	-0.84	-0.56	-0.36
	20	3.90	3.67	1.35	0.27	0.00	0.27	1.35	3.68	3.90

Table 27: Limiting regular wave height for OC4-CTV24 system: floating versus fixed turbine.

		Wave direction [deg]								
		0	45	90	135	180	225	270	315	360
Wave period [s]	5	-0.50	0.35	0.03	-0.46	0.63	-0.46	0.03	0.35	-0.50
	7.5	-0.25	0.10	-0.38	1.09	-0.12	1.08	-0.38	0.10	-0.25
	10	-0.21	0.61	1.14	0.74	0.31	0.74	1.14	0.61	-0.21
	12	1.06	1.83	2.97	1.43	0.94	1.43	2.97	1.83	1.06
	15	0.72	0.50	0.13	0.35	0.59	0.35	0.13	0.50	0.72
	17.5	-2.77	-2.96	-2.89	-1.24	0.13	-1.24	-2.90	-2.96	-2.77
	20	0.86	1.96	6.66	8.17	1.04	8.17	6.66	1.96	0.86

Table 28: Limiting regular wave height for OC4-PSV80 system, longitudinal configuration: floating versus fixed turbine.

		Wave direction [deg]								
		0	45	90	135	180	225	270	315	360
Wave period [s]	5	3.46	-0.08	0.07	-0.17	-0.32	-0.16	-0.03	0.05	3.46
	7.5	-3.66	0.03	0.03	-0.46	-1.35	-0.74	0.05	-0.63	-3.66
	10	2.63	1.30	1.19	-0.40	2.57	0.68	0.63	-0.38	2.63
	12	2.92	1.86	2.26	-1.57	3.13	1.33	1.37	-0.76	2.92
	15	0.13	0.25	0.59	0.71	0.17	0.15	0.39	0.42	0.13
	17.5	-2.45	-2.53	-2.91	-3.65	-3.32	-1.94	-1.23	-1.90	-2.45
	20	9.89	4.80	2.17	1.54	3.58	7.25	6.06	6.23	9.89

Table 29: Limiting regular wave height for OC4-PSV80 system, lateral configuration: floating versus fixed turbine.

## 7.5 Results: long-term approachability in Aguçadoura, Portugal

Long-term approachability for the OC4 floating system was calculated for a location off the coast of Aguçadoura, Portugal. For a given sea state, the extreme responses of the relevant transfer functions were calculated through the methodology illustrated in Section 7.2.5. These values were compared to the respective access thresholds to determine whether the wind turbine

was approachable or not. Results are shown in the next Subsections in terms of approachability i.e. percentage of time in which access indicators are below threshold.

### **7.5.1 Offshore climate**

The illustrated methodology is applied to a hypothetical floating wind turbine located off the coast of Aguçadoura, Portugal (latitude: 41.3750°, longitude: -8.8750°), where the water depth is about 42 m. Wave and wind data with 1 hour resolution were extracted from the reanalysis database of IH Cantabria, for a thirty four years (1980-2013). Wave spectrum was supposed to have a JONSWAP distribution with a shape factor of 3.3. Figure 24 show the wave rose while Table 21 the scatter diagram for wave significant height and peak period.

The wave significant height has been below 1 m for 12% of the time, and below 2 m for 62 % of the time, while the wave period has been between 7.5 s and 13.5 s for 78% of the time. Computations reveal that one dominant wave direction characterizes the location: 92% of the waves come from the W-NW sector.

The box plot in Figure 89 illustrates the variation of the mean monthly significant wave height. A strong seasonality is ascertained, together with a marked variability during the winter months. July is the month where the wave height tends to be smaller and less variable. As opposite, January is the month where wave height is larger, and more variable.

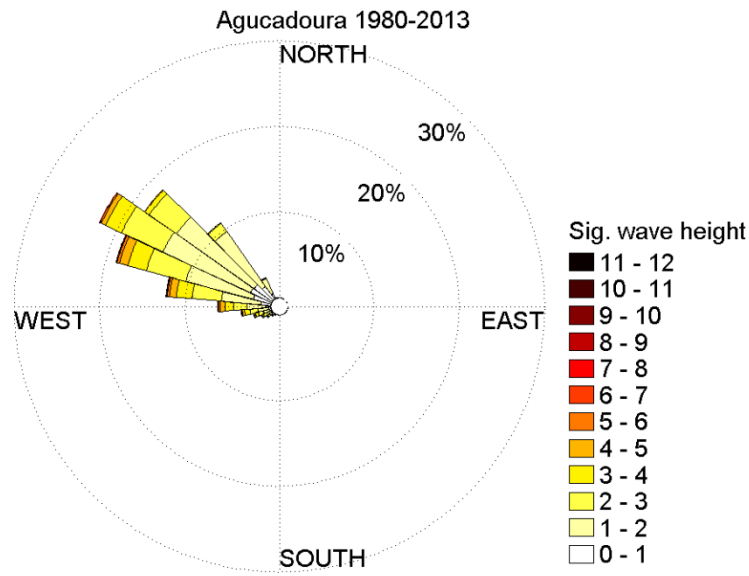


Figure 88: Wave rose for Aguçadoura, Portugal in the period 1980-2013.

		Significant wave height [m]							
		0.5	1.5	2.5	3.5	4.5	5.5	6.5	
Wave peak period [s]	2	0%	0%	0%	0%	0%	0%	0%	0%
	3	0%	0%	0%	0%	0%	0%	0%	0%
	4	0%	0%	0%	0%	0%	0%	0%	0%
	5	0%	0%	0%	0%	0%	0%	0%	0%
	6	0%	0%	0%	0%	0%	0%	0%	1%
	7	1%	2%	0%	0%	0%	0%	0%	3%
	8	2%	6%	1%	0%	0%	0%	0%	9%
	9	3%	9%	1%	0%	0%	0%	0%	14%
	10	3%	10%	2%	0%	0%	0%	0%	15%
	11	2%	9%	4%	1%	0%	0%	0%	16%
	12	1%	7%	5%	2%	0%	0%	0%	14%
	13	0%	3%	4%	2%	1%	0%	0%	10%
	14	0%	2%	3%	2%	1%	0%	0%	8%
	15	0%	1%	2%	1%	1%	0%	0%	6%
	16	0%	0%	1%	1%	0%	0%	0%	2%
	17	0%	0%	0%	0%	0%	0%	0%	1%
	18	0%	0%	0%	0%	0%	0%	0%	1%
	19	0%	0%	0%	0%	0%	0%	0%	0%
	20	0%	0%	0%	0%	0%	0%	0%	0%
		12%	50%	23%	9%	4%	1%	0%	100%

Table 30: Wave scatter diagram for Aguçadoura, Portugal in the period 1980-2013.

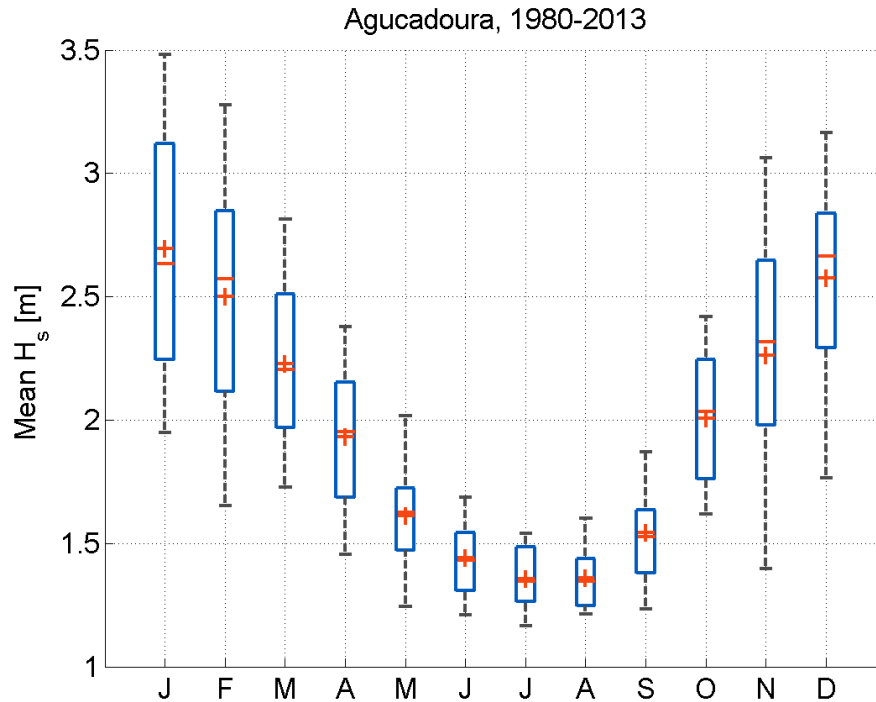


Figure 89: Monthly variation of mean wave significant height at Agucadoura, Portugal in the period 1980-2013.

### 7.5.2 Access with CTV24

The average approachability with the CTV24 in the period 1980-2013 was 13.8%, considering a fender friction coefficient of 1.2 and a confidence factor of 90%. This value corresponds to 50 days/year.

Changing the fender friction coefficient and the confidence factor sensibly changes approachability results, as shown in Figure 90. Increasing the friction coefficient to 1.6 would give increase approachability to 23.0%, while increasing the confidence factor to 99% would decrease approachability to 8.7%. It is up to the wind farm operator to find a good tradeoff between approachability and risk during the walk-to-work transfer. Figure 91 and Figure 92 show the variation of approachability with respect to the wave significant height. For the studied case, access was never possible when for wave significant height above 1.5 m.

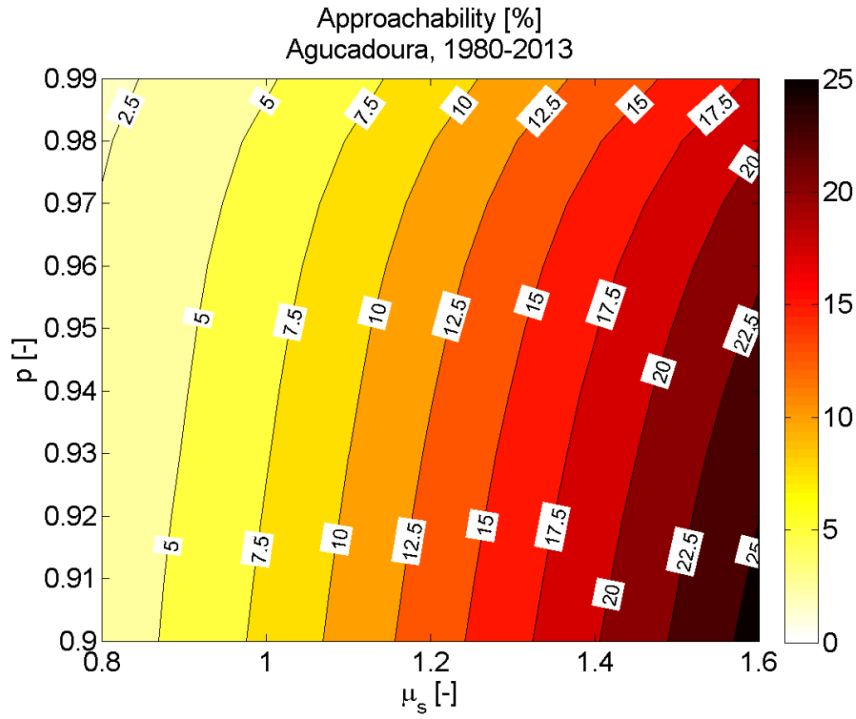


Figure 90: Approachability for OC4-CTV24 system at Aguçadoura as a function of fender friction coefficient and confidence factor.

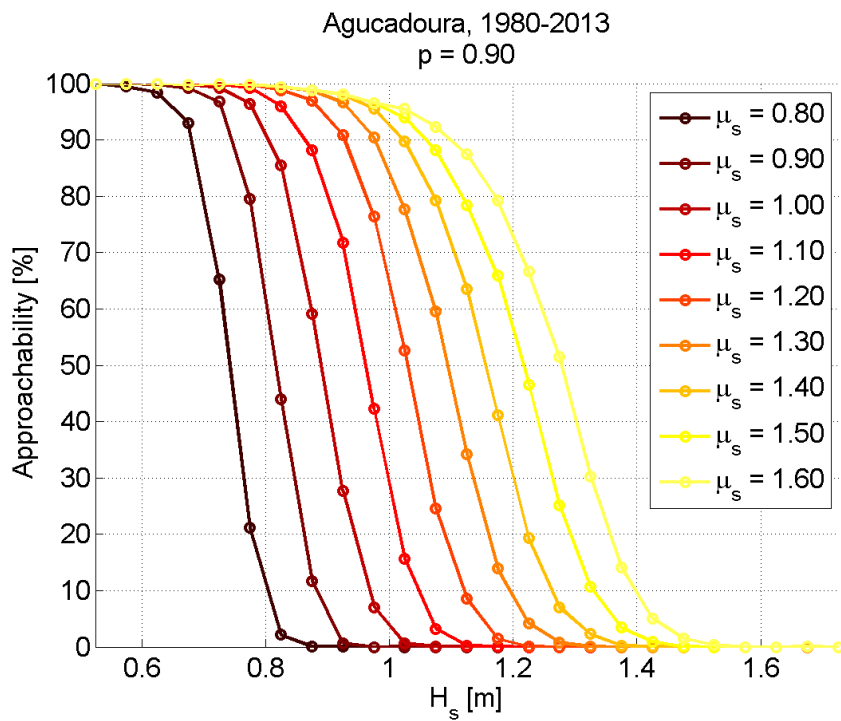


Figure 91: Approachability for OC4-CTV24 system at Aguçadoura as a function of wave significant height and fender friction coefficient.

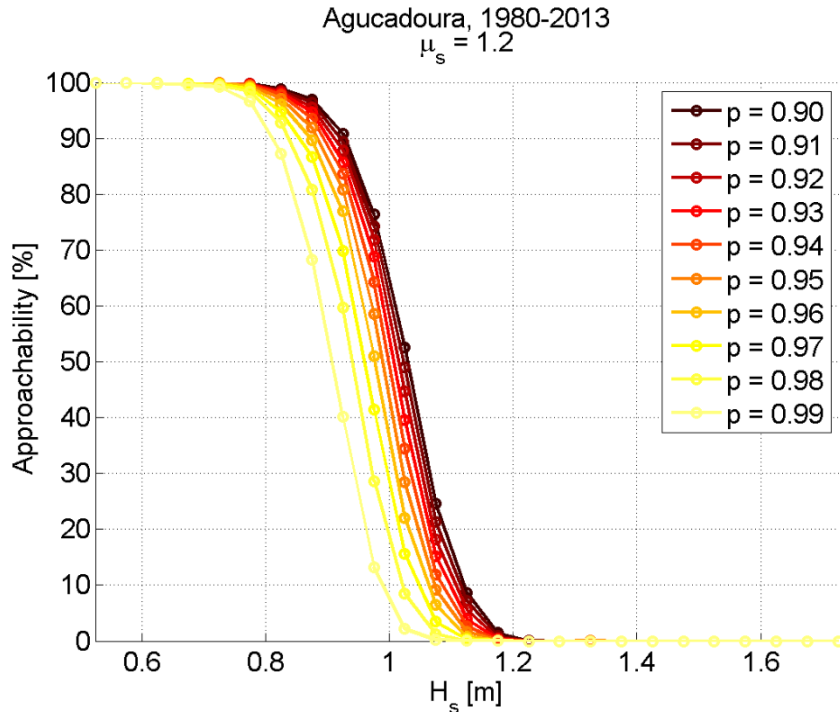


Figure 92: Approachability for OC4-CTV24 system at Aguçadoura as a function of wave significant height and confidence factor.

It is interesting to what is the time variability of approachability. Figure 93 depicts a box plot for the monthly mean approachability. Consistently with the wave height regime (see Figure 89), approachability is higher during summer (being September the month with highest approachability), and much lower during winter (being January the month with the lowest approachability). A very strong variability is observed, which depends on the variability of wave climate at Aguçadoura: this emphasizes the need for long-term, reliable data in order to reduce uncertainty when designing operation and maintenance strategies for offshore wind farms. Results are more dispersed for summer months. This is because in these periods wave height is relatively low and other parameters such as wave direction, spreading and peak period play a relevant role in the response of the vessel. As opposite, during winter months wave height is so high such that access is almost never possible, and wave direction and peak period poorly influence results.

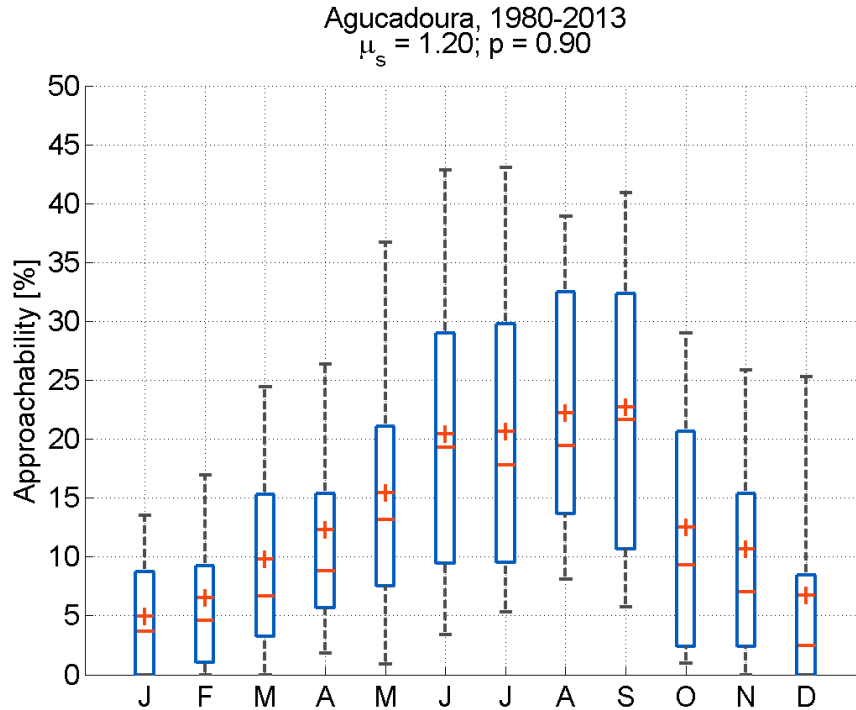


Figure 93: Monthly approachability of OC4-CTV24 system at Agucadoura and variation over years.

### 7.5.3 Access with PSV80 with transversal configuration

The average approachability with the PSV80 (transversal configuration) in the period 1980-2013 was 75.8%, considering the compensation limits given in Table 24 and a confidence factor of 90%. This value corresponds to 277 days/year.

Changing the compensation limits and the confidence factor sensibly changes approachability results, as shown in Figure 94: Increasing the compensation limits by 20 % (i.e.  $\Delta L = 1.2$ ) would give increase approachability to 85.6%, while increasing the confidence factor to 99% would decrease approachability to 66.9%. Again, it is up to the wind farm operator to choose the optimal level of safety. Figure 95 and Figure 96 show the variation of accessibility with respect to the wave significant height. For the studied case, access is possible with wave heights up to 4.5 m.

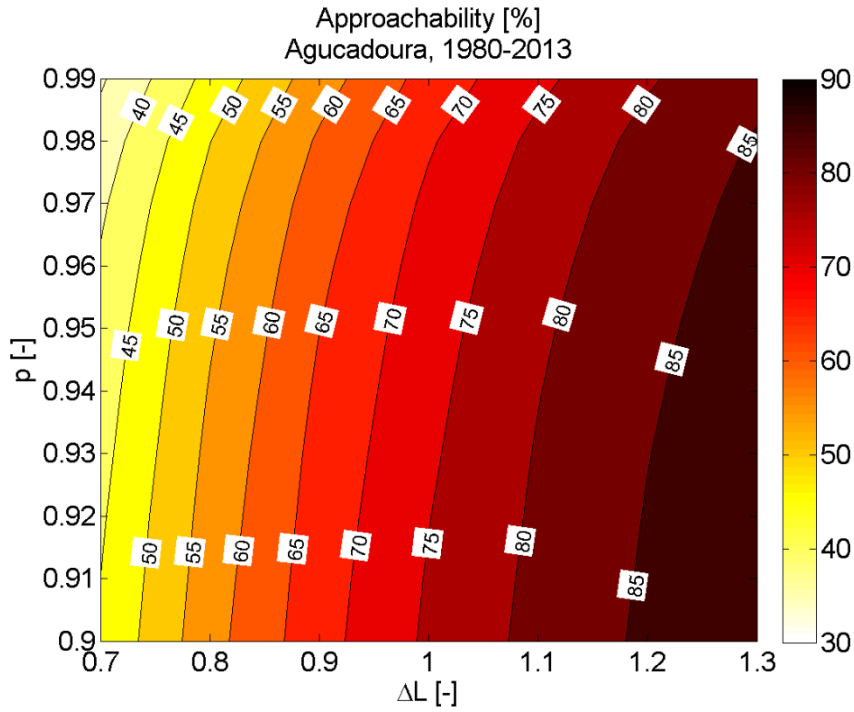


Figure 94: Approachability for OC4-PSV80 system (transversal configuration) at Agucadoura as a function of compensation limits relative change and confidence factor.

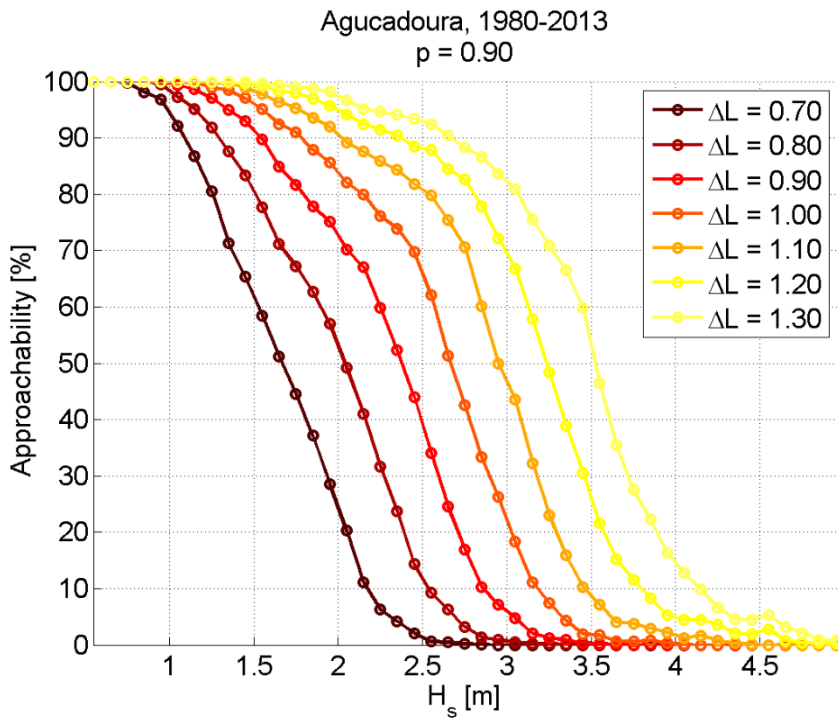


Figure 95: Approachability for OC4-PSV80 system (transversal configuration) at Agucadoura as a function of wave significant height and compensation limits change.

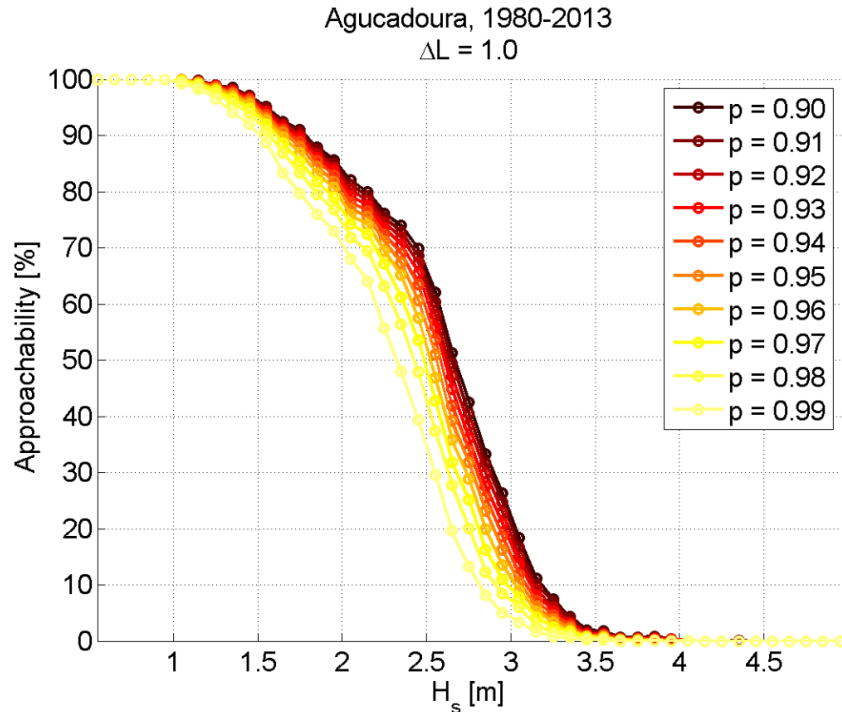


Figure 96: Approachability for OC4-PSV80 system (transversal configuration) at Aguçadoura as a function of wave significant height and confidence factor.

Furthermore, Figure 97 illustrates monthly mean approachability and its variation over years. As expected, approachability is higher during summer (being August the month with highest approachability), and much lower during winter (being January the month with the lowest approachability). Differently from what observed for the CTV24, approachability is much more variable during winter months that during summer months. This is because during summer months the wave height is so low for the PSV80 that access is almost always possible, no matter of wave period and heading.

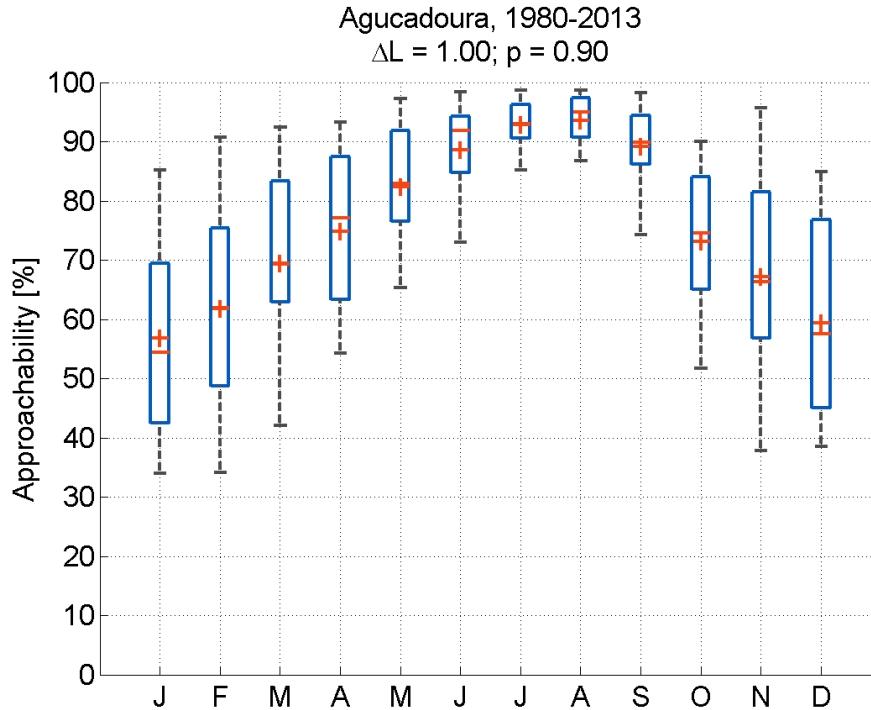


Figure 97: Monthly accessibility of OC4-PSV80 system (transversal configuration) at Aguçadoura and variation over years.

## 7.6 Conclusions

This chapter illustrated a methodology to evaluate the feasibility of walk-to-work transfer for inspection and maintenance of a floating offshore wind turbine. A numerical tool in the frequency domain was developed. This imposed to linearize viscous damping and mooring system forces. Two types of vessels were investigated: a catamaran equipped with fender (CTV24) and a larger platform supply vessel equipped with a motion compensated gangway (PSV80).

The contact point between the catamaran fender and the floating platform bumpers was modelled as a ball joint. Access was considered possible when no-slip conditions occur at the joint and when relative roll and yaw rotations between the two bodies are small. Contact forces and relative rotations depend on wave period and wave heading, and so does the maximum regular wave height for which access is possible. Noticeably, contact forces are largest when the relative

motion between the two bodies would be largest, if they were free to move. This does not necessarily occur in correspondence of the natural frequencies of the two bodies.

For what concerns the PSV80, the gangway was supposed to be infinitely close to the platform without touching it. Access is considered possible when the relative motion between the gangway tip and the floating platform are below the hydraulic system compensation limits. Relative motions and limiting regular wave height depend on both the wave period and wave direction. Beam sea with low wave period is the worst operating condition, being related to the excitation of the vessel roll natural mode.

Results for limiting regular wave height were compared to those obtained for a fixed wind turbine. For low wave periods, no differences were found. For intermediate wave periods, the floating system resulted to be more accessible than the fixed system. For large wave periods, close to the platform heave natural period, the floating systems performs much worse than the fixed one.

Long-term approachability was calculated for the offshore location of Aguçadoura, Portugal using a statistical method that allows evaluating short-term response extremes. The average approachability for the CTV24 was 13.8 %. Changing the fender static friction coefficient and the confidence factor changes non-linearly the results. Allowable wave significant heights are in the range of 1.0-1.5 m. A marked seasonal variability was found, together with an equally marked year-by-year variability.

For the PSV80, the average approachability was 75.8%. Also in this case, changing the compensation limits and the confidence factor give a non-linear change in the values of approachability. Allowable significant wave heights are in the range of 3.5-4.0 m. Again, a strong time-variability of the results was found.

Further work should include extending the numerical analysis to time domain and evaluate physical model performance in wave tank tests. It is important to assess the effect that currents and drift forces may have on the response of the multibody system. Also, it would be interesting to study the variability of the limiting wave height, for different sea conditions including wind seas, swell seas, combined wind and swell sea and multidirectional seas.

The proposed methodology can represent a valuable source of information for decision-making during personnel transfer to and from offshore floating platforms. In addition, at the design stage it can help in choosing the best vessel and the best inspection strategy, given the characteristics of the specific wind farm.

# Downtime and floating wind farm energy yield

---

---

## 8.1 Motivation and state-of-the-art review

As widely discussed in the previous Chapters, access to an offshore wind farm during operation is needed to perform either routine inspection activities or maintenance/replacement of broken components.

Routine activities can be planned in advance from the logistic point of view, usually take place during summer months and concern the most relevant components of the wind farm [40]. As opposite, non-routine activities such as maintenance or replacement of broken components are difficult to plan due to the stochastic nature of failures. Breakdowns occurring during winter can impose long downtimes due to the occurrence of harsh weather conditions that delay access and consequent reparation of broken components. Remarkably, winter season is also associated to higher wind resource. In the long haul, this brings uncertainties reflected into an increased financial risk for investors and wind farm operators.

In order to reduce the operational expenditure, a wind farm operator should look for a tradeoff between availability of the turbines and maintenance costs. This can be obtained designing long-term inspection and maintenance strategies based on the specific characteristics of the operated wind farm. The assessment of O&M strategies is often entrusted to numerical tools, also due to the short accumulated experience with existing systems (especially for floating turbines).

This Chapter aims at developing a basic framework to evaluate the impact of downtime, due to failures and operational stops, on the long-term energy production of an offshore floating wind farm.

A wide variety of models have been developed to model O&M costs [129], most of them confidential or not available for use outside the respective developer companies. These include, among others: NOWIcob [130] by SINTEF Energy Research, O2M by DNV-GL [131] and OMCE [118] by the Energy Research Center of the Netherlands. Each software has different peculiarities and models different management aspects of the wind farm operation. To the Author's knowledge, for none of them there are results published considering long-term hindcast data and floating platforms.

## 8.2 Methodology

The methodology proposed in this Chapter is based on the following steps:

- 1) definition of basic reliability concepts;
- 2) modelling of failure and reparation times through a discrete event model;
- 3) modelling of operational stops through a floating wind turbine model;
- 4) modelling of farm wake effects through a wind farm model;
- 5) integration of the models and simulation of the wind farm lifetime.

These five points are discussed in Section 8.2.1 to Section 8.2.5. Furthermore, this methodology was applied to a floating wind farm located off the coast of Santander, Spain: results are presented in Section 8.3. Finally, Section 8.4 contains conclusions about the content of this Chapter and gives indications for future work.

### 8.2.1 Definition of basic reliability concepts

The occurrence of failures in engineering applications is most often unpredictable. Condition monitoring systems represent valid tools to detect faults and to increase the overall availability of a power plant. Nevertheless, failures present a non-deterministic nature that, for offshore wind applications, is accentuated by the variability of environmental loading. Therefore, failure density with respect to time  $t$  is usually modelled by means of probability functions. In this Chapter, an exponential probability density function (pdf) with constant failure rate  $\lambda$  is used as:

$$\phi_f(t) = \lambda e^{-\lambda t} \quad \text{Equation 83}$$

It is important stating that typically failure rates are not constant in reality but follow a “bathtub” distribution. Nevertheless, it is believed that a constant failure rate is sufficient for the research purposes of this work. The methodology proposed here has a general purpose and more complex failure rates can be included. The cumulative distribution function (cdf) associated to the pdf in Equation 83, which indicates the probability the component has failed at time  $t$ , is calculated as:

$$\Phi_f(t) = \int_0^t \phi_f(t) dt = 1 - e^{-\lambda t} \quad \text{Equation 84}$$

The duration of maintenance activities offshore is also characterized by a relatively high degree of uncertainty, depending on the variability of metocean conditions and availability of technicians and access means. Reparation times are modelled by means of a lognormal pdf, as [132]:

$$\phi_r(t) = \frac{1}{s_r t \sqrt{2\pi}} e^{-\frac{[\ln(t-m_r)]^2}{2s_r^2}} \quad \text{Equation 85}$$

where  $m_r$  and  $s_r$  are the mean and standard deviation of the logarithm of the sample values. The associated cdf, which indicates the probability of a certain reparation being carried within a time  $t$ , is defined as:

$$\Phi_r(t) = \int_0^t \phi_r(t) dt = \frac{1}{2} \left[ 1 + \operatorname{erf} \left( \frac{\ln t - m_r}{s_r \sqrt{2}} \right) \right] \quad \text{Equation 86}$$

Figure 98 shows sample probability and cumulative distribution functions of failure and reparation times, based on the Equations given above.

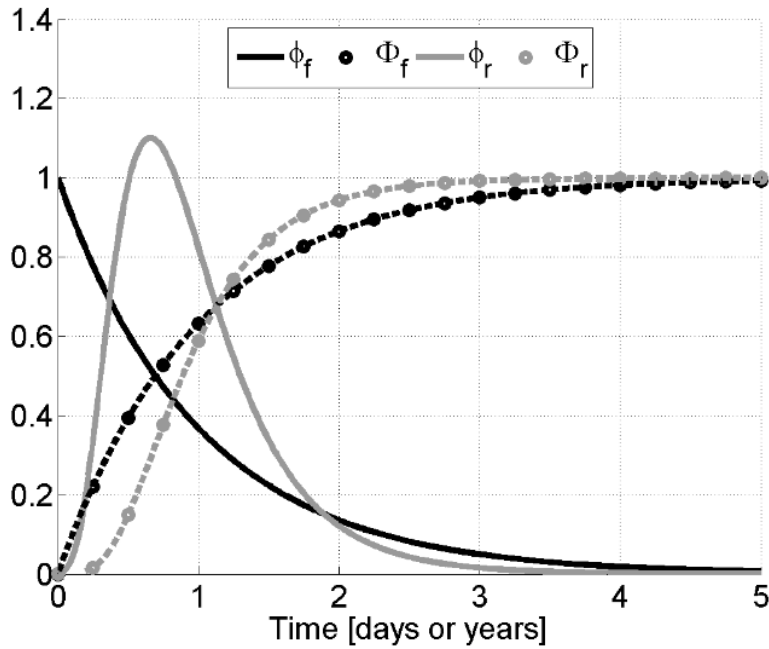


Figure 98: Example of exponential ( $\lambda=1$ ) and lognormal ( $\mu=1, \sigma=0.5$ ) pdf and cdf.

### 8.2.2 Discrete event model

Once appropriate distribution functions are defined, failure and reparation times for any component of the wind farm can be simulated stochastically. The sequence of failures and reparations, which in this Chapter are referred to as “events”, represents the frame for simulating a single lifetime of the wind farm.

Assume a wind farm with  $N$  wind turbines, each of them with  $C$  components. Given the maximum expected number of events  $I$ , it is possible to introduce:

- A vector  $\mathbf{t}_e$  ( $I$  by  $1$ ), which contains the occurrence times of the events of the wind farm.
- A matrix  $\mathbf{T}$  ( $N$  by  $C$ ), which contains the occurrence time of the next event for each component.
- An array  $\mathbf{S}$  ( $N$  by  $C$  by  $I$ ), which contains Boolean variables indicating the state of each component in correspondence of each event: 0 if it is broken, 1 if it is working.

The flow chart of the discrete event simulation is presented in Figure 99. First, the simulation needs to be initialized: the first event occurring during the farm lifetime is its start-up, thus the event counter  $i$  is set to 1 and  $\mathbf{t}_e [i=1]=0$ . In this moment, all the components are working and none of them has either failed or been repaired: therefore,  $\mathbf{S}$  is initialized as a matrix of ones. The next event that would occur for any of the components is therefore a failure and each element of the matrix  $\mathbf{T}$  is initialized simulating failure times as:

$$T[n, c] = \Phi_{f,nc}^{-1} = -\frac{\ln[1 - \Phi_{f,nc}]}{\lambda_{nc}}; n = 1, 2, \dots, N; c = 1, 2, \dots, C \quad \text{Equation 87}$$

where  $\Phi_{f,nc}$  is randomly generated using a uniform random distribution between 0 and 1. The scalar  $T[n, c]$  represents, at this point, the time at which component  $c$  of turbine  $n$  will fail, according to the random failure model implemented. The discrete event simulation then starts with updating the event counter,  $i=2$ , and calculating the occurrence time of the next event,  $\mathbf{t}_e [i=2]$ , which value is given by the smallest element in  $\mathbf{T}$ ,  $T[n, c]$ . Since component  $c$  of turbine  $n$  is working ( $S[n, c]=1$ ), the event must be a failure and thus its Boolean variable is changed from 1 to 0. The component must then be repaired and the reparation time interval  $T^*$  is calculated inverting Equation 86, as:

$$T^* = \Phi_{r,nc}^{-1}$$

Equation 88

where a uniform distributed random  $\Phi_{r,nc}$  (between 0 and 1) is supposed. Summing up this quantity to  $T[n,c]$  in matrix  $\mathbf{T}$  gives a new value for  $T[n,c]$ , the time of the next event (repair) associated to component  $c$  of turbine  $n$ . The scalar  $T[n,c]$  represents, at this point, the time at which component  $c$  of turbine  $n$  will be repaired, according to the model implemented. The event counter  $i$  is updated ( $i=3$ ) and the next event time is again calculated as the minimum of  $\mathbf{T}$ . Suppose that now  $t_e [i=3]$  results to be again  $T_{nc}$ , just calculated for component  $c$  of turbine  $n$ . This component had failed and must be repaired: its state variable changes from 0 to 1. The component starts again working as if it were new, which implies that it can again fail according to its failure rate and the time in which the failure event will occur is  $T[n,c]=T[n,c]+T^*$ , where  $T^*$  is in this case a new failure time interval calculated according to Equation 87. The event counter is updated and the process is repeated until the lifetime of the farm has been reached (i.e.  $t_e [i]$  is higher than the farm planned lifetime,  $t_{end}$ ).

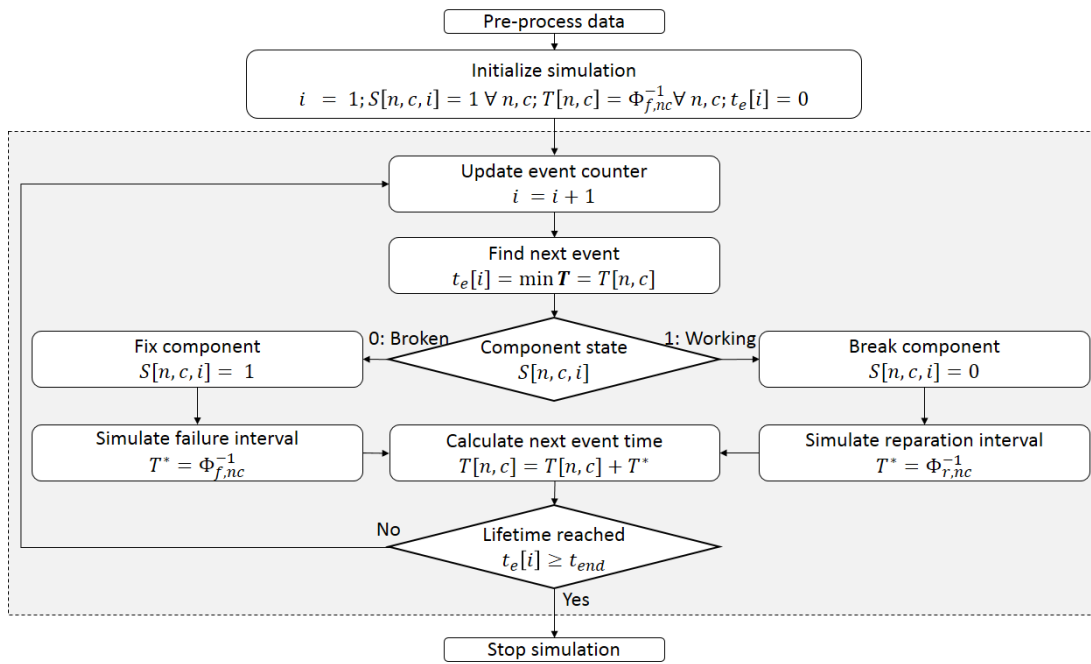


Figure 99: Flow chart of the discrete event model.

### 8.2.3 Operational stops

The procedure for evaluating operational stops was discussed in Chapter 5 of this thesis. It is recalled that the rigid body motion of the floating wind turbine is solved considering first order wave loads, quasi-static mooring loads and quasi-static aerodynamic loads. The floating turbine response is simulated only for a subset of metocean data, selected with a maximum dissimilarity algorithm. Operational parameters are then interpolated for the whole set of available metocean data through radial basis functions. When any of these parameters is above a specific operational threshold, it is assumed that the wind turbine must be shut down for safety issues.

### 8.2.4 Wind farm model

In order to efficiently extract power from the wind, a turbine needs to change the axial momentum of the flow by means of an axial (thrust) force [97]. Consequently, the flow speed behind the wind turbine is reduced, until it recovers the undisturbed value far downstream. This means that, inside a farm, downwind turbines may take a lower wind speed and thus generate less energy. Several wake models were proposed to model these phenomenon: among them, one of the simplest and most used was introduced by Jensen [133], [134]. For a wind turbine  $p$ , located downstream of turbine  $q$  at a distance  $d_{pq}$  projected on the wind direction, the wake velocity deficit  $D_{pq}$  can be calculated as:

$$D_{pq} = 1 - \frac{V_p}{V_q} = \frac{1 - \sqrt{1 - C_T(V_q)} \frac{A_{pq}}{A_p}}{\left(1 + \frac{\kappa d_{pq}}{R}\right)^2} \quad \text{Equation 89}$$

where  $V_p$  and  $V_q$  are longitudinal mean wind speeds at wind turbines  $p$  and  $q$ ,  $C_T(v_q)$  the thrust coefficient of wind turbine  $q$ ,  $\kappa$  the wake decay factor,  $R$  the rotor radius,  $A_p$  the rotor area

and  $A_{pq}$  the intersection area between wind turbine  $p$  and the wake produced by wind turbine  $q$ . The wake is supposed to expand along the wind direction, so that its radius can be expressed as:

$$R_{wake} = R + d_{pq}\kappa \quad \text{Equation 90}$$

The cumulative wake velocity deficit at turbine  $p$ , due to all the other wind turbines, can be evaluated as [134]:

$$(D_p)^2 = \sum_{q=1}^{N_{u,p}} (D_{pq})^2 \quad \text{Equation 91}$$

where  $N_{u,p}$  is the total number of wind turbines upstream of wind turbine  $p$ . One can finally get the wind speed at turbine  $p$ , for a given undisturbed mean wind speed  $V_0$ , as:

$$V_p = V_0(1 - D_p) \quad \text{Equation 92}$$

The wind speed seen by the wind turbine can then be used to calculate the power it generates. It is here supposed that platform motions do not affect the wake system inside the wind farm. This approximation is fair since the expected displacement of the floaters is much smaller than the distance between turbines.

### 8.2.5 Models coupling and integration: lifetime simulation

The discrete event, wind farm and the floating wind turbine models can be integrated to simulate the lifetime of the floating wind farm as presented in Figure 100.

First, the events history for the current lifetime is simulated. This is done through a discrete event simulation (see Section 8.2.2) that provides the events occurrence times (vector  $t_e$ ) together with the state of each component in correspondence of each event (array  $S$ ). This approach supposes that failures and reparations are not correlated with wear of components, platform

motions or metocean conditions. Then the event counter  $i$  is restarted; also, the time step counter  $j$  and the lifetimes counter  $k$  are set to 1. Each wind turbine is marked with an identification number (progressive integers); before starting the lifetime simulation, the set of active wind turbines includes them all as:

$$n_a = \{1, 2, \dots, N\} \text{ (start-up)} \quad \text{Equation 93}$$

The simulation of the wind farm lifetime is then controlled by the time vector  $t_s$ , at which metocean conditions (wind, waves, currents) are sampled. If the current simulation time  $t_s[j]$  coincides with the next event occurrence time  $t_e[i]$ , then the event counter is updated and so it is the set of active wind turbines, as those whose components are all working:

$$n_a = \{n \in \{1, 2, \dots, N\} | S[n, c, i] = 1 \forall c \in \{1, 2, \dots, C\}\} \text{ (event update)} \quad \text{Equation 94}$$

It is worth noticing that, for a correct and consistent implementation,  $t_e$  values should be interpolated over the elements of  $t_s$  during pre-process, which is an acceptable error as long as the sample time  $\Delta t_s$  of  $t_s$  is small enough. Then, platform motions are calculated using the floating wind turbine model and the current value for the operating parameter,  $x[j]$ , is calculated. This value is compared to some threshold  $x_{lim}$  to decide whether the wind farm would undergo an operational stop or not. If yes, the set of active wind turbines  $n_a$  is the empty set, as:

$$n_a = \{\emptyset\} \text{ (operational stop)} \quad \text{Equation 95}$$

Then, the wind farm model is applied to calculate the mean wind speed at each of the active wind turbines,  $V_n[j]$ . The power generated by the wind farm at the current time step is finally calculated as:

$$P[j] = \sum_{n=\{n_a\}} P(V_n[j]) = \sum_{n=\{n_a\}} \frac{1}{2} \rho A V_n^3[j] C_p(V_n[j]) \quad \text{Equation 96}$$

where  $\rho$  is the air density,  $A$  the wind turbine rotor area and  $C_p$  its power coefficient.

Calculations continue until the lifetime of the wind farm has been reached.

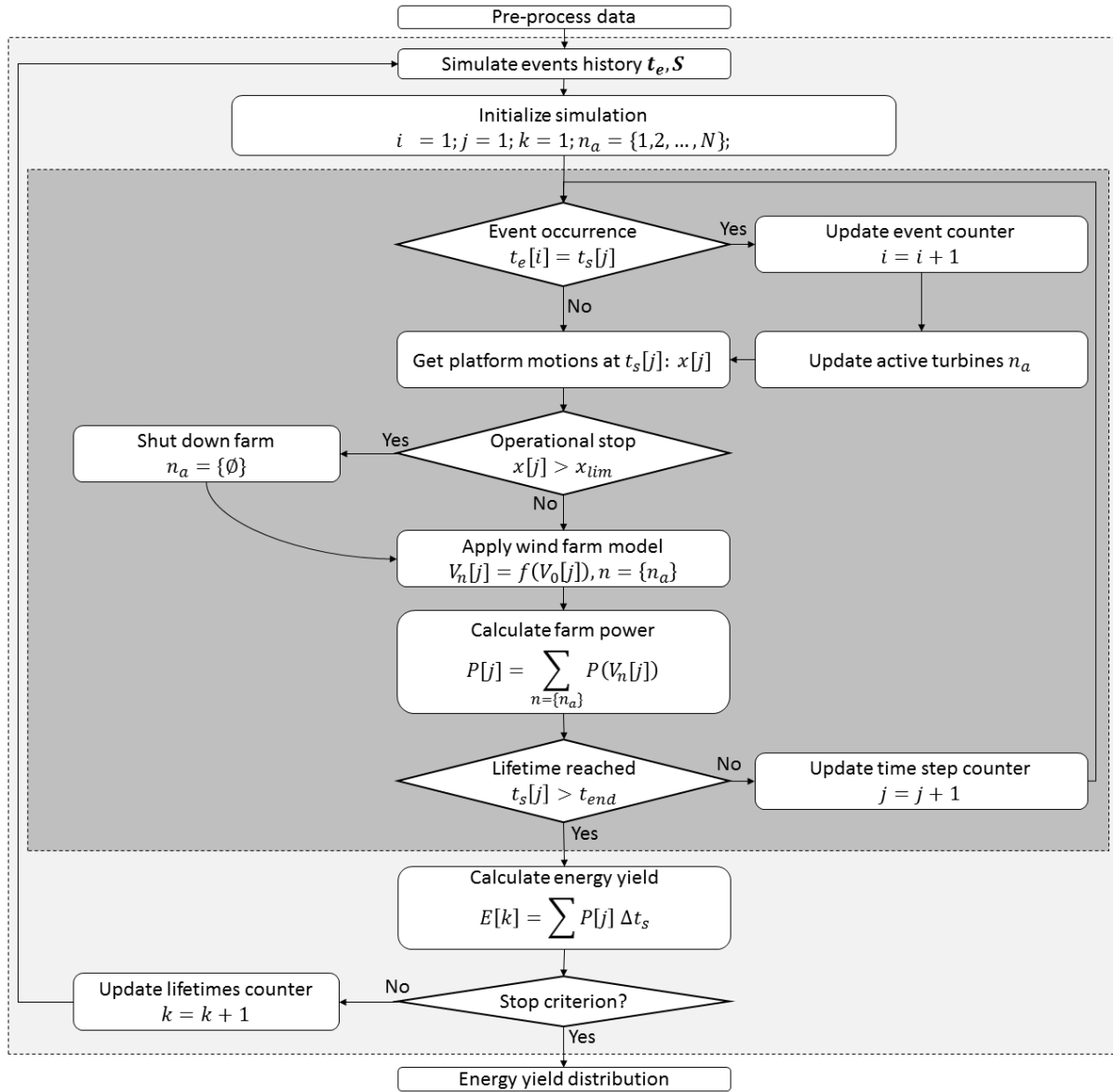


Figure 100: Flow diagram of the lifetime simulation model.

Due to the random nature of failures and reparation times, multiple lifetimes need to be simulated until the population of the variable(s) under investigation is large enough and with a

stable statistical distribution. Once this happens, it is not necessary to execute further simulations, since the information that these would add would not be of statistical relevance. This suggests checking the statistical properties of the population during the simulation process, until a specific level of stability is found. In this work, the stop criterion (see bottom of Figure 100) for the simulation was the following:

- The variable under investigation is the wind farm energy yield, calculated for lifetime  $k$  as:

$$E[k] = \sum_j P[j] \Delta t_s \quad \text{Equation 97}$$

- Lifetimes are simulated in series, one after the other. At the end of each lifetime the statistics of the energy yield population are updated through the calculation of mean ( $\mu$ ), standard deviation ( $\sigma$ ), skewness ( $\gamma_1$ ) and kurtosis ( $\beta_2$ ). For example the mean value  $\mu[k]$  corresponding to the  $k$ -th simulation is:

$$\mu[k] = \frac{\sum_{m=1}^k E[m]}{k} \quad \text{Equation 98}$$

- After each simulation, the coefficient of variation (COV) of the four mentioned parameters is calculated based on the previous 250 samples. This measures the progressive stabilization of the observed statistical parameters.
- The simulation stops when the COV is smaller than 1/100, contemporarily for all the four parameters  $\mu$ ,  $\sigma$ ,  $\gamma_1$  and  $\beta_2$ .

## 8.3 Results: floating wind farm in Santander, Spain

### 8.3.1 Offshore climate

The illustrated methodology is applied to a hypothetical wind farm installed off the coast of Santander, Spain. This is the same location used in Chapter 5. To recall it, wind data (mean speed, mean direction) and wave data (significant height, peak period, mean direction) with a time resolution of one hour were extracted for the twenty years period between 1994 and 2013 from IH Cantabria reanalysis databases (see Chapter 4). Table 31, Table 32 and Table 33 show the scatter diagrams for wind and wave conditions. The average wind speed at 90 m height has been 7.08 m s<sup>-1</sup>, while the most probable wind directions were E, SSE and W. The significant wave height has been below 2.5 m for 80% of the time, being NW the dominant wave direction. The wave peak period has been below 12 s for 75% of the time.

		Wind speed [m s <sup>-1</sup> ] @ 90m height										
		1	3	5	7	9	11	13	15	17	19	
Wave direction [deg]	0	N	0%	1%	0%	0%	0%	0%	0%	0%	0%	2%
	22.5	NNE	0%	1%	1%	0%	0%	0%	0%	0%	0%	3%
	45	NE	1%	1%	1%	1%	0%	0%	0%	0%	0%	4%
	67.5	ENE	1%	1%	2%	2%	1%	1%	0%	0%	0%	8%
	90	E	0%	1%	2%	3%	2%	1%	1%	0%	0%	11%
	112.5	ESE	0%	1%	1%	1%	1%	0%	0%	0%	0%	5%
	135	SE	0%	1%	1%	0%	0%	0%	0%	0%	0%	2%
	157.5	SSE	0%	1%	1%	0%	0%	0%	0%	0%	0%	2%
	180	S	0%	1%	1%	1%	0%	0%	0%	0%	0%	4%
	202.5	SSW	0%	1%	2%	2%	2%	1%	1%	0%	0%	10%
	225	SW	0%	1%	2%	1%	0%	0%	0%	0%	0%	6%
	247.5	WSW	0%	1%	2%	1%	0%	0%	0%	0%	0%	5%
	270	W	1%	2%	2%	2%	2%	1%	1%	1%	1%	13%
	292.5	WNW	1%	1%	2%	2%	2%	1%	1%	1%	1%	12%
315	NW	0%	2%	2%	1%	1%	1%	0%	0%	0%	7%	
337.5	NNW	0%	1%	1%	1%	0%	0%	0%	0%	0%	4%	
		7%	19%	21%	18%	13%	9%	5%	3%	2%	1%	100%

Table 31: Scatter diagram I. Wind speed, wind direction. Santander 1994-2013.

		Significant wave height [m]												
		0.25	0.75	1.25	1.75	2.25	2.75	3.25	3.75	4.25	4.75		5.25	
Wave peak period [s]	4	1%	1%	1%	0%	0%	0%	0%	0%	0%	0%	0%	3%	
	5	1%	3%	1%	1%	0%	0%	0%	0%	0%	0%	0%	7%	
	6	0%	2%	2%	1%	1%	0%	0%	0%	0%	0%	0%	6%	
	7	1%	2%	1%	1%	1%	1%	0%	0%	0%	0%	0%	7%	
	8	1%	4%	3%	1%	1%	1%	1%	0%	0%	0%	0%	11%	
	9	1%	4%	4%	2%	1%	1%	0%	0%	0%	0%	0%	13%	
	10	1%	3%	4%	3%	1%	1%	0%	0%	0%	0%	0%	13%	
	11	0%	2%	3%	3%	2%	2%	1%	0%	0%	0%	0%	14%	
	12	0%	1%	1%	2%	2%	1%	1%	1%	0%	0%	0%	9%	
	13	0%	1%	1%	1%	1%	1%	1%	1%	1%	0%	0%	8%	
	14	0%	0%	1%	1%	1%	1%	1%	1%	1%	0%	0%	5%	
	15	0%	0%	0%	0%	0%	0%	0%	0%	0%	0%	0%	2%	
			6%	24%	22%	16%	11%	7%	5%	3%	2%	1%	1%	100%

Table 32: Scatter diagram II. Significant wave height, wave peak period. Santander 1994-2013.

		Significant wave height [m]												
		0.25	0.75	1.25	1.75	2.25	2.75	3.25	3.75	4.25	4.75		5.25	
Wave direction [deg]	0	N	0%	1%	1%	0%	0%	0%	0%	0%	0%	0%	0%	2%
	22.5	NNE	0%	2%	1%	0%	0%	0%	0%	0%	0%	0%	0%	3%
	45	NE	0%	1%	0%	0%	0%	0%	0%	0%	0%	0%	0%	2%
	67.5	ENE	0%	0%	0%	0%	0%	0%	0%	0%	0%	0%	0%	0%
	90	E	0%	0%	0%	0%	0%	0%	0%	0%	0%	0%	0%	0%
	247.5	WSW	0%	0%	0%	0%	0%	0%	0%	0%	0%	0%	0%	0%
	...	...	...	...	...	...	...	...	...	...	...	...	...	...
	292.5	WNW	1%	3%	2%	1%	0%	0%	0%	0%	0%	0%	0%	8%
	315	NW	2%	12%	14%	11%	8%	6%	4%	3%	2%	1%	1%	64%
	337.5	NNW	1%	4%	4%	2%	1%	1%	0%	0%	0%	0%	0%	15%
			6%	24%	23%	16%	11%	7%	5%	3%	2%	1%	1%	100%

Table 33: Scatter diagram III. Significant wave height, mean wave direction. Santander 1994-2013.

## 8.3.2 Wind farm definition

### 8.3.2.1 Wind farm layout

The wind farm object of this study is composed by ten OC4 semisubmersible platforms mounting the NREL 5 MW wind turbine (see Chapter 4). The turbines have a regular arrangement (two rows of five turbines each) with a uniform spacing of 800 m, having taken the Alpha Ventus farm layout as reference [77]. The optimal orientation of the farm, i.e. the angle each of the rows forms with the North-South direction, is calculated as that giving the highest energy yield based on the farm model presented in Section 8.2.4 and the available hindcast data. Figure 101 shows the energy yield of the farm as a function of its orientation. Electricity production was highest (2734 GWh) when the farm is rotated by 145 degrees clockwise, from the North-South direction.

The farm layout chosen in this study is therefore that presented in Figure 102. It is worth mentioning that, for the optimal farm orientation, wake effects account for a production loss of 1.34%: without using the wind farm model, the energy yield would have been 2771 GWh.

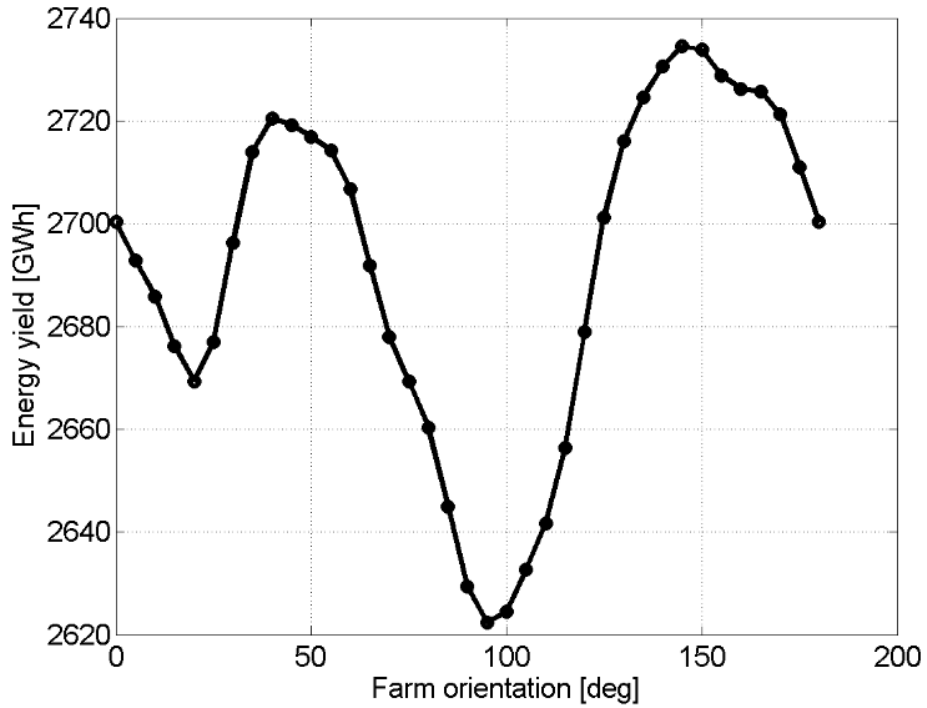


Figure 101: Energy yield as a function of wind farm orientation based on hindcast data (Santander, 1994-2013).

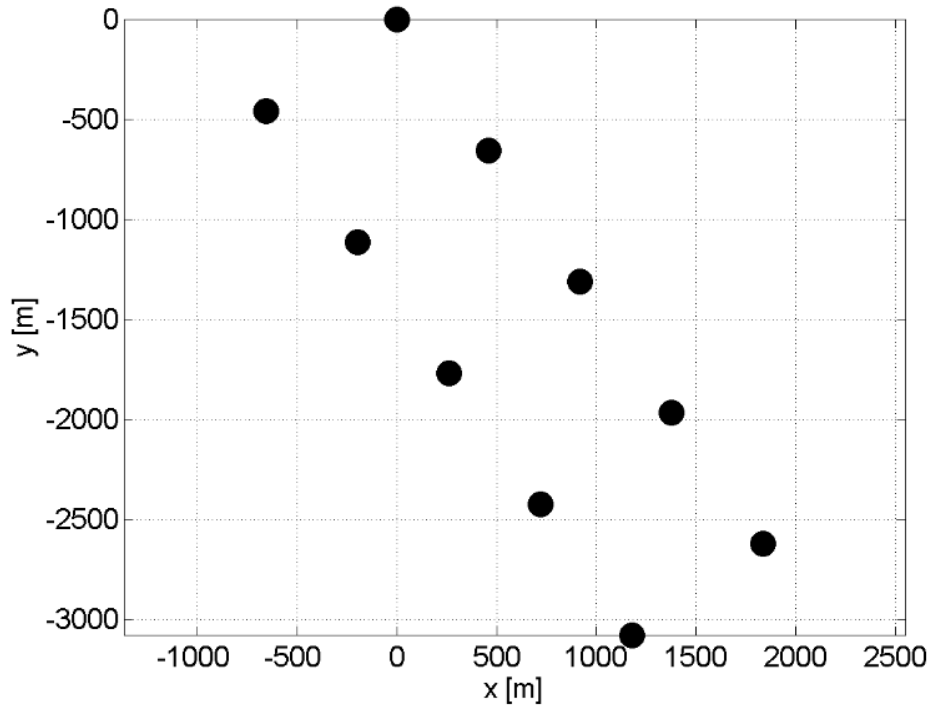


Figure 102: Optimal farm orientation based on hindcast data (Santander, 1994-2013).

### 8.3.2.2 Failure and reparation data

The failure rate and mean repair time of the main wind turbine components considered in this work are shown in Table 34. They come from an extensive data collection carried out in Germany for onshore wind turbines [43]. Highest failure rate is associated to the electrical system (0.57 fails/year, or a failure every 1.75 years), while the highest mean repair time corresponds to the gearbox (6.21 days). Unfortunately, it was not possible to find equally comprehensive data for offshore wind farms and all the related specific components (farm cables, offshore substation, export cable et cetera).

Component	Failure rate [year <sup>-1</sup> ]	Mean repair time [days]
Electrical system	0.57	1.53
Electronic control	0.43	1.59
Sensors	0.25	1.41
Hydraulic system	0.23	1.36
Yaw system	0.18	2.70
Rotor hub	0.17	3.71
Mechanical brake	0.13	2.89
Rotor blades	0.11	2.60
Gearbox	0.10	6.21
Generator	0.11	5.39
Support and housing	0.10	4.90
Drive train	0.05	5.71

Table 34: Failure rate and mean repair time for different wind turbine components. Onshore data.

Probability density function for failure time and reparation time are those introduced in Section 8.2.1. The failure rates of Table 34 corresponds to  $\lambda$  in Equation 83. On the other hand, the mean repair time  $\mu_r$  is used to calculate  $m_r$  and  $s_r$  in Equation 86 as:

$$m_r = \ln \left[ \frac{\mu_r}{\sqrt{1 + \left(\frac{\sigma_r}{\mu_r}\right)^2}} \right]; s_r = \sqrt{\ln \left[ 1 + \left(\frac{\sigma_r}{\mu_r}\right)^2 \right]} \quad \text{Equation 99}$$

where a coefficient of variation of 0.5 is considered to calculate the standard deviation of the reparation time,  $\sigma_r$ .

### 8.3.2.3 Operational data

The floating wind turbine model is used to evaluate the floating platform motions, based on the hindcast data available (presented in Table 31, Table 32 and Table 33). The operational parameter chosen to evaluate the performance of the wind turbines is the norm of the hub acceleration (95% quantile of occurrence). When this parameter is above a certain threshold, all the wind turbines are supposed to be stopped for safety issues.

Since metocean data are known before the lifetime simulations (hindcast data are used), it is possible to calculate platform motions during data pre-process and then feed the results to the

lifetime simulator. Figure 103 shows the pdf and cdf of hub acceleration, for the considered wind turbine and the available hindcast data.

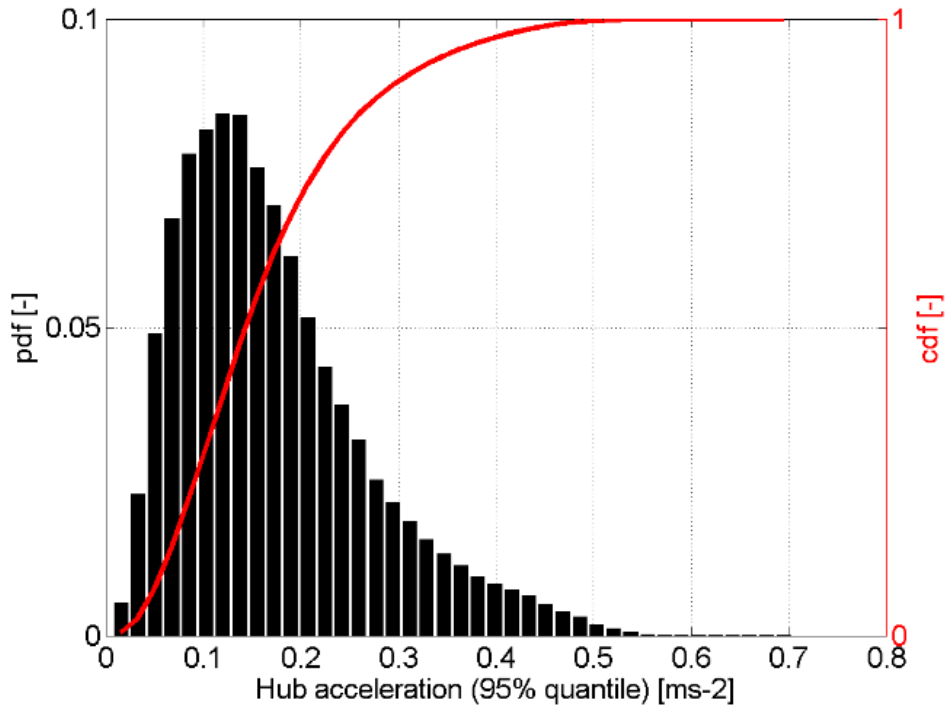


Figure 103: pdf and cdf for of hub acceleration for OC4 system, based on hindcast data (Santander, 1994-2013).

### 8.3.3 Simulation sets

The simulation of the wind farm lifetime is executed according to the methodology introduced in Section 8.2 and the data given in Section 8.3.2. Several case studies were modelled to evaluate the influence of different models/parameters on the results.

Case Study 1, which represents the baseline simulation, uses onshore failure and repair data and does not account for operational stops. Case Study 2, on turn, considers operational stops corresponding to different hub acceleration thresholds. Case Study 3 aims at investigating the sensitivity of results to failure rates, using onshore repair times and not accounting for operational stops. Case Study 4, finally, investigates the sensitivity of the results to mean

reparation times, using onshore failure rates and not accounting for operational stops. A summary of the properties of each Case Study is presented in Table 35.

<b>Simulation set</b>	<b>Failure rates</b>	<b>Reparation times</b>	<b>Operational stops</b>
Case Study 1	Faultstich 2010	Faultstich 2010	No
Case Study 2	Faultstich 2010	Faultstich 2010	Yes
Case Study 3	Variable	Faultstich 2010	No
Case Study 4	Faultstich 2010	Variable	No

*Table 35: Summary of the Case Studies analyzed.*

### **8.3.3.1 Case Study 1: baseline simulation**

The first objective of the baseline simulation is to check the validity of the chosen stop criterion, looking at the variation of the energy yield distribution with the population size. Results are shown in Figure 104. The black curves in the illustration represent the mean ( $\mu$ ), standard deviation ( $\sigma$ ), skewness ( $\gamma_1$ ) and kurtosis ( $\beta_2$ ) of the energy yield as a function of the simulation number. The red curves, plotted in logarithmic scale, represent the COV of the corresponding variables, based on the previous 250 points as illustrated in Section 8.2.5. As it can be seen, the COV curves show a decreasing trend as the number of simulations is increased. In addition, a relevant level of noise is observed. In this Case Study, the simulation reached the stop criterion (relative change of all the COV below 1/100) after 5739 simulated lifetimes. The mean value of the energy yield has a very small relative change, as data samples are added. A similar trend is observed for the standard deviation. On turn, the skewness and kurtosis change more (especially the skewness) and thus impose a larger number of simulations before reaching the stop criterion.

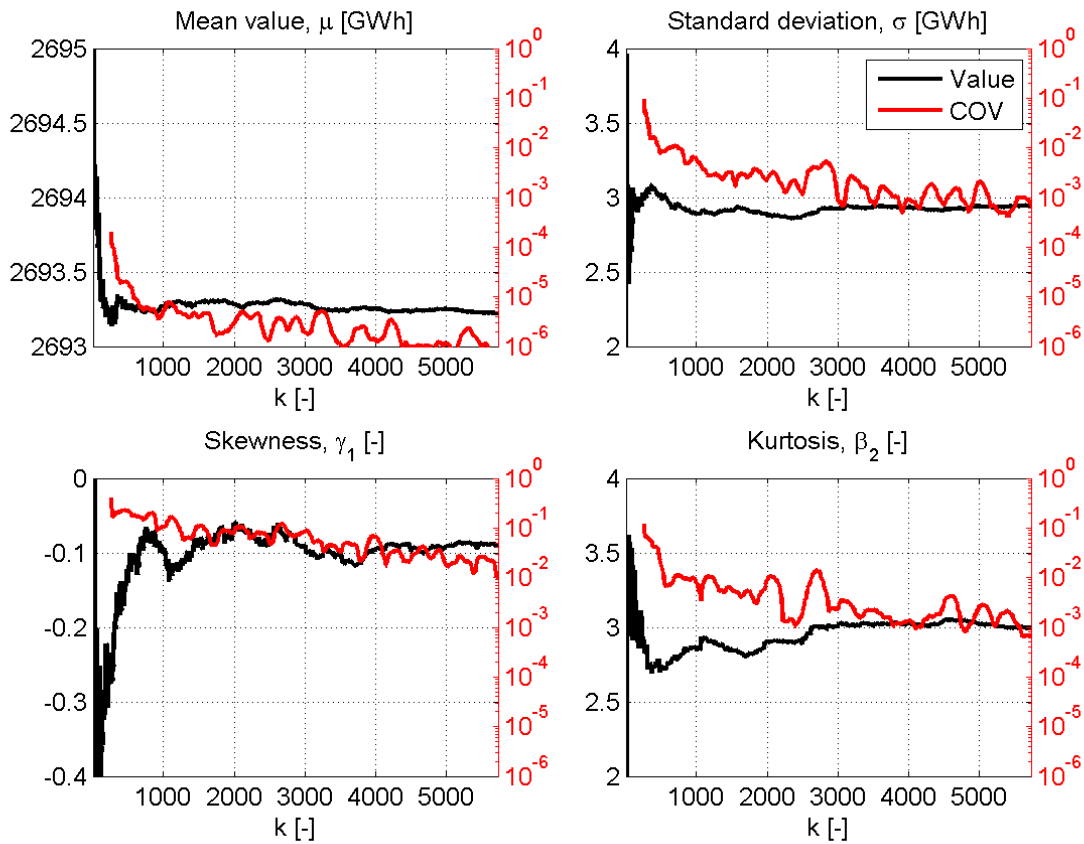


Figure 104: Variation of energy yield statistics as a function of the simulation block number, Case Study 1

Once the energy yield has reached a sufficiently stable distribution, it is possible to discuss its statistical properties. Figure 10 illustrates the pdf and cdf of the energy yield, based on the 5739 simulations of the baseline case study. The mean value of the energy yield is 2693.3 GWh: comparing this to that calculated in Section 3.2.1 (2734 GWh), it can be observed that downtime due to failures is responsible for a reduction of 1.49%. Considering the current feed-in tariff for Germany (184€/MWh during 8 years and 154€/MWh for the following 12 years [135]), this energy loss would have decreased the incomes by 6.8 M€. The standard deviation is 2.94 GWh and thus the coefficient of variation is 0.11%, which indicates low dispersion of the results around the mean value. It is worth noticing that variability in the results comes only from the random occurrence of failures/repairs, being the metocean conditions the same in every simulated lifetime. In

addition, reparation times are supposed to be independent of metocean conditions that is not true in reality. Nevertheless, a variability of the energy yield corresponding to six standard deviations (plus or minus three) would represent a variability of 1.5 M€ of the incomes, considering the German support scheme.

Furthermore, Figure 106 shows the mean yearly energy yield and the mean yearly wind speed at site. As it can be noticed, energy production is directly related to the mean wind speed at site. A sensible year-by-year variation is observed, which remarks again the importance of possessing long-term hindcast data.

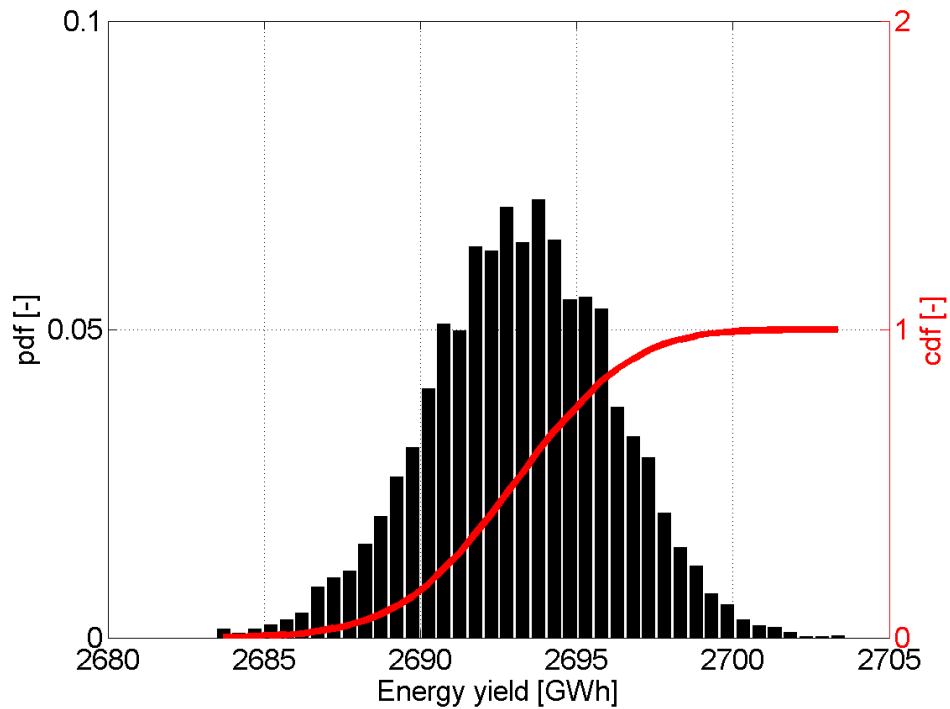


Figure 105: Energy yield pdf and cdf for Case Study 1 at Santander, 1994-2013.

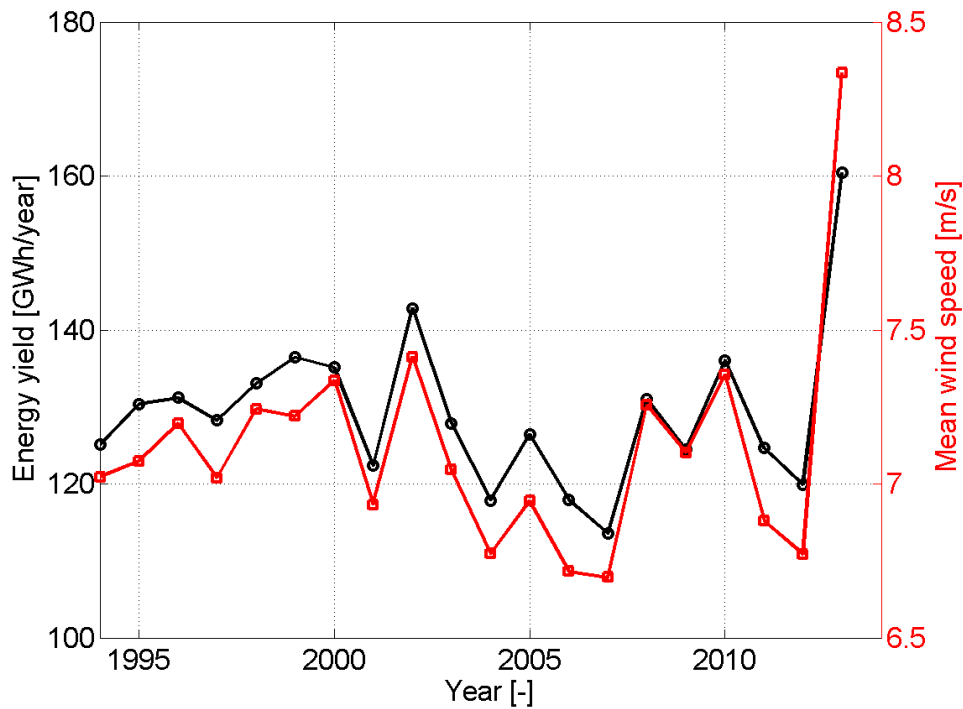


Figure 106: Yearly mean energy yield for Case Study1 at Santander, 1994-2013.

### 8.3.3.2 Case Study 2: influence of operational stops

The second Case Study aims at investigating the influence of the operational stops over the distribution of the energy yield. When the hub acceleration of the wind turbines is above a given safety threshold, it is supposed that the machines must be stopped and thus cannot produce electricity. Several acceleration thresholds were investigated: 0.25, 0.30, 0.35, 0.40 and 0.45  $\text{m s}^{-2}$ , which correspond to a probability of exceedance of 16.3%, 10.1%, 5.7%, 3.0% and 1.1% respectively (see Figure 103). Statistical parameters of energy yield distribution converge with a trend similar to that for “Case study 1”. Table 36 and Figure 107 show the results for this case study, where  $\Delta\mu(E)$  and  $\Delta\sigma(E)$  stand for relative change of mean and standard deviation of energy yield, compared to Case Study 1. As expected, the mean energy yield increases as the acceleration threshold is increased i.e. the turbines operate in a wider range of metocean conditions; the opposite happens for the standard deviation. Remarkably, setting an acceleration threshold of 0.45

$\text{m s}^{-2}$ , which was exceeded only 1.1% of the time, would have given a decrease of 3.8% of the mean energy yield. This is because often (but not always) large accelerations are associated to highly energetic winds. Such an energy loss would have represented a 16.2 M€ income decrease, considering the German feed-in tariff.

$x_{\text{lim}} [\text{m s}^{-2}]$	$\text{Pr}(x > x_{\text{lim}}) [\%]$	$\mu(\text{E}) [\text{GWh}]$	$\sigma(\text{E}) [\text{GWh}]$	$\Delta\mu(\text{E}) [\%]$	$\Delta\sigma(\text{E}) [\%]$
0.25	16.3%	1588.5	1.72	-41.1%	-41.6%
0.30	10.1%	1956.0	2.08	-27.5%	-29.4%
0.35	5.7%	2240.6	2.38	-16.9%	-19.2%
0.40	3.0%	2443.5	2.61	-9.4%	-11.4%
0.45	1.1%	2596.1	2.80	-3.8%	-4.8%

Table 36: Statistics of energy yield for Case Study 2.

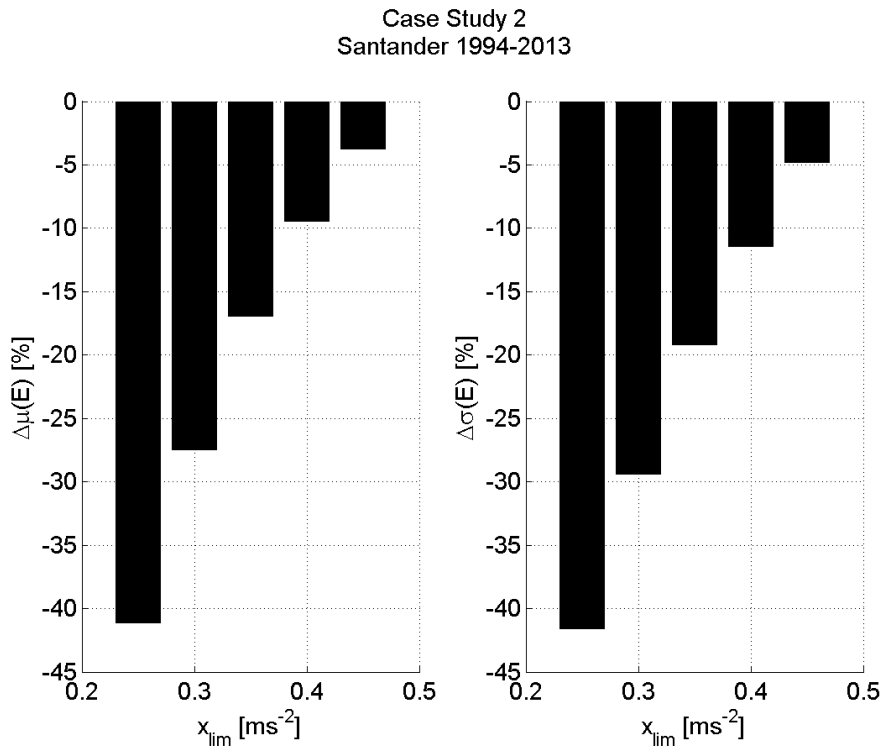


Figure 107: Dependence of mean energy yield variation to acceleration threshold, Case Study 2.

### 8.3.3.3 Case Study 3: influence of failure rate

This Case Study aims at investigating the sensitivity of the results to the failure rate. Therefore, several simulations have been run considering failure rates 25%, 50%, 75%, 100% and 125% higher than those in Table 34. This attempts at simulating the increased failure probability

for floating wind turbines, compared to onshore, due to stronger wind conditions and platform motions. Statistics of the energy yield distribution are collected in Table 37 and represented in Figure 108. As it can be noticed, the energy yield mean decreases as the failure rate increases: more failures give a longer total downtime. As opposite, the standard deviation increases with the failure rate. Doubling the failure rate (i.e.  $\Delta\lambda = 100\%$ ) would result in a 1.6% decrease of the mean energy yield and a 38.7% increase in its standard deviation. This would have represented a decrease of 6.2 M€ of the mean income, and a variability (six standard deviations) of 2.2 m€ considering the German support scheme.

$\Delta\lambda$ [%]	$\mu(E)$ [GWh]	$\sigma(E)$ [GWh]	$\Delta\mu(E)$ [%]	$\Delta\sigma(E)$ [%]
25%	2687.0	3.26	-0.4%	10.7%
50%	2676.6	3.54	-0.8%	20.3%
75%	2666.1	3.85	-1.2%	30.7%
100%	2655.7	4.08	-1.6%	38.7%
125%	2645.4	4.33	-1.9%	47.1%

Table 37: Statistics of energy yield for Case Study 3.

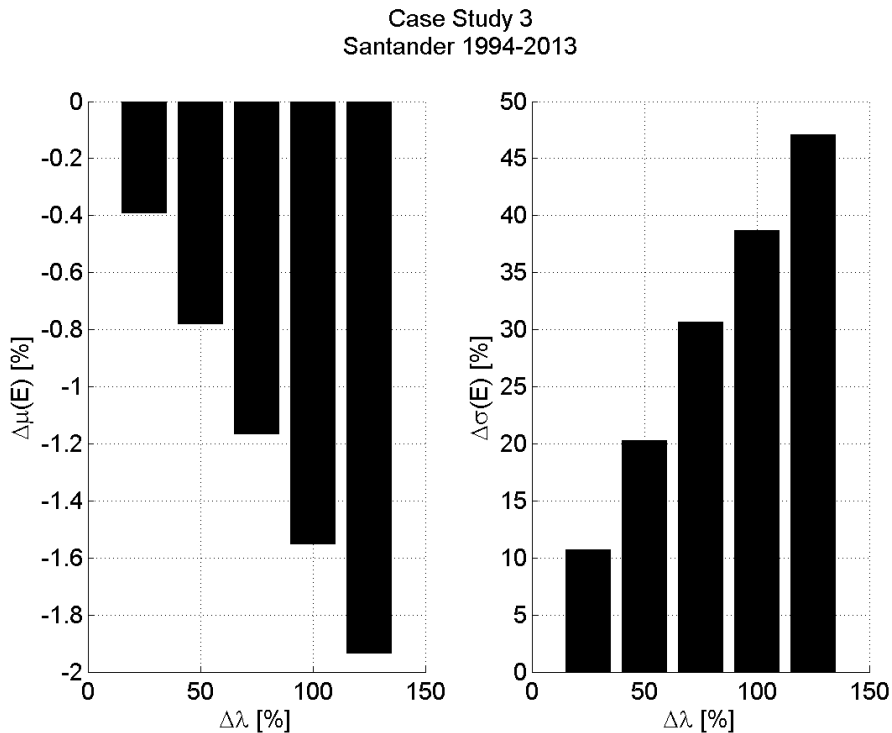


Figure 108: Dependence of energy yield variation to failure rate variation.

### 8.3.3.4 Case Study 4: influence of repair time

This case study aims at investigating the sensitivity of the results to the mean repair time. Therefore, several simulations have been run considering mean repair times 25%, 50%, 75%, 100% and 125% higher than those in Table 34. This aims at simulating the increased reparation times offshore, where waiting periods for favourable weather conditions increase turbines downtime. Statistics of the energy yield distribution are collected in Table 38 and Figure 109. As expected, the energy yield mean value decreases as the mean reparation time increases. The standard deviation of the energy yield, on turn, increases with the mean reparation time. Doubling the mean repair time would lower the mean energy yield by 1.6% and increase its standard deviation by 88.4%. This would have represented a decrease of 6.2 M€ of the mean income, and a variability (six standard deviations) of 2.8 M€ considering the German support scheme.

$\Delta\mu_r$ [%]	$\mu(E)$ [GWh]	$\sigma(E)$ [GWh]	$\Delta\mu(E)$ [%]	$\Delta\sigma(E)$ [%]
25%	2687.0	3.61	-0.4%	22.7%
50%	2676.6	4.23	-0.8%	43.7%
75%	2666.1	4.88	-1.2%	65.8%
100%	2655.7	5.55	-1.6%	88.4%
125%	2645.4	6.21	-1.9%	111.0%

Table 38: Statistics of energy yield for Case Study 4.

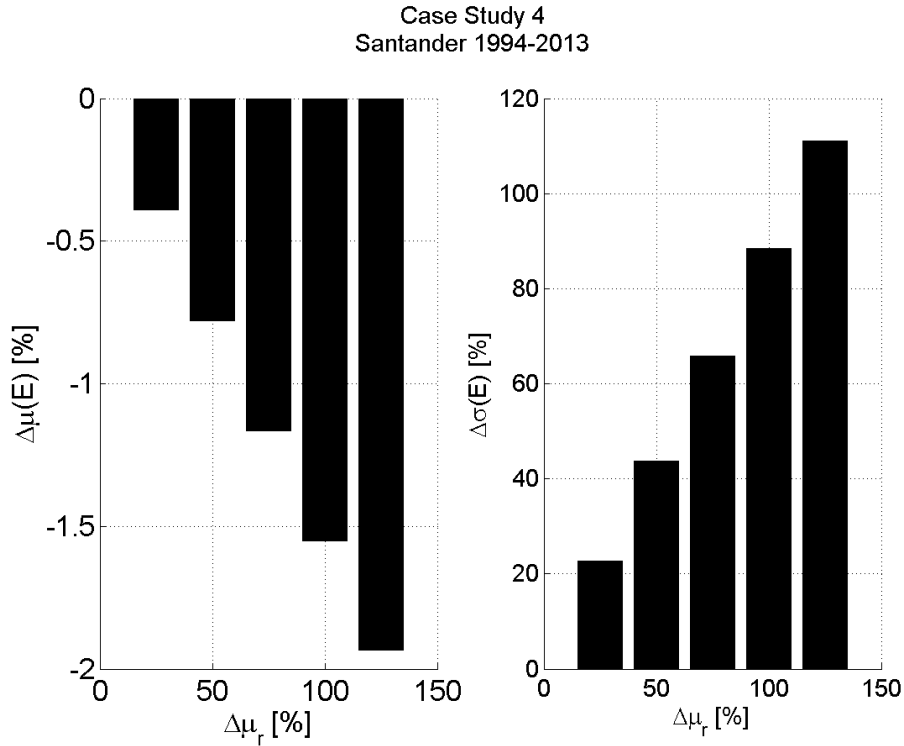


Figure 109: Dependence of energy yield variation to mean repair time variation.

## 8.4 Conclusions

This Chapter presented a methodology to evaluate the impact of downtimes on the long-term energy yield of a floating wind farm. Three different models were described and integrated: a discrete event model, a floating wind turbine model and a wind farm model. The discrete event model simulates failure occurrence and reparation times, the floating wind turbine model simulates platform motions while the wind farm model simulates wake effects inside the wind farm. Downtime is given by failures and operational stops (associated to large platform motions). A sample floating wind farm, consisting of 10 turbines, was simulated with hindcast data for the coast of Santander, Spain. Wake effects accounted for 1.34% of energy loss in the long-term. On average, 5000 lifetimes need to be simulated until the distribution of energy yield is statistically

stable. Among the studies statistical parameters, skewness is asks for a higher number of simulations in order to reach a stable value.

The downtime associated to onshore failure data gives a decrease of 1.49 % of the mean energy yield, compared to the case with no failures. This loss of energy corresponds to a 6.8 m€ income decrease, considering the current German feed-in tariff. It was possible to quantify the decrease of the mean energy yield corresponding to an increase of either the probability of exceedance of the hub acceleration, the mean failure rates or the mean reparation times. An acceleration threshold with a probability of exceedance of 1.1% gave a 3.8% decrease of the mean energy yield. Doubling either failure rates or mean reparation times gave a 1.6% decrease of the mean energy yield.

In all the case studies, the coefficient of variation of the energy yield was found to be very little. This indicates that most probably uncertainty for current offshore farms is not related to the failure rates of the components, but to the availability of weather windows at failure time (that was not modelled here, indeed). It has been interesting to quantify such behavior. Nevertheless, the economic impact of such little uncertainty is still remarkable.

This methodology represents a first step towards the implementation of a numerical model for the evaluation of long-term O&M strategies for offshore floating wind farms. Two main issues will be addressed in the near future. The first is the use of Markov models to simulate the variability of metocean conditions and avoid using the same hindcast data for all the computed lifetimes. The second is the use of an accessibility model, able to evaluate the accessibility of the floating platforms based on available weather windows (see Chapter 6 and Chapter 7). In a second stage, the possible presence of condition monitoring systems will be considered, to reformulate failure probability of the studied components.

---

---

# Chapter 9

## Conclusions

---

---

The main purpose of this thesis was to reduce uncertainty and risks associated to the long-term operation and maintenance of floating wind turbines. This final chapter draws up conclusions related to this thesis and provides a set of recommendations, based on the results obtained, that may give useful guidelines to wind farm operators. Quantitative results are contained in the Conclusions section of the previous chapters; here, a qualitative summary of the findings of this work is proposed.

Chapter 1 gave an outlook of the role of renewable energy for power generation. Onshore wind and photovoltaic were identified as sector leaders, being the technologies with the lowest levelized energy cost (LCOE). Offshore wind registered an impressive increase both in terms of installed capacity and average investments. This was mainly due to the increased energy resource and decreased visual/noise pollution at sea, and the limited amount of land close to demand centers. The current LCOE for offshore wind is between 106 and 176 €/MWh, with intentions to bring it stably below 100 €/MWh by 2020. The little availability of shallow water locations, for which fixed offshore wind structures are economically viable, is driving the interest of industry towards the use of floating systems. This would open up vast potential markets with high wind resources. The successful experience with full-scale prototypes (Hywind, WindFloat, Fukushima) and the planning of the first floating wind farms indicate the industry high confidence in such technology.

Chapter 2 illustrated some of the major challenges for the implementation of floating wind energy. Availability was identified as a key driver for cost reduction of offshore wind. Downtime due to operational stops, components failure and weather delays is responsible for lowering availability of current offshore wind farms. Inspection, maintenance and condition monitoring activities are needed activities to reduce downtime. However, their impact on the LCOE of offshore wind is very relevant as they can account for 25% of it. The trend of increasing water depth and distance from the shore for future farms (both fixed and floating) emphasize the importance of correctly planning long-term O&M strategies.

Based on the challenges identified in Chapter 2, the objectives of this dissertation were stated in Chapter 3. Among several, four topics were identified as of primary importance for the future deployment of floating wind energy: the relationship between operational stops and long-term energy yield of a floating wind turbine, the temporal and spatial variation of accessibility parameters, the modelling of walk-to-work access and the impact of downtime on the energy production of a floating wind farm. All of them deal with the long-term behavior of such systems, which still has a high degree of uncertainty due to the small experience with real installations.

Chapter 4 provided a description of data used throughout the dissertation. High resolution metocean hindcast data is provided by reanalysis databases developed at IH Cantabria. Data related to an open-source floating wind turbine was presented as well.

Chapter 5 illustrated a methodology for evaluating the influence of operational stops on the long-term energy yield of a floating wind turbine. Hub acceleration and tower inclination were identified as relevant operating parameters, being related to inertial and static loading of the wind turbine structure. Operating parameters were simulated for a subset of the available metocean data, selected using a maximum dissimilarity algorithm, and then interpolated over the whole set of data

using radial basis functions. It was found that tower inclination is mainly dependent on wind speed and direction, while hub acceleration on wind speed, wave significant height and wave-wind misalignment. Remarkably, large accelerations were calculated for wind speeds below cut-out. This suggests that for floating wind turbines operational stops may also be associated to wave parameters, besides to wind speed. This methodology can be used to find a good tradeoff between system reliability and energy production of future installations.

Chapter 6 presented results of a vast accessibility analysis carried out for the North Sea. Spatial and temporal variation of accessibility parameters was calculated using 23 years of hindcast data. Two maintenance activities were studied: light repair operations and heavy repair operations, which are characterized by different requirements concerning metocean conditions. Results were found to have a very strong seasonality and variability over years. Harsh climate of far offshore locations is associated to long mean waiting times, which can vary sensibly from year to year. Remarkably, waiting times for weather windows during daylight regime can be 4-5 times higher than normal. It was also noticed that results are extremely sensitive on the access thresholds of the different maintenance strategies. These findings indicate the importance of using long-term, reliable hindcast data when designing maintenance strategies for offshore wind. In addition, they highlight the need for further research, development and innovation in access systems able to widen the range of operating conditions of the existing ones.

Chapter 7 illustrated in detail a methodology to evaluate the walk-to-work accessibility of offshore wind floating platforms. The vessel-platform system was modelled as a constrained multi-body system in the frequency domain. In addition, it was presented a method to linearize mooring and quadratic damping forces acting on the two bodies. Two types of vessels were studied: a small catamaran equipped with fender and a larger vessel equipped with a motion-compensated gangway.

Results indicated that the maximum wave height for which personnel transfer is possible is largely affected by wave period and heading. Furthermore, it was found that access with floating wind turbines is not necessarily more difficult than for fixed wind turbines, depending on wave conditions. The feasibility of walk-to-work operations should rely on tools based both on science and field experience. It is advisable to take into account more metocean parameters, besides wave significant height. The developed methodology demonstrates that there is room for optimizing vessels and approach strategies in order to maximize the efficiency and safety of access.

Chapter 8 eventually presented a methodology to evaluate the impact of downtime on the energy production of a floating wind farm. Three numerical models were integrated: a discrete event model, a floating wind turbine model and a wind farm model. The impact of downtime on the mean energy production and expected income was significant. Nevertheless, uncertainty in energy yield distribution was calculated to be very small. In addition, the correlation between the mean energy yield and failure rates, mean reparation times and probability of non-exceedance of the hub acceleration threshold was quantified. Results indicate that uncertainty is related not only to failure rates but also (and most importantly) to the weather pattern present when the failure occurs. Therefore, large effort should be dedicated to the study of suitable logistic solutions able to deal with processes with such an unpredictable nature.

This thesis was realized with passion and dedication. The methodologies developed at the best of the author's scientific skills. The results illustrated with all the possible honesty and critic attitude. I hope that such piece of work will be a source of inspiration for other engineers and scientists, and that will be somehow of help to the progress of the renewable energy sector.

## Resumen en castellano

---

---

### 1. Introducción

Durante las últimas décadas se ha hecho evidente un cambio de tendencia en la generación de energía a nivel mundial. El porcentaje de electricidad producida con fuentes renovables, excluyendo hidroeléctricas, pasó de 0.6% en 1973 a 5.7% en 2013 [1].

Este crecimiento ha sido confirmado en 2014, a pesar de la disminución en el consumo mundial de energía y de los bajos precios del petróleo: la instalación de potencia renovable creció a un ritmo anual más rápido (hasta 97 GW de potencia total instalada hasta dicho año) y representó más del 34% de la capacidad instalada en todo el mundo [3], [4]. De hecho, durante ese mismo año, los datos demostraron por primera vez una marcada desconexión entre el crecimiento económico y las emisiones de CO<sub>2</sub> [5].

El cambio climático, la contaminación a nivel local, la seguridad energética y la inestabilidad geopolítica de los países productores de petróleo aceleraron el desarrollo de tecnologías renovables para la generación de energía. De esta forma, se prevé una inversión media anual de 203 millones de euros hasta 2020 [4]. Entre todas las fuentes de generación, la energía eólica terrestre lidera el crecimiento global habiendo representado un tercio del aumento de capacidad renovable en 2014 [3]. El coste de la energía eólica terrestre es cada vez más comparable con la de los combustibles fósiles estando entre 53-70 €/MWh y en algunos casos alrededor de 44 €/MWh (Brasil, Egipto, Sudáfrica, parte de Estados Unidos) [7].

Según Naciones Unidas, el 44% de la población mundial vive en zonas costeras [8], disponiendo normalmente de espacio limitado para el desarrollo de energías renovables terrestres, siendo esta circunstancia un problema para algunas de esas regiones que demandan gran cantidad de energía. Por tanto, para estas regiones, el aprovechamiento de la energía en el mar, como la energía eólica marina, resulta muy importante desde un punto de vista estratégico.

La eólica marina presenta varias ventajas, en comparación con la terrestre: los vientos son menos turbulentos y más sostenidos, mientras que la contaminación visual y el ruido se reducen en gran medida.

A finales de 2015, la capacidad de eólica offshore instalada en todo el mundo alcanzó los 12 GW [10]. Europa, que lidera el sector con una cuota de 11 GW [11], está mostrando una importante tendencia creciente en términos de potencia instalada e inversiones. La mayoría de las granjas se encuentran en el Mar del Norte (69%), donde un alto recurso energético y una gran plataforma continental favorecieron el despliegue de dicha tecnología. A finales de 2015, la inversión total en el sector ha sido de 13.3 millones de euros, la más alta jamás registrada [12].

La Figura 1 muestra el coste nivelado de la energía (LCOE) para la eólica marina en el período 2000-2020, tanto para los proyectos ya encargados como para los propuestos [14]. Como se puede observar, la tendencia ha ido aumentando gradualmente hasta 2012. La razón principal de esto es el aumento de la distancia de la costa, que refleja el deseo de los desarrolladores de aprovechar los mayores recursos energéticos offshore localizados, pero también aumentan los costes en muchos aspectos de la cadena de suministro. La tendencia de los costes después de 2012 es más alentadora, ya que el LCOE se ha estabilizado en el rango entre 106 y 176 €/MWh. No obstante, la expectativa para el 2020 es que el coste de los proyectos esté por debajo de 100 €/MWh.

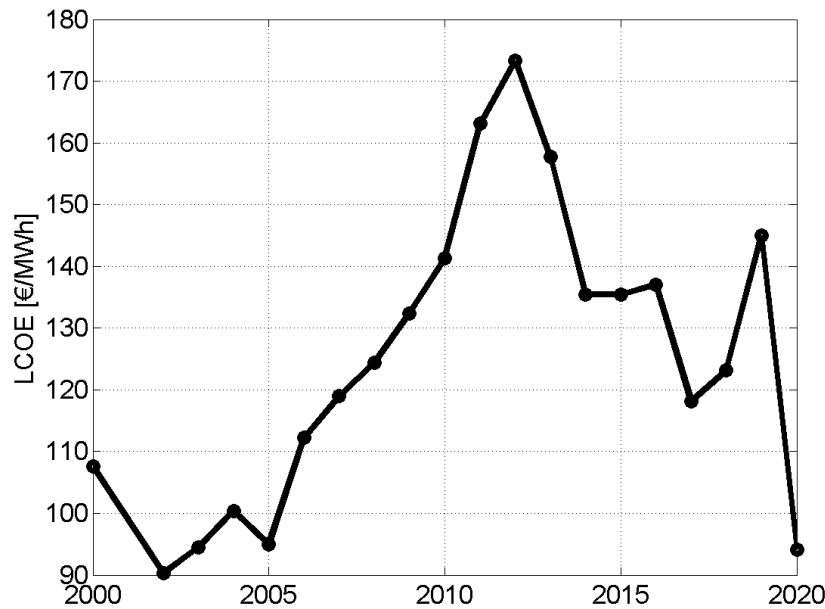


Figura 1: Coste nivelado de la energía eólica marina.

La energía eólica marina ha demostrado ser fuente de energía eficiente y fiable, y se prevé desempeñar un papel importante en el futuro *mix* energético, particularmente en Europa [7]. Sin embargo, el uso de estructuras fijas sufre una limitación importante: no es económicamente eficiente cuando la profundidad del agua es superior a 50 m [17]. La cantidad limitada de sitios de aguas poco profundas restringe además el mercado de este tipo de tecnología. Muchas regiones no presentan una batimetría favorable para el desarrollo de la eólica marina con la tecnología actual: entre ellos España, Portugal, la mayor parte de los países del Mediterráneo, la costa oeste de Estados Unidos, China y la costa oriental de Japón.

Una alternativa natural a las estructuras fijas es la instalación de turbinas eólicas flotantes. Esto ayudaría tanto el desbloqueo de nuevos mercados como la explotación de los grandes recursos eólicos lejos de la costa. En la actualidad se están desarrollando diferentes conceptos de turbinas eólicas flotantes. Entre todas las alternativas de plataformas flotantes, las más utilizadas están siendo la tipología “SPAR”, la “semi-sumergible” y la “TLP” (Tension Leg Platform), que se

muestran en la Figura 2 de izquierda a derecha, respectivamente. Cada uno de ellas presenta diferentes ventajas y desventajas, relacionadas con la estabilidad estática, la estabilidad dinámica, la fabricación, el sistema de fondeo y los costes de instalación [19].



*Figura 2: Conceptos de turbinas eólicas flotantes.*

Por el momento, pocos prototipos a escala real se han instalado en mar. Entre ellos, destacan los proyectos Hywind (Statoil, 2 MW, Noruega [20]), WindFloat (Principle Power y EDP, 2 MW, Portugal [23]) y Fukushima (consorcio Fukushima FORWARD, 2 MW y 7 MW, Japón [25], [26]). La operación exitosa de estos prototipos ha llevado a sus respectivos desarrolladores a planificar los primeros parques eólicos flotantes [22], [24].

El coste de las turbinas flotantes es sin duda alto en comparación con el de las fijas. Un estudio realizado por Garrad Hassan calcula que, para un parque eólico flotante de 500 MW instalado en aguas de 50 m de profundidad, el coste de la energía podría alcanzar los 128 €/MWh [28]. Sin embargo, existe la posibilidad de una reducción importante de los costes, ya que estos sistemas pueden dar cabida a turbinas más grandes e instalarse más lejos de la costa, haciendo que la producción energética pueda aumentar sustancialmente. Además, por lo general pueden ser

ensamblados en tierra y remolcados en el mar hasta su emplazamiento, lo que reduce la duración de los trabajos marinos de instalación y el uso de grandes buques de apoyo offshore, cuyos fletes son altos y disponibilidad pequeña..

Para el año 2020, EWEA prevé que la potencia eólica marina en Europa puede ser alcanzar 40 GW, y que se vea aumentada hasta 150 GW en 2030 [17]. Este crecimiento sólo puede lograrse a través de la implementación de sistemas flotantes para aguas profundas.

## **2. Planteamiento del problema**

Por un lado, la disponibilidad (*availability*) de una turbina eólica se define como el porcentaje de tiempo en que es capaz de producir electricidad; mientras que por otro lado, el tiempo de inactividad (*downtime*) se define como el porcentaje de tiempo en que ésta es incapaz de generar energía. La falta de disponibilidad, que implica una pérdida de producción energética, por lo general se asocia a fallos en los equipos, a mantenimiento preventivo o a paradas operativas.

Cuando un equipo falla, debe ser reparado lo antes posible. La duración de la reparación depende principalmente del tamaño del componente a reparar/remplazar, de la complejidad de la reparación y de la accesibilidad al parque eólico marino y a la plataforma en sí. El mantenimiento preventivo se realiza para preservar o restablecer la fiabilidad del equipo mediante la sustitución de los componentes desgastados antes del fallo. Mientras, que las paradas operativas de la turbina eólica en condiciones meteorológicas particularmente severas, se llevan a cabo para evitar daños en la máquina que pudiesen desembocar en un fallo crítico de la misma.

De esta forma, los parques eólicos marinos actuales suelen alcanzar una disponibilidad entre el 80% y el 95%, mientras que en tierra firme se consiguen normalmente valores de hasta 97% [29]. La Figura 3 muestra los datos de disponibilidad para parques eólicos marinos existentes,

recogidos por Fraunhofer-IWES [31]. Como se puede apreciar, algunos han tenido muy baja disponibilidad en ciertos años. No obstante, se remarca la tendencia positiva de los parques Egmond (Holanda) y Alpha Ventus (Alemania).

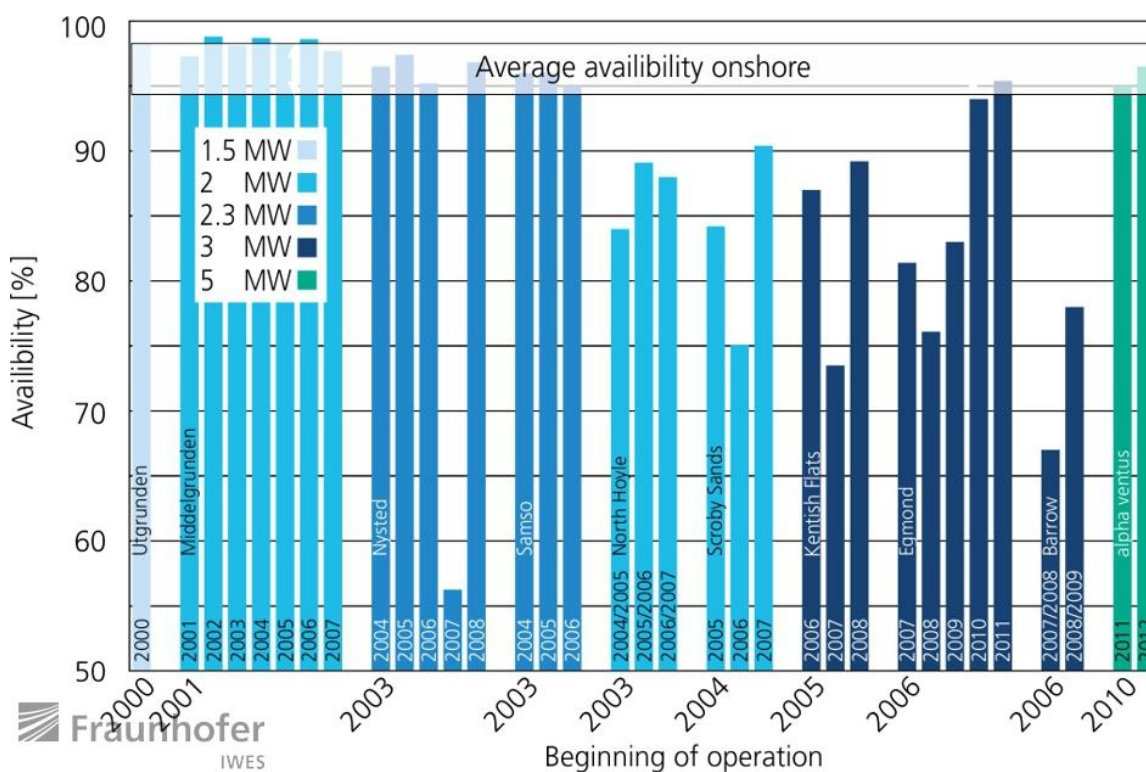


Figura 3: Disponibilidad de parques eólicos marinos existentes (fuente: Fraunhofer IWES).

En la gran mayoría de los casos, los bajos niveles de disponibilidad están asociados a la dificultad operativa para reparar componentes en alta mar, a problemas de tipo logístico y a retrasos debidos a condiciones meteorológicas adversas [33]–[38].

La disponibilidad de un parque eólico marino está fuertemente relacionada con su LCOE, como se muestra en la Figura 4. Es evidente que hacer la eólica marina competitiva no depende sólo de la reducción de los gastos de capital, sino también de una operación eficiente y económica de los parques a largo plazo.

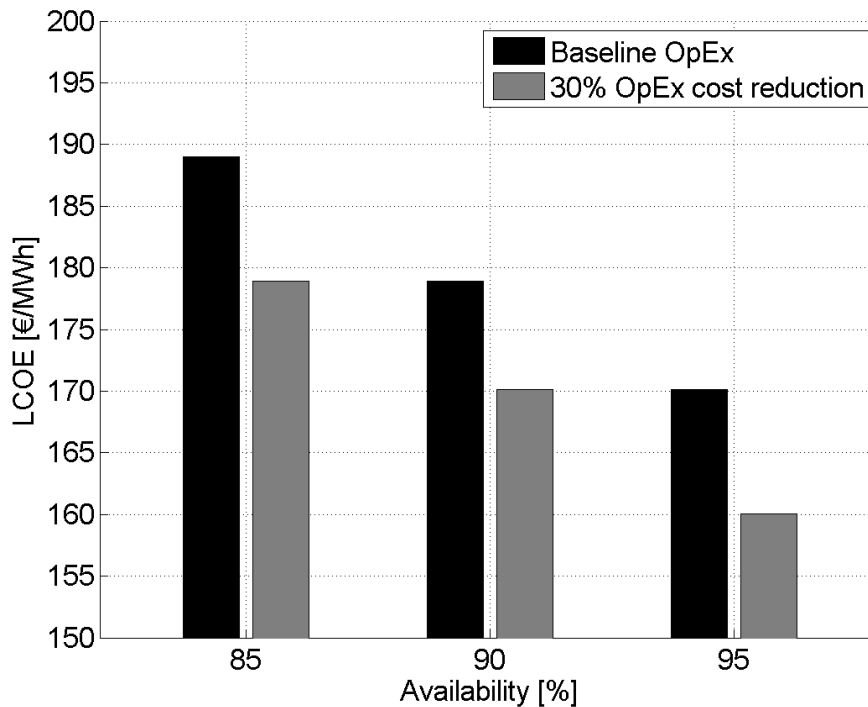


Figura 4: Relación entre disponibilidad y LCOE para un parque eólico marino.

La operación de un parque eólico incluye todas las actividades necesarias para garantizar una producción de electricidad segura y continua. Por lo general, un parque eólico marino está diseñado para una vida útil de 20-25 años. Para poder alcanzar altos niveles de disponibilidad en un periodo tan largo y sobrevivir en alta mar, deben llevarse a cabo adecuadas actividades de inspección y mantenimiento [40]–[42].

Los datos recogidos durante el programa WMEP [43] mostraron que para turbinas en tierra se producen, de forma promediada, 2.4 fallos al año que dan lugar a 6 días de tiempo de inactividad. Estos datos de tiempo de inactividad se prevén peores para estructuras en el mar, teniendo en cuenta que las turbinas tienden a ser más grandes (y por lo tanto más propensas a tener mayores tasas de fracaso [44]) y que las condiciones meteoceánicas puede complicar las operaciones de acceso, inspección y mantenimiento. Para parques eólicos offshore, se estima que sean necesarias del orden de cuatro a seis visitas por turbina al año [45].

A los aerogeneradores offshore se puede acceder tanto en helicóptero como en barco. Los barcos pueden asegurar la transferencia de personal de dos maneras (concepto *walk-to-work*): bien empujando sobre la plataforma a la altura de la superficie libre a través de una defensa o *fender* (véase la Figura 5), permitiendo a los técnicos agarrarse a una escalera montada en la estructura; o bien a través de una pasarela de compensación de movimientos (*gangway*) por medio de la cual el personal pueda caminar hasta la torre, la pieza de transición o la escalera de acceso, sin que haya contacto entre el barco y la plataforma (ver Figura 6).



Figura 5: Concepto “walk-to-work”: acceso por medio de una defensa.



Figura 6: Concepto “walk-to-work”: acceso por medio de una pasarela.

Sin duda, todas las operaciones relacionadas con el acceso, inspección y mantenimiento deben ser realizadas dentro de rigurosos límites de seguridad para evitar cualquier accidente que pueda poner en peligro la salud del personal involucrado. Existen varias normativas para regular las operaciones marinas y la transferencia de personal en la mar [52]–[56] y varias remarcan la importancia de utilizar datos meteorológicos fiables y de largo plazo para la evaluación del acceso.

Por lo general, las actividades de operación y mantenimiento (O&M) tienen costes tanto fijos como variables. Los costes totales pueden variar considerablemente en función del sitio de instalación del parque eólico. Entre los factores que influyen en los costes, aquellos que se consideran de más importancia son la distancia entre el parque y las instalaciones de mantenimiento, y las condiciones meteoceánicas en el emplazamiento del parque [59]–[62].

Debido a la inmadurez de la industria y a las particularidades específicas de los diferentes lugares de emplazamiento, es difícil tener una estimación precisa de los costes de O&M. Garrad Hassan estima que pueden representar hasta el 25% del LCOE [63]. Lo que hace pensar que, debido a la complejidad de estas actividades y su impacto en el coste de la energía, podría ser aún más relevante para los sistemas flotantes en comparación con los sistemas fijos. Los movimientos de la plataforma pueden imponer paradas operacionales, disminuir la fiabilidad de los componentes y complicar las operaciones de acceso, inspección y mantenimiento por medio de barcos y helicópteros [19]. Además, la breve experiencia con prototipos a escala real se refleja en un alto nivel de incertidumbre sobre el rendimiento a largo plazo de tales estructuras.

Sin embargo, es cierto que todas las actividades relacionadas con las O&M representaran un desafío importante para los parques offshore presentes y futuros. La industria de la energía eólica marina necesita combinar estrategias rentables y seguras de forma simultánea, para garantizar una operación exitosa a largo plazo y hacer esta tecnología cada vez más competitiva.

### 3. Objetivos

El objetivo principal de este trabajo es el desarrollo de metodologías que puedan reducir la incertidumbre y los riesgos asociados a la operación y el mantenimiento a largo plazo de parques eólicos flotantes. Teniendo en cuenta toda la información recopilada, este tema se ha identificado como uno de los retos para la futura competitividad de la energía eólica flotante. La motivación para la realización de tal esfuerzo está específicamente dada por los siguientes puntos:

- La importancia creciente de la energía eólica marina en la mezcla global de energía renovable.
- El potencial mercado y la posible reducción del coste de tecnologías flotantes.
- El impacto que O&M tienen en el LCOE de la energía eólica marina.
- Los riesgos y costes asociados al acceso a las estructuras marinas.

Los pocos años de experiencia acumulada en el sector, dejan patente la necesidad de innovación, investigación y desarrollo en la materia. De hecho, esta tesis está lejos de pretender ser una solución definitiva a la operación y el mantenimiento de los aerogeneradores en entorno marino, ya que es un tema extraordinariamente amplio. Sin embargo, se han identificado cuatro problemas específicos que han llevado al desarrollo de metodologías que se espera puedan ayudar al progreso del sector. Los problemas estudiados son:

- La relación entre paradas operacionales y de producción energética a largo plazo
- La variabilidad temporal y espacial de los parámetros de accesibilidad
- Modelado de la transferencia *walk-to-work* de personal a una plataforma flotante.
- La influencia de los fallos sobre la generación de electricidad de un parque flotante.

Cada uno de estos temas se detalla respectivamente en las Secciones 5, 6, 7 y 8 de este capítulo.

## **4. Datos referentes a la climatología y a la plataforma utilizada**

Como el comportamiento a largo plazo resulta ser una fuente de incertidumbre para las turbinas eólicas flotantes, en la presente tesis se trata de hacer un gran uso de datos meteoceánicos obtenidos mediante técnicas de reanálisis para tener en cuenta esta circunstancia. En los últimos años, las bases de datos de reanálisis han representado una valiosa fuente de información para una amplia gama de aplicaciones de ingeniería offshore y costera [66]–[68]. La presente investigación emplea las bases de datos desarrolladas por el Instituto de Hidráulica Ambiental de Cantabria (IH Cantabria). De esta forma, se dispone de series temporales de condiciones de oleaje y viento a largo plazo, con alta resolución espacial y temporal. Esta información fue calibrada a través de datos de satélite y validadas con datos de campo.

En cuanto a los parámetros de estado de la mar, IH Cantabria ha generado un conjunto de datos globales de oleaje, llamado GOW (Global Ocean Waves) [69]. La resolución espacial es de  $0.125^\circ$  tanto en latitud como en longitud, mientras que la resolución temporal es de una hora y se dispone de datos desde 1979 a 2014. Los datos se proporcionan en forma de altura de ola significativa, periodo de pico y dirección media.

Los datos de viento provienen de la base de datos SeaWind II [74]. La resolución espacial es de  $0.125^\circ$  tanto en latitud como en longitud, la resolución temporal de una hora disponiendo de datos desde 1990 a 2013. Los datos se proporcionan en forma de velocidad media (evaluada a una altura de 90 m, altura típica del buje de turbinas de 5 MW objetos de este estudio [78]) y dirección media.

El conjunto de metodologías desarrolladas en la presente tesis han sido aplicadas a una turbina flotante compuesta por la plataforma semi-sumergible OC4 y el aerogenerador de NREL 5 MW [78], [79]. La Tabla 1 incluye un resumen con sus características.

<b>Masa y geometría</b>		
Desplazamiento	13473	t
Calado	20	m
Diámetro columna principal	6.5	m
Diámetro columnas secundaria	12	m
Diámetro placas de “heave”	24	m
Profundidad del centro de masa	13.46	m
Inercia en “roll/pitch”	6.827E+9	kg m <sup>2</sup>
Inercia en “yaw”	1.226E+10	kg m <sup>2</sup>

*Tabla 1: Características de la plataforma OCA.*

## 5. Paradas operacionales y producción de una turbina flotante

Los aerogeneradores flotantes son sistemas complejos sujetos a la acción combinada de viento, olas y corrientes. Se pueden producir grandes cargas para velocidades de viento inferiores a los valores de *cut-out* tradicionales (25 m / s, por lo general) e imponer una parada operacional, es decir la desconexión de la máquina para evitar un daño no deseado de cualquier componente. El tiempo de inactividad resultante se asocia a una disminución de la disponibilidad y a su correspondiente pérdida de producción energía.

En este apartado se incluye una metodología para reducir el tiempo de cálculo de evaluación de la respuesta a largo plazo de una turbina eólica flotante y el impacto de las paradas operativas en la producción de energía. La metodología propuesta se basa en los siguientes cinco pasos:

- *Extracción de un subconjunto de datos metoceanicos a través de técnicas avanzadas de selección.* Con base en la exitosa experiencia en trabajos anteriores en aplicaciones de ingeniería costera y offshore [72], [88], [89], el algoritmo de máxima disimilitud (MDA) es el elegido para este trabajo.
- *Simulación directa de la respuesta de la turbina para el subconjunto seleccionado.* Se ha resuelto la dinámica de cuerpo rígido de la plataforma a través de la ecuación de Cummins [92]. Se han considerado fuerzas hidrodinámicas del primer orden (masa añadida,

amortiguamiento potencial, fuerzas de excitación) y un modelo casi-estático de las fuerzas del sistema de fondeo [104]. Las fuerzas aerodinámicas se han simplificado considerando una única fuerza axial, aplicada en el buje de la turbina y calculada por medio del coeficiente de empuje estático [99].

- *Identificación de los parámetros operacionales más relevantes.* Los parámetros operacionales que se han identificado como más relevantes han sido el cabeceo y el balanceo de la plataforma, junto a la aceleración del buje de la turbina, en cuanto relacionados con cargas estáticas y dinámicas producidas en el sistema [19], [105].
- *Reconstrucción de los parámetros operacionales para el conjunto original de datos metoceanicos.* Una vez calculados los parámetros operacionales para el subconjunto seleccionado de datos metoceanicos, es posible extrapolar los resultados para el conjunto original a través de técnicas de interpolación no lineales. El método utilizado aquí se basa en funciones de base radial (RBF) La aproximación RBF se ha aplicado con éxito en muchos campos, incluyendo aplicaciones de ingeniería costera [72], demostrando de tener una mayor precisión en comparación con otros métodos de interpolación [106].
- *Evaluación del impacto de las paradas operativas en la producción de largo plazo.* Cuando cualquiera de los parámetros operacionales supera un determinado umbral, se supone que la turbina eólica ha de ser parada y por lo tanto no puede generar electricidad. Con el fin de cuantificar estos efectos, se han calculado los valores de disponibilidad y de factor de capacidad a largo plazo.

La metodología desarrollada se ha aplicado al sistema flotante OC4 suponiéndolo instalado en la costa de Santander, España. El cabeceo y el balanceo de la plataforma han resultado ser

fuertemente dependientes de la velocidad media y de la dirección del viento, produciéndose sus mayores valores en la zona de la velocidad nominal del viento (véase las Figura 7 y Figura 8).

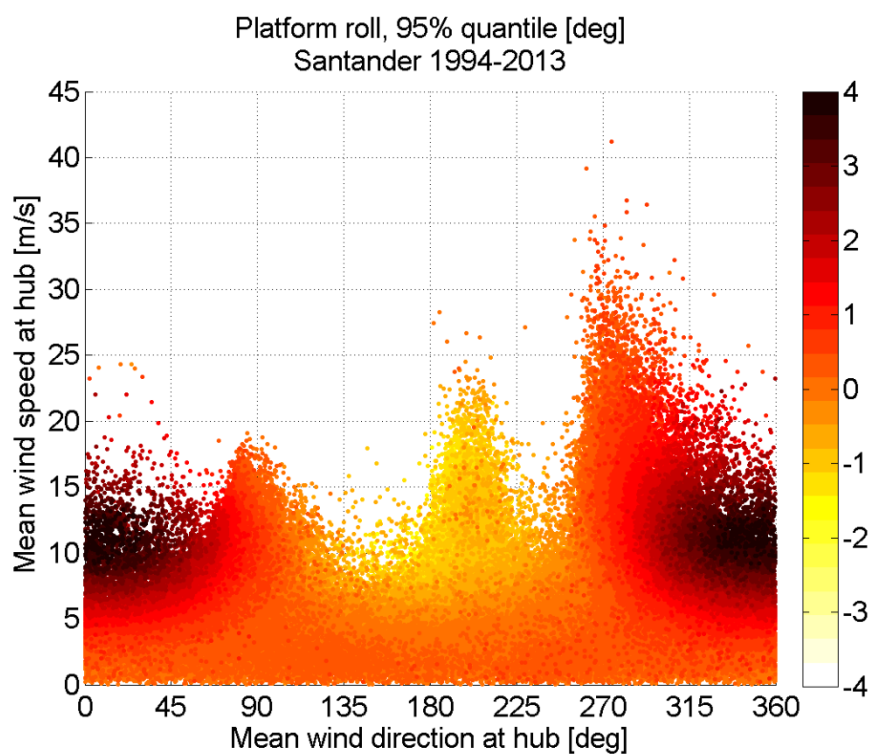


Figura 7: Alabeo de la plataforma (cuantil 95%) en función de velocidad media y dirección del viento.

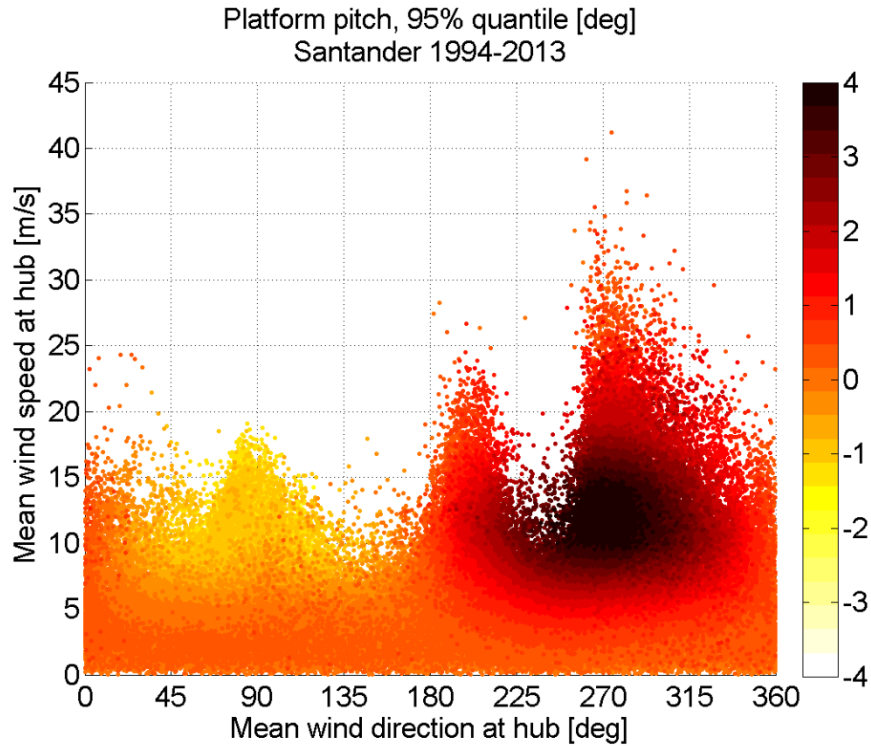


Figura 8: Cabeceo de la plataforma (cuantil 95%) en función de velocidad media y dirección del viento.

La aceleración del buje, por otro lado, está influenciada también por las condiciones de oleaje y sus valores más altos ocurren cuando se produce la alineación del viento y las olas (Figura 9 y Figura 10). Sorprendentemente, se ha observado que se pueden originar grandes aceleraciones por debajo de la velocidad de *cut-out* de la turbina.

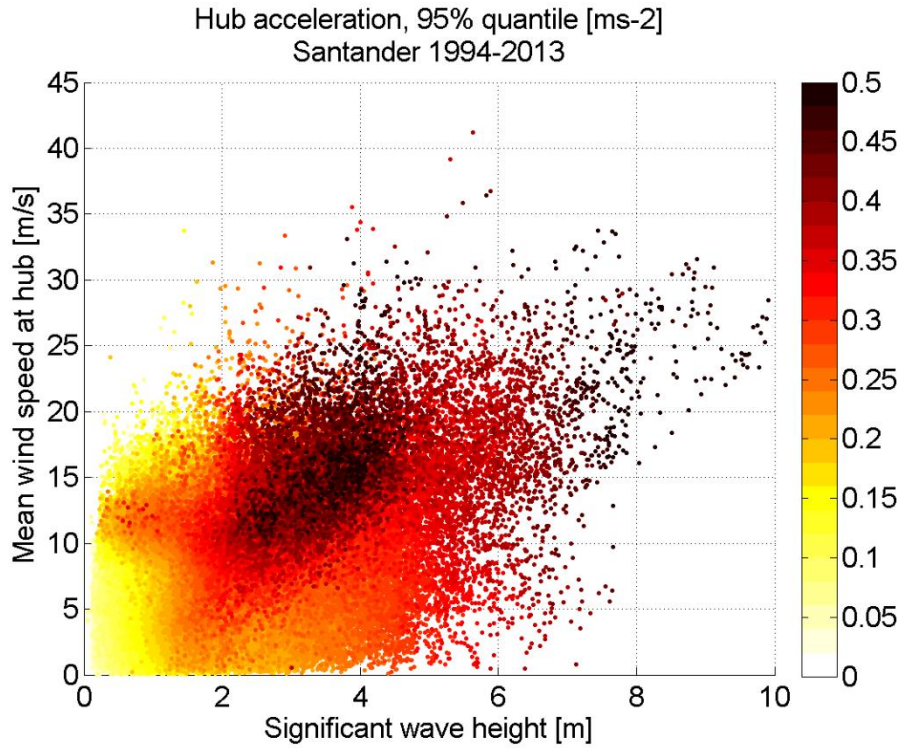


Figura 9: Aceleración del buje (cuantil 95%), en función de velocidad media del viento y altura de ola significativa.

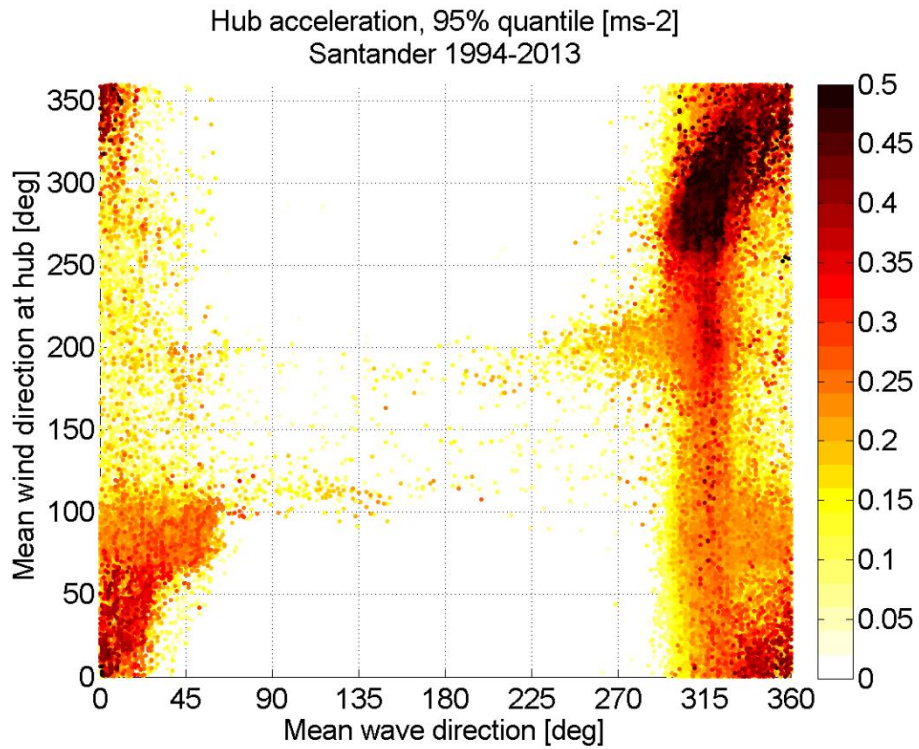


Figura 10: Aceleración del buje (cuantil 95%), en función de la dirección de viento y olas.

La disponibilidad y el factor de capacidad de la turbina disminuyen de forma no lineal al reducir los umbrales operacionales (Figura 11 y Figura 12). Los resultados dependen también del cuantil de ocurrencia por medio del cual se evalúan los parámetros operacionales.

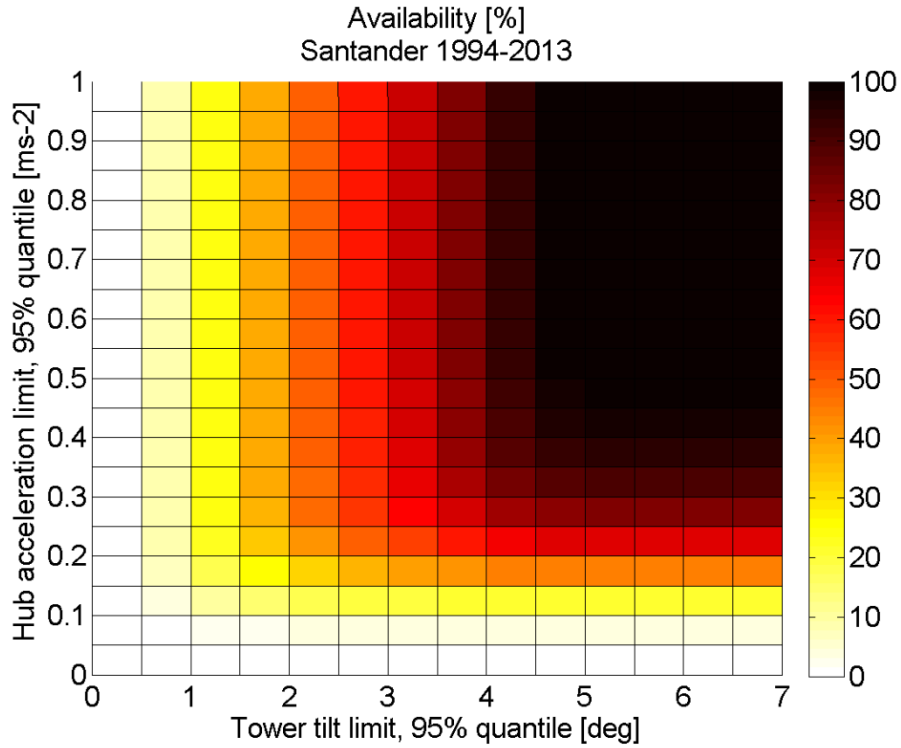


Figura 11: Disponibilidad de largo plazo de la turbine flotante, en función de los umbrales operacionales.

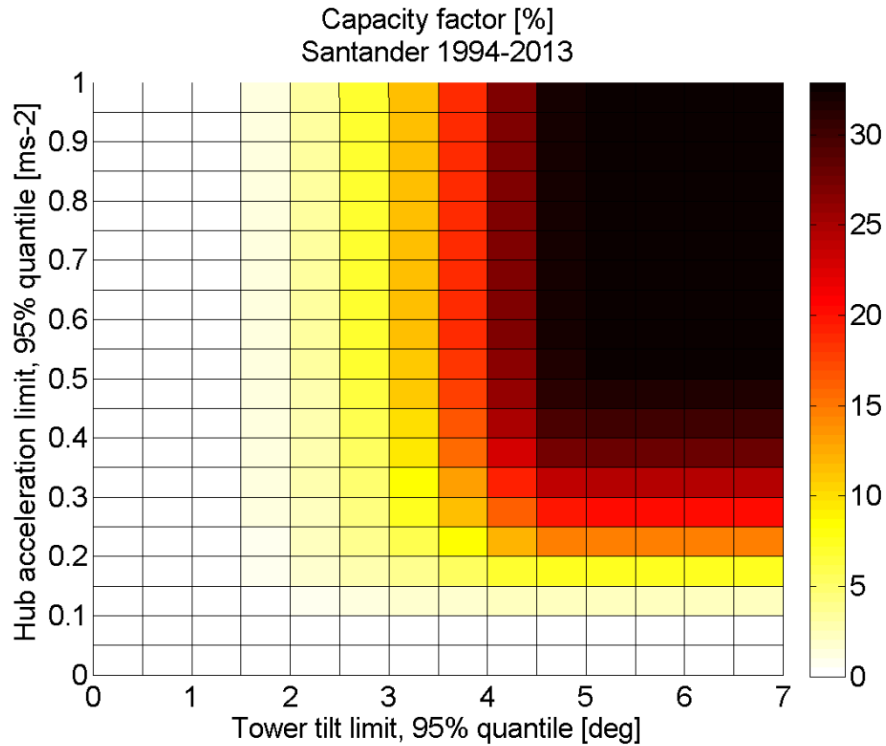


Figura 12: Factor de capacidad de largo plazo de la turbina flotante, en función de los umbrales operacionales.

Esta metodología puede resultar útil durante varias etapas de la vida útil de un parque eólico flotante. De hecho, tanto en el diseño como en la operación de los aerogeneradores, puede dar directrices importantes para evaluar el mejor compromiso entre la fiabilidad y producción de energía.

## 6. Variabilidad de los parámetros de accesibilidad

Para alcanzar altos niveles de disponibilidad y sobrevivir en el entorno marino, los aerogeneradores deberán someterse a adecuadas actividades de inspección y mantenimiento. Una planificación eficiente de tales actividades pasa por una evaluación precisa de la *accesibilidad*.

Para ser eficientes a largo plazo, las estrategias de operación y mantenimiento deben tener en cuenta la variación temporal de la accesibilidad y su sensibilidad respecto a los umbrales meteoceánicos. Además, la comprensión de su variación espacial puede ser útil en la evaluación de

posibles ubicaciones para la instalación de un parque eólico marino. La mayoría de los estudios anteriores se basan en la evaluación de datos meteorológicos y oceanográficos sólo para pocos puntos dados [112], [113], [115], algunos de ellos también para períodos de tiempo cortos [116].

Este apartado tiene como objetivo proporcionar una definición matemática de varios parámetros de accesibilidad y determinar su variación espacial y temporal en el Mar del Norte, a través de los datos de reanálisis del IH Cantabria. El análisis se centra en el Mar del Norte debido a su importancia en el desarrollo actual y futuro de la energía eólica marina: a principios de 2015 tuvo la mayor proporción de los parques eólicos construidos, en construcción y concedidos en Europa (63,3%, 84,8% y 75%, respectivamente ) [111].

Se han definido parámetros como *aproximabilidad*, *ventana climática*, *tiempo de espera* y *accesibilidad* mediante el uso de la teoría de conjuntos. Se ha definido la *aproximabilidad* (“approachability”) como el porcentaje de tiempo en el cual los parámetros metoceanicos están por debajo de los umbrales de las varias estrategias de acceso. Una *ventana climática* es una serie de instantes de tiempo consecutivos para los cuales la acercabilidad es posible. El *tiempo de espera* es el tiempo entre dos ventanas climáticas de una cierta longitud. Y por último, la *accesibilidad* (“accessibility”) se definió como la acercabilidad por medio de ventanas climáticas de una cierta longitud.

Se evaluaron estos parámetros para todo el Mar del Norte, teniendo en cuenta la estacionalidad y el régimen de la luz del día para dos tipos de actividades: mantenimiento menor y mantenimiento mayor. La disponibilidad de datos de reanálisis con alta resolución espacial y temporal permitió obtener resultados precisos, para el período 1990-2012. Se estudiaron dos casos: acceso con barco o helicóptero para actividades de mantenimiento menores (Caso I) y acceso por medio de buque “jack-up” para actividades de mantenimiento mayores (Caso II). Los sectores

norte y este del Mar del Norte se caracterizan por tener un clima de oleaje más duro, pero también por un recurso eólico más alto (Figura 13 y Figura 14).

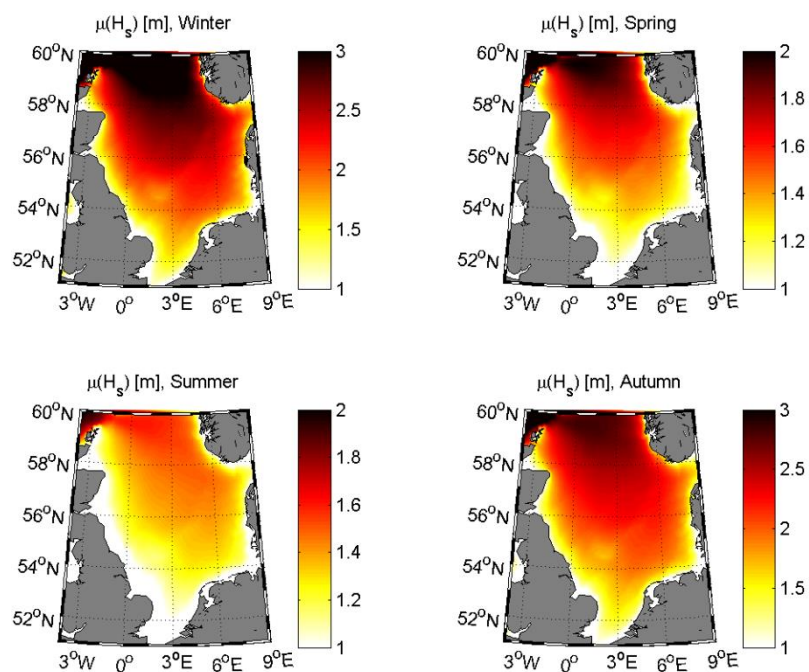


Figura 13: Altura de ola significativa en el Mar del Norte, 1990-2012.

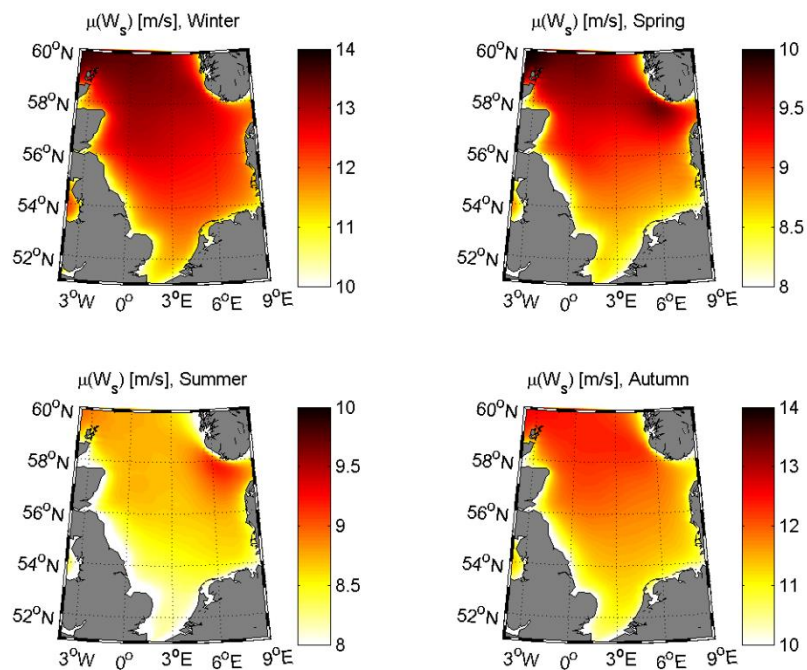


Figura 14: Velocidad media del viento en el Mar del Norte, 1990-2012.

Todos los parámetros de accesibilidad tienen una fuerte estacionalidad (véanse por ejemplo Figura 15, Figura 16 y Figura 17).

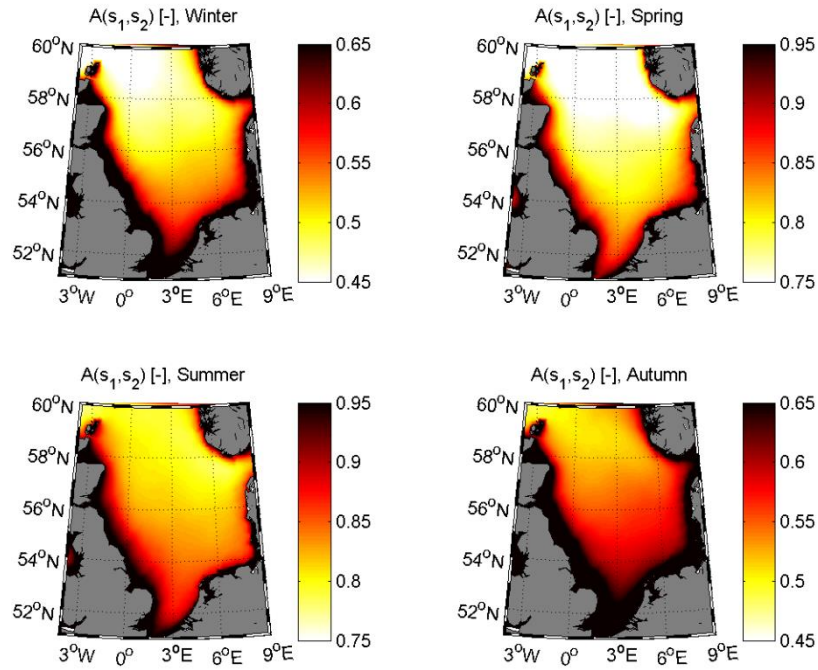


Figura 15: Caso I. Aproximabilidad con barco o helicóptero,  $A(s_1, s_2)$ .

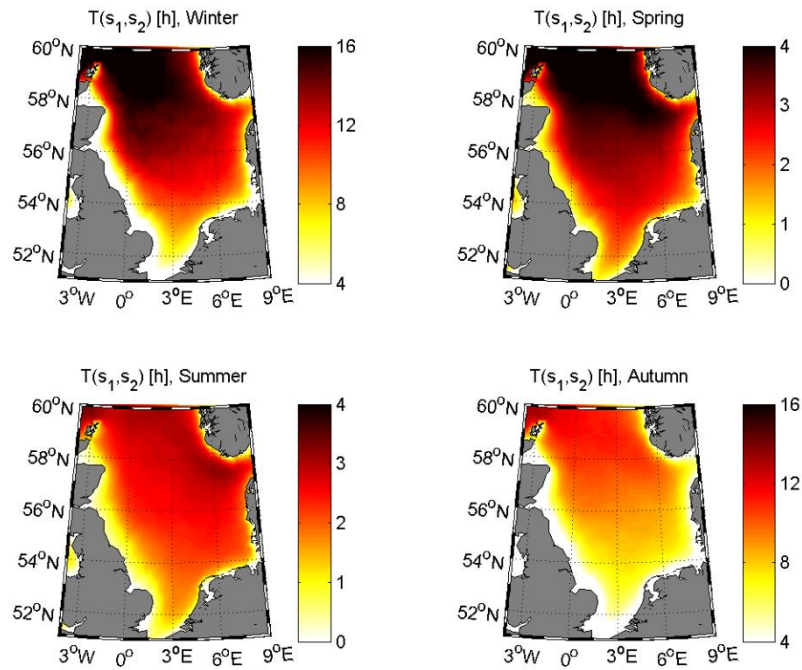


Figura 16: Caso I. Tiempo medio de espera con barco o helicóptero,  $T(s_1, s_2)$ .

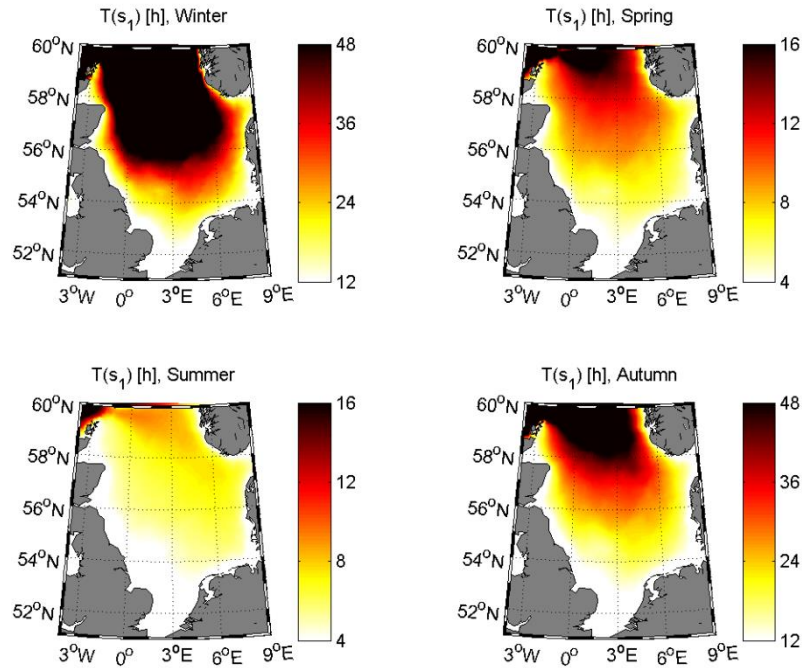


Figura 17: Caso II. Tiempo medio de espera con buque de tipo “jack-up”,  $T(s_1)$

Los resultados se han detallado para varios parques eólicos existentes. Entre ellos, Dogger Bank (Reino Unido) resultó ser el que tiene el recurso eólico más alto pero también los índices más bajos de accesibilidad. Debido a su reducida exposición, Greater Gabbard (Reino Unido) y Thornton Bank III (Bélgica) son los dos parques con tiempo de espera medio en día menor y menos variable (coeficiente de variación de 0.13 para mantenimiento menor, 0.20 para mantenimiento mayor). Estos resultados remarcan la importancia de usar datos de largo plazo a la hora de diseñar estrategias de mantenimiento de parques eólicos marinos.

Finalmente, es muy importante resaltar que los parámetros de accesibilidad pueden cambiar de forma no lineal, tal como se modifican los límites de altura de ola y de velocidad del viento (Figura 18 y Figura 19). La mejora de los medios de acceso es fundamental para poder alcanzar altos valores de disponibilidad de los parques.

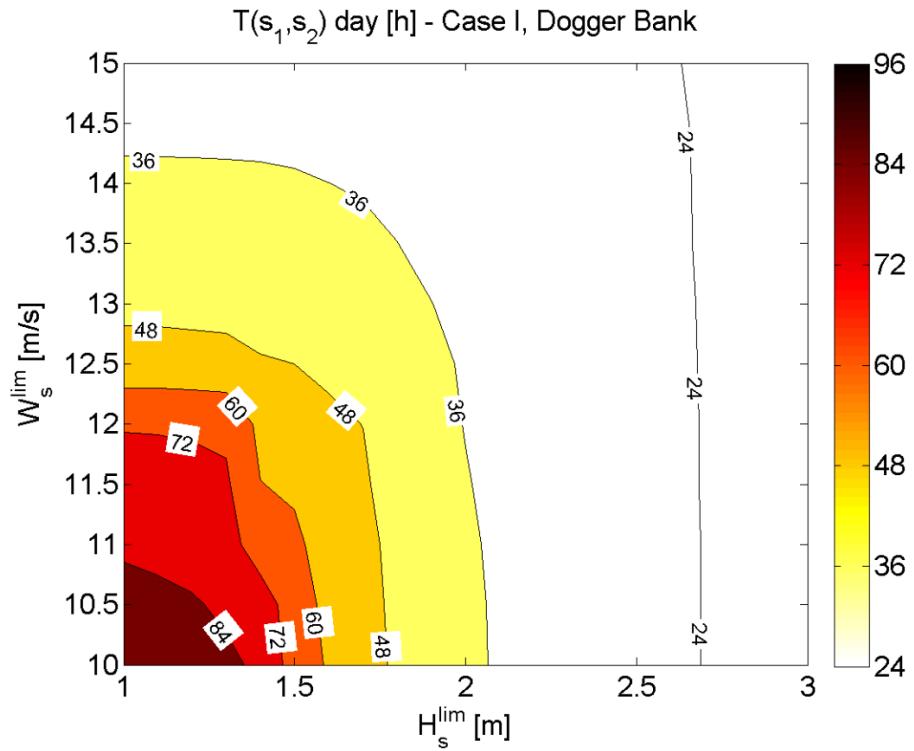


Figura 18: Caso I. Variación del tiempo medio de espera en día en función de los umbrales operacionales. Parque eólico Dogger Bank.

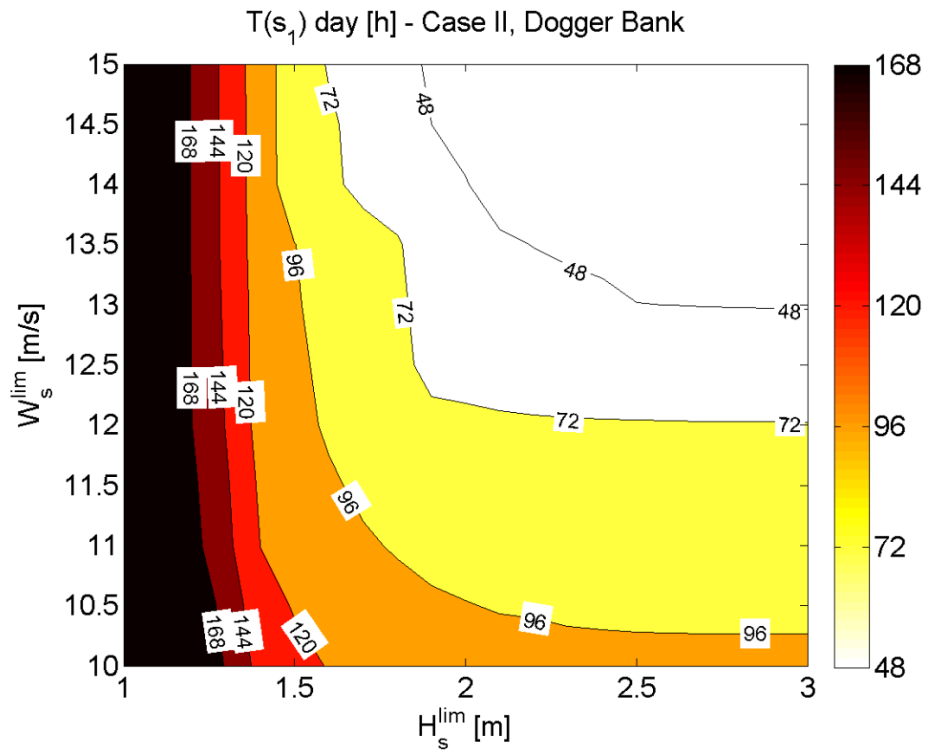


Figura 19: Caso II. Variación del tiempo medio de espera en día en función de los umbrales operacionales. Parque eólico Dogger Bank.

## 7. Modelado del acceso *walk-to-work* a turbinas flotantes

La evaluación de los indicadores de accesibilidad se basa en la definición de los umbrales de seguridad asociados a parámetros meteoceánicos específicos. Por ejemplo, el acceso para mantenimiento menor, que ocurre frecuentemente por medio de buques de pequeño desplazamiento conocidos como Crew Transfer Vessels (CTV), puede realizarse cuando la altura de ola significativa está por debajo de 1.5-2.0 m o por medio de buques de mayor desplazamiento, como es el caso de buques de apoyo offshore (PSV-Platform Support Vessel, OSV-Offshore Support Vessel o ASV-Accommodation Support Vessel) con pasarela de compensación incorporada, cuya transferencia de personal es posible para alturas de ola mayores. Los proveedores de estos buques, por lo general, relacionan la posibilidad de acceso sólo con este parámetro meteoceánico, sin tener en cuenta período o dirección de ola.

Cuando el acceso se realiza mediante embarcaciones, los técnicos suelen caminar directamente desde el buque a la plataforma (concepto *walk-to-work*). El riesgo asociado a la transferencia de personal y el número de incidentes que se produjeron durante operaciones marinas en parques eólicos y plataformas de petróleo [48]–[51] hace necesaria la búsqueda de posibles métodos de diseño para complementar la experiencia de campo de las partes involucradas.

Se necesitan, por tanto, herramientas que puedan predecir la respuesta dinámica de un buque y una plataforma durante la transferencia de técnicos. En la literatura, se ha podido encontrar tan sólo estudios relacionados con aerogeneradores fijos, tanto en el dominio del tiempo [125] como en el dominio de la frecuencia [123]. Sin embargo, estos modelos no evalúan la interacción hidrodinámica entre buque y plataforma. Además, para turbinas flotantes no se han realizado estudios aún, siendo este apartado de la presente tesis totalmente innovador en ese sentido, al ser el primer estudio de accesibilidad para plataformas flotantes.

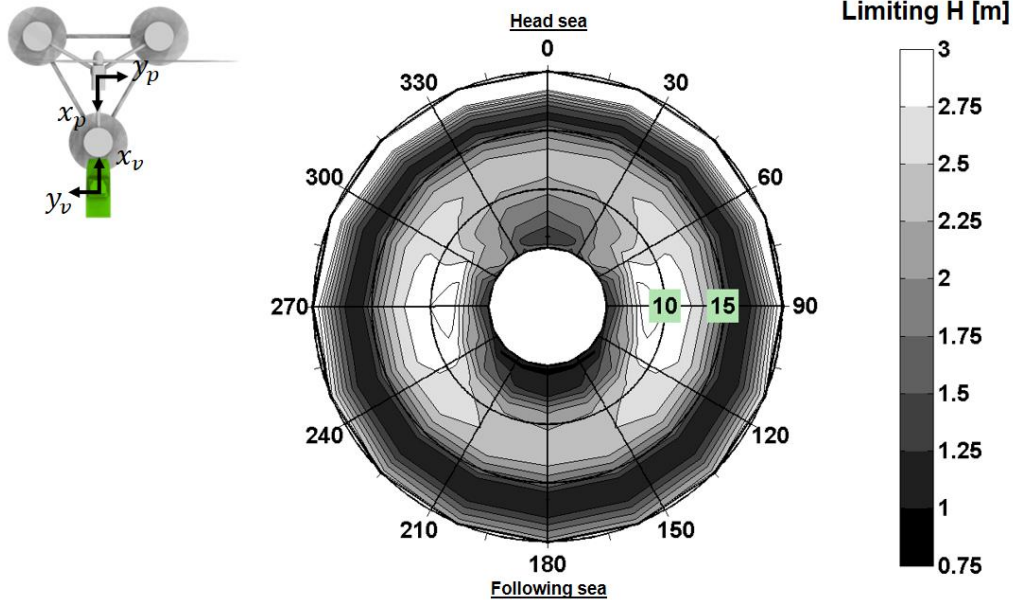
Esta sección tiene como objetivo el desarrollo de una metodología para el cálculo de los movimientos acoplados de una turbina eólica flotante y de un buque de servicio durante la transferencia de personal, para poder definir niveles seguros de accesibilidad. La metodología se basa en los siguientes cuatro puntos:

- *Definición de la ecuación de movimiento para el sistema acoplado buque-plataforma.* El sistema multi-cuerpo se ha modelado en el dominio de la frecuencia [94], donde los coeficientes hidrodinámicos han sido calculados por medio del programa SESAM de DNV [95]. Además, se han modelado posibles fuerzas de contacto debidas a vínculos cinemáticos entre los dos cuerpos según la formulación de Sun [126].
- *Linealización de las fuerzas del sistema de fondeo.* La plataforma flotante está anclada al fondo marino por medio de varias líneas de fondeo. La relación entre el movimiento de la plataforma y las fuerzas del sistema de fondeo no es lineal, por lo que esta relación se ha linealizado por medio de simples consideraciones de cinemática de cuerpos rígidos.
- *Linealización de las fuerzas de amortiguación viscosas.* Las fuerzas de amortiguamiento viscoso en el agua tampoco son lineales (están formadas por una componente lineal y otra no lineal). En muchos ensayos físicos o numéricos se modela este comportamiento por medio de coeficientes cuadráticos. Tales fuerzas se han linealizado a través de una técnica conocida como linealización armónica [127]. De esta forma, igualando el trabajo hecho por la fuerza no lineal cuadrática en un ciclo de ola al trabajo hecho por la fuerza lineal equivalente en el mismo ciclo de ola, se obtienen los coeficientes de amortiguamiento lineales.
- *Cálculo de respuestas extremas.* Bajo la hipótesis de linealidad, es posible calcular la varianza de un proceso por medio de su función de transferencia y del espectro del oleaje,

para un cierto estado de mar. Suponiendo que las crestas de dicho proceso siguen una distribución de Rayleigh, es posible calcular su respuesta extrema por medio de funciones estadísticas [57], [128]. Una vez calculado el valor máximo esperado para procesos específicos (fuerzas de contacto, movimiento relativo entre cuerpos), esto se puede comparar con umbrales de seguridad dados para establecer la posibilidad de acceso a la plataforma flotante.

Se han tenido en cuenta dos tipos de buques en el presente estudio: un CTV de tipo catamarán de 24 m de eslora equipado con defensa o fender (CTV24) y un buque de apoyo a plataformas de 80 m de eslora equipado con una pasarela con sistema de compensación de movimientos (PSV80).

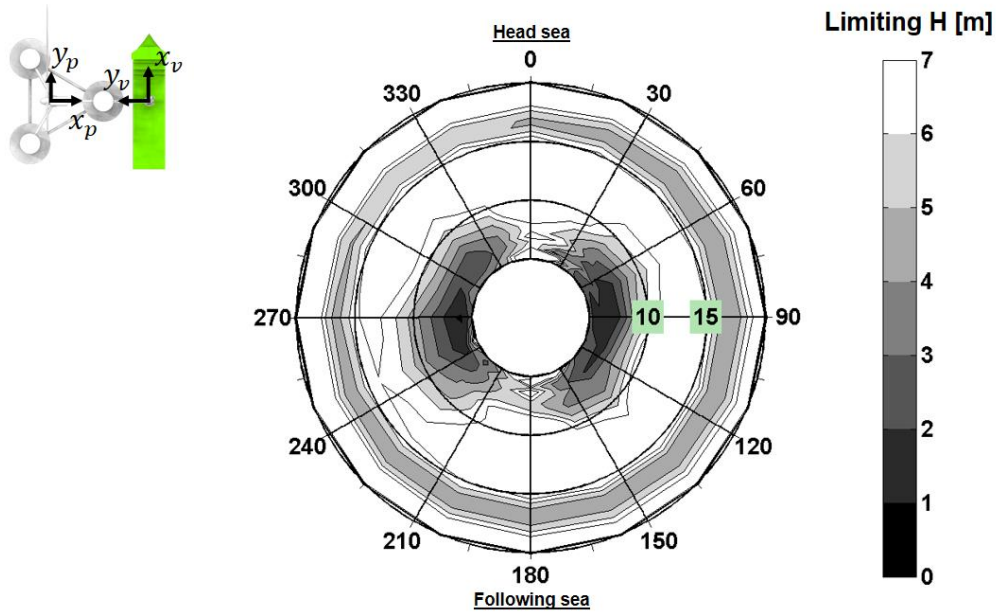
Para el CTV24, el punto de contacto entre la defensa y los parachoques o *bumpers* de la plataforma flotante se ha modelado como una rotula, desde el punto de vista cinemático. El acceso se ha considerado posible en presencia de condiciones de no-deslizamiento entre buque y plataforma, y pequeñas rotaciones relativas entre los dos cuerpos. Las fuerzas de contacto y las rotaciones relativas dependen del período y del rumbo de las olas. Por tanto, lo mismo ocurre con la altura de ola regular máxima para la cual el acceso es posible (Figura 20). De esta forma, las fuerzas de contacto son mayores cuando el movimiento relativo entre los dos cuerpos es mayor, si los cuerpos pudieran moverse sin vínculos.



### Floating wind turbine

Figura 20: Altura de ola limitante para el sistema OC4-CTV24.

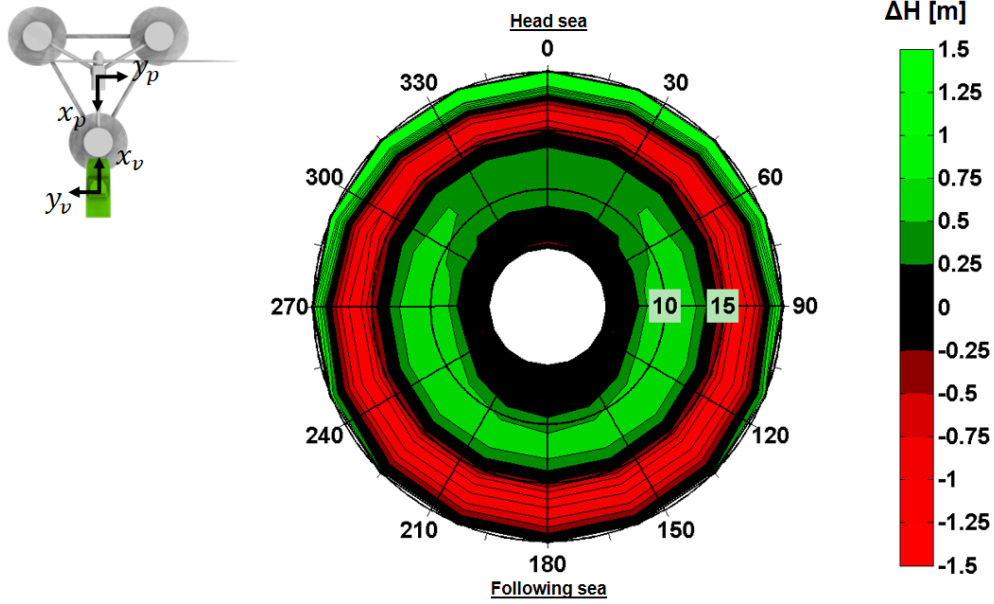
En el caso del PSV80, la pasarela se ha supuesto infinitamente cercana a la plataforma pero sin contacto. El acceso se ha considera posible cuando los movimientos relativos entre la punta de la pasarela y la plataforma flotante están por debajo de los límites de compensación del sistema hidráulico de la pasarela de compensación. Los movimientos relativos y la limitación de altura de las olas regulares dependen tanto del período de las olas como de la dirección de las mismas (Figura 21).



### Floating wind turbine

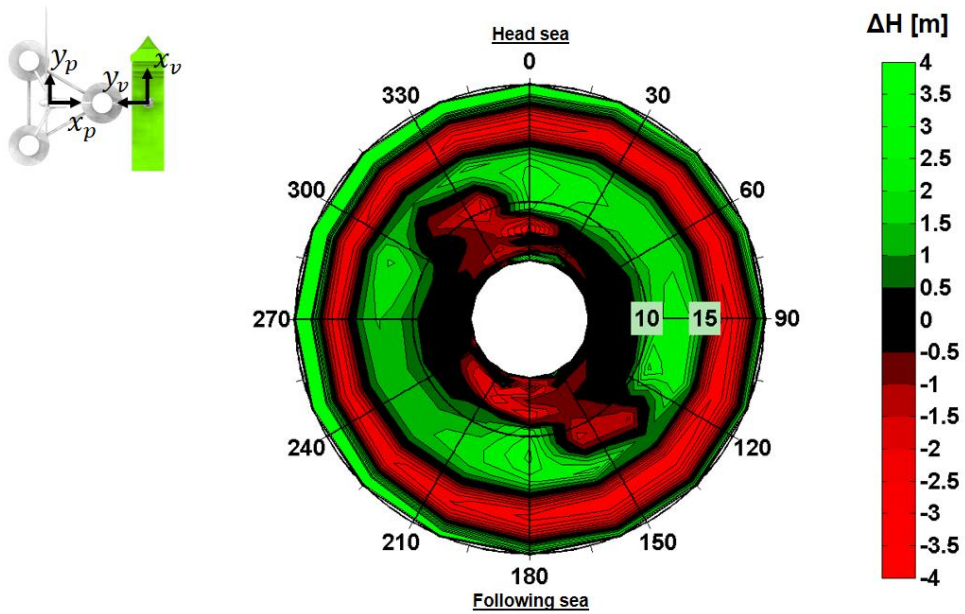
Figura 21: Altura de ola limitante para el sistema OC4-PSV80.

También se ha realizado una comparativa de altura de ola regular máxima entre turbina flotante y turbina fija. Para períodos de ola pequeños (hasta 7-8 s), no se encontraron diferencias entre el acceso a plataforma flotante o a fija. Para los períodos intermedios de oleaje (de 8 a 14 s), el sistema flotante resultó ser más accesible que el sistema fijo. Mientras que para periodos de ola grandes (más de 14 s), cerca del periodo natural de cabeceo de la plataforma, el sistema flotante resulta ser de mucho peor acceso que a la turbina fija (Figura 22 y Figura 23, donde se representa la diferencia entre la altura de ola limitante para turbina flotante y fija).



**Floating VS fixed wind turbine**

Figura 22: Altura de ola limitante para el sistema OC4-CTV24. Turbina fija y turbina flotante.



**Floating VS fixed wind turbine**

Figura 23: Altura de ola limitante para el sistema OC4-PSV80. Turbina fija y turbina flotante.

La aproximabilidad a largo plazo desde CTV y PSV a plataforma flotante se ha calculado para la ubicación en alta mar de Aguçadoura, Portugal. La acercabilidad media mediante CTV24

fue del 13.8% (50 días al año). Variar el coeficiente de fricción estática de la defensa del buque o el factor de confianza en el cálculo de las respuestas extremas da origen a una variación no-lineal de los resultados, haciendo que se suba o baje en función de diferentes combinaciones ese porcentaje de *acercabilidad*. La altura de ola significativa admisible estuvo en un rango de 1.0-1.5 m. Además, se ha encontrado una marcada variabilidad estacional de los resultados, junto a una gran variabilidad año tras año.

Para el PSV80, la accesibilidad media fue de un 75.8% (277 días al año). También en este caso, la variación de los parámetros del sistema (límites de compensación y del factor de confianza) ha producido una correlación no lineal respecto a los resultados de accesibilidad. La altura de ola significativa máxima llegó a valores entre 3.0-4.5 m. Al igual que para el CTV24, se ha registrado una fuerte variabilidad temporal de los resultados (tanto estacional como anual).

La metodología propuesta puede representar una valiosa fuente de información para la toma de decisiones durante la transferencia de personal técnico de O&M hacia y desde plataformas flotantes offshore. En la etapa de diseño, puede ayudar a elegir el buque más adecuado y la mejor estrategia de O&M, teniendo en cuenta las características del parque eólico específico. De la misma forma, también se considera una buena metodología para la optimización en función de la accesibilidad de buques de transferencia de personal y de pasarelas de compensación.

## **8. Impacto de los fallos sobre la producción de un parque flotante**

El acceso a un parque eólico marino es generalmente necesario para llevar a cabo actividades de inspección rutinarias o de mantenimiento/sustitución de componentes rotos.

Las actividades rutinarias se pueden planificar con antelación desde el punto de vista logístico. Por lo general tienen lugar durante los meses de verano y conciernen a los componentes

más relevantes del parque eólico [40]. Por el contrario, las actividades no rutinarias, tales como mantenimiento o sustitución de componentes rotos son difíciles de programar debido a la naturaleza aleatoria de los fallos y pueden afectar a cualquier componente del parque eólico. Las averías que ocurren en invierno pueden imponer largos tiempos de parada debido a la ocurrencia de condiciones climáticas adversas que retrasan el acceso. Esto hace que la producción anual se vea afectada, ya que el invierno es también el periodo donde el recurso eólico suele ser más alto. A largo plazo, esto trae incertidumbres que se reflejan en un aumento del riesgo financiero para los inversores y operadores de parques eólicos.

Con el fin de reducir los costes de O&M, el operador busca un equilibrio entre la disponibilidad de las turbinas y los costes de mantenimiento. Esto se puede obtener diseñando estrategias de inspección y mantenimiento a largo plazo basadas en las características específicas del parque eólico operado.

La evaluación de tales estrategias de operación puede llevarse a cabo mediante herramientas numéricas. A lo largo de los años, se ha desarrollado una amplia variedad de modelos para modelar los costes de operación y mantenimiento [129], siendo la mayoría de ellos confidenciales o no disponibles para su uso fuera de las respectivas empresas promotoras. Hasta donde llega el conocimiento del autor, ninguno de ellos incluye la posibilidad de simular plataformas flotantes.

Esta sección tiene por objetivo desarrollar un marco básico para la evaluación del impacto del tiempo de parada, debido a fallos y paradas operativas, en la producción de energía a largo plazo de una parque eólico flotante. La metodología propuesta se basa en los siguientes pasos:

- *Modelización de fallos y reparaciones a través de un modelo de eventos discretos.* La ocurrencia de fallos y reparaciones (“eventos”) se ha simulado aleatoriamente mediante

funciones de distribución exponencial y normal logarítmica, respectivamente. La línea temporal de los eventos constituye el marco para poder simular la vida útil del parque.

- *Modelización de paradas operacionales a través de un modelo de turbina eólica flotante.* El modelo de evaluación de las paradas operacionales ha sido desarrollado y detallado en la Sección 5 de este Capítulo.
- *Modelización de los efectos de estela en el parque a través de un modelo de parque.* Con el fin de extraer de manera eficaz energía del viento, una turbina tiene que variar la cantidad de movimiento axial del flujo por medio de una fuerza axial [97]. En consecuencia, la velocidad de flujo detrás del aerogenerador se reduce, hasta que se recupere el valor no perturbado aguas abajo. Esto significa que, dentro de un parque, las turbinas aguas abajo pueden recibir una velocidad del viento inferior a la no perturbada y, por lo tanto, generar menos energía. Este fenómeno se ha simulado por medio del modelo de Jensen [133], [134].
- *Integración de los modelos y simulación de la vida útil del parque.* Los modelos de fallos, de paradas operacionales y de efectos de estela en el parque se han integrado. Como la ocurrencia de fallos se ha modelado de manera aleatoria, es necesario simular un elevado número de vidas útiles hasta que la función de distribución de la energía producida ha sido estadísticamente estable. Es decir, la simulación se para cuándo las muestras que se van añadiendo a la distribución no varían sus parámetros estadísticos (media, desviación típica, curtosis y asimetría).

La metodología desarrollada se ha aplicado a un parque eólico flotante situado en la costa de Santander, España. Se ha necesitado simular unas 5000 vidas útiles hasta que la distribución de la energía producida fuese estadísticamente estable. Entre los parámetros estudiados, la curtosis es

la que ha necesitado más simulaciones (Figura 24). La distribución de la energía producida se adapta bien a una distribución normal para todos los casos estudiados (Figura 25)

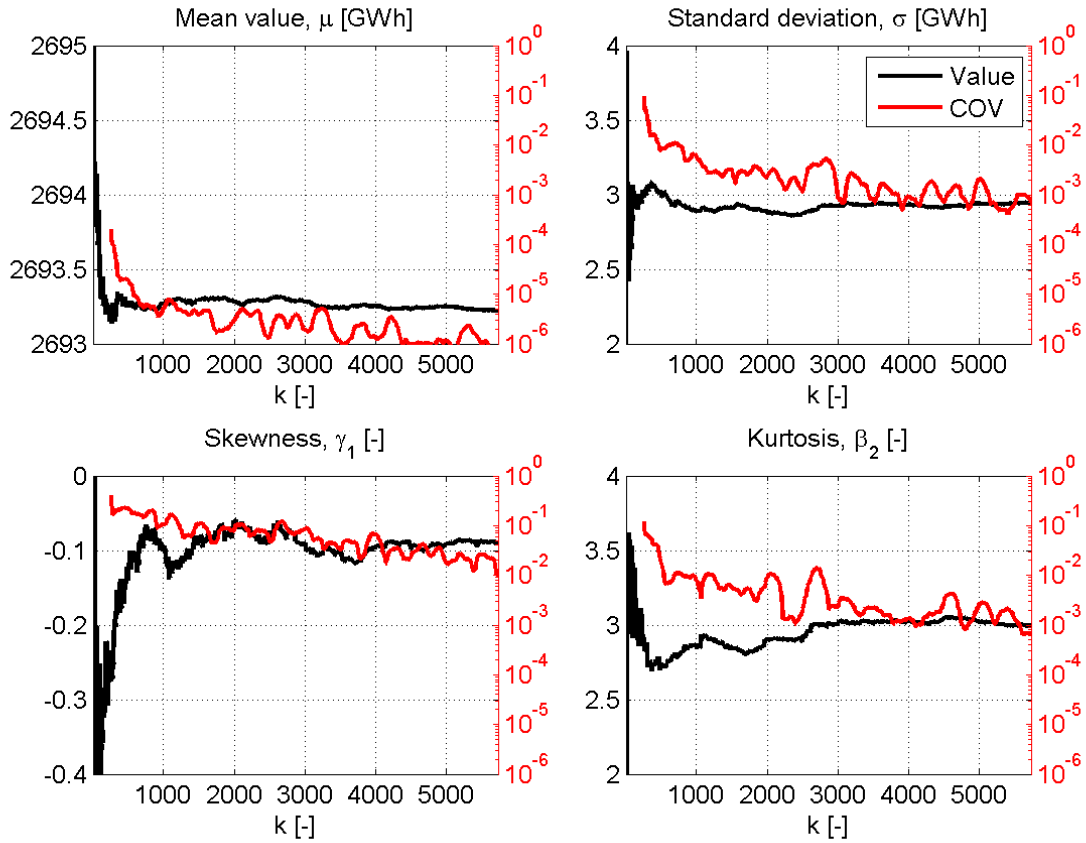


Figura 24: Variación de las estadísticas de la producción de energía, en función del número de bloques de simulación.

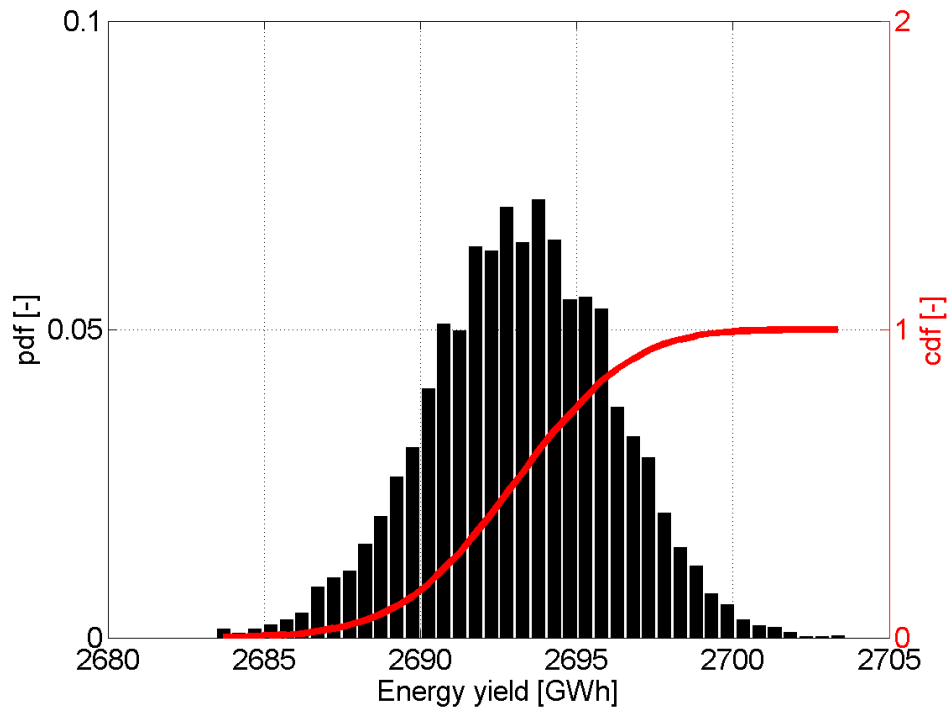


Figura 25: pdf y cdf de la producción de energía.

El tiempo de inactividad asociado a los fallos (tasas de fallo de turbinas en tierra) da una disminución de 1.49% de la producción media, en comparación con el caso sin fallos.

Se ha observado que la producción media baja con la probabilidad de excedencia de la aceleración del buje, las tasas de fallo y los tiempos de reparación medios. Del mismo modo, la desviación estándar de la producción aumenta con esos parámetros. Los resultados se han detallado en las Tabla 2, Tabla 3 y Tabla 4.

$x_{lim}$ [ $m s^{-2}$ ]	$Pr(x > x_{lim})$ [%]	$\mu(E)$ [GWh]	$\sigma(E)$ [GWh]	$\Delta\mu(E)$ [%]	$\Delta\sigma(E)$ [%]
0.25	16.3%	1588.5	1.72	-41.1%	-41.6%
0.30	10.1%	1956.0	2.08	-27.5%	-29.4%
0.35	5.7%	2240.6	2.38	-16.9%	-19.2%
0.40	3.0%	2443.5	2.61	-9.4%	-11.4%
0.45	1.1%	2596.1	2.80	-3.8%	-4.8%

Tabla 2: Estadísticas de la producción de energía (influencia de las paradas operacionales).

$\Delta\lambda$ [%]	$\mu(\mathbf{E})$ [GWh]	$\sigma(\mathbf{E})$ [GWh]	$\Delta\mu(\mathbf{E})$ [%]	$\Delta\sigma(\mathbf{E})$ [%]
25%	2687.0	3.26	-0.4%	10.7%
50%	2676.6	3.54	-0.8%	20.3%
75%	2666.1	3.85	-1.2%	30.7%
100%	2655.7	4.08	-1.6%	38.7%
125%	2645.4	4.33	-1.9%	47.1%

Tabla 3: Estadísticas de la producción de energía (influencia de las tasas de fallo).

$\Delta\mu_r$ [%]	$\mu(\mathbf{E})$ [GWh]	$\sigma(\mathbf{E})$ [GWh]	$\Delta\mu(\mathbf{E})$ [%]	$\Delta\sigma(\mathbf{E})$ [%]
25%	2687.0	3.61	-0.4%	22.7%
50%	2676.6	4.23	-0.8%	43.7%
75%	2666.1	4.88	-1.2%	65.8%
100%	2655.7	5.55	-1.6%	88.4%
125%	2645.4	6.21	-1.9%	111.0%

Tabla 4: Estadísticas de la producción de energía (influencia de los tiempos medios de reparación).

## 9. Conclusiones

El objetivo general de esta tesis es reducir en la medida de lo posible la incertidumbre y los riesgos (tanto financieros como de trabajo) asociados a la operación y mantenimiento a largo plazo de parques eólicos flotantes. Este último apartado contiene un conjunto de soluciones que se espera puedan dar pautas útiles a los operadores de los futuros parques eólicos marinos.

En el apartado 5 se ha ilustrado una metodología para evaluar la influencia de las paradas operacionales en la producción a largo plazo de una turbina eólica flotante. El resultado principal ha sido el cálculo de grandes aceleraciones para velocidades del viento relativamente bajas. Esto sugiere que las paradas operacionales para turbinas flotantes pueden estar asociadas a parámetros de oleaje, además de a la velocidad del viento. Esta metodología se puede utilizar para encontrar un buen compromiso entre fiabilidad y producción de futuras instalaciones marinas.

En el apartado 6 se han presentado los resultados de un amplio análisis de accesibilidad en el Mar del Norte. La variación espacial y temporal de los parámetros de accesibilidad se ha calculado utilizando 23 años de datos meteoceánicos. Se estudiaron dos actividades de mantenimiento (menor y mayor) que se caracterizan por tener diferentes requisitos relativos a las

condiciones meteorológicas y oceánicas. Los resultados tienen una fuerte estacionalidad y una gran variabilidad anual a lo largo de los años analizados. Además, se ha encontrado que la accesibilidad es muy sensible a los umbrales de acceso de las diferentes estrategias de mantenimiento. Los resultados de este apartado indican la importancia del uso de base de datos de largo plazo para el diseño de estrategias de O&M. Además, ponen de relieve la necesidad de investigación e innovación en el desarrollo de sistemas de acceso para parques eólicos.

En el apartado 7 se ha propuesto una metodología para evaluar la accesibilidad *walk-to-work* a plataformas eólicas flotantes en alta mar desde dos estrategias de transferencia diferentes: a través de buque de pequeños desplazamiento por empuje y a través de buque de gran desplazamiento con pasarela de compensación de movimientos. Los resultados han indicado que la altura de ola máxima para la que la transferencia de personal sea posible, depende en gran medida del período y del rumbo del oleaje. Además, se ha expuesto que el acceso a plataformas flotantes no es necesariamente más difícil que para estructuras fijas, dependiendo por supuesto de los periodos propios de los cuerpos que intervienen y de las condiciones de oleaje. Esta metodología de evaluación de acceso puede ayudar al diseño de nuevos buques o la operación de los ya existentes, con el fin de maximizar la eficiencia y la seguridad de las operaciones de transferencia de personal de O&M.

Por último, en el apartado 8 se ha presentado una metodología para evaluar el impacto del tiempo de inactividad en la producción de energía de un parque eólico flotante. Se ha podido cuantificar el impacto de los fallos y de las paradas operacionales sobre la producción y su incertidumbre a largo plazo. Los resultados han indicado que los fallos en si no generan mucha variabilidad en la producción a largo plazo del parque eólico. De hecho, las tasas de fracaso utilizadas son relativamente bajas. La incertidumbre se relaciona con los patrones metoceanicos

presentes cuando se produce el fallo. Aunque esto ya fuese una circunstancia conocida, ha sido interesante cuantificarlo por medio de un estudio detallado. Esta metodología puede representar un buen punto de partida para el desarrollo de un modelo integrado de simulación de O&M para parques flotantes offshore.

Este trabajo ha sido realizado con pasión y dedicación. Las metodologías se han desarrollado según los conocimientos científicos del autor y de su valioso grupo de trabajo. Se han mostrado los resultados con la mayor honestidad y espíritu crítico posible. El autor espera que esta tesis sea una fuente de inspiración para otros ingenieros y científicos, y que pueda ayudar de alguna forma al progreso del sector de la energía renovable.

### Scientific contribution of this thesis

---

---

#### Papers published or under review in peer reviewed SCI journals

- Martini, M., Guanche, R., Losada, I.J., Vidal, C., 2016. *Accessibility assessment for operation and maintenance of offshore wind farms in the North Sea*, **Wind Energy**, doi: 10.1002/we.2028 (published online).
- Guanche, R., Martini, M., Jurado, A., Losada, I.J., 2016. *Walk-to-work accessibility assessment for floating offshore wind turbines*, **Ocean Engineering**, 116, 216–225. doi:10.1016/j.oceaneng.2016.03.013 (published online).
- Martini, M., Guanche, R., Armesto, J.A., Losada, I.J., Vidal, C., 2015. *Met-ocean conditions influence on floating offshore wind farms power production*. **Wind Energy**. Vol. 19(3), 399-420, doi:10.1002/we.1840.
- Martini, M., Jurado, A., Guanche, R., Losada, I.J., 2016. *Probabilistic assessment of floating wind turbine access by catamaran vessel*, **Energy Procedia**, Vol. 95 249-260, special issue for 13<sup>th</sup> Deep Sea Offshore Wind R&D Conference, EERA DeepWind'2016. doi: 10.1016/j.egypro.2016.09.233.
- Martini, M., Guanche, R., Losada-Campa, I., Losada, I.J. 2016. *The impact of downtime over the long-term energy yield of a floating wind farm*, **Renewable Energy**, under review.

## Papers in other journals

- Martini, M., de Andres, A., 2015. *INORE: The International Network on Offshore Renewable Energy*. **Energia, Ambiente e Innovazione - ENEA**. doi:10.12910/EAI2015-051.
- Jurado, A., Martini, M., Guanche, R., Losada, I.J., 2016. *Modelo para el análisis de la accesibilidad de personal a plataformas flotantes: W2W (walk-to-work)*, **Ingenieria Naval**, N. 944.

## Conference papers

- Martini, M.; Jurado, A.; Guanche, R.; Losada, I.J., 2016. *Evaluation of walk-to-work accessibility for a floating wind turbine*, in: **ASME 35th International Conference on Ocean, Offshore and Arctic Engineering**. Busan, South Korea, June 19–24, 2016. Volume 6: Ocean Space Utilization; Ocean Renewable Energy. Paper No. OMAE2016-54416, pp. V006T09A038; 8 pages, doi:10.1115/OMAE2016-54416.
- Martini, M., Guanche, R., Armesto, J.A., Losada, I., 2015. *Met-ocean conditions influence over floating wind turbine energy production*, in: **ASME 34th International Conference on Ocean, Offshore and Arctic Engineering**. St. John's, NL, Canada, May 31–June 5, 2015. Volume 9: Ocean Renewable Energy. Paper No. OMAE2015-41078, pp. V009T09A056; 8 pages, doi:10.1115/OMAE2015-41078.
- Martini, M., Guanche, R., Armesto, J.A., Losada, I., 2015. *Long-term floating wind turbine performance under met-ocean conditions*, in: **EWEA Offshore**. Copenhagen, Denmark.

## Conference posters

- Martini, M., Guanche, R., Armesto, J.A., Losada, I.J., 2015. *Life span performance assessment of a floating offshore wind turbine*, in: **Bilbao Marine Energy Week**. Bilbao, Spain.
- Martini, M., Guanche, R., Losada, I.J., 2015. Definition of O&M strategies for floating Wind farms, in: **INORE European Symposium**, Naples, Italy.
- Martini, M., Guanche, R., Losada, I.J., 2014. Definition of O&M strategies for floating Wind farms, in: **INORE European Symposium**, La Vega, Spain.

---

---

## References

---

---

- [1] International Energy Agency, “Key world energy statistics 2015,” 2016.
- [2] US Energy Information Administration, “International energy statistics,” 2016. [Online]. Available:  
<https://www.eia.gov/cfapps/ipdbproject/IEDIndex3.cfm?tid=44&pid=44&aid=1>.  
[Accessed: 30-Apr-2016].
- [3] International Energy Agency, “Renewable energy medium-term market report 2015,” 2015.
- [4] REN21, “Renewables 2015 global status report,” 2016.
- [5] International Energy Agency, “World energy outlook 2015,” 2016.
- [6] Frankfurt School of Finance & Management, “Global trends in renewable energy investment 2015,” 2015.
- [7] International Renewable Energy Agency, “Renewable energy technologies: cost analysis series - Wind power,” 2012.
- [8] United Nations, “Human settlements on the coast,” 2016. [Online]. Available:  
<http://www.oceansatlas.org/servlet/CDSServlet?status=ND0xODc3JjY9ZW4mMzM9KiYzNz1rb3M~>.
- [9] windpoweroffshore.com, “Dong announces Vindeby decommissioning,” 2016. [Online]. Available: <http://www.windpoweroffshore.com/article/1382887/dong-announces-vindeby-decommissioning>. [Accessed: 19-Apr-2016].
- [10] Global Wind Energy Council, “Global wind statistics 2015,” 2016.
- [11] European Wind Energy Association, “The European offshore wind industry – key trends

## References

---

- and statistics 2015,” 2016.
- [12] ewea.org, “Record 13bn euro invested in offshore wind in 2015: 3GW new capacity,” 2016. [Online]. Available: <http://www.ewea.org/news/detail/2016/02/02/record-13bn-euro-invested-in-offshore-wind-in-2015-3gw-new-capacity/>. [Accessed: 19-Apr-2016].
- [13] European Wind Energy Association, “Green growth: the impact of wind energy on jobs and the economy,” 2012.
- [14] International Renewable Energy Agency, “Renewable power generation costs in 2014,” 2015.
- [15] Financial Times, “Dong Energy in offshore wind cost breakthrough,” 05-Jul.
- [16] OffshoreWIND.biz, “Vattenfall Wins Kriegers Flak Tender with EUR 49.9 per MWh Bid.” .
- [17] European Wind Energy Association, “Deep water - The next step for offshore wind energy,” 2013.
- [18] National Oceanic and Atmospheric Administration, “GSHHG - A Global Self-consistent, Hierarchical, High-resolution Geography Database.” [Online]. Available: <http://www.ngdc.noaa.gov/mgg/shorelines/gshhs.html>. [Accessed: 12-Nov-2016].
- [19] S. Butterfield, W. Musial, J. Jonkman, and P. Sclavounos, “Engineering challenges for floating offshore wind turbines,” National Renewable Energy Laboratory. NREL/CP-500-38776. Golden, CO, USA, Report, 2007.
- [20] Statoil, “Hywind demo,” 2015. [Online]. Available: [www.statoil.com](http://www.statoil.com). [Accessed: 22-Oct-2015].
- [21] offshoreWIND.biz, “First Hywind Scotland foundation taking shape.” [Online]. Available: <http://www.offshorewind.biz/2016/03/18/first-hywind-scotland-foundation-taking-shape/>. [Accessed: 19-Apr-2016].

## References

---

- [22] Statoil, “Hywind Scotland Pilot Park,” 2015. [Online]. Available: <http://www.statoil.com/en/TechnologyInnovation/NewEnergy/RenewablePowerProduction/Offshore/HywindScotland>. [Accessed: 08-Oct-2015].
- [23] Principle Power, “WindFloat,” 2015. [Online]. Available: <http://www.principlepowerinc.com/>. [Accessed: 22-Oct-2015].
- [24] Principle Power, “WindFloat pacific OSW project.” Sacramento, CA, USA, 2014.
- [25] I. Ishishara and T. Shigeru, “Fukushima floating offshore wind farm demonstration project (Fukushima FORWARD) - Construcion of phase I,” 2013.
- [26] I. Ishishara and T. Shigeru, “Fukushima floating offshore wind farm demonstration project (Fukushima FORWARD) - Construcion of phase II,” 2015.
- [27] fukushima-forward.jp, “The installation of ‘Fukushima Hamakaze’ in the testing area.” [Online]. Available: [http://www.fukushima-forward.jp/english/news\\_release/news160801.html](http://www.fukushima-forward.jp/english/news_release/news160801.html). [Accessed: 12-Nov-2016].
- [28] GL Garrad Hassan, “Cost of energy of floating wind,” 2012.
- [29] J. Phillips, O. Fitch-Roy, P. Reynolds, and P. Gardner, “A guide to UK offshore wind operations and maintenance,” 2013.
- [30] Y. Feng, P. J. Tavner, and H. Long, “Early experiences with UK Round 1 offshore wind farms,” in *Proceedings of the Institution of Civil Engineers: energy*, 2010, pp. 167–181.
- [31] Fraunhofer IWES, “Availability of offshore wind farms,” 2016. [Online]. Available: [http://windmonitor.iwes.fraunhofer.de/windmonitor\\_en/4\\_Offshore/4\\_zuverlaessigkeit/3\\_Verfuegbarkeit/](http://windmonitor.iwes.fraunhofer.de/windmonitor_en/4_Offshore/4_zuverlaessigkeit/3_Verfuegbarkeit/). [Accessed: 31-Mar-2016].
- [32] Dong Energy, “Anholt offshore wind farm reaches mileston,” 2014. [Online]. Available: <http://www.dongenergy.com/en/media/newsroom/news/articles/anholt-offshore-wind->

## References

---

- farm-reaches-milestone.
- [33] Subsea world news, “Fault on sea cable to Anholt offshore wind farm,” 2015. [Online]. Available: <http://subseaworldnews.com/2015/02/23/subsea-cable-defect-at-anholt-owf/>. [Accessed: 08-Oct-2015].
- [34] Subsea world news, “Anholt Subsea Cable Fixed,” 2015. [Online]. Available: <http://subseaworldnews.com/2015/03/25/anholt-subsea-cable-fixed/>. [Accessed: 08-Oct-2015].
- [35] London Array consortium, “Generation mileston for London Array.” [Online]. Available: <http://www.londonarray.com/project/generation-milestone-for-london-array/>. [Accessed: 31-Mar-2016].
- [36] Power Engineering International, “The London Array turns two,” 2015. [Online]. Available: <http://www.powerengineeringint.com/articles/print/volume-23/issue-8/features/the-london-array-turns-two.html>. [Accessed: 31-Mar-2016].
- [37] windpoweroffshore.com, “Bard 1 transmission problems continue,” 2014. [Online]. Available: <http://www.windpoweroffshore.com/article/1297004/bard-1-transmission-problems-continue>. [Accessed: 31-Mar-2016].
- [38] offshorewindindustry.com, “Troubleshooting continues,” 2014. [Online]. Available: <http://www.offshorewindindustry.com/news/troubleshooting-continues>. [Accessed: 31-Mar-2016].
- [39] Douglas-Westwood, “Global offshore wind project d atabase,” 2011.
- [40] Det Norske Veritas, “Design of Offshore Wind Turbine Structures,” DNV-OS-J101, 2014.
- [41] Det Norske Veritas, “Design of Floating Wind Turbine Structures,” DNV-OS-J103, 2013.
- [42] Det Norske Veritas, “Offshore Substations for Wind Farms,” DNV-OS-J201, Report, 2013.

## References

---

- [43] S. Faulstich, B. Hahn, and P. J. Tavner, “Wind turbine downtime and its importance for offshore deployment,” *Wind Energy*, vol. 14, no. 3, pp. 327–337, 2010.
- [44] F. . Spinato, P. J. . Tavner, G. J. W. . van Bussel, and E. . Koutoulakos, “Reliability of wind turbine subassemblies,” *Renew. Power Gener. IET*, vol. 3, pp. 387–401, 2009.
- [45] C. Knudsen Tveiten, E. Albrechtsen, J. Heggset, M. Hofmann, E. Jersin, B. Leira, and P. K. Norddal, “HSE challenges related to offshore renewable energy,” SINTEF. Trondheim, Norway, 2011.
- [46] W. Yang, P. J. Tavner, C. J. Crabtree, Y. Feng, and Y. Qiu, “Wind turbine condition monitoring: technical and commercial challenges,” *Wind Energy*, vol. 17, no. 5, pp. 673–693, May 2014.
- [47] D. Coronado and K. Fischer, “Condition monitoring of wind turbines: state of the art, user experience and recommendations,” 2015.
- [48] International Association of Oil & Gas Producers, “Water transport accident statistics,” Report No. 434 – 10, 2010.
- [49] J. Spouge, P. Strong, and R. Proctor, “Risks of marine transfer of personnel offshore,” 2014.
- [50] International Marine Contractors Association, “Safety flashes,” 2015. [Online]. Available: <http://www.imca-int.com/safety-environment-and-legislation/safety-flashes.aspx>.
- [51] The Crown Estate, “Offshore wind operational report 2015,” 2016.
- [52] Det Norske Veritas, “Marine Operations, General,” DNV-OS-H101, 2011.
- [53] Det Norske Veritas, “Marine Operations, Design and Fabrication,” DNV-OS-H102, Report, 2012.
- [54] G9 Offshore Wind Health and Safety, “Good practice guideline working at height in the offshore wind industry,” 2014.

## References

---

- [55] International Marine Contractors Association, “Transfer of personnel to and from offshore vessels,” 2010.
- [56] Sgurr Energy Ltd., “Offshore wind and marine energy health and safety guidelines,” 2014.
- [57] Det Norske Veritas, “Environmental Conditions and Environmental Loads,” DNV-RP-C205, 2010.
- [58] A. Smith, T. Stehly, and W. Musial, “2014-2015 Offshore wind technologies market report,” 2015.
- [59] J. Jacquemin, D. Butterworth, C. Garret, N. Baldock, and A. Henderson, “Inventory of location specific wind energy cost,” 2011.
- [60] B. Maples, G. Saur, M. Hand, R. van de Pietermen, and T. Obdam, “Installation, operation and maintenance strategies to reduce the cost of offshore wind energy,” National Renewable Energy Laboratory. NREL/TP-5000-57403. Boulder, CO, USA, 2013.
- [61] BVG Associates, “Pathways to cost reduction in offshore wind technology: technology workstream,” 2012.
- [62] International Energy Agency, “Technology roadmap - Wind energy,” 2013.
- [63] GL Garrad Hassan, “Offshore Wind - Operations and maintenance opportunities in Scotland - An insight into opportunities for Scottish ports and the O&M supply chain,” 2013.
- [64] Deloitte, “Establishing the investment case wind power,” 2015.
- [65] BVG Associates, “UK content analysis of Robin Rigg offshore wind farm operations and maintenance,” 2012.
- [66] K. Onogi, J. Tsutsui, H. Koide, M. Sakamoto, S. Kobayashi, H. Hatsushika, T. Matsumoto, N. Yamazaki, H. Kamahori, K. Takahashi, S. Kadokura, K. Wada, K. Kato, R. Oyama, T. Ose, N. Mannoji, and R. Taira, “The JRA-25 Reanalysis,” *J. Meteorol. Soc. Japan*, vol. 85,

## References

---

- pp. 369–432, 2007.
- [67] E. Kalnay, M. Kanamitsu, R. Kistler, W. Collins, D. Deaven, L. Gandin, M. Iredell, S. Saha, G. White, J. Woollen, Y. Zhu, M. Chelliah, W. Ebisuzaki, W. Higgins, J. Janowiak, K. C. Mo, C. Ropelewski, J. Wang, A. Leetmaa, and others, “The NCEP/NCAR 40 year reanalysis project,” *Bull. Am. Meteorol. Soc.*, vol. 77, no. 3, pp. 437–471, 1996.
- [68] S. Uppala, P. W. Kallberg, A. J. Simmons, U. Andrae, V. Da Costa Bechtold, M. Fiorino, J. K. Gibson, J. Haseler, A. Hernandez, G. A. Kelly, X. Li, K. Onogi, S. Saarinen, N. Sokka, R. P. Allan, E. Andersson, K. Arpe, M. A. Balmaseda, and others, “The ERA-40 Re-Analysis,” *Q. J. R. Meteorol. Soc.*, vol. 131, no. 612, pp. 2961–3012, 2005.
- [69] B. G. Reguero, M. Menéndez, F. J. Méndez, R. Mínguez, and I. J. Losada, “A Global Ocean Wave (GOW) calibrated reanalysis from 1948 onwards,” *Coast. Eng.*, vol. 65, pp. 38–55, 2012.
- [70] H. L. Tolman, “User manual and system documentation of WaveWatch-III version 3.14,” U. S. Department of Commerce, National Oceanic and Atmospheric Administration, National Weather Service, National Centers for Environmental Prediction. Camp Springs, MD, USA, 2009.
- [71] N. Booij, R. Ris, and L. Holthuijsen, “A third generation wave model for coastal region, I: model description and validation,” *J. Geophys. Res.*, vol. 104, no. C4, pp. 7649–7666, 1999.
- [72] P. Camus, F. J. Mendez, and R. Medina, “A hybrid efficient method to downscale wave climate to coastal areas,” *Coast. Eng.*, vol. 58, no. 9, pp. 851–862, 2011.
- [73] P. Camus, F. J. Mendez, R. Medina, A. Tomas, and C. Izaguirre, “High resolution downscaled ocean waves (DOW) reanalysis in coastal areas,” *Coast. Eng.*, vol. 72, pp. 56–68, 2013.

## References

---

- [74] M. Menéndez, A. Tomas, M. García-Díez, L. Fita, J. Fernández, F. J. Méndez, and I. J. Losada, “A methodology to evaluate regional-scale offshore wind energy resources,” in *OCEANS 2011 IEEE*, 2011.
- [75] W. C. Skamarock, J. B. Klemp, J. Dudhia, D. O. Gill, D. M. Baker, M. G. Duda, X.-Y. Huang, W. Wang, and J. G. Powers, “A description of the advanced research WRF version 3,” National Center for Atmospheric Research, Boulder, CO, USA, 2008.
- [76] D. P. Dee, S. M. Uppala, A. J. Simmons, P. Berrisford, P. Poli, S. Kobayashi, U. Andrae, M. A. Balmaseda, G. Balsamo, P. Bauer, P. Bechtold, A. C. M. Beljaars, L. van de Berg, J. Bidlot, N. Bormann, C. Delsol, R. Dragani, and others, “The ERA-Interim reanalysis: configuration and performance of the data assimilation system,” *Q. J. R. Meteorol. Soc.*, vol. 137, no. 656, pp. 553–597, 2011.
- [77] Alpha Ventus Consortium, “Alpha Ventus fact sheet,” 2015. [Online]. Available: [http://www.alpha-ventus.de/fileadmin/user\\_upload/av\\_Factsheet\\_engl\\_Dec2012\\_2.pdf](http://www.alpha-ventus.de/fileadmin/user_upload/av_Factsheet_engl_Dec2012_2.pdf). [Accessed: 08-Oct-2015].
- [78] J. Jonkman, S. Butterfield, W. Musial, and G. Scott, “Definition of a 5-MW reference wind turbine for offshore system development,” National Renewable Energy Laboratory. NREL/TP-500-38060. Golden, CO, USA, 2009.
- [79] A. Robertson, J. Jonkman, M. Masciola, H. Song, A. Goupee, A. Coulling, and C. Luan, “Definition of the semisubmersible floating system for phase II of OC4,” National Renewable Energy Laboratory. NREL/TP-5000-60601. Golden, CO, USA, 2014.
- [80] American Bureau of Shipping, “Floating offshore wind turbines installations,” 2014.
- [81] “Long-term stochastic dynamic analysis of a combined floating spar-type wind turbine and wave energy converter (STC) system for mooring fatigue damage and power Prediction,”

## References

---

- in *ASME 342th International Conference on Ocean, Offshore and Arctic Engineering*, 2014.
- [82] J. Amundsen, “Consequences of introducing a cut-out wave height on a floating wind turbine concept,” Norwegian University of Life Sciences, 2013.
- [83] Y. Guanche, R. Guanche, P. Camus, F. J. Mendez, and R. Medina, “A multivariate approach to estimate design loads for offshore wind turbines,” *Wind Energy*, vol. 16, no. 7, pp. 1091–1106, 2013.
- [84] R. Guanche, L. Meneses, J. Sarmiento, C. Vidal Pascual, and I. J. Losada, “Methodology to obtain the life cycle mooring loads on a semisubmersible wind platform,” in *ASME 33rd International Conference on Ocean, Offshore and Arctic Engineering*, 2014.
- [85] T. Hastie, R. Tibshirani, and J. Friedman, *The Elements of Statistical Learning*. New York, USA: Springer, 2001.
- [86] T. Kohonen, *Self-Organizing Maps*, 3rd ed. Berlin, Germany: Springer-Verlag, 2000.
- [87] R. W. Kennard and L. A. Stone, “Computer aided design experiments,” *Technometrics*, vol. 11, pp. 137–148, 1969.
- [88] P. Camus, F. J. Mendez, R. Medina, and A. S. Cofiño, “Analysis of clustering and selection algorithms for the study of multivariate wave climate,” *Coast. Eng.*, vol. 58, no. 6, pp. 453–462, 2011.
- [89] G. Jeans, R. Gibson, and O. Jones, “A new quantitative assessment of current profile clustering methods for riser engineering,” in *ASME 34th International Conference on Ocean, Offshore and Arctic Engineering*, 2015.
- [90] P. Willet, “Molecular diversity techniques for chemical databases,” *Inf. Res.* 2, vol. 3, 1996.
- [91] A. Polinsky, R. Feinstein, S. Shi, and A. Kuki, “Librain: software for automated design of exploratory and targeted combinational libraries,” in *Molecular Diversity and*

## References

---

- Combinatorial Chemistry*, A. C. Society, Ed. Washington D.C., USA, 1996, pp. 219–232.
- [92] W. E. Cummins, “The impulse response function and ship motions,” in *Symposium on Ship Theory*, 1962.
- [93] O. Faltinsen, *Sea Loads on Ships and Offshore Structures*. Cambridge, UK: Cambridge University Press, 1993.
- [94] T. Ogilvie, “Recent progress towards the understanding and prediction of ship motions,” in *5th Symposium on Naval Hydrodynamics*, 1964.
- [95] Det Norske Veritas, “SESAM user manual HydroD,” 2011.
- [96] A. D. de Andrés, R. Guanache, J. A. Armesto, F. del Jesus, C. Vidal, and I. J. Losada, “Time domain model for a two-body heave converter: model and applications,” *Ocean Eng.*, vol. 72, pp. 116–123, 2013.
- [97] M. O. L. Hansen, *Aerodynamics of wind turbines*. London, UK: Earthscan, 2008.
- [98] J. Jonkman, “Dynamics modeling and loads analysis of an offshore floating wind turbine,” National Renewable Energy Laboratory. NREL/TP-500-41958. Golden, CO, USA, 2007.
- [99] M. Karimirad and T. Moan, “A simplified method for coupled analysis of floating offshore wind turbines,” *Mar. Struct.*, vol. 27, no. 1, pp. 45–63, 2012.
- [100] T. J. Larsen and A. M. Hansen, “How 2 HAWC2, the user’s manual,” 2007.
- [101] T. J. Larsen and T. D. Hanson, “A method to avoid negative damped low frequent tower vibrations for a floating, pitch controlled wind turbine,” *J. Phys. Conf. Ser. - Sci. Mak. Torque from Wind*, vol. 75, 2007.
- [102] B. Skaare and F. G. Nielsen, “Blade pitch control in a wind turbine installation,” 13/131,620, 2013.
- [103] S. W. Smiths, *Digital Signal Processing*. Newton, MA, USA: Newnes, 2003.

## References

---

- [104] M. Masciola, “Instructional and theory guide to the Mooring Analysis Program,” Boulder, CO, 2013.
- [105] B. S. Kallesøe, U. S. Paulsen, A. Køhler, and H. F. Hansen, “Aero-hydro-elastic response of a floating platform supporting several wind turbines,” in *49th AIAA Aerospace Sciences Meeting including the New Horizons Forum and Aerospace Exposition*, 2011.
- [106] R. Franke, “Scattered data interpolation: test of some methods,” *Math. Comput.*, vol. 38, pp. 181–200, 1982.
- [107] S. Rippa, “An algorithm for selecting a good value for the parameter  $c$  in radial basis function interpolation,” *Adv. Comput. Math.*, pp. 193–210, 1999.
- [108] International Electrotechnical Commission, “Wind turbines - Part 1: Design Requirements,” IEC 61400-1, 2005.
- [109] J. Jonkman and M. Buhl Jr, “FAST User’s Guide,” National Renewable Energy Laboratory. NREL/EL-500-38230. Golden, CO, USA, 2005.
- [110] O. J. Waals and R. R. T. van Dijk, “Truncation methods for deep water mooring systems for a catenary moored FPSO and a semi taut moored semi submersible,” in *Deep offshore technology conference*, 2004.
- [111] European Wind Energy Association, “The European offshore wind industry – key trends and statistics 2014,” 2015.
- [112] N. Silva and A. Estanqueiro, “Impact of weather conditions on the windows of opportunity for operation of offshore wind farms in Portugal,” *Wind Eng.*, vol. 257–268, no. 3, p. 37, 2013.
- [113] G. J. W. van Bussel and W. A. A. M. Bierbooms, “Analysis of different means of transport in the operation and maintenance strategy for the reference DOWEC offshore wind farm,”

- in *OWEMES Offshore Wind and other marine renewable Energy in Mediterranean and European Seas*, 2003.
- [114] W. A. A. M. van Bussel, G J W; Bierbooms, “The DOWEC offshore reference windfarm: analysis of transportation for operation and maintenance,” *Wind Eng.*, vol. 27, pp. 381–391, 2003.
- [115] J. Dowell, A. Zitrou, L. Walls, and T. Bedford, “Analysis of wind and wave data to assess maintenance access to offshore wind farms,” in *ESREL 22nd European Safety and Reliability Association Conference*, 2013.
- [116] M. O’Connor, T. Lewis, and G. Dalton, “Weather window analysis for Irish west coast wave data with relevance to operations & maintenance of marine renewables,” *Renew. Energy*, vol. 52, pp. 57–66, 2013.
- [117] L. Rademakers and H. Braam, “O&M aspects of the 500 MW offshore wind farm at NL7,” Energy Research Center of the Netherlands. Petten, Netherlands, 2002.
- [118] R. P. van de Pieterman, H. Braam, T. S. Obdam, L. Rademakers, and T. J. J. van der Zee, “Optimisation of maintenance strategies for offshore wind farms,” in *The Offshore Conference*, 2011.
- [119] E. Dogget, G. H. Kapla, and P. K. Seidelmann, “Almanac for computers,” Washington D.C., USA, 1978.
- [120] “4coffshore.com.” [Online]. Available: [www.4coffshore.com](http://www.4coffshore.com). [Accessed: 09-Mar-2015].
- [121] D. J. Salzmann, “Ampelmann - Development of the Access System for Offshore Wind Turbines,” Uitgeverij BOXPress, Oisterwijk, Delft, Netherlands, 2010.
- [122] J. Van Der Tempel, F. W. Gerner, D. J. Cerda, and A. J. Gobel, “Vessel, a motion platform, a control system, a method for compensating motions of a vessel and a computer program

- product,” United States Patent and Trademark Office, USA, Patent, 2013.
- [123] M. Wu, “Numerical analysis of docking operation between service vessels and offshore wind turbines,” *Ocean Eng.*, vol. 91, pp. 379–388, 2014.
- [124] I. B. Sperstad, E. E. Halvorsen-Weare, M. Hofmann, L. M. Nonås, M. Stålhane, and M. Wu, “A Comparison of Single- and Multi-parameter Wave Criteria for Accessing Wind Turbines in Strategic Maintenance and Logistics Models for Offshore Wind Farms,” *Energy Procedia*, vol. 53, pp. 221–230, 2014.
- [125] D. González, M. Lemmerhirt, M. Abdel-Maksoud, M. König, and A. Duster, “Numerical and experimental investigation regarding the landing of a catamaran vessel at an offshore wind turbine in waves,” in *ASME 34th International Conference on Ocean, Offshore, and Arctic Engineering*, 2015.
- [126] L. Sun, R. Eatock Taylor, and Y. S. Choo, “Response of interconnected floating bodies,” *IES J. Part A Civ. Struct. Eng.*, vol. 4, no. 3, pp. 143–156, 2011.
- [127] T. I. Fossen, *Handbook of Marine Craft Hydrodynamics and Motion Control*. Trondheim, Norway: John Wiley & Sons, 2011.
- [128] L. H. Holthuijsen, *Waves in Oceanic and Coastal Waters*. New York: Cambridge University Press, 2007.
- [129] M. Hofmann, “A review of decision support tools for offshore wind farms with an emphasis on operation and maintenance strategies,” *Wind Eng.*, vol. 35, no. 1, pp. 1–16, 2011.
- [130] M. Hofmann and I. B. Sperstad, “NOWIcob – A Tool for Reducing the Maintenance Costs of Offshore Wind Farms,” *Energy Procedia*, vol. 35, pp. 177–186, 2013.
- [131] Det Norske Veritas, “Operations planning (O2M) for offshore wind farms,” 2016. [Online]. Available: <https://www.dnvgl.com/services/operations-planning-o2m-for-offshore-wind->

## References

---

- farms-5158. [Accessed: 20-Nov-2016].
- [132] R. Bovaird and H. Zagor, “Lognormal distribution and maintainability in support system research,” *Nav. Res. Logist. Q.*, vol. 8, pp. 343–356, 2006.
- [133] N. O. Jensen, “A note on wind generator interaction,” Risø National Laboratory. RISØ-M-2411. Roskilde, Denmark, 1984.
- [134] N. O. Jensen, I. Katic, and J. Høstrup, “A simple model for cluster efficiency,” in *European Wind Energy Association Conference and Exhibition*, 1986.
- [135] offshoreWIND.biz, “Offshore wind support schemes: current status of European support schemes.” [Online]. Available: <http://www.offshorewind.biz/2015/01/19/offshore-wind-support-schemes-current-status-of-european-support-schemes/>. [Accessed: 19-Apr-2016].

This page is intentionally left blank.

This page is intentionally left blank.



Defended on 7<sup>th</sup> April 2017

Environmental Hydraulics Institute "IHCantabria"

C/Isabel Torres 15, 39011

Santander, Spain.